Supercurrent and dynamics in carbon nanotube Josephson Junction in the Kondo regime

Diana Watfa

▶ **To cite this version:**

Diana Watfa. Supercurrent and dynamics in carbon nanotube Josephson Junction in the Kondo regime. Quantum Physics [quant-ph]. Université Paris-Saclay, 2020. English. NNT : 2020UP-ASP015 . tel-03164238

HAL Id: tel-03164238

https://theses.hal.science/tel-03164238v1

Submitted on 9 Mar 2021

HAL is a multi-disciplinary open access archive for the deposit and dissemination of scientific research documents, whether they are published or not. The documents may come from teaching and research institutions in France or abroad, or from public or private research centers.

L'archive ouverte pluridisciplinaire **HAL**, est destinée au dépôt et à la diffusion de documents scientifiques de niveau recherche, publiés ou non, émanant des établissements d'enseignement et de recherche français ou étrangers, des laboratoires publics ou privés.

Thèse de doctorat

NNT: 2020UPASP015

Supercurrent and dynamics in carbon nanotube Josephson Junction in the Kondo regime

Thèse de doctorat de l'Université Paris-Saclay

École doctorale n°564, physique en Île-de-France (PIF)
Spécialité de doctorat: Physique
Unité de recherche: Université Paris-Saclay, CNRS, Laboratoire de Physique des Solides, 91405, Orsay, France.
Référent: Faculté des sciences d'Orsay

Thèse présentée et soutenue à Orsay, le 30 Septembre 2020, par

Diana Watfa

Composition du jury:

M. Pascal Simon Professeur, Université Paris-Saclay	Président du jury
M. Franck Balestro Maitre de conférence, Université Grenoble Alpes	Rapporteur
Mme. Julia Meyer Professeure, Université Grenoble Alpes	Rapporteur
M. Fabio Pistolesi Directeur de recherche, Laboratoire Ondes et Matière d'Aquitaine, Bordeaux	Examinateur
M. Takis Kontos Directeur de recherche, Laboratoire Pierre Aigrain, Paris	Examinateur
M. Richard Deblock Directeur de recherche, Laboratoire de Physique des Solides, Orsay	Directeur de thèse
M. Meydi Ferrier Maitre de conférence, Université Paris-Saclay	Invité

To the beautiful soul of my mother

who taught me about dreams and how to catch them

Acknowledgment

In spring 2017, I have joined the mesoscopic physics group at LPS-Orsay for my master 2 internship. Then I got the opportunity to do a Ph.D. with the same group. Today, after 3 years I am leaving them and, in my pocket, besides my Ph.D. degree, a lot of joy, memories, and gratitude. These three years have been a long and rich adventure, full of invaluable research and personal experience and it is my pleasure to thank those who made it possible.

Foremost, I would like to express my sincere gratitude to my advisor Richard Deblock for giving me the opportunity to do research and providing invaluable guidance throughout this work. Your patience, motivation, enthusiasm, and immense knowledge helped me in all the time of research and writing of this thesis. You taught me everything: starting from how to fabricate samples, carry out the experiment, and most important the methodology to carry out the research and to present it as clearly as possible. Thank you for being always available when I needed your advice, help, and for carefully reading and amending my thesis manuscript. I learned a lot of things under your supervision and I really cannot find the right words to properly express how much I am grateful to you.

Besides my advisor, I would like to thank my thesis committee: Pascal Simon, Julia Meyer, Franck Balestro, Takis Kontos, Fabio Pistolesi, and Meydi Ferrier for their acceptance to evaluate my work and for their insightful comments and discussions.

Many thanks also to Helene Bouchiat, Meydi Ferrier, and Sophie Guéron for all the discussions, for your time to answer any questions, for the encouragement you gave me at every critical moment, and for your comments on my manuscript and presentation. To all the mesoscopic physics members, Sandrine Autierè-Laurent, Alik Kasumov, Alexei Chepelianskii, Miguel Monteverde, Alexandre Bernard, Jorge Vallejo Bustamante, Ziwei Dou, thanks a lot for your mutual support, help, advice and for the good atmosphere that enabled me to proceed with this work. Thanks to all the former mesoscopic group members who crossed my path during the past three years. Especially my dearest Kamila Yunusova, with whom I have shared the same office and a lot of chocolate, I enjoyed your company and all the conversation we had.

I gratefully acknowledge the great contributions of Tomáš Novotný and Alžběta Kadlecová in this thesis. Their work on the theoretical side was the starting point of the interpretation and understanding of our experimental results. Many thanks go to Raphaëlle Delagrange, my thesis predecessor, first for initiating the experiment I performed during my Ph.D. and second for our many fruitful discussions. Thanks to Julien Basset for letting me be part of the Tungsten nanowires experiment. Thanks also to Raphaël Weil for his constant help in the nanofabrication.

Thanks to Jean-Pierre Dalac, Gilles Guillier, and Pascale Senzier for providing us with the helium needed to perform our experiment. Thanks to the great help of all the administrative staff who have explained to me the basic concepts of the French administration even when I did not speak a word of French. Thank you for your extreme patience: Veronique Thieulart, Ciham Zaaboul, and Marie-France Mariotto. Also, many thanks to Inès Safi and Laura Bocher for their care.

I would like also to thank my master's responsible, Fouad El Haj Hassan, Arnaud Bournel, Pierre Seneor and Thierry Gacion for their permanent support and guidance.

I would like to sincerely thank my friends at the lab, Shayma Essghaier, Brendan Le Pennec, Quentin Barthélemy, and Alex Louat for all the good times and coffee breaks we had together. A big thank goes to my lifelong friends who despite the distance have supported me during all this work: Marwa, Ahmad, Ali, Hanine, and Christine. I wish you all the best of luck!

Of course, one of the fundamental pillars of my life is my family. For that reason, I dedicate this milestone to each of them. My Dad, you have raised me to be strong and independent. But no matter what, I will always be your little girl, and I will always need you. Your endless love, support, and encouragement throughout my life gave me the strength to chase my dreams. Everything I am today is all because of you. I love you.

To my sisters, Linda, Nancy, Zaynab, and Lynn. I do not have the words to tell you how truly fortunate I feel to have you in my life. Thank you for your consistent love and support. Without you, I could not get through the hard times, thank you for being my strong safety net!

A special thank goes to my sister Nancy and her husband Hassan. Since my arrival in France, you have made me feel at home. Thanks a lot for always cheering me up, for all the good times, vacations, weekends we spent together. I am so glad to have you always by my side.

During this journey, I became an aunt for the first time, thank you Bella-Loubna and Fouad junior for lighting up my life. Auntie loves you!

I would like also to thank my husband's family, my mother-in-law, father-in-law, and all the rest: Chaza, Likaa, Houssam, and Hassan, for their love and support. I am so grateful that I became a member of your family.

Thanks to my In-laws, Hassan, and Mohammad for always being by my side. My aunts, uncles, and cousins deserve my wholehearted thanks as well. My aunt, Jamola, whom I lost a few years I go, I cannot thank everyone without mentioning you. I love you and I miss you so much.

Last but not least, to the love of my life, my husband Ibrahim. Getting married was the greatest thing that happened during this journey. Since the first day we met, I felt that with you by my side, I can go through anything. Your care, kindness, support, and trust provided me with the strength to accomplish this work. You were always by my side, in thick and thin. And I will be always there for you as well. You have bestowed me with my biggest source of happiness, that is your love! I will love you forever and always.

To my guardian angel, my beautiful mama. My mind knows that you are in a better place, where there is no pain. But I can feel how close you are because you do live in my heart. I am sure that you are watching and guiding me in every single step I make. I can only hope to one day become half the woman you were: Strong, loving, and patient. I want you to know that I will always love you. Thanks for being a great mum. I hope that you are proud of me.

Thank you, Lord, for always being there for me.

Those 3 years have tough me that I am strong even when I feel weak. That I can go through life's difficult moments, pick myself up, and move forward. Now, I am moving to a new chapter with hope, knowledge, and confidence. I am gratefully blessed for all that I have and looking forward to what is to come.

Contents

Résumé de la thèse

Introduction

Ce travail de thèse s'inscrit dans le cadre de la physique mésoscopique, qui vise à mesurer et comprendre les propriétés électroniques de conducteurs qui sont quantiquement cohérents de par leur faible taille (typiquement en dessous du micron) et du fait de leur basse température (en dessous d'1K). Nous nous sommes particulièrement intéressés aux propriétés de boites quantiques, des systèmes avec un nombre faible et ajustable d'électrons, connectées à des contacts supraconducteurs. On a donc ainsi une jonction Josephson dont la partie normale est constituée par la boite quantique. Cette thèse s'est particulièrement attachée à un aspect relativement peu exploré de ce type de jonctions : leur dynamique. Cela s'est fait en mesurant l'effet Josephson AC d'une telle jonction, réalisée avec une boite quantique constituée par un nanotube de carbone.

L'effet Josephson AC consiste en la génération par une jonction supraconductrice d'un courant oscillant lorsqu'une tension de polarisation lui est appliquée. C'est grâce à cet effet que les jonctions tunnel supraconductrices peuvent être utilisées comme émetteurs haute fréquence, ou bien comme étalon de tension grâce à la précision métrologique de l'effet Josephson AC. Pour des jonctions Josephson impliquant un système conducteur, mesurer l'effet Josephson AC permet de sonder les états qui portent le supercourant à fréquence finie et hors d'équilibre. Ainsi de telles mesures ont démontrées la protection topologique dans différents systèmes topologiques, chose qui n'est pas mesurable avec une mesure DC.

Dans cette thèse, nous avons utilisé l'effet Josephson AC pour induire des transitions dans une jonction Josephson à base de boite quantique entre un état singulet et un état doublet de spin. Dans ce type de jonction, l'interaction Coulombienne conduit au blocage de Coulomb qui amène un état doublet s'il y a un nombre impair d'électrons dans la boite. Cet état doublet entrave le passage des paires des Cooper, ce qui se manifeste par un faible supercourant et un changement de signe de la relation courant-phase. On parle alors de jonction π. Cependant, un état singulet peut être restauré si l'effet Kondo, qui apparait également pour un nombre impair d'électrons, a une échelle d'énergie, fixée par la température Kondo, plus grande que le gap supraconducteur. L'effet Kondo résulte d'une interaction entre une impureté magnétique localisée et les électrons de conduction d'un métal et conduit à un état fortement corrélé avec une résonance Kondo à l'énergie de Fermi des contacts métalliques.

Cette transition entre état doublet et singulet a généré un intérêt théorique important. Expérimentalement, il est à présent bien établi que cette transition peut être induite à l'équilibre par une tension grille, un champ magnétique ou une différence de phase supraconductrice. Une partie de cette thèse est dédiée à la mesure de l'effet Josephson AC dans une jonction Josephson basée sur un nanotube de carbone pour sonder sa dynamique. Cela est réalisé en utilisant une détection

haute-fréquence "on-chip", dans un régime où effet Kondo et effet de proximité coexistent.

Pour améliorer la détection à basse température, nous avons réalisé deux autres expériences. Dans la première nous avons réalisé au laboratoire des lignes de polarisations filtrées, de type filtre passe-bas, avec lesquelles nous avons mesuré la température électronique à l'aide d'un transistor à un électron. Dans la seconde expérience, nous avons fabriqué et mesuré un nouveau type de micro-résonateur supraconducteur utilisant un matériau à forte inductance cinétique, à savoir des nanofils de tungstène déposé sous faisceau d'ions hélium focalisés. Ce type de résonateur pourrait s'avérer très utiles pour le couplage "on-chip" haute-fréquence et ainsi aider à la détection de l'émission Josephson AC de jonctions hybrides.

0.1 Boites quantiques à base de nanotube de carbone

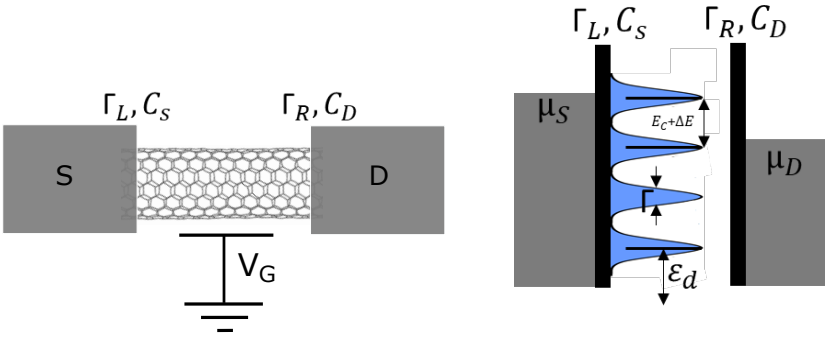

Figure 1: Gauche : schéma d'une boite quantique à base de nanotube de carbone (CNT QD) avec les contacts de source (S), de drain (D) et une grille électrostatique couplée capacitivement à la boite quantique, utilisée pour contrôler le nombre d'électrons. Droite : spectre de niveaux d'énergie discret de la CNT QD, illustrant les différentes échelles d'énergie pertinentes : E_C l'énergie de charge, le couplage aux électrodes de gauche et de droite Γ_L et Γ_R, le couplage total aux électrodes $\Gamma = \Gamma_L + \Gamma_R$, ΔE l'écart entre niveaux et ϵ_d la position du niveau d'énergie.

Les nanotubes de carbone (CNTs) ont une longueur de plusieurs microns pour une largeur de quelques nanomètres. Quand un nanotube est connecté à des électrodes métalliques, il peut se comporter comme une boite quantique pour des transmissions relativement faibles avec les contacts. A cause du confinement des électrons, une boite quantique présente un spectre discret de niveaux électroniques. La figure 1 montre un tel spectre avec des niveaux à une énergie ϵ_d, un écart moyen entre niveaux ΔE, un élargissement Γ due au couplage aux électrodes métalliques et une énergie de charge $E_C = e^2/2C$, avec C la capacité totale de la boite quantique. E_C est l'énergie nécessaire pour ajouter un électron à la boite quantique. Le couplage de la boite aux électrodes métalliques permet d'effectuer des mesures de transport au travers du nanotube.

0.2 Effet Josephson AC dans une boite quantique à base de nanotube de carbone

Dans cette partie, nous présentons les résultats expérimentaux sur la mesure de l'effet Josephson DC et AC dans une boite quantique à base de nanotube de carbone dans le régime Kondo. Nous nous focaliserons sur l'effet Josephson AC, qui constitue la partie centrale de ce travail de thèse.

0.2.1 Dispositif expérimental

Pour mesurer l'émission Josephson d'une jonction Josephson constituée d'un nanotube de carbone connecté à deux électrodes supraconductrices, nous avons choisi de coupler cette jonction à un détecteur quantique. Dans ce travail, le détecteur est une jonction tunnel supraconductrice (une jonction supraconducteur/isolant/supraconducteur (SIS)). Les contacts du nanotube de carbone sont réalisés avec un bicouche palladium/aluminium qui présente un gap de $\Delta_{Pd/Al} = 50 \pm 5\mu eV$. D'autres échantillons avec un tricouche palladium/niobium/aluminium, présentant un gap plus important $\Delta_{Pd/Nb/Al} = 170\mu eV$ ont également été mesurés. Le CNT est couplé au détecteur quantique via un résonateur supraconducteur réalisé sur le même échantillon. Le nanotube et le détecteur sont alors bien couplés seulement aux fréquences de résonance du circuit de couplage, qui sont attendues à $\nu_0 = 12GHz$, $\nu_0 = 31GHz$ et $\nu_0 = 51GHz$. Le dispositif expérimental est représenté sur la figure 2.a.

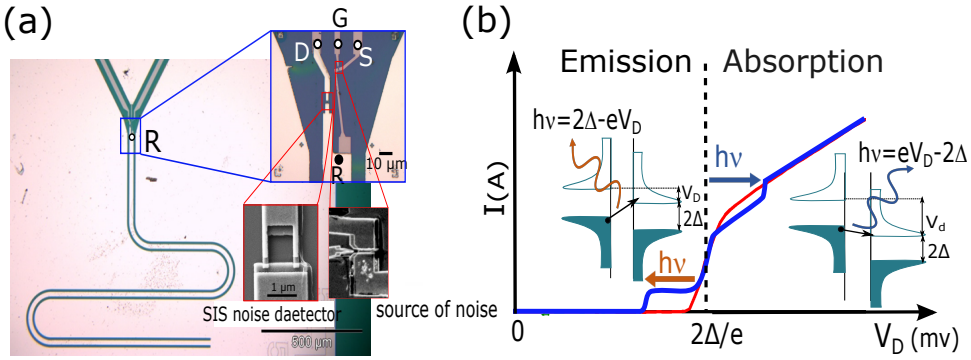

Figure 2: (a) La jonction Josephson à base de nanotube de carbone est couplée au détecteur quantique SIS par un résonateur à ligne de transmission. (b) Courbe rouge : caractéristique courant-tension typique d'une jonction SIS. Courbe bleue : Caractéristique courant-tension calculée du détecteur sous irradiation montrant des marches de courant photo-assisté I_{PAT}. Lorsque le détecteur est polarisé à une tension inférieure à $2\Delta/e$, il est sensible à l'émission de photon par le CNT. Lorsque la tension est supérieure à cette valeur, le détecteur est essentiellement sensible à l'absorption.

La détection de l'émission AC est basée sur la mesure du courant tunnel photo-assisté (PAT) de quasi-particules dans le détecteur SIS. La caractéristique courant-tension typique d'une jonction SIS est montrée sur la figure 2.b. L'absorption ou l'émission de photon d'énergie hν par le détecteur

modifie cette caractéristique courant-tension. Si la jonction détectrice est polarisée avec une tension V_d telle que $\mid V_d \mid < 2\Delta/e$, un courant PAT apparait si un photon d'énergie $h\nu > 2\Delta - \mid V_d \mid$ est absorbé. Ainsi une marche de courant PAT de largeur hν/e apparait sur la caractéristique $I(V)$ avec une amplitude reliée à l'intensité de la radiation absorbée. Le courant PAT est donc directement relié à l'émission haute fréquence du CNT couplé au détecteur.

0.2.2 Résultats expérimentaux

Caractérisation du nanotube dans l'état normal

Pour caractériser l'échantillon et déterminer ces paramètres, à savoir son énergie de charge U, le couplage aux contacts Γ et l'asymétrie des contacts Γ_R/Γ_L, l'échantillon est d'abord mesuré dans l'état normal. Pour cela, un champ magnétique de 0.1T est appliqué pour rendre les contacts Pd/Al normaux. La conductance différentiel dI/dV_{SD} du CNT dans le régime normal est présentée sur la figure 3.a. en fonction de la tension de polarisation V_{SD} et de la tension de grille V_g. Cette méthode de caractérisation nécessite un champ magnétique de plus de 1T pour les échantillons avec contacts de Pd/Nb/Al, ce qui interdit une extraction fiable des paramètres de la boite quantique dans le régime normal. Nous nous focaliserons donc dans la suite sur les échantillons avec les contacts Pd/Al. Il est à noter toutefois que les échantillons avec des contacts Pd/Nb/Al présentent des comportements qualitativement similaires à ceux avec contacts Pd/Al.

Le diagramme de stabilité présente des diamants de Coulomb avec une dégénérescence 4, typique d'une boite quantique à base de CNT sans défaut. Pour un nombre impair d'électrons dans la boite, l'effet Kondo se manifeste par une augmentation de la conductance à tension nulle. Nous nous sommes focalisés sur deux zones Kondo A et B avec un nombre d'électron N=1 et 3. Le maximum de conductance est plus petit que $2e^2/h$, indiquant une légère asymétrie des contacts. Les paramètres de ces deux zones Kondo sont résumés dans le tableau 1. Sur la figure 3 nous montrons également une autre zone de grille, dénommée ci-après la région C, avec une conductance similaire à celle des zones A et B mais sans trace d'effet Kondo.

	T_K(K)	T_K(μeV)	U (meV)	Γ(meV)	a	Δ(meV)	T_K/Δ
Kondo A	1.1	97.9	3.9	0.62	3.3	0.05	1.958
Kondo B	1.7	146.5	4	0.75	2.5	0.05	2.93

Table 1: Paramètres de la boite quantique à base de nanotube de carbone dans les zones Kondo A et B.

Mesure du supercourant

Lorsque le champ magnétique appliqué est ramené à zéro, les contacts du nanotube de carbone deviennent supraconducteurs. La figure 3.b montre la résistance différentielle de l'échantillon en fonction du courant de polarisation et de la tension de grille. La boite quantique présente un supercourant relativement important, modulé par la tension grille, dans la zone présentant de l'effet Kondo en régime normal. C'est une bonne indication que le système se comporte comme une jonction de type 0, avec un état fondamental qui reste l'état singulet de type Kondo. L'amplitude du courant critique, c'est à dire la valeur maximale du supercourant, est déduite de la caractéristique tension-courant de la jonction dans le cadre d'un modèle de jonction avec un shunt résistif et capacitif

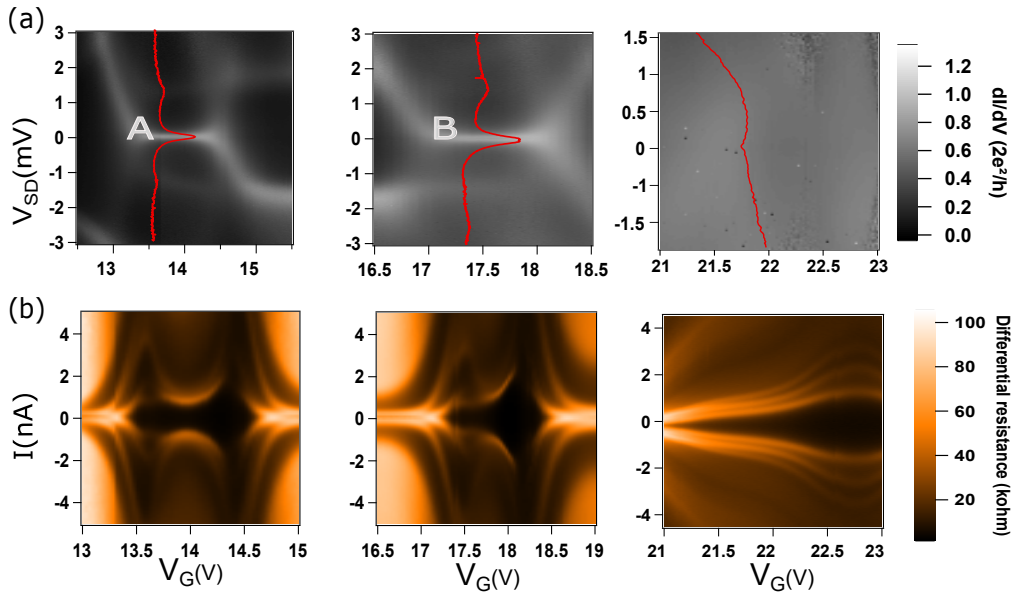

Figure 3: Diagramme de stabilité de la boite quantique à base de nanotube de carbone dans le régime normal. (a) Conductance différentielle dI/dV_{SD} en fonction de la tension de polarisation V_{SD} et de la tension grille V_g. Le nanotube de carbone montre un effet Kondo de type SU(2). Pour un nombre impair d'électrons, deux zones Kondo sont observées dans la zone de grille sélectionnée, l'une pour l'occupation N=1 (zone A) et l'autre pour l'occupation N=3 (zone B). Les courbes de conductance montrées en surimpression (en rouge) sont prises aux tensions grille 14V, 17.5V et 21.5V. (b) Résistance différentielle du CNT en fonction du courant de polarisation et de la tension grille V_g, dans la même zone que (a).

(modèle RCSJ). Ce modèle tient compte de l'environnement électromagnétique de la jonction. Le résultat de ce traitement est montré sur la figure 4.

Une forte réduction de l'émission Josephson

Pour mesurer l'émission Josephson aux fréquences de résonance du circuit de couplage, nous polarisons le détecteur à une tension V_d inférieure au seuil d'apparition du courant de quasi-particules, de telle sorte que 2Δ-h$\nu_0 < eV_d < 2\Delta$ avec ν_0 la fréquence fondamentale du circuit résonant. Cette polarisation est gardée constante pendant la mesure. Nous modulons la tension dans le CNT autour d'une tension donnée et mesurons le courant PAT continu et alternatif au travers du détecteur.

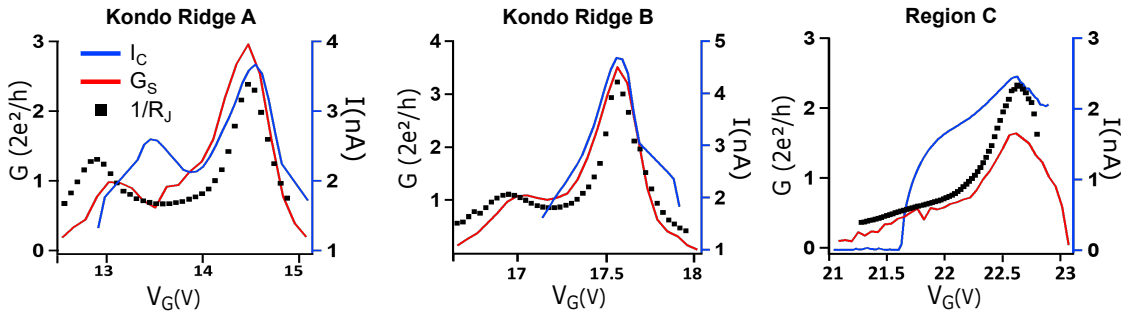

Figure 4: Dépendance en grille du courant critique I_C et de l'inverse de la résistance R_J, extraits du modèle RCSJ (voir texte), ainsi que de la conductance mesurée dans l'état supraconducteur G_s. Les trois zones A, B et C montrent un supercourant et une conductance modulée en grille, avec un comportement très similaire pour $1/R_J$ et G_S.

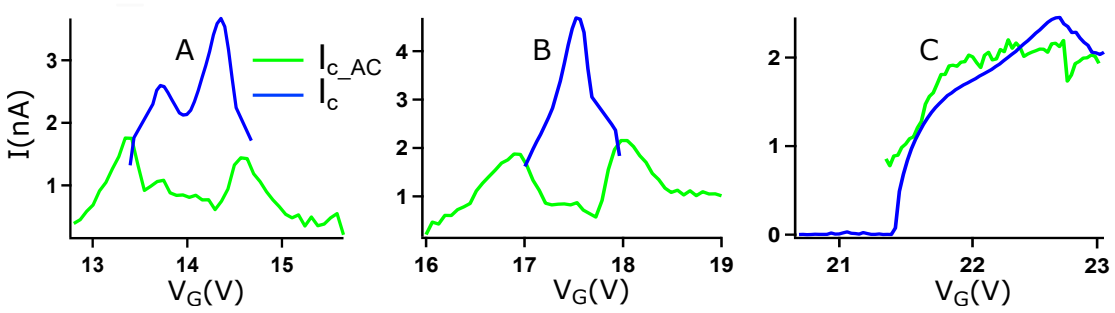

Figure 5: Comparaison du courant critique I_C et du courant critique dynamique I_C^{AC} pour les zones A, B et C.

Sur la figure 5 est tracée l'amplitude de l'effet Josephson AC, notée I_C^{AC} et appelée courant critique dynamique, déduite de l'amplitude du courant PAT. Le résultat principal de cette mesure est que le courant critique dynamique ne suit pas le comportement du courant critique dans les zones présentant de l'effet Kondo dans le régime normal. En effet il y a une forte réduction de ce courant critique dynamique près du centre des régions Kondo A et B, alors que c'est précisément la zone où le courant critique est augmenté grâce aux corrélations Kondo. Cette réduction n'a pas lieu dans la zone C pour laquelle le courant critique dynamique suit le même comportement que le courant critique. La forte diminution du courant critique dans les zones Kondo A et B suggère que la jonction Josephson à base de CNT se comporte alors dynamiquement comme une jonction π, alors que le comportement statique est celui d'une jonction 0. C'est le résultat central de cette thèse.

Interprétation

Pour avoir une compréhension quantitative du comportement de la boite quantique dans les régions A et B nous avons effectué des calculs basés sur les techniques numériques du groupe de

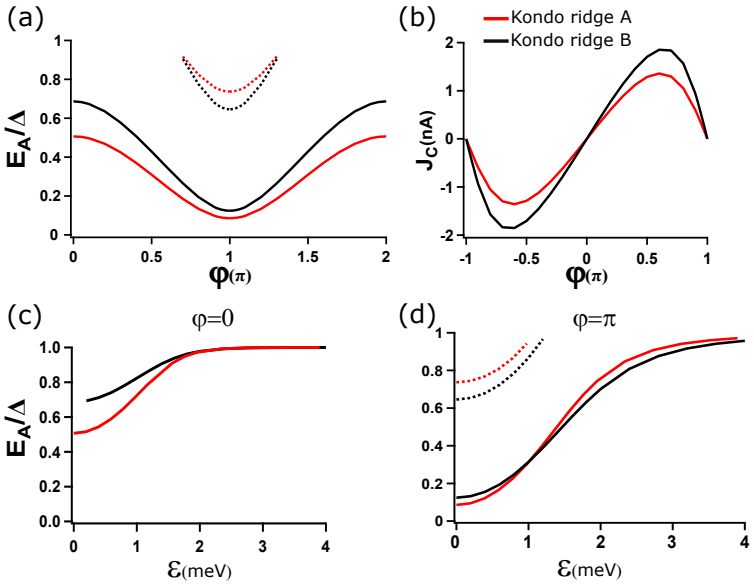

Figure 6: Résultats des calculs NRG. (a) Spectre en énergie du système à N corps et (b) amplitude du supercourant en fonction de la différence de phase supraconductrice φ au point de dégénérescence particule-trou obtenu par des calculs NRG pour les zones Kondo A et B. (c) Evolution de l'énergie des états liés d'Andreev (ABS) à $\varphi = 0$ en fonction de la position du niveau d'énergie ϵ de la boite quantique, contrôlée par la tension grille. Cela mesure le détachement des ABS du continuum d'excitation de QPs. (d) Evolution du spectre d'énergie du système à N corps à $\varphi = \pi$.

renormalisation (NRG) en collaboration avec A. Kadlecová et T. Novotny (Université de Prague, République Tchèque). Ces calculs utilisent les paramètres déduits des mesures dans le régime normal. Le spectre d'énergie de la jonction au point de symétrie particule-trou est montré sur la figure 6.a. Ce spectre représente la différence en énergie des états excités avec l'état fondamental, de type singulet. Les états excités sont l'état doublet, de dégénérescence 2 (ligne pleine) qui correspond à l'énergie de l'état lié d'Andreev (ABS), et l'état excité singulet (ligne pointillée). L'état doublet ne touche pas le continuum d'excitation de quasi-particule du fait des interactions électron-électron. Pour des raisons techniques le calcul NRG ne fournit pas la valeur de l'état excité singulet pour des écarts en énergie supérieurs à $E_A = \Delta$. Le calcul NRG confirme que l'état fondamental du système est toujours de type singulet et conduit à un supercourant de quelques nanoampères (voir figure fig.6.b), compatible avec les données expérimentales. Le système présente une dépendance en phase de type jonction 0. Les calculs NRG permettent également de prévoir l'évolution de l'écart au continuum (à la phase $\varphi = 0$) ainsi que la valeur minimale de l'écart en énergie entre l'état doublet et l'état fondamental singulet (à la phase $\varphi = \pi$). Cette évolution est montrée sur la figure 6.

Nous attribuons la réduction de l'émission Josephson à la dynamique du passage par effet tunnel de quasiparticules (QP) dans la boite quantique. Nous avons évalué la dynamique à tension de polarisation nulle de ces quasiparticules, qui mène à l'occupation de l'état doublet. Pour ce faire nous avons calculé les taux d'injection et d'échappement des QP en tenant compte de l'environnement

électromagnétique de la jonction. Celui-ci est essentiellement constitué par le circuit de couplage résonant. Nous en avons déduit la probabilité P_D pour le système d'être dans l'état doublet en fonction de la position du niveau d'Andreev E_A. Pour $E_A > 0.2\Delta$, cette probabilité est extrêmement faible (inférieur à 0.05) et explique pourquoi le système se comporte comme une jonction 0 pour la mesure de courant critique à basse fréquence.

Cependant lorsqu'on applique une tension de polarisation à la jonction, ce qui est le cas dans une mesure d'effet Josephson AC, le taux d'injection de QP peut être sensiblement plus important. De plus, proche du point de symétrie particule-trou, l'état doublet présente un écart en énergie avec le continuum de quasi-particules à cause des interactions électron-électron. Cela maintient le taux d'échappement des QP relativement bas, même si la phase de la jonction évolue dans le temps. Par conséquent la probabilité pour le système d'être dans l'état doublet s'accroit lorsque la jonction est polarisée en tension. Cela conduit à une réduction du courant critique dynamique I_{AC}^C car le courant dans l'état doublet est plus faible que dans l'état fondamental singulet.

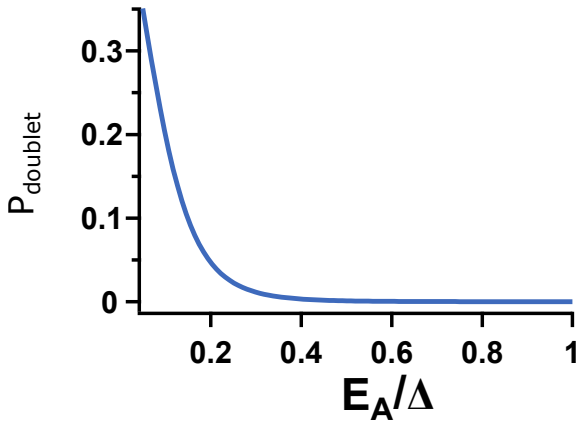

Figure 7: Probabilité pour la jonction de se trouver dans l'état doublet en fonction de l'énergie E_A de l'état lié d'Andreev.

Lorsqu'on s'éloigne du point de symétrie particule-trou, en changeant le valeur de ϵ avec la tension grille, l'écart en énergie entre l'état doublet et le continuum d'excitation au-dessus de Δ est réduit de manière significative (figure 6.c). La probabilité pour une QP présente dans la boite quantique de s'échapper s'accroit alors par des processus tunnel de type Demkov-Osherov entre l'état doublet et le continuum du fait de l'évolution en phase de la jonction. Simultanément l'énergie minimum de l'état doublet, à $\varphi = \pi$, augmente. Cela réduit le taux d'injection des QP dans la boite quantique. Ces deux effets conduisent à une augmentation de la probabilité du système d'être dans l'état fondamental singulet et donc à une remontée du supercourant effectif. C'est ce qui est mesuré dans l'expérience.

On peut extraire de l'amplitude de l'émission AC mesurée dans l'expérience la probabilité P_D d'être dans l'état doublet. Pour cela on suppose que l'amplitude du courant critique dynamique est donnée par $I_{AC}^C = P_D J_D + (1 - P_D) J_S$, avec J_S l'amplitude de la première harmonique de la relation courant phase dans l'état singulet, et J_D celle dans l'état doublet. Ces deux quantités sont déduites des calculs NRG et représentées sur la figure 3.d.

On considère dans un premier temps un scénario où la cohérence en phase n'est pas préservée et où donc seule l'amplitude des supercourants dans l'état singulet et doublet importe. Avec une probabilité 1 d'être dans l'état doublet proche du point de dégénérescence particule-trou, on rend qualitativement compte de la réduction du supercourant observé expérimentalement. Un accord plus quantitatif peut être obtenu avec une probabilité finie d'être dans l'état doublet dans un scénario où le signe du supercourant, positif pour l'état singlet et négatif pour l'état doublet, importe et donc où la cohérence en phase est préservée (fig.3.c-d). Cependant cette dernière situation impose une contrainte forte sur le modèle utilisé pour décrire la dynamique de la jonction.

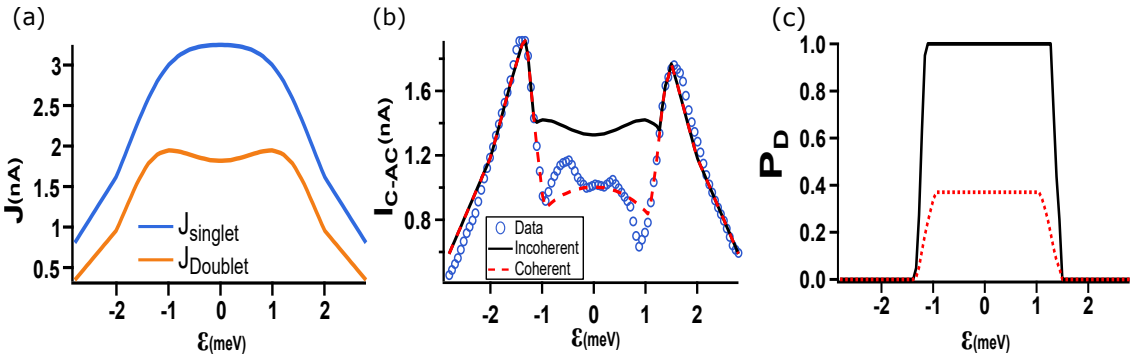

Figure 8: (a) Amplitude de la première harmonique de la relation courant-phase pour les états singulet et doublet pour la zone Kondo A, déduite des calculs NRG. (b) Comparaison entre les données expérimentales pour la zone Kondo A (cercles bleus) et l'amplitude calculée pour le courant critique dynamique I_{AC}^{C}, obtenu en introduisant une probabilité finie pour le système d'être dans l'état doublet. Dans le modèle "cohérent" la cohérence en phase est préservée (ligne pointillée rouge) alors que dans la modèle incohérent (ligne pleine noire) elle ne l'est pas.

0.3 Conclusion

Pour conclure sur cette partie de la thèse, nous avons sondé la dynamique d'une jonction Josephson à base de nanotube de carbone en mesurant son émission Josephson grâce à une technique de détection "on-chip". Nous avons montré que cette émission était fortement réduite dans des zones de tension grille pour lesquels le courant critique était important grâce à l'action combinée de l'effet Kondo et de l'effet de proximité supraconducteur. Grace à des calculs théoriques NRG, il a été possible de prédire le spectre d'énergie et le supercourant du système étudié à partir des paramètres issus des mesures dans le régime normal. La réduction observée de l'émission Josephson dans les zones Kondo peut alors être expliqué par des transitions entre état singulet et doublet induite par la dynamique des quasi-particule dans la boite quantique constituée par le nanotube de carbone.

0.4 Résonateur à haute inductance cinétiques à base de nanofils de tungstène

Dans cette partie sont résumés les résultats obtenus sur la réalisation et la mesure de microrésonateurs supraconducteurs fabriqués avec des nanofils de tungstène obtenu par dépôt assisté sous un faisceau d'ions hélium focalisé (He-FIB). Les nanofils ainsi réalisés présentent de meilleures propriétés supraconductrices que ceux réalisés sous faisceaux d'électrons. Comparé au FIB utilisant des ions gallium, le FIB avec ions hélium permet d'atteindre une meilleure résolution, de réduire les dommages et la contamination de l'échantillon et d'éviter l'implantation d'ions gallium.

La figure 9 montre les deux modèles de résonateur hybride qui ont été testés durant cette thèse. L'un est un résonateur utilisant une ligne de transmission coplanaire (figure 9a-b-c) réalisé avec un nanofil de tungstène. Le reste du résonateur est réalisé en niobium. L'autre type de résonateur est un résonateur à composant discret où la partie inductive et capacitive sont séparées (fig.9-d). La partie inductive est constituée d'un nanofil de tungstène.

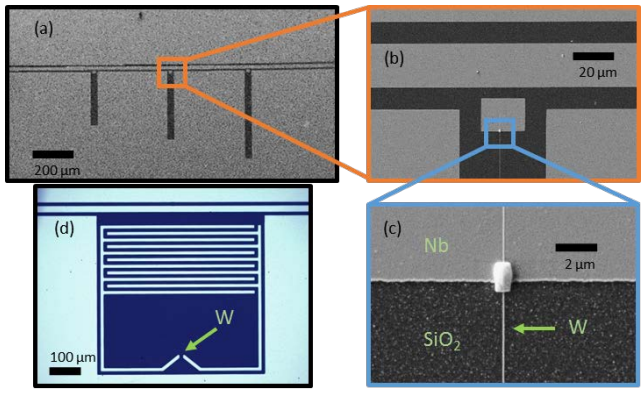

Figure 9: (a) Image obtenue par microscopie électronique à balayage de l'échantillon avec un résonateur de type ligne de transmission. Une ligne de transmission horizontale permet d'adresser trois résonateurs de type $\lambda/4$ réalisés en tungstène (W), qui sont placés verticalement sur l'image. (b) Agrandissement de la zone de couplage entre la ligne de transmission et un résonateur W. (c) Fil de tungstène déposé avec une zone de raccord plus large et plus épaisse avec le contact de niobium.

0.4.1 Propriétés supraconductrices des nanofils de tungstène.

Pour mesurer les propriétés supraconductrices (température critique T_C, champ magnétique critique et courant critique) des nanofils de tungstène utilisés pour les résonateurs, nous avons fabriquer des nanofils (nommés ci-après NW1, NW2, and NW3) de longueur 5.9μm sur un échantillon dédié au mesure de transport électrique. L'échantillon a été refroidi jusqu'à une température de 1.8K dans un appareil de caractérisation, un "Physical Property Measurement System (PPMS" de la compagnie Quantum Design, avec la possibilité d'appliquer un champ magnétique de 9T. Un des échantillons a pu également être refroidi à plus basse température dans un réfrigérateur à dilution.

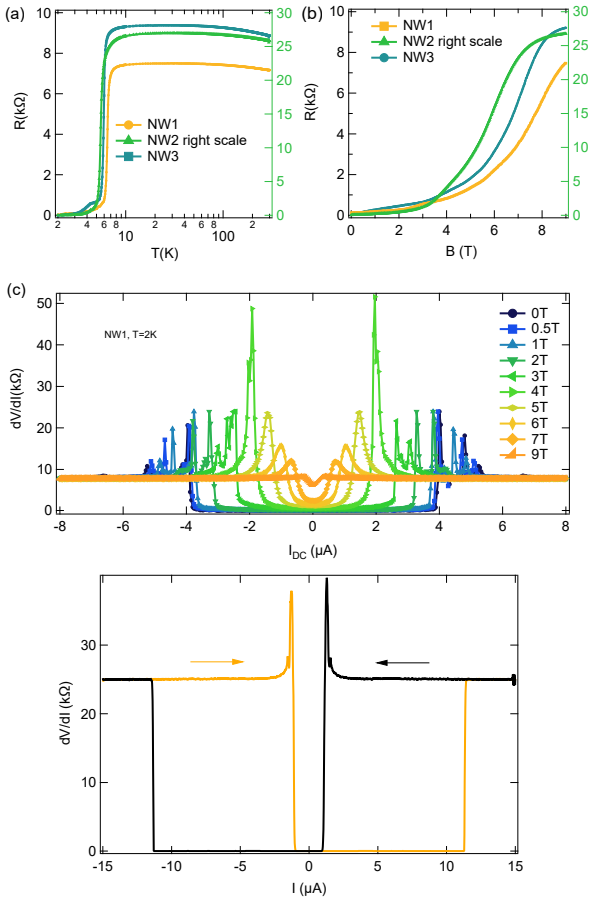

Figure 10: Résistance des nanofils de tungstène listés sur le tableau 1.1 en fonction de la température T (a) et du champ magnétique perpendiculaire (b). (c) Résistance de l'échantillon NW1 en fonction de la température pour différentes valeurs du champ magnétique B. (d) Résistance différentielle dV/dI en fonction du courant de polarisation à basse température pour l'échantillon NW1.

La figure 10 montre la résistance différentielle en fonction de la température (fig.10.a) et du champ magnétique (fig.10.b) pour les trois nanofils mesurés. Entre la température ambiante et les plus basses températures, la résistance augmente légèrement ($\approx 5\%$) pour finalement présenter une transition vers un état supraconducteur à une température autour de $T_c \in [5-6.5]$K. Les mesures en champ magnétique sont effectuées en fixant la température sous la température critique à T=2 K, et en variant le champ magnétique perpendiculaire entre 0 et 9T. Les nanofils sont supraconducteurs avec une résistance qui développe le comportement en champ magnétique d'un supraconducteur de type 2. En définissant le champ critique Hc_2 comme étant le champ pour lequel le nanofil présente une résistance moitié de celle dans l'état normal, nous voyons que chacun des fils mesurés possède un champ Hc_2 supérieur à 5T.

Pour mesurer la valeur du courant critique I_C, nous avons mesuré la résistance différentielle

dV/dI en fonction de courant de polarisation I_{DC}. La figure 10.c montre cette quantité pour le nanofil NW1 à $T = 2K$ pour différents champs magnétiques. Pour NW1, le courant critique à champ nul est de 4.0 μA and il décroit lorsqu'on augmente le champ magnétique. A cette température le courant est non-hystérétique. Pour les nanofils NW2 et NW3, le courant critique à champ nul est de 1.3 et 3.8 μA respectivement. Pour étudier le courant critique à plus basse température, le nanofil NW2 a été refroidi à 10mK dans un réfrigérateur à dilution. La résistance différentielle en fonction du courant de polarisation est montrée sur la figure 10.d. Le courant critique augmente jusqu'à 12μA, avec une hystérésis d'origine thermique.

0.4.2 Résonateurs micro-onde incluant un nanofil de tungstène

Pour mesurer les propriétés micro-onde des nanofils de tungstène, les deux types de résonateurs présentés précédemment ont été refroidis à basse température, et le spectre de transmission S_{21} mesuré avec un analyseur vectoriel.

De la valeur de la fréquence de résonance, il est possible d'extraire l'inductance cinétique du nanofil de tungstène. On peut alors la comparer à la valeur théorique attendue à basse température :

$$L_{K,\square} \approx \frac{R_\square h}{2\pi^2 \Delta_0}. \tag{1}$$

avec $\Delta_0 = 1.76 k_B T_c$. Avec $T_c \in [5 - 6.5]$K et $R_\square$ la résistance par carré, qui vaut typiquement 100 Ω pour les nanofils fabriqués, on prévoit une valeur d'inductance cinétique $L_{K,\square} \in [7 - 25]$ pH/$\square$. Pour le résonateur à élément discret, la fréquence de résonance est de l'ordre de 4.46GHz avec un facteur de qualité de 4000. Connaissant la capacitance et l'inductance géométrique estimées par simulation numérique, cela conduit à une inductance cinétique $L_{K,\square} = 15.4\ pH/\square$, une valeur 250 fois plus importante que l'inductance géométrique. Le résonateur de type ligne coplanaire conduit sensiblement à la même valeur d'inductance cinétique mais avec un facteur de qualité plus faible, de l'ordre de 700.

La figure 11.a montré la dépendance en température de S_{21} à basse puissance. La dépendance de la fréquence de résonance et du facteur de qualité peuvent être relativement bien compris dans le cadre d'un modèle de type Mattis-Bardeen, qui décrit la conductivité complexe du supraconducteur à haute fréquence.

La dépendance en fonction du champ magnétique dans le plan du résonateur à élément discret a pu être mesuré jusqu'à 130mT. La fréquence de résonance et le facteur de qualité varie peu (pour $Q_i :< 10\%$ et pour $f_{res} :< 0.05\%$), montrant que ce type de résonateur sont relativement insensibles à des champs magnétiques dans le plan.

Enfin la dépendance en fonction de la puissance micro-onde S_{21} permet d'extraire le paramètre Kerr. Nous avons trouvé un paramètre Kerr non-linéaire $K/2\pi = 200 \pm 120$ Hz/photon at 4.465 GHz (T=10mK), et 74 Hz/photon at 3.55 GHz(T=1.5K).

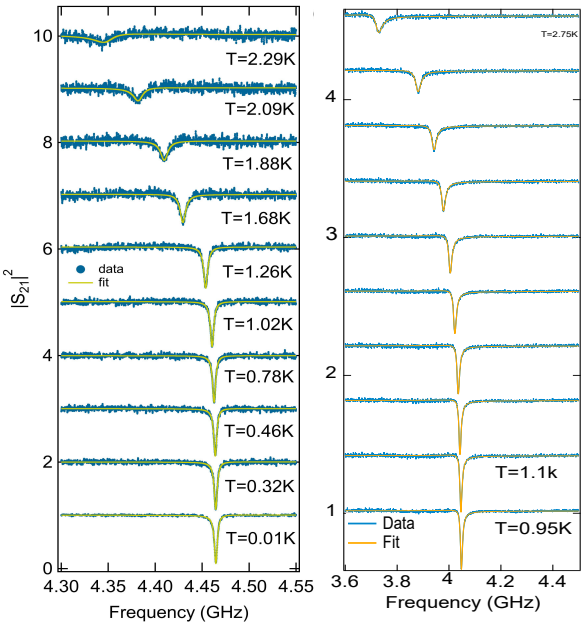

Figure 11: Dépendance en température du spectre en transmission pour le résonateur à élément discret (à gauche) et pour celui de type ligne de transmission (à droite). Ces deux types de résonateurs résonnent dans la gamme du GHz.

0.4.3 Conclusion

Cette partie de la thèse portait sur la réalisation et la mesure d'un nouveau type de résonateur micro-onde hybride, fabriqué en partie en niobium et pour la partie à haute inductance cinétique avec des nanofils en tungstène déposés sous un faisceau d'ion focalisé d'hélium. Deux types de résonateurs ont été testés, l'un à élément discret et l'autre avec une ligne de transmission. Ces résonateurs présentent une très forte inductance cinétique, de l'ordre de $L_K = 15$ pH/□, 250 fois plus importante que l'inductance géométrique.

0.5 Mesure de la température électronique à l'aide d'un transistor à un électron

Cette section résume la mesure de la température électronique dans un réfrigérateur à dilution sans hélium liquide équipé de ligne de polarisation DC réalisée avec des lignes coaxiales résistives. Cette mesure s'est faite en utilisant comme thermomètre primaire un transistor à un électron (SET pour "single electron transistor").

Une image de l'échantillon est montrée sur la figure 12. L'échantillon, réalisé par évaporation sous angle de deux couches d'aluminium, est refroidi dans un réfrigérateur de la marque Cryoconcept à travers de lignes coaxiales résistives réalisées au laboratoire et thermalisées à chaque étage du réfrigérateur. Ces lignes agissent comme des filtres passe-bas. La conductance différentielle de l'échantillon est mesurée avec une détection synchrone.

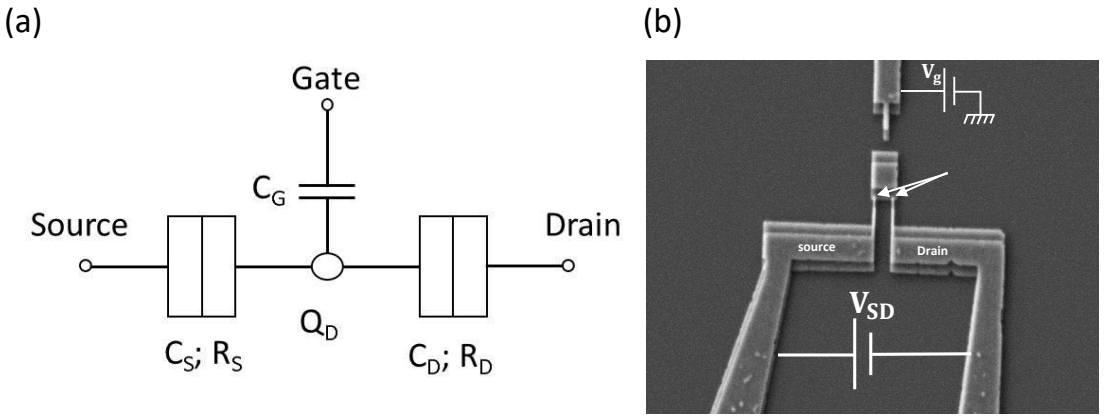

Figure 12: (a) Schéma équivalent d'un transistor à un électron (SET). (b) Image obtenue au microscope électronique à balayage du SET mesuré. La structure est réalisée en aluminium en utilisant de l'évaporation sous angle. Les barrières tunnel sont obtenues par oxydation de l'aluminium. Un faible champ magnétique est appliqué pour rendre l'aluminium normal.

La carte de conductance de la figure 13.a montré la conductance différentielle dI/dV_{SD} du SET en fonction de la tension grille V_g et de la tension source-drain V_{SD}. Un champ magnétique est appliqué pour supprimer la supraconductivité de l'aluminium. La valeur de l'énergie de charge $E_C = 22 \pm 2\mu$eV est extraite de la largeur des diamants de Coulomb en fonction de la tension de polarisation. Lorsqu'on mesure la conductance à tension nulle en fonction de la tension de grille on obtient des pics réguliers de conductance. La figure 13.b montre ainsi 4 pics de Coulomb.

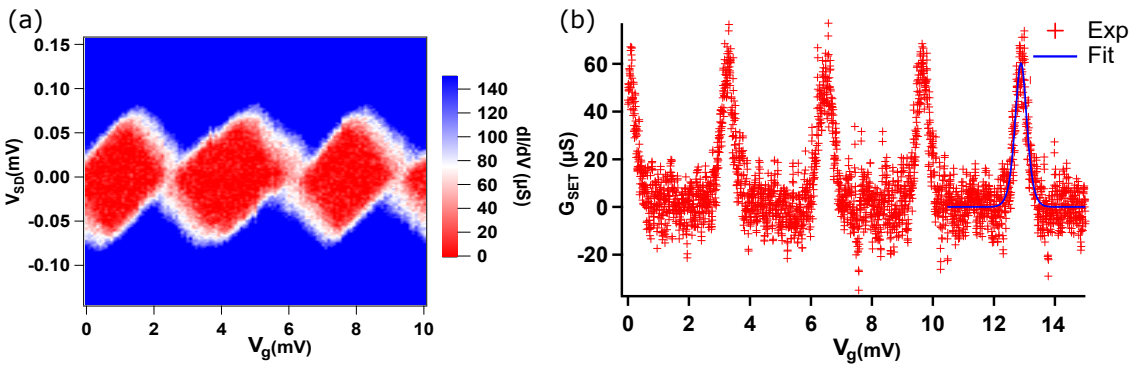

Figure 13: (a) Carte de conductance du SET en fonction de la tension grille V_g et la tension source-drain V_{SD}. (b) Pic de blocage de Coulomb observé sur la conductance du SET G_{SET} en fonction de la tension de grille V_g. Ces pics sont utilisés pour extraire la température électronique à l'aide de l'équation 2.

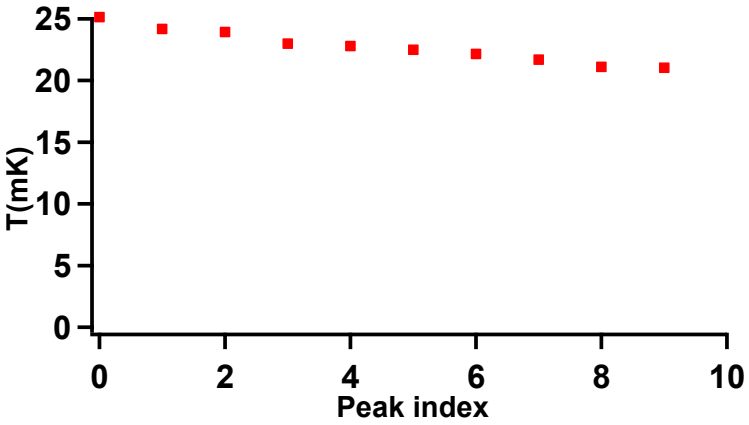

Figure 14: Température électronique en fonction de l'index du pic de conductance considéré. Nous trouvons $T_{electronic} = 23 \pm 2mK$.

La largeur de ces pics de conductance à tension de polarisation nulle constitue un moyen bien connu de mesurer la température électronique de manière absolue. Le SET constitue de ce fait un thermomètre primaire. Pour un ilot métallique avec une densité d'état constante et connecté à des contacts via des jonctions tunnel, la conductance peut s'écrire :

$$G_{SET}(\delta V_g) = \frac{G_\infty}{2} \frac{2E_C(\delta V_g/\Delta)/k_BT}{\sinh(2E_C(\delta V_g/\Delta)/k_BT)}. \quad (2)$$

avec $G_\infty = \frac{G_S G_D}{G_D+G_S}$ la valeur de la conductance à haute tension, avec G_S et G_D la conductance du drain et de la source. Δ=e/C_g est la période en tension grille et δV_g la variation de tension grille par

rapport au point de dégénérescence de charge. Chaque pic de la figure 13.b est ajusté en utilisant la formule 2, et la valeur de la température électronique en est déduite pour différents pics de conductance (figure 13). Nous en déduisons une température électronique de $T_{electronic} = 23 \pm 2mK$ alors que la température de base du réfrigérateur est de 10mK.

0.5.1 Conclusion

Nous avons ainsi montré que l'utilisation de câbles coaxiaux résistifs réalisés au laboratoire permettait d'obtenir une température électronique de $T_{electronic} = 23 \pm 2mK$ pour une température de base du réfrigérateur sans hélium liquide de 10mK. Cette température a pu être mesurée grâce à une thermomètre primaire exploitant le blocage de Coulomb : le transistor à un électron.

Conclusion

Au cours de cette thèse nous avons sondé la dynamique d'une jonction Josephson avec comme lien faible un nanotube de carbone en mesurant son émission Josephson. Nous avons montré que cette émission était fortement réduite dans des zones de tension grille pour lesquelles le courant critique est augmenté du fait de l'action conjuguée de l'effet Kondo et de l'effet de proximité supraconducteur. A l'aide de technique numérique du groupe de renormalisation et des paramètres du système obtenu dans le régime normal, il a été possible de calculer le spectre d'énergie et le supercourant de la jonction. La réduction dynamique du courant critique est alors attribuée à la dynamique des quasi-particules dans la boite quantique qui conduit à une transition entre l'état singulet et doublet de spin.

Nous avons par ailleurs fabriqué et testé un nouveau type de micro-résonateur supraconducteur hybride combinant du niobium en couche mince et des nanofils de tungstène déposés sous faisceau d'ions hélium focalisé. Ces derniers présentent une très forte inductance cinétique. Deux types de résonateur, à éléments discrets ou bien à ligne de transmission, ont été mesurés à basse température. Ils présentent tous deux des résonances dans la gamme du GHz avec une très forte inductance cinétique. Ces résonateurs sont prometteurs comme éléments supraconducteurs non-linéaires compacts à forte impédance, utiles en électroniques quantiques ainsi que comme circuit de couplage pour la détection haute fréquence "on-chip".

Dans le souci d'obtenir de meilleures mesures à basse température, nous avons fabriqué des lignes de polarisation de type filtre passe-bas avec des câbles coaxiaux résistifs réalisés au laboratoire. Cela permet d'obtenir une températures électroniques $T_{electronic} = 23 \pm 2mK$, pour une température de base de réfrigérateur à dilution sans hélium liquide de 10mK. Cette température électronique a été mesurée avec un transistor à un électron.

Introduction

Quantum transport refers to the investigation of coherent ($\sim$ ten to a few hundred nanometers) and cold circuits ($\sim$100mK). Consequently, quantum transport experiments require the fabrication of low-dimensional circuits. Because of their intermediate size between macroscopic and microscopic scales, these circuits are called mesoscopic.

One of the most studied systems in the field of Quantum transport is quantum dots (QD). Quantum dots are so small such that their energy levels are quantized due to confinement effects, for that QD are referred to as "artificial atoms". The advantage of using a QD is that its parameters can be controlled. For example, it is possible to control the number of electrons on the dot by an electrostatic gate. Coupling a QD to metallic normal electrodes, allows us to probe many interesting quantum effects. Depending on the coupling strength between the QD and the two reservoirs, the QD exhibits different transport phenomena such as the Coulomb blockade, Kondo effect. If the electrodes are superconducting, another quantum phenomenon, proximity-induced superconductivity will emerge.

The Kondo effect was initially observed in alloys with magnetic impurities, through the anomalous increase of resistance as temperature drop as explained by Jun Kondo. The electrons at the Fermi energy tend to screen the magnetic moment of the impurity, forming a many-body spin-singlet state of binding energy expressed as a Kondo temperature T_k. This Kondo screening gives rise to a resonance in the density of states. Kondo effect can occur also in a quantum dot with an unpaired spin in its highest occupied energy level. However, in QD, the Kondo resonance opens a transmitting channel, thus the conductance increases. The first observation of the Kondo effect in quantum dots was made in GaAs-based two-dimensional structures. The Kondo effect has now been seen in quantum dots based on a wide variety of nano-scale devices such as carbon nanotubes, C_{60} molecules, organic molecules, and semiconductor nanowires.

S-wave superconductivity is a spin-singlet ground state where electrons condense in Cooper pairs with pairing energy Δ (superconducting gap) and phase φ. The formation of Cooper pairs is due to attractive electron-electron interaction mediated by the phonons. A non-dissipative current "supercurrent" can flow through a superconductor, which is driven by a superconducting phase instead of a voltage gradient. When a weak link of length L such as a quantum dot is connected to superconducting electrodes, it can support a supercurrent at zero bias voltage due to the superconducting proximity effect, provided that the phase coherence is preserved along the length L. The current through the quantum dot and the phase are related through the current-phase relation (CPR). In such a system, the presence of the Coulomb interaction results in Coulomb blockade, which gives rise to a doublet state if there is an odd number of electrons on the dot. This doublet state hinders the flow of supercurrent, which manifests as a reduction of the critical current and a sign reversal of the DC current-phase relation. One has then a π junction. However, if the Kondo temperature T_K exceeds the superconducting gap energy Δ, the Kondo screening survives and resonant Cooper pair tunneling occurs. In this limit, the Kondo effect and superconductivity cooperate to restore the singlet state i.e. the 0-junction.

The competition between these two effects has been already investigated at equilibrium, by monitoring the current phase relation of CNT based Josephson junctions. These experiments have

revealed phase-dependent quantum transitions between the magnetic doublet state and the Kondo screened singlet non-magnetic state of the quantum dot. In the present work, we show that the dynamics of this induced transition can be probed by the Ac Josephson emission of carbon nanotube-based Josephson Junction.

The Ac Josephson effect is the phenomenon by which a superconducting weak link that is voltage biased generates an oscillating current. This is why superconducting tunnel junctions can be used as GHz radiation emitter or to define the voltage standard thanks to the metrological precision of the AC Josephson effect. In Josephson junctions involving a normal material, measuring the AC-Josephson effect allows probing the states that carry the supercurrent at finite frequency and out-of-equilibrium. For instance, its measurement demonstrated the topological protection in several topological systems, that was not accessible through DC measurement.

The manuscript is organized as follows. Chapter one is dedicated to the description of carbon nanotubes and their physics. Then we discuss transport through a carbon nanotube quantum dot.

In chapter two, we present the different fabrication, cooling, and measuring techniques performed to realize this work. Chapter three details the Kondo effect. Chapter four presents a general introduction to superconductivity.

Chapter five deals with the Josephson effect in a quantum dot. We present the different transport regimes arising from the competition between Coulomb blockade interactions and superconductivity. What happens when superconducting correlations compete with the Kondo effect? The last section of this chapter is devoted to answering this question.

In chapter six we present the central topic of this thesis: The dynamics of a carbon nanotube-based Josephson junction. We probe the dynamics of our system by measuring the AC Josephson emission of the junction and compare it to its DC Josephson current. The AC emission is measured by coupling the carbon nanotube to an on-chip detector (a Superconductor-Insulator-Superconductor junction), via a resonant circuit. In the first part, we represent the experimental setup used for measurement. In the second part, we present the experimental results. Measurement of the Ac emission of the CNT in the gate regions that exhibit Kondo features in the normal state shows that this emission is strikingly reduced in the gate region where the critical current is enhanced due to the interplay of the Kondo effect and superconducting proximity effect. In the last section, we present the renormalization group calculation performed to understand the behavior of our CNT QD along with several interpretations. We show that the collapse of the AC emission observed experimentally is due to the transition between the singlet state and the doublet state. This transition can be traced to the dynamics of quasiparticle in the quantum dot.

Finally, to improve our detection methods at low temperature, we performed two other experiments which are presented in the last chapter of this thesis. In the first experiment, we have designed and measured a new type of superconducting micro-resonator, based on a high kinetic inductance material, namely tungsten nanowires deposited using a helium focus ion beam. This kind of resonator can be very useful to improve the resonant coupling for on-chip detection and thus provide a better measurement of the AC Josephson emission of carbon nanotube-based Josephson junction. In the second experiment, we have tested new home-made filtering of DC lines in a cryo-

free dilution refrigerator recently installed in the group, by measuring the electronic temperature of a single electron transistor.

Chapter 1

Electronic properties of carbon nanotube quantum dots

Since their discovery in 1991 [1], carbon nanotube has become of a great interest. Due to its unique structural and electronic properties, CNT becomes a building block for several applications: bio sensors [2, 3], radio frequency applications [4], flexible electronic [5], photonic circuits [6, 7] and transistors [8].

This chapter is devoted to the description of the system that we are studying: a carbon nanotube (CNT). First, we will present the structural and electronic properties of the carbon nanotube. Then, we explain the mesoscopic transport through a carbon nanotube quantum dot (CNT QD).

1.1 Single wall carbon nanotube

1.1.1 Geometrical properties

A carbon nanotube can be seen as a graphene sheet rolled into a cylinder. This graphene layer can be rolled in many different directions, described by the chiral vector $\vec{C_h} = n\vec{a_1} + m\vec{a_2}$, which is a linear combination of the unit vectors $\vec{a_1}$ and $\vec{a_2}$ of a graphene sheet with n and m integers. The value of n and m determines the structure of the CNT. The tube's diameter, chiral angle θ, unit vectors, number of atoms in the unit cell, can all be deduced from (n, m) numbers. Nanotubes with (n, n) ($\theta = 0°$) and (n, 0) ($\theta = 30°$) are armchair and zigzag, respectively. For n$\neq$m and $0 < \theta < 30$ the tube is said to be chiral (See fig.1.1). Carbon nanotubes often grow in bundles, ropes or they appear nested within each other. They are consequently, named multi-wall carbon nanotubes (MWCNTs). In the following, we will limit ourselves to the description of single-wall carbon nanotubes (SWCNTs).

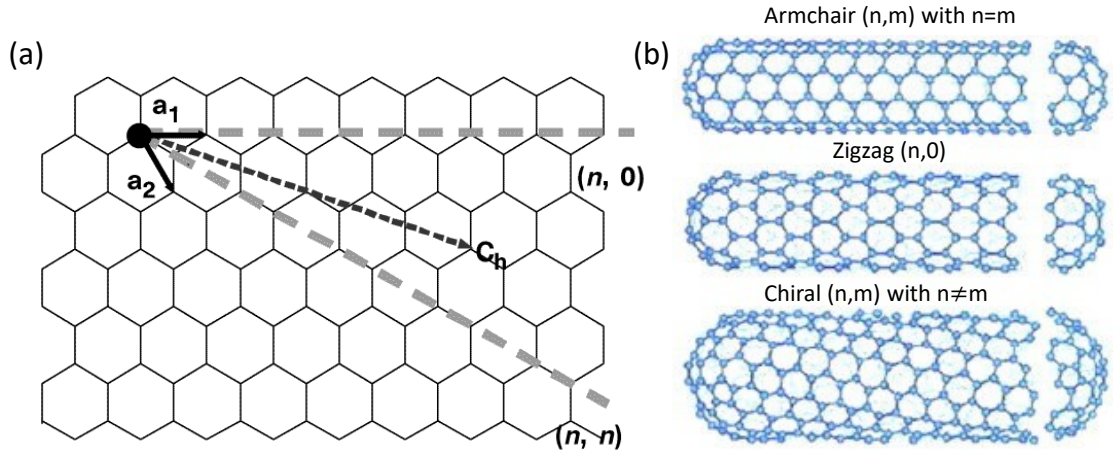

Figure 1.1: (a) Hexagonal lattice of a graphene sheet rolled into a CNT around a chiral vector $\vec{C_h}$.(b) Carbon nanotubes with different structures: armchair (n, n), zigzag (n, 0) and chiral (n, m).Taken from [9].

1.1.2 Electronic band structure of carbon nanotubes

To know whether the carbon nanotube is metallic or superconducting, one must calculate its band structure. The dispersion relation of CNT can be determined from the one of graphene by projecting the graphene band dispersion into the 1D longitudinal CNT dimension.

Dispersion relation of graphene

Graphene is made up of carbon atoms arranged in hexagonal honeycomb-like structure as shown in fig.1.1(a), with unit cell vector $\vec{a_1}$ and $\vec{a_2}$ such that:

$$\vec{a_1} = \frac{a}{2}(3, \sqrt{3}),\ \vec{a_2} = \frac{a}{2}(3, -\sqrt{3}) \tag{1.1}$$

with $a \approx 1.4$Åis the carbon-carbon distance. In the reciprocal space of graphene, the reciprocal-lattice vectors are:

$$\vec{b_1} = \frac{2\pi}{3a}(1, \sqrt{3}),\ \vec{b_2} = \frac{2\pi}{3a}(1, -\sqrt{3}) \tag{1.2}$$

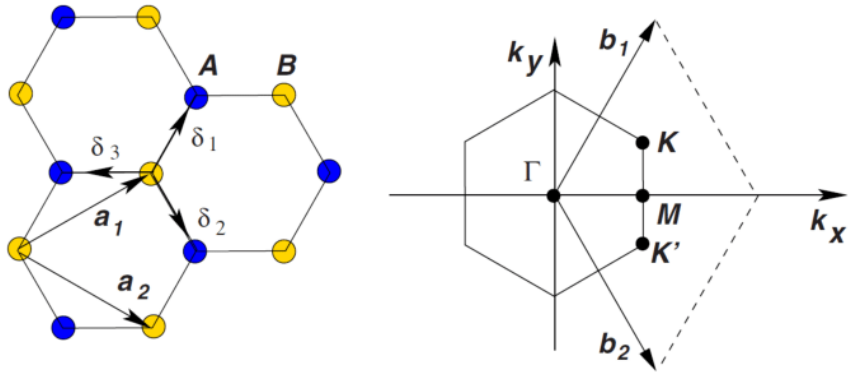

Figure 1.2: Left: Honeycomb lattice structure of graphene with $\vec{a_1}$ and $\vec{a_2}$ unit cell vectors and δ_i with i=1,2,3 is the nearest neighbor vectors. A and B denotes two inequivalent atomic sites. Right: Corresponding Brillouin zone. Dirac cones are located at the K and K' points. Taken from [10].

Figure.1.2 shows the graphene lattice structure in the real and reciprocal space. In the Brillouin zone (BZ), the Fermi surface is reduced to six points. Only two of them are independent, whereas the rest are equivalent by symmetry. These two points are called the Dirac point: K and K' located at the corners of the graphene BZ.

At low energy ($\epsilon < 1$ eV) near the Dirac point K, the dispersion relation of graphene can be calculated using the tight binding model for the π orbital electrons:

$$E_{\vec{k}} = \pm\hbar \mid \vec{k} - \vec{k}_{K,K'} \mid v_f \tag{1.3}$$

where $\vec{k}$ is the wave vector and v_f is the Fermi velocity. This dispersion relation (See fig.1.3) shows that the carriers in graphene are Dirac fermions which should be described by Dirac relativistic equation.

Carbon nanotube band structure

The energy band structure of CNT is then derived from the one of graphene, by introducing periodic boundary conditions due to the cylindrical geometry of the tube. Since a CNT is considered as an infinitely long cylinder with a very small diameter, the wave vector $k_{\parallel}$ (parallel to the tube axis) is continuous but the wave vector $k_{\perp}$ (perpendicular to the tube axis) becomes quantized $k_{\perp}.\vec{C_h}$=2πp

The CNT band structure can be obtained by cutting the energy dispersion of graphene along the allowed k$\perp$ lines values. If the cutting line crosses at the K point then the CNT is metallic, otherwise, it is semi-conducting with a finite gap of the order of $\sim$0.5 eV.

Another way to determine whether a given nanotube is metallic or semiconducting is the indices (n, m), deduced from the intersection of $k_{\perp}$ with the Dirac points. For a given (n, m) if n-m is multiple of 3, then the tube is metallic. Thus:

- Armchair tubes (n, n) are metallic.

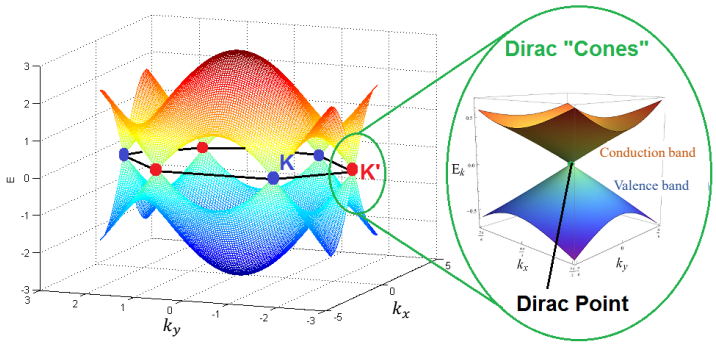

Figure 1.3: The energy dispersion of graphene showing the six Dirac points where the valence band and conduction band meet and zoom around the Dirac point K'.

- Zigzag tubes (n,0) or chiral tubes (n, m), if n-m=3l, (where l is an integer), tubes metallic. If not, the tubes are semiconducting.

The dispersion relation of carbon nanotube of different chiral numbers is shown in fig.1.5.

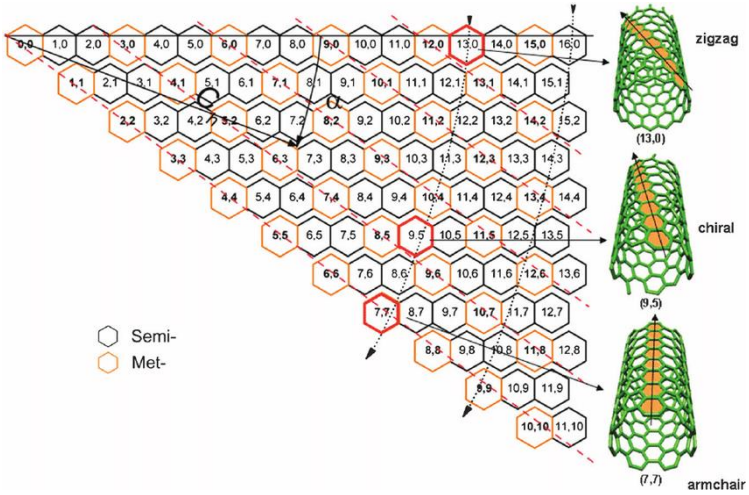

Figure 1.4: Chirality map of a carbon nanotube. Adapted from [11].

Fig.1.4 summarize the metallic and semiconducting families of carbon nanotubes according to their chiral numbers.

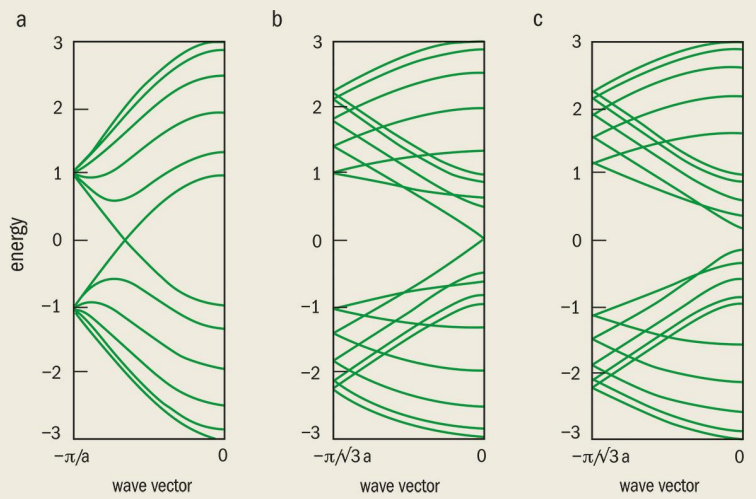

Figure 1.5: The band structure for carbon nanotubes, E given in eV and wave vector in $^{-1}$. (a) (5,5) Armchair, (b) (9,0) zigzag, (c) (10,0) zigzag nanotubes. The Fermi level is located at zero energy. (5,5) and (9,0) are metallic nanotubes while (10,0) is semiconducting.

CNT four-fold energy level structure Due to its peculiar band structure, the CNT possesses two orbitals to degenerate conducting channels. This degeneracy can be traced back to the presence of two equivalent dispersion cones (K and K') in graphene. The orbital degeneracy can be understood as the way an electron can circles around a graphene cylinder, clockwise or anti-clockwise. However, electrons can have spin up or spin down, so each orbital level can be spin degenerate (K↑,K↓), same for K' valley. In total the CNT have one four-fold degenerate channel (K↑,K↓,K'↑,K'↓) as shown in fig.1.6.

In this work, the contacts of the nanotubes are separated by L = 400 nm, which is lower than the mean free path $l_e = 0.5 - 10\mu m$, thus the transport through the CNT is rather ballistic and coherent.

The maximum conductance of a CNT can be calculated using the Landauer-Büttiker formula given by:

$$G = s\frac{e^2}{h}\sum_m T_m \tag{1.4}$$

With s being the degeneracy of the channels (For example s=2 for spin 1/2). In this formalism a coherent conductor is described by m transport channels with transmission T_m $(0 < T_m < 1)$. Thus, for a CNT with one four-fold degenerated channel, the maximum conductance is $G = 4\frac{e^2}{h}$, corresponding to a resistance of 6.45kΩ.

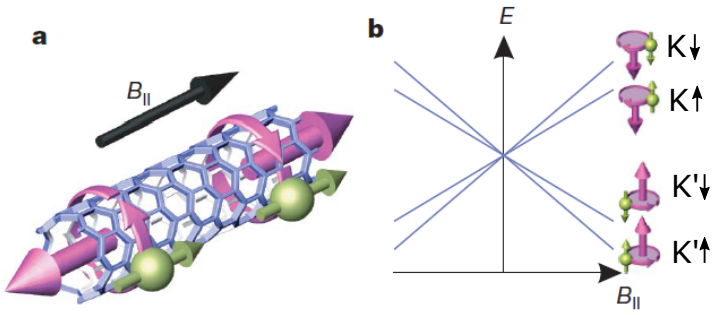

Figure 1.6: (a) Electrons confined in a nanotube segment have quantized energy levels, each four-fold degenerate in the absence of spin-orbit coupling and defects. The purple arrow at the left (right) illustrates the magnetic moment arising from the clockwise (anticlockwise) orbital motion around the nanotube. The green arrows indicate positive moments due to spin. (b) Expected energy splitting for a defect-free nanotube in a magnetic field B parallel to the nanotube axis in the absence of spin-orbit coupling: At B=0 T, all four states are degenerate. With increasing B, each state shifts according to its orbital and spin magnetic moments, as indicated by purple and green arrows, respectively. Taken from [53].

1.2 Electronic transport in a carbon nanotube

To perform transport measurements, a single isolated carbon nanotube is contacted between two metallic electrodes which could be normal or superconductor. In what follows, we explain the physics of a Quantum dot, then we introduce the specific properties of a carbon nanotube quantum dot (CNT QD). After that, we show the different transport regimes for a CNT QD, from Coulomb blockade to the co-tunneling process and appearance of the Kondo correlation.

1.2.1 Quantum dot

When the electron wavelength is comparable to the size of a system such as in a quantum dot, electrons are confined in a set of discrete energy levels resembling that of an atom. For that quantum dot are said to be "artificial atoms". Quantum dots exits in different size and materials: single molecules [12], metallic [13] or superconducting nanoparticles, lateral or vertical dots in semiconductor heterostructures [14], semiconducting nanowires [15], or carbon nanotubes [16].

Due to the small size of the dot, the capacitance of the QD with the gate and the leads induces a strong charging energy $E_C = e^2/2C$ (C being the total capacitance of the QD) which has to be paid each time one needs to add an electron on the dot. Ec∼few meV for a typical QD. When $\Gamma < E_C$, the energy levels on the dot are clearly defined and a discrete energy spectrum of single-particle levels is formed at energies ϵ_d with a mean level spacing ΔE, of broadening width Γ, with Γ the total coupling constant to the metallic electrodes.(See fig.1.7).

Depending on the transparency of the contacts the QD exhibits three transport regimes:

- Strong coupling regime, $\Gamma \gg E_C$

- Week coupling regime, $\Gamma \ll E_C$ given that $k_B T < E_C$

- Intermediate regime, $\Gamma \approx E_C$

The three different transport regimes will be explained in detail in the following section, focusing on the case of a carbon nanotube quantum dot.

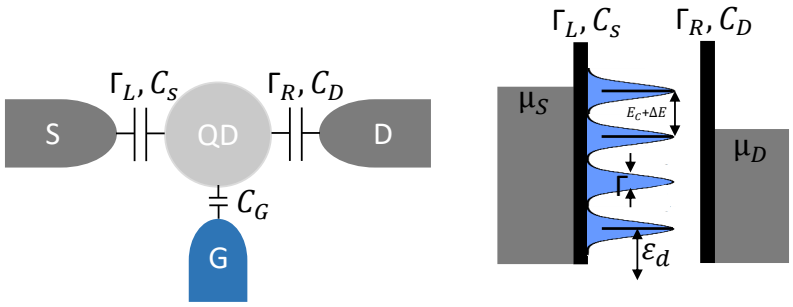

Figure 1.7: Left: Schematic of a quantum dot (QD) with the source (S), the drain (D) leads and a capacitively coupled gate (G), used to control the number of electrons on the QD. Right: Discrete energy levels of a QD, showing the relevant energy scales, the charging energy E_C, the couplings with the left and right reservoirs Γ_L and Γ_R, the total coupling $\Gamma = \Gamma_L + \Gamma_R$, ΔE the energy level spacing and ϵ_d the position of the energy levels in the dot.

1.2.2 Carbon nanotube quantum dot

When a carbon nanotube is connected to metal electrodes, if the transmission of the contacts is low compared to the charging energy, the CNT will behave as a quantum dot at low temperatures. To measure electrical transport through a CNT, the tube must be coupled via tunnel barriers to metallic electrodes with which electrons can be exchanged.

When a CNT is brought into contact with metallic electrodes, and the Fermi level in the CNT is higher in energy than that in the metal, electrons move from the CNT into the metal leaving a positive background of ionized atoms leading to the formation of Schottky barriers at the interface. This phenomenon is more important in semiconductor nanotubes. However, due to defect or curvature, there is often a small gap forming even for metallic SWNT.

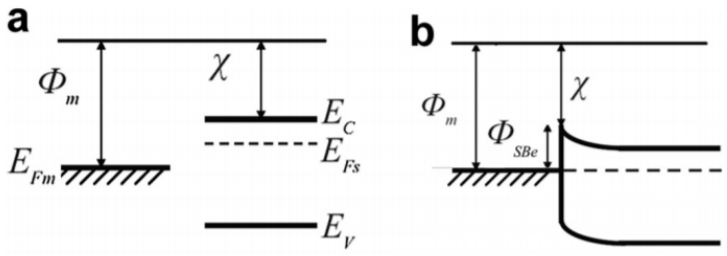

Figure 1.8: (a) Energy band diagram before contact is made between a metal and a semiconductor. (b) When contact is made, the Fermi levels equilibrate and a Schottky barrier arises. ϕ_m is the work function of the metal which is the energy needed to remove an electron from the Fermi level into the vacuum and χ is the electron affinity of the semiconductor which is the energy needed to remove an electron from the bottom of the conduction band. Taken from [17].

Due to the formation of the Schottky barrier, the transparency of the contacts can be modified depending on the position of the Fermi energy of the CNT with respect to the metal. The position of the Fermi level is controlled by the capacitively coupled gate electrodes. For a CNT contacted between two metallic electrodes 200 nm apart (L=200nm), the value of the level spacing $\Delta E=\frac{hv_f}{2L}$ will be in the order of few meV, same as the charging energy E_C. Thus, for a given gate voltage, only one of its discrete energy levels participates to transport. Each of these energy levels is four-fold degenerate unless the orbital degeneracy is lifted with an energy gap δE. This gives two two-fold quasi-degenerate levels.

Weak coupling or Coulomb blockade regime

When the CNT is weakly coupled to the electrodes i.e. $\Gamma \ll E_C$, the interaction effect becomes dominant and the QD is in the so-called 'Coulomb blockade' regime. In this regime, the CNT will be considered as a quantum dot that possesses the same energy diagram shown in fig.1.7. Here $E_C = \frac{e^2}{C_\Sigma}$ is the energy needed to overcome Coulomb interaction and add a single electron on the dot, with $C_\Sigma = C_s + C_d + C_g$ is the total capacitance of the CNT QD. To add one electron to the QD, one should pay the charging energy E_c, since at low temperature (T$\sim$10 mK) the thermal fluctuation is not enough to overcome this charging energy, the only way to lift the Coulomb blockade is by changing the source-drain voltage V_{SD} and/or the gate voltage V_g. The total energy of the dot U(N) is given by:

$$\sum_1^N E(N) = \frac{Q^2}{2C_\Sigma} + \sum_{n=1}^N E(n) = \frac{(e(N-N_0) - (C_g V_g) + (C_s V_s + C_d V_d))^2}{2C_\Sigma} + \sum_{n=1}^N E(n) \qquad (1.5)$$

where N_0 represents the number of electrons at V_G=0.

The electrochemical potential μ(N), which is by definition the energy required for adding the N^{th} electron to the dot:

$$\mu(N) = E(N) - E(N-1) = E_C(N - N_0 - \frac{1}{2}) - E_C\frac{q}{e} + E_N, \qquad (1.6)$$

with $q = C_g V_g + (C_s V_s + C_d V_d)$, is the induced charged due to the three electrodes The discrete levels are separated by an addition energy defined by:

$$E_{add} = \mu(N) - \mu(N-1) = E_c + \Delta E \tag{1.7}$$

ΔE=0, when two consecutive electrons are added to the same spin-degenerate level or a different orbital degenerate channel.

For transport to occur, a level of the dot must fall within the bias window between the electrochemical potential of the source (μ_S) and drain (μ_D) electrodes, i.e. $\mu_S > \mu > \mu_D$ with $V_{SD}=(\mu_S - \mu_D)/e$. In this case, an electron can tunnel in and out of the dot carrying a finite current. If no level lies within the bias window, the number of electrons is fixed inside the dot and there is no current flow. This is known as the Coulomb blockade. (see fig.1.9).

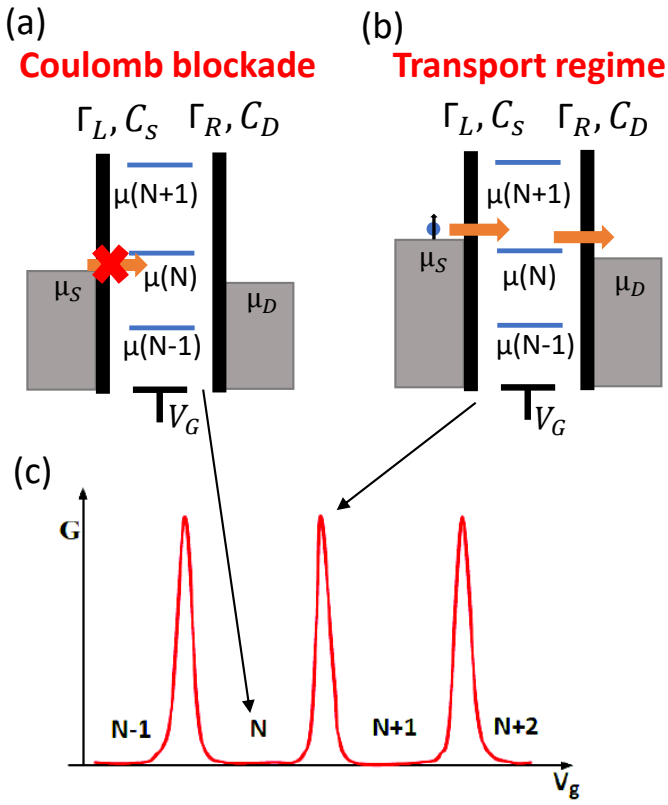

Figure 1.9: (a) No level drops in the bias window of μ_S and μ_D. Transport is energetically forbidden, no current flows through the dot. It is Coulomb blocked. (b) By tuning the gate voltage, the ladder of energy level is shifted, such that an energy level of the dot coincides with Fermi energy and resonant single electron tunneling occurs. (c) Coulomb peaks in conductance versus gate voltage at zero bias. The valleys correspond to the Coulomb blockade.

Coulomb blockade can be lifted by changing the voltage applied to the gate electrode which

shifts the whole ladder of electrochemical potential levels up or down, or by changing the bias voltage (V_{SD}) to open the bias window. When the μ(N) drops into the bias window, the N^{th} electron can tunnel from the dot to the drain followed by tunneling of another electron from the source onto the dot. The number of electrons in the quantum dot then alternates between N-1 and N. Only after one electron tunnels off to the drain can another electron come onto the dot from the source. This cycle is known as sequential single electron tunneling.

Applying a finite bias voltage V_{SD} ($\mu_S - \mu_D$=eV_{SD}) between the source and drain electrodes opens up a bias window between μ_S and μ_D. For transport to occur μ_N should be within the bias window such that it aligned with a filled electronic state of one electrode and an empty electronic state of the other one. Thus, electrons can tunnel through the QD. For this condition to be fulfilled $\mu_S > \mu_N > \mu_D$. If this is not the case, the QD is in the Coulomb blockade regime.

Varying the gate voltage V_G can shift the energy level ladder. Each time an energy potential level of the QD is aligned with the source and drain Fermi energy, sequential tunneling occurs, and a peak in conductance is observed as shown in fig.1.9.c. However, in the valleys between the peaks in gate voltage, the number of electrons on the dot is fixed due to the Coulomb blockade. The distance between the peaks corresponds to $\alpha E_{add} = \alpha(E_C + \Delta E)$, where $\alpha = \frac{C_g}{eC}$ is the lever arm which relates the gate voltage scale to the electrochemical potential. When sweeping both the gate voltage V_G and source-drain voltage V_{SD} at the same time, and measure the differential conductance (G=dI/dV_{SD}), one obtains the so-called stability diagram of a quantum dot.

Let us consider a QD occupied by N number of electrons, it is thus in a charge state N. The number of charges can change in four ways. An electron can tunnel into the dot either from the left or right electrode, thus the charge state becomes N+1. Alternatively, an electron can tunnel from the dot into the left or right electrodes, and the N is replaced by N-1. Here we also must consider the work done by the voltage source V_{SD} to bring a new charge e onto the QD. Let us consider a simple case where and the bias voltage is assumed to be anti-symmetrically applied on both contacts ($V_s = -V_d = V_{SD}/2$). The electrostatic potential of the four previous processes is given by:

$$\begin{aligned} E(N \pm 1) - E(N) &= E_C(N - N_0 \pm \frac{1}{2}) + E_C\frac{q}{e} + E_N \pm eV_{SD}/2 \\ &= E_c(N - N_0 + \frac{1}{2} + \frac{C_gV_g + (C_s - C_d)V_{SD}/2}{e}) + E_N \pm eV_{SD}/2 \end{aligned} \tag{1.8}$$

The transport occurs only if $E(N \pm 1) - E(N) > 0$. In the $V_{SD} - V_G$ plane each inequality is represented by a straight line. Such four lines bound a diamond. Inside the diamond, the number of electrons is fixed due to the Coulomb blockade, and no current flows. Outside the diamonds, the Coulomb blockade is lifted and single electron tunneling takes place. We have the same diamond shifted by $\pm\frac{e}{C_g}$, $\pm\frac{2e}{C_g}$, ... along the V_G axis. The diamonds touch each other at the so-called 'charge degeneracy point', where the energy level is aligned with both μ_S and μ_D, and a current can flow even if $V_{SD}$is infinitely small. From the shape of Coulomb diamonds, the energy of excited states ΔE as well as the charging energy can be extracted.

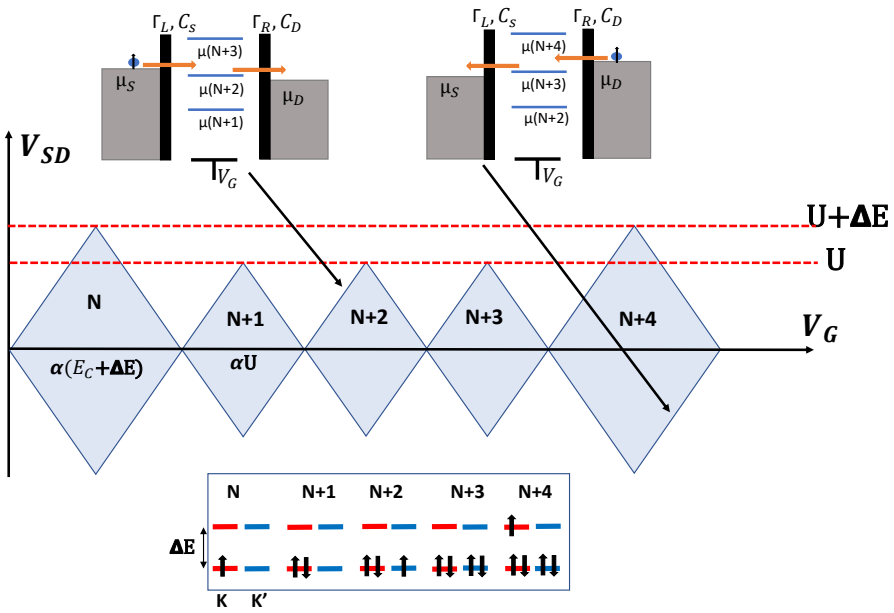

Figure 1.10: Stability diagram for a four-fold degenerate CNT. Coulomb diamonds in differential conductance dI/dV_{SD}, versus V_{SD} and V_G. Each edge of the diamond-shaped regions corresponds to single particle transfer. Inside the diamonds, the number of electrons is fixed by the Coulomb blockade. Each diamond corresponds to an integer number of electrons on the QD. From its size, one can determine the value of E_C and ΔE.

For fourfold degenerate energy level QD, to add the first electron, one should pay the charging energy E_c plus the single energy level spacing ΔE(N^{th}diamond), to add the second, third, and fourth electron one should pay only E_c. Now the level is full, and the next level could be filled. Thus, the stability diagram is composed of three consecutive "small" diamonds of addition energies E_c followed by a "larger" one of addition energy $E_c + \Delta E$ (See fig.1.10). Fig.1.11 represents the differential conductance of a single-wall carbon nanotube QD, the contacts of the CNT are made with Au/Pd bilayers 400 nm apart. The sequence of one large diamond followed by three smaller ones of approximately equal size suggests that the measured SWCNT is four-fold degenerate.

A four-fold degenerate CNT will exhibit a stability diagram as shown in fig.1.10. However, orbital degeneracy can be lifted by spin-orbit coupling, orbital mixing, and magnetic field, leading to two doublets, namely (K↑, K↓) and (K'↑, K'↓). The distribution of the two electrons in the two levels depends on the relative values of the exchange coupling J, which tends to maximize the spin, and the breaking of degeneracy δE [19]. When orbital degeneracy is broken by the energy δE, the stability diagram will be modified. fig.1.12 shows the stability diagram of spin 1/2 degenerate CNT. We observe a "large" diamond (N^{th}) of height $E_c+\Delta E$, followed by a "small" one of addition energy E_c (N+1), now to add the third electron, the addition energy is $E_c + \delta E$, this will lead to a "middle-sized" diamond (N+2) which is slightly bigger than the previous one, followed by again a "small" diamond (N+3) of height E_c.

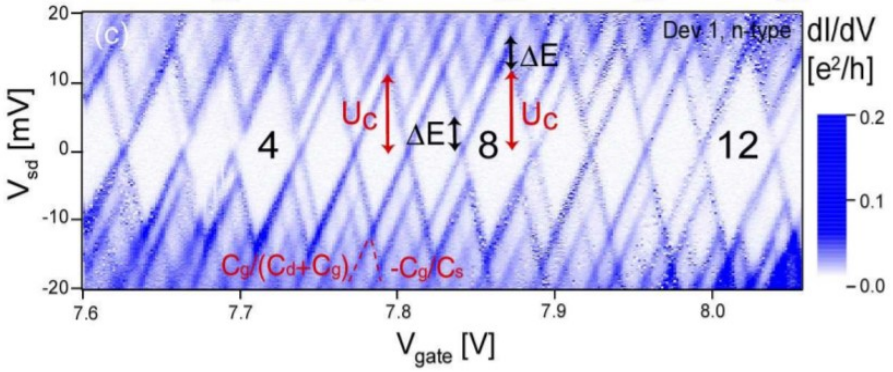

Figure 1.11: The differential conductance as a function of source-drain (V_{sd}) and gate voltage (V_g) at 4K of a carbon nanotube QD. Clear traces of Coulomb blockade are observed. The pattern of a large diamond followed by three smaller ones suggests a (nearly) fourfold degeneracy (including spin) of the single-electron dot states. The charging energy and level spacing can be extracted as shown by the red and black arrows, respectively. Adapted from [18].

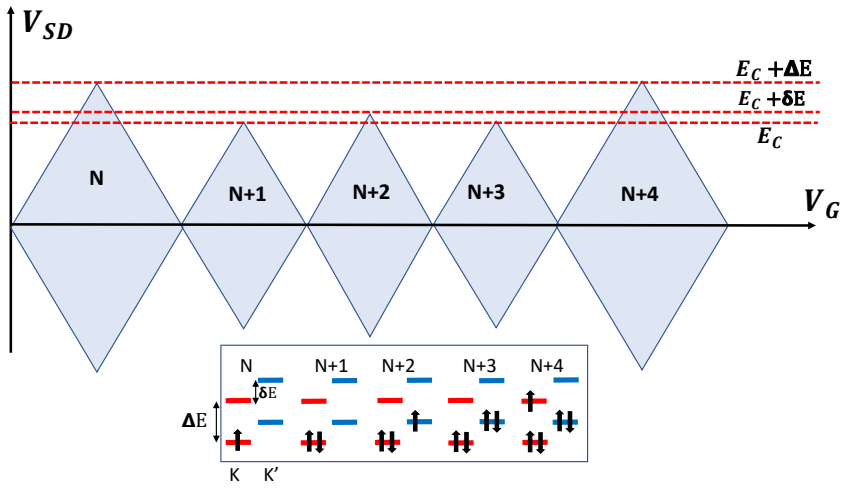

Figure 1.12: Stability diagram for a two-fold degenerate CNT. Due to the breaking of orbital degeneracy, the adding energy of N+2 diamonds increase by δE.

Strong coupling regime

In the strong coupling regime, the QD is well-coupled to the electrodes such that $\Gamma \gg E_C$. The QD is said to be open, the transmission of an electron through the dot is possible for any gate voltage, and no coulomb diamonds are observed. If the contacts are symmetric the conductance reaches its maximum value $\frac{2e^2}{h}$ for a single orbital level due to spin degeneracy and $\frac{4e^2}{h}$ if the level is spin and orbital degenerate.

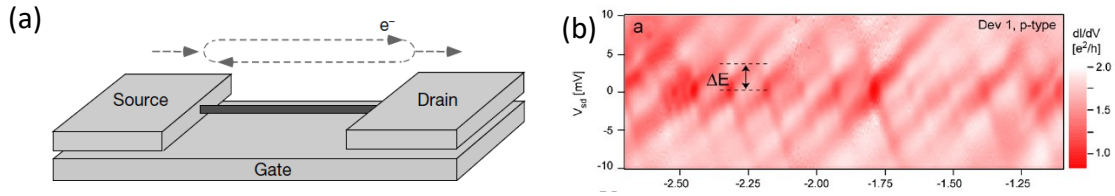

Figure 1.13: (a) Schematic diagram of a CNT (represented in dark grey) device illustrating the multiple electron reflection that gives rise to the observed interference pattern in conductance [20]. (b) Differential conductance dI/dV_{SD}, versus V_{SD} and V_G, showing a Fabry–Perot interference pattern, i.e., an open quantum dot. The maximum conductance is lower than $\frac{4e^2}{h}$ which means that the contacts are not fully symmetric. Taken from [18].

In this regime, the nanotube is considered as a coherent electron waveguide where electron waves can be reflected several times at the CNT/metal interface, analogous to the light transmission in an optical Fabry-Perot cavity [18, 20, 28] (see Fig1.13.(a)). CNT possesses two propagation modes owing to its orbital degeneracy. Electrons in the two propagating modes acquire different phase shifts as they travel through the nanotube. The phase change as a function of electron energy is responsible for the oscillating patterns as a function of V_{SD} and V_g as shown in fig.1.13(b).

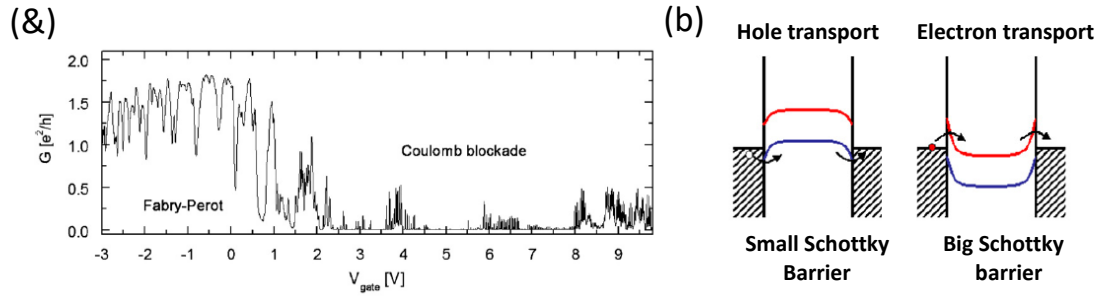

Figure 1.14: (a) Linear conductance versus gate voltage. For negative gate voltage, high conductance Fabry–Perot oscillations are observed. The positive gate voltage is dominated by the Coulomb blockade. (b) Schematic band diagrams of a small band gap CNT, the band bending is controlled by the gate voltage. The red/blue band is the conduction/valence band, respectively. Left: the condition for hole transport through the valence band. Holes tunnel into/out of the valence band through a relatively small Schottky barrier. Right: condition for electron transport through the conduction band, where electrons tunnel into/out of the conduction band through a larger Schottky barrier. Thus, high conductance is observed through the valence band in contrast to low conductance through the conduction band, i.e., Fabry–Perot interference versus Coulomb blockade regime. Taken from [18].

By sweeping the gate voltage one can induce the transition from an open (Fabry–Perot interference) to a closed quantum dot (Coulomb blockade) in the same sample as shown in fig.1.14. By

applying a negative gate voltage, the Schottky barrier for hole transport is relatively small leading to a relatively high conductance. Transport can be changed to electron transport through the conduction band by applying a positive voltage to the gate. The Schottky barrier is in this case significantly larger leading to a low coupling of the SWCNT to the electrodes.

Intermediate coupling regime

In the intermediate coupling regime, the electrical contacts are sufficiently transparent ($U \approx \Gamma$), such that transport is not only possible through sequential tunneling but can also involve higher-order tunneling processes through virtual states. In this regime, the Heisenberg uncertainty principle allows the tunneling of an electron in and out of the dot during a very short time scale of the order $\frac{h}{U}$. Even under Coulomb blockade conditions, two electrons can co-tunnel coherently through the dot without changing its occupancy. This process is known as the "Co-tunneling process".

Co-tunneling processes The co-tunneling process can be either elastic or inelastic. In the case of elastic co-tunneling one electron can tunnel into the dot into a forbidden virtual state and have to leave the dot during a very short time scale t $\sim \frac{h}{\Gamma}$, such that t is of the order of the time scale associated to the charging energy $\sim \frac{h}{U}$, i.e. if $\Gamma \approx$U. At the end of this process, the energy state of the dot does not change as shown in fig.1.15.a.

Fig.1.15.b shows the inelastic co-tunneling process. The tunneling of an electron from the left lead into the dot is immediately followed by the tunneling of another electron from the dot into the right lead, leaving the dot in an excited state due to the creation of an electron-hole pair.

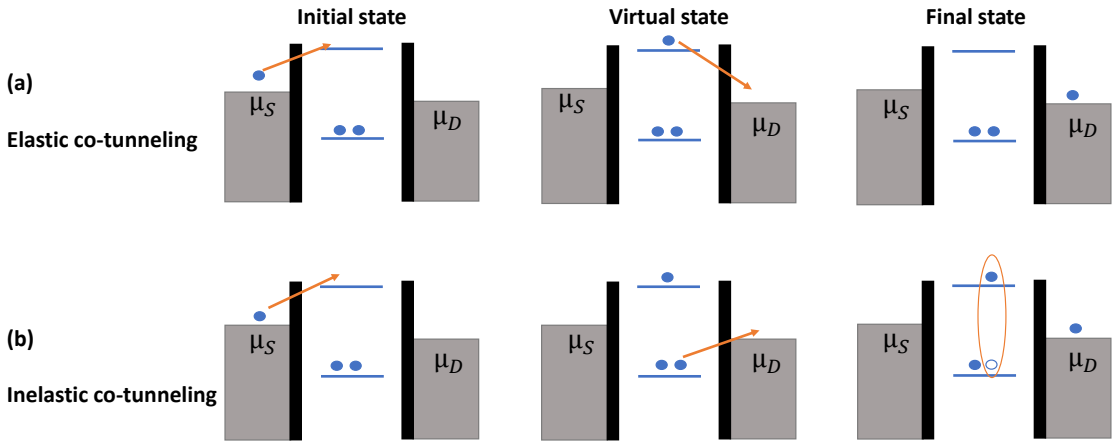

Figure 1.15: Co-tunneling processes in a QD that leads to a current flowing through the QD overcoming Coulomb blockade. (a) Elastic co-tunneling, an electron can tunnel through the QD during a very short time scale, the initial and final state of the QD is the same. (b) In-elastic co-tunneling leaves the dot in an excited state due to the creation of an electron-hole pair.

Fig.1.15 represents the co-tunneling process without considering the spin of the dot. However, considering the dot's spin during elastic co-tunneling leads to richer physics.

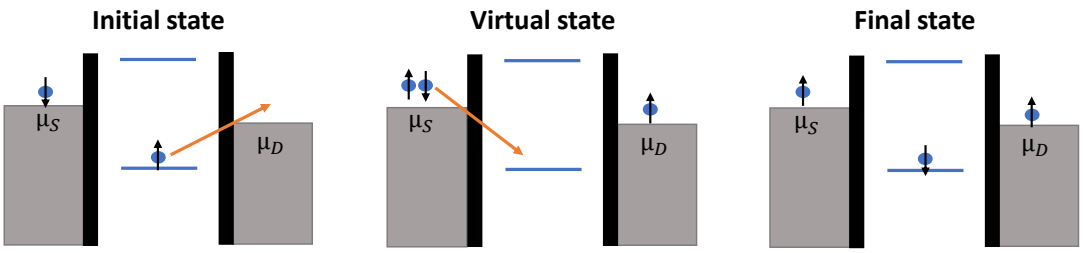

Figure 1.16: Spin flip elastic co-tunneling, the initial state and the final state of the dot have opposite spins. The localized spin in the dot is completely screened by the spins of electrons in metallic reservoirs.

Initially, the dot is occupied by an electron of spin 'up'. After passing a virtual intermediate state, a spin 'up' electron can tunnel from the dot and be replaced immediately by tunneling of spin 'down' electron into the dot. The transfer of electron through the dot is accompanied by a spin-flip process. The coherent superposition of all possible co-tunneling processes involving spin flip can result in a time-averaged spin equal to zero. Thus, the localized spin on the dot is screened by the spins of electrons in metallic leads. This spin-flip co-tunneling process is the origin of the Kondo effect in quantum dots which will be discussed in detail in section 3.4).

1.2.3 Conclusion

In this chapter, we presented the system that we are studying during this work: A Carbon nanotube quantum dot. We have shown that a CNT sandwiched between two metallic contacts can be considered as a quantum dot with a discrete energy level spectrum. The electronic transport through a CNT QD depends on transmission between metallic contacts and the tube. A highly coupled CNT is said to be open. However, a weakly coupled CNT behaves as a quantum dot in the Coulomb blockade regime. The Four-fold degeneracy of a CNT is revealed by analyzing the shape and size of the Coulombs diamonds. In the intermediate regime, due to co-tunneling, the Kondo effect in a QD emerges.

Chapter 2

Experimental techniques

2.1 Nanofabrication and Measurement Setup

In this section, we present the different nanofabrication techniques used to fabricate the desired sample, the system used to cool it down, and the techniques used to perform the electrical transport and high frequency measurements.

The sample is made of a carbon nanotube (CNT) contacted between two superconducting contacts, which make it possible to induce superconductivity through it. In order to detect the emission of the CNT, the CNT is coupled to an on-chip detector, a superconductor-insulator-superconductor (SIS) junction, via a coplanar waveguide resonator.

2.1.1 Synthesis of carbon nanotubes

Various methods can be used for the synthesis of carbon nanotubes. Depending on the way of extraction of the carbon atoms from the used precursors or target and the temperature, these processes can be divided into two groups: physical or chemical.

Physical methods typically use high energy sources, such as plasma in an arc discharge experiment [21] or laser ablation [22], to extract the carbon atoms. These methods require a very high temperature between 3000°C and 4000°C. However, in chemical methods, the carbon atoms are extracted through catalytic decomposition of precursors (Carbon monoxide [23], ethanol [24], methane [25], ethylene [26]) on metal nanoparticles at a temperature in the range of $500 - 1200$ °C.

In our experiment, the carbon nanotube is synthesized by chemical vapor deposition (CVD) where acetylene is used as a precursor. This process has been developed by one of the group's members: Alik Kasumov [27]. On a silicon substrate, a very thin layer of iron catalyst (thickness of few nm) is deposited by sputtering. The substrate with the catalyst is placed in a quartz tube and then introduced into the oven shown in fig.2.1. The system is pumped down to pressure lower than 0.1 mbar and heated progressively until a temperature is around 900°C. Then few mbar of pure acetylene is introduced into the oven during 9s then pumped out and extracted from the oven using a cold trap at liquid nitrogen temperature. When the acetylene molecules touch the heated catalyst, it is cracked on the edges of the catalyst, and nanotubes are formed. When the synthesis is over, the oven is cooled down to room temperature. The carbon nanotubes synthesized by this process have a diameter around 1-5 nm and length of few micrometers, with a reduced number of

defects and a clean surface compared to arc discharge or laser ablation technique [27]. After CVD, the sample is observed with a scanning electron microscope (SEM) with an Inlens detector, with this detector we probe the charging effect associated with the presence of carbon nanotubes. An SEM picture of carbon nanotubes grown during this work is shown in fig.2.1.

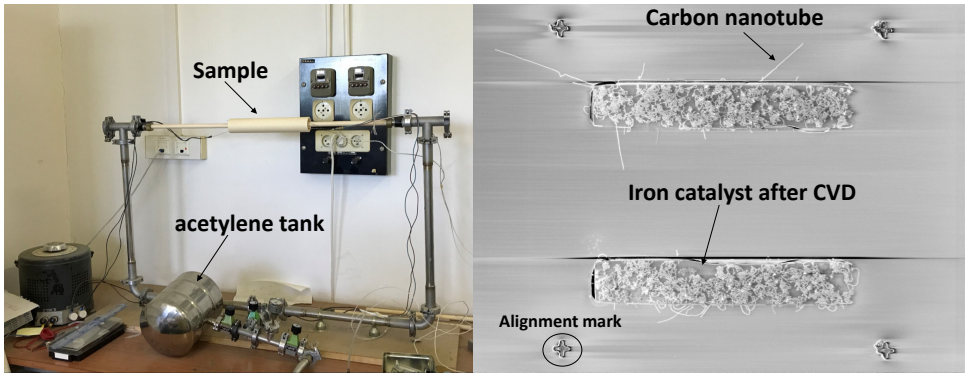

Figure 2.1: Left: Picture of the oven where the CVD synthesis of carbon nanotube takes place. Right: scanning electron microscope image of the sample after CVD, the carbon nanotubes are observed.

2.1.2 Fabricating the sample

Lithography technique

To draw a nanoscale designed pattern on the sample, electron beam lithography is performed with a scanning electron microscope. Before starting the lithography process, we deposit a thin layer of electron-sensitive resist by spin-coating. The thickness of the layer is increasing with the polymer viscosity and decreasing with the speed rotation of the spin coater.

In this experiment, we used a bilayer of resists MMA EL10/PMMA A3:

- MMA EL10 (methyl methacrylate, EL means ethyl lactate) is spin-coated during 60s at 2000 rpm (thickness ∼550 nm).
- PMMA A3(poly methyl methacrylate) is spin-coated during 60s at 4000 rpm (thickness ∼100 nm).

Since the polymer was conserved in a solution, we heat the sample after each resist coating for two minutes at 180°C to let the solvent evaporate. The PMMA/MMA bilayer gives a large undercut profile upon exposure and development. The importance of this undercut appears in the fabrication of tunnel junctions. During lithography, the electron beam is accelerated by a voltage 30 keV with a dose equals 320 µC/cm². Note that two SEM diaphragms, leading to different electron currents are used during lithography: 7.5 µm (current: 16 pA) and 120 µm (current: 10 nA) for precise and coarse patterns, respectively. During exposure, the pattern is written directly onto the electron sensitive resist, point by point following the pattern designed previously with CAD software (DesignCad). The exposure causes a change in the chemical properties of the polymer, which can

be eliminated by proper development. This is done by making the sample soak during 60s in a solution of MIBK (methyl buthyl ketone) diluted at 1:3 with isopropanol at room temperature. After the development of the sample, one obtains a positive mask with the desired design which is ready for metallic deposition.

In this work, the sample is fabricated in two steps. First, we fabricate the contact on the CNT and, in a second step, design the SIS junction and the resonator.

connecting the carbon nanotube

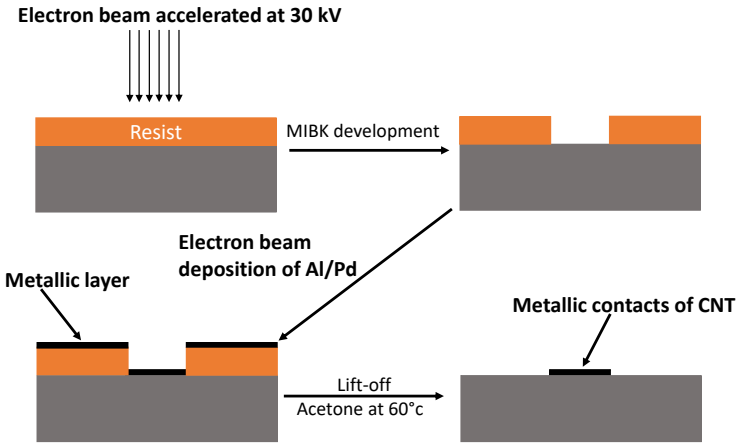

Figure 2.2: Schematic description of all the steps to make metallic contacts on a carbon nanotube, as described in the text.

After CVD, one of the nanotubes is chosen and contacted between two metallic electrodes. For this purpose, the contact of the tube and the side gate are drawn using CAD software (DesignCad) in the right position thanks to the SEM image of the sample with alignment marks as the one shown in fig.2.1. Then the sample is spin-coated with a bilayer of resist. Note that at this step the formation of an undercut is useful to make the lift-off easier. Then electron beam lithography with a small current is performed followed by developments with MIBK.

Metal deposition The metal used to connect the tube is chosen to be superconducting. We have chosen Al because its superconductivity can be destroyed by a rather small magnetic field. This allows characterizing the normal state of the CNT without affecting his property, especially the Kondo effect. The deposition of Al is preceded by the deposition of a thin layer of palladium Pd. Pd is necessary since it provides high transparency contact to the carbon nanotube [28], but it reduces the superconducting gap compared to bare aluminum. The two metals are deposited by e-gun metal deposition under the following conditions:

- Pd: 7 nm at a rate of 0.2nm/s,(e-gun current I=200mA), pressure $P = 9 \times 10^{-8} mbar$, angle of evaporation θ=0°.

- Al: 73 nm at a rate of 1nm/s, (e-gun current I=200mA), pressure $p = 2 \times 10^{-7} mbar$, angle of evaporation θ=0°.

To reach an optimal value of vacuum pressure, the chamber is pre-deposited with Niobium, which helps decrease vacuum pressure.

Lift-off After metallic deposition, the sample is placed in acetone at 60°C for almost 1 hour. Acetone will dissolve the resist and the metallic layer covering it will be removed. The whole procedure is summarized in fig.2.2.

Fabricating Josephson Junctions

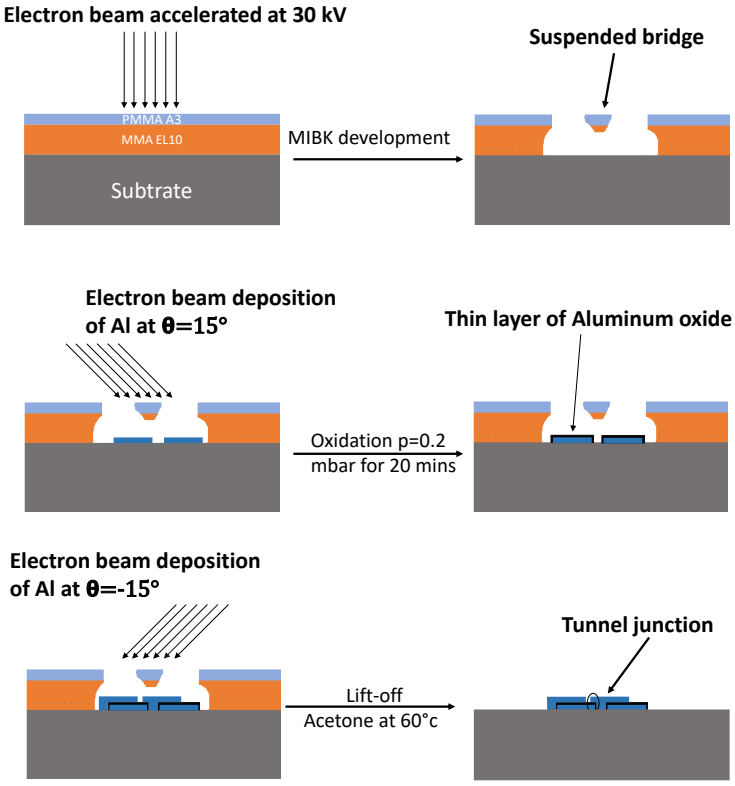

Figure 2.3: Schematic description of all the steps to fabricate a tunnel junction with directional angular deposition.

Once the contacts of the CNT are deposited, the sample undergoes another lithography step, where the tunnel junction and the resonator cavity are drawn with small and high current, respectively. For metallic deposition, we use the angular evaporation technique (see fig.2.3) which consists first of depositing 100nm of Aluminum at a θ=-15°. Then the Al layer is oxidized by 0.2 mbar of oxygen

for 20 minutes forming a thin layer of aluminum oxide of the order of nanometer. Finally, the AlO_x layer is covered by 120 nm of Al deposited with an angle of 15°. After the metallic deposition, the sample is inserted in hot acetone for 60 minutes. Acetone dissolves all the unexposed resist and we are left with a metallic layer of the desired pattern. The obtained junctions have typically a surface of 200nm×200nm and their resistance of the order of tens of kΩ. The value of the resistance depends highly on the oxidation process. Since AlO_x is very fragile and can break if any overvoltage pulse is applied to the junction, one should wear an antistatic bracelet and ground carefully the equipment during manipulation. Fig.2.4 shows a detailed SEM image of the sample, the CNT and the Josephson junction are coupled on-chip to a coplanar waveguide resonator made with aluminum.

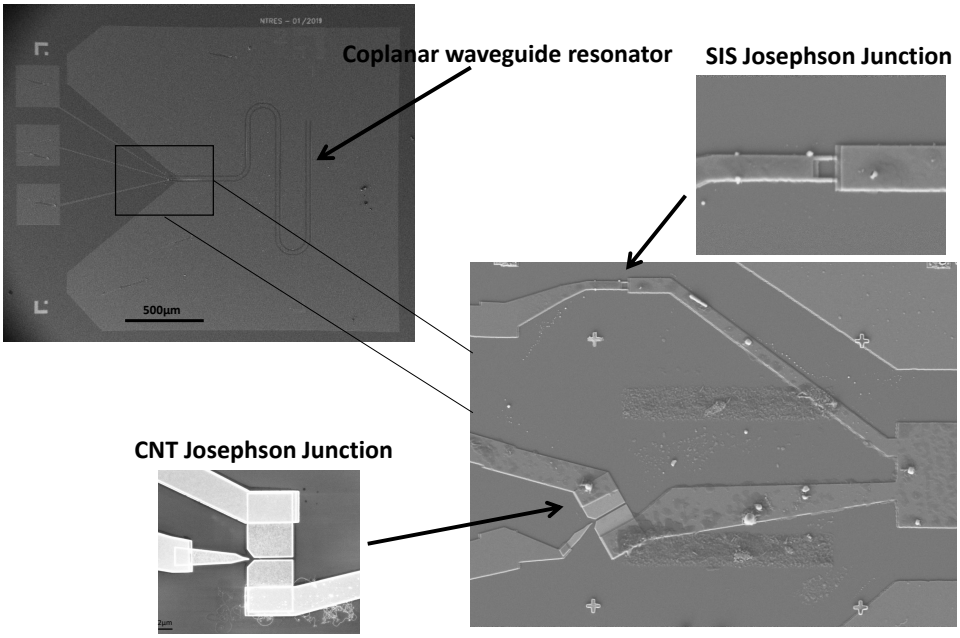

Figure 2.4: SEM image of the sample. A CNT connected to two metallic reservoirs 400 nm apart made with Al/Pd coupled on-chip via a coplanar waveguide to an SIS quantum detector.

2.1.3 Carbon nanotube samples with side gates

During this Ph.D., I have worked with Meydi Ferrier on fabricating a new carbon nanotube device. An SEM image of the sample is represented in Fig.2.5. In this sample, the CNT is contacted between two metallic contacts made with 7nm-Pd/23nm-Al 400 nm apart, with three gates. One central gate G_1 is used to tune the electrochemical potential and the two other side gates G_2 and G_3 aims to tune the transmission amplitudes of the barriers. To fabricate this sample, we perform the same lithography and metallic deposition steps explained previously. However, since for the side gates we aim at a very small width $\sim$ 50 nm, we have used CSAR 62 as a resist, which is based on methyl styrene-co-α-chloromethacrylate with the addition of halogenated acid. This resist provides high sensitivity and resolution up to 10 nm. By tuning the transparency of the contacts, we will

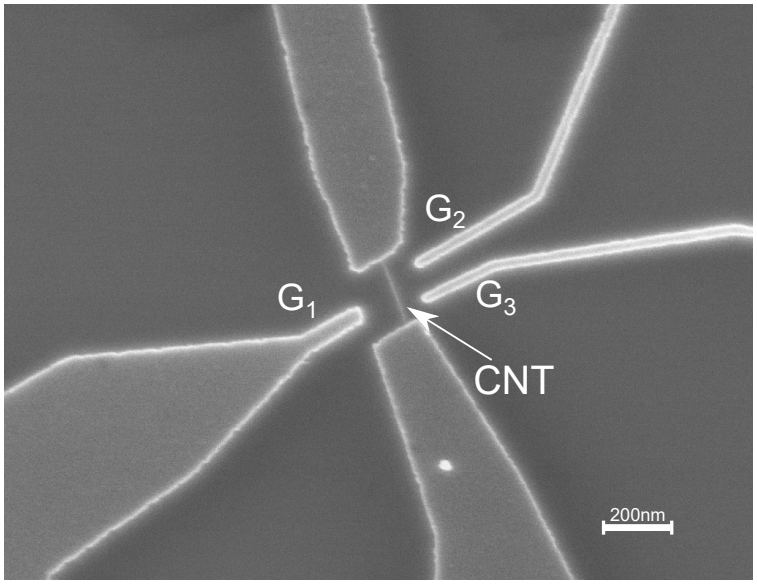

Figure 2.5: SEM image of the CNT sample with three gates. The small gates G_2 and G_3 are ∼50 nm in width and used to tune the transparency of the contacts.

be able to control the contact asymmetry $a = \Gamma_L/\Gamma_R$, thus we will have access to many different transport regimes within the same sample.

2.1.4 Cryogenic cooling

In order to investigate the electronic transport properties of CNT devices, a low-temperature environment is required, below 50 mK. This temperature can be reached by using the $^3He/^4He$ wet dilution fridge. However, during this work, we install a new dry fridge of base temperature around 10 mK. The electronic temperature of this dry fridge was measured using a single electron transistor thermometer, the calculated value is around 22 mK (See Chapter 7 section 7.1) for the detailed measurement). In what follow we describe the operation principle of wet and dry dilution refrigerators.

Wet dilution fridge

In a dilution refrigerator, the low temperature is achieved by using a mixture of $^3He/^4He$. A vacuum pump at room temperature is used to circulate the mixture through the dilution fridge.

The wet dilution fridge is initially cooled down at 4.2K by a liquid helium bath. When the fridge is cold and running, the $^3He/^4He$ mixture is injected by a vacuum pump and undergoes a cool down to around 3k by the vapors of the still. On its way to the mixing chamber, the mixture passes through a series of impedances (Z_1 and Z_2) that perform Joule-Thomson expansions of the $^3He/^4He$ mixture cooling it down below 1 K. Its temperature further decreases inside the continuous heat exchanger due to the counter flow of the liquid towards the still. Finally, the

mixture arrives at the mixing chamber. When cooled down below 1K, the mixture undergoes spontaneous phase separation to form a ^3He-rich phase (the concentrated phase) and a ^3He-poor phase (the dilute phase).

Dilution cooling occurs in the mixing chamber which is connected to the still through a distillation column. In the mixing chamber, two phases of the $^3He/^4He$ mixture, the concentrated phase (practically 100% ^3He) and the dilute phase (about 6.4% ^3He and 93.6% ^4He), are in equilibrium and separated by a phase boundary.

As we pump ^3He vapor from the liquid inside the still, the ^3He concentration in the liquid will decrease. The difference in ^3He concentration between the still and the mixing chamber results in an osmotic pressure gradient along the distillation tube. This osmotic pressure pulls ^3He from the mixing chamber where it is separated from the ^4He. On its way to the still the cold, dilute ^3He cools the incoming ^3He via the heat exchangers. Meanwhile in the mixing chamber, the ^3He percentage of the diluted phase is reduced, which leads to the flow of ^3He from the concentrated phase to the diluted phase to maintain the 6.4% ^3He in the diluted phase . The process of moving the ^3He through the phase boundary is endothermic and removes heat from the mixing chamber environment, thus a base-temperature of 50 mK is achieved. The pumped ^3He is then re-injected using a compressor into the cryostat completing the cycle.

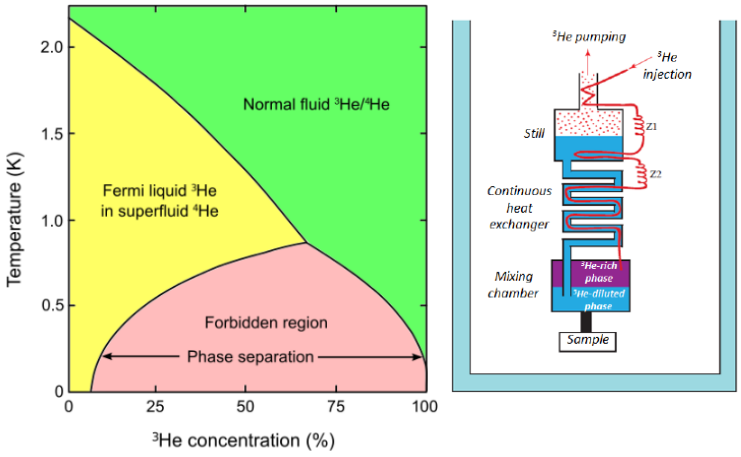

Figure 2.6: Left: phase diagram of $^3He/^4He$ mixture, when cooled down below 1k, the mixture separates into two phases with the ^3He/-rich phase floating on top of the heavier ^4He/-rich phase which contains 6.4%^3He/ . Right: Schematic diagram of a wet $^3He/^4He$ dilution refrigerator. In the mixing chamber the mixture undergoes spontaneous phase separation to form a ^3He-rich phase (the concentrated phase) and a ^3He-poor phase (the dilute phase).

Dry dilution fridge

In a dilution refrigerator instead of using liquid helium, a pulse Tube cryocooler is used to cool down the mixture down to 4K. The refrigeration temperature is achieved by the continuous expansion and compression of the working gas which is ^4He within a closed volume.

When the pulse tube (PT) started, the only cold part of the system is the cold head of the

PT. First, the mixture is pre-cooled by the cold head, which will in turn cool down the Mixing Chamber (and the other parts of the fridge) before the condensation. During the pre-cooling phase, the mixture is injected directly into the pumping line surrounding the cold head of the pulse tube. Afterward, the mixture goes in the Joule-Thomson exchanger, then in the still and the mixing chamber. Finally, the mixture goes out from the Mixing Chamber to the fast pumping line and then out from the refrigerator to the gas handling system 'GHS' (The GHS consist of the mixture tank, the primary pump, the turbopump, the compressor, the auxiliary primary pump, and the electrical box). This process continues until the Mixing chamber is at 4k. The process is summarized in fig.2.7.a.

To reach the lowest temperature on the mixing chamber plate, the circulation of the mixture is reversed (as shown in fig.2.7.a) and condensation of the mixture starts.

The mixture undergoes the same thermodynamics cycle described in the previous section. A given amount of mixture is used during the condensation. After the condensation is finished, the fridge is kept running at its lowest temperature $\sim$ 10 mk. In this work, we have installed a new dry dilution refrigerator, which was used to characterize a high kinetic impedance resonator made with tungsten at 10 mK (See chapter 7 section 7.2).

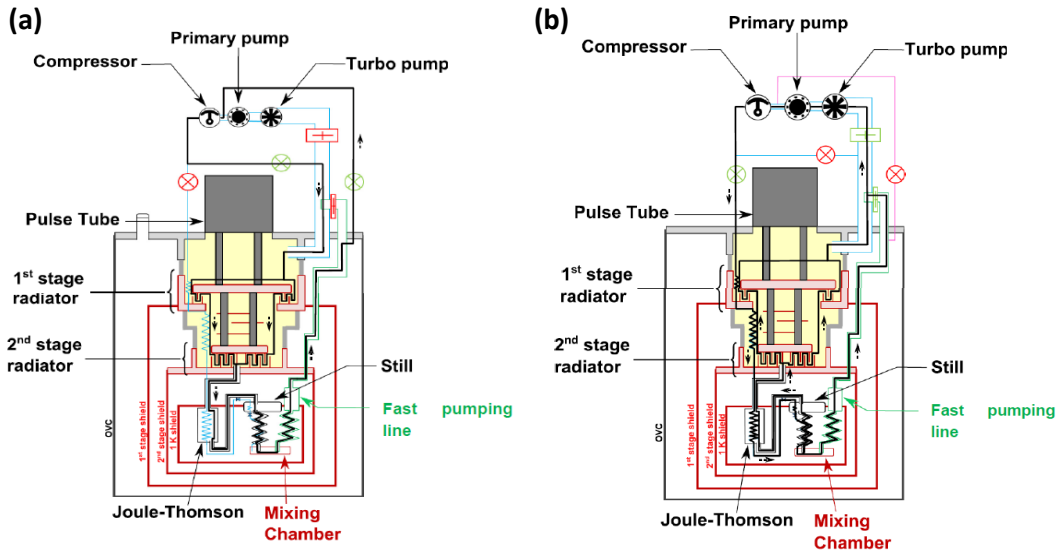

Figure 2.7: (a): Working scheme of the gas circulation during the pre-cooling mode. (b): Working scheme of the gas circulation during the Condensation mode.

2.1.5 Wiring and filtering

In this work the CNT sample is measured at 50 mK using a wet dilution refrigerator equipped with a superconducting magnet, providing a magnetic field going from 0 to 1 T.

The sample to measure is thermally connected to the coldest part of the dilution fridge: the mixing chamber and measured through low pass filtered lines with a standard lock-in amplifier technique. The sample is connected to the BNC connector on top of the dilution fridge by DC

lines made of manganin wires of resistance 30Ω, an alloy of copper, manganese, and nickel. The resistivity of this alloy depends very weakly on temperature. The DC filtering is achieved by two filters: a π-filter on the top of the fridge at room temperature which filters frequencies above 10 kHz if the sample resistance is about 5Ωk and a 100nF capacitance placed close to the sample.

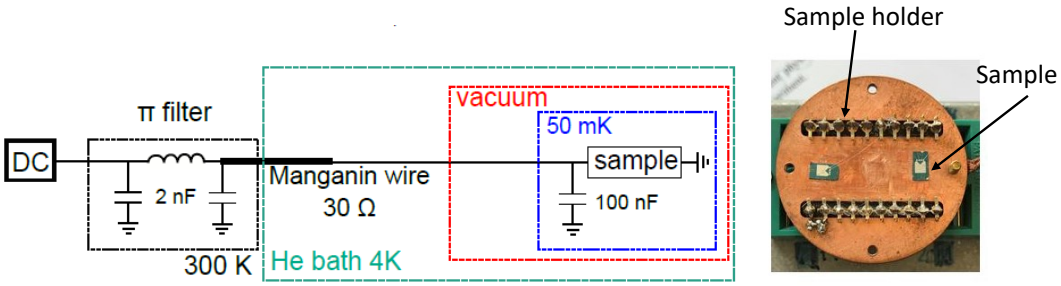

Figure 2.8: Left: Schema of the DC wiring and filtering of the dilution fridge we used. The sample is thermally connected to the mixing chamber of the dilution fridge and electrically connected to the top of the dilution fridge by manganin wires. The filtering consists of a π-filter at room temperature as well as a capacitance of 100 nF placed close to the sample [60]. Right: Two Samples are connected via thin Al/Si wires to a sample holder made with copper.

2.1.6 Sample measurement

Here I present two examples of measurements we have performed, the measurements of the differential conductance and differential resistance versus the gate and the source-drain bias voltage.

For the differential conductance measurements, the CNT is DC voltage biased and AC biased. One side of the sample is grounded to the fridge, so the current is measured from the voltage across the 1KΩ resistance in the superconducting (normal) state. Differential conductance dI/dV is measured directly with a lock-in amplifier, and the DC voltage is measured with a voltmeter. For the differential resistance measurements, the CNT is current biased. dV/dI and the DC voltage are measured directly with a lock-in amplifier and a voltmeter respectively at 0.1 nA modulations.

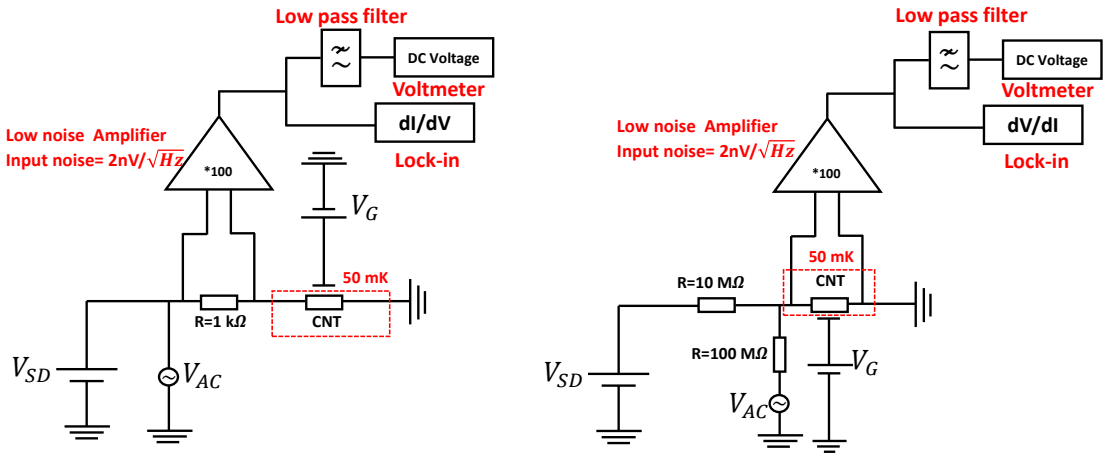

Figure 2.9: Example of electrical setup used in measurements. Left: Measurements of the Differential conductance of the CNT, the current is deduced from the voltage across the 1kΩ resistance. Right: Measurements the differential resistance of the CNT, the voltage across it is measured directly.

Chapter 3

Kondo effect

In normal metals, the main contribution to the resistivity is the electron-phonon scattering. As temperature decrease, the electrons can travel more easily as the lattice vibrations of the metallic crystal decrease. At zero temperature, the phonon population is zero and the finite residual resistivity is explained by the scattering with the defects of the metal. However, the resistance of alloys with magnetic impurities (e.g. in gold) is found to increase [29] at low temperature. In 1964, the theoretical physicist Jun Kondo explained this upturn of electrical resistance by the so-called Kondo effect [30]. The Kondo effect is a many-body phenomenon that can appear when there is some localized, non-zero spin degree of freedom coupled to a Fermi sea of conduction electrons. The conduction electrons of the host metal tend to screen the localized spin. This screening leads to the formation of a macroscopic coherent state called the 'Kondo cloud'. The Kondo cloud has a large scattering cross-section. Thus, the conduction electron scattering is enhanced, and eventually the resistance increases. The temperature below which this phenomenon occurs is called the Kondo temperature T_K [31].

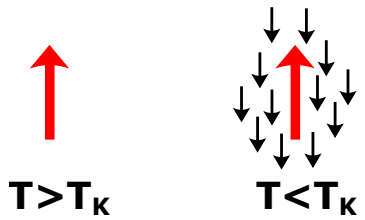

Figure 3.1: For $T > T_K$, the magnetic impurity is decoupled from the conduction electrons. If, $T < T_K$ conduction electrons and the magnetic impurity interact coherently and form a Kondo cloud.

3.1 Kondo Hamiltonian

In the Kondo model, the Kondo effect can be described by the following Hamiltonian:

$$\mathcal{H}_{Kondo} = \sum_{k\sigma} \epsilon_k c^{\dagger}_{k\sigma} c_{k\sigma} + J\vec{S}.\vec{s_b} \tag{3.1}$$

The first term corresponds to the kinetic energy of the conduction electrons while the second one describes the exchange interaction J between a localized magnetic moment of spin $\vec{S}$, and the conduction electrons with spin $\vec{s_b}$. The operator $c^{\dagger}_{k\sigma}$ ($c_{k\sigma}$) creates (destroys) a conduction electron with momentum k, and spin σ. J represents the strength of the interaction between the local conduction electron and the local moment states. Assuming $J < 0$, Kondo used a perturbation theory to calculate the resistivity due to the scattering with the impurity:

$$R(T) = R_0[1 - 2J\rho \log\left(\frac{k_B T}{D}\right)] \tag{3.2}$$

where R_0 is a constant, ρ is the conduction band density of state at the Fermi energy, and D the bandwidth of the density of state. The perturbation theory provides a good description of the magnetic impurity systems for $T > T_K$ but the expansion breaks down at $T < T_K$. The perturbative approach gives a logarithmic divergence of the resistance at low temperature, while experimental studies show that the resistivity is given by the power law of T with T^2 terms. Non-perturbative techniques are required to investigate the low-T regime.

3.1.1 Renormalization Group

A complete understanding of the Kondo problem comes from renormalization. Anderson has proposed a poor man's scaling [32] consisting of the renormalization of the Kondo Hamiltonian by rescaling of all parameters. The scaling approach leads to the concept of the existence of a fixed point when J(D) becomes scaling-invariant. The system is then described by the fixed point. However, this approximation led to the divergence of the coupling constant J at a finite cutoff $D = T_K$ which must be an artifact since the model can not have any phase transition at finite temperature.

The correct solution can only be obtained by the renormalization group technique [33]. The idea is to divide the conduction band into a set of discrete electron levels each one is called "Kondo state". Then one solves the Kondo Hamiltonian for each Kondo state by numerical methods. This proceeds in steps. First one solves the impurity coupled to the first Kondo state. The next step is to add the second Kondo state and solve the combined coupling of the first and second conduction band states to the impurity. Then one adds the third state, then the fourth state, and so forth. This corresponds to solving for the eigenvalues at successively smaller and smaller energy scales. The major result of this approximation was the demonstration that there is a unique stable fixed point in the one-channel Kondo model: $J \to \infty$, which means that the smaller is the energy scale, the stronger is the effective coupling to the impurity. In another word, this effective antiferromagnetic coupling increases for electrons close to the Fermi level. This leads to a resonance in the density of states of a width of the order of T_K pinned to the Fermi energy, which is called the Kondo resonance. The Kondo effect is characterized by a single energy scale, T_K, which is a scaling invariant. It can be expressed in terms of the coupling J and the density of state N_0:

$$k_B T_K \propto e^{\frac{-1}{N_0|J|}} \tag{3.3}$$

3.2 Anderson model

A localized magnetic state, can be modeled by the Anderson single level impurity model, where the magnetic impurity is viewed as having one energy level with an unpaired electron at energy level ϵ_0, and a Coulomb repulsion U. All energy levels below ϵ_0 are fully occupied with electrons, and all energy levels above ϵ_0 are unoccupied.

The position of ϵ_0 can be tuned by the gate voltage. The state giving rise to the Kondo effect, consisting of a localized degenerate state coupled to an electron reservoir, is well characterized by the Anderson Hamiltonian [37]:

$$\mathcal{H} = \sum_{k\sigma} \epsilon_k c^\dagger_{k\sigma} c_{k\sigma} + \sum_\sigma \epsilon_\sigma d^\dagger_\sigma d_\sigma + U n_{d\uparrow} n_{d\downarrow} + \sum_{k\sigma} (v_k d^\dagger_\sigma c_{k\sigma} + v^*_k c^\dagger_{k\sigma} d_\sigma) \tag{3.4}$$

The first two terms account for the conduction electrons and the impurity, respectively, where $c^\dagger_{k\sigma}$ ($c_{k\sigma}$) creates (destroys) an electron in the leads with momentum k, spin σ, and energy ϵ_k. The third term represents the Coulomb repulsion when the level is filled with two electrons of opposite spin, and the last term is the coupling between the conduction electrons and the impurity with amplitude v_k. For an isolated impurity $v_k = 0$. This Hamiltonian has four eigenstates: $|0\rangle$ with energy 0, the two degenerate states $|\uparrow\rangle$, $|\downarrow\rangle$ with energy ϵ_0 and the doubly occupied state $|\uparrow\downarrow\rangle$ with energy $2\epsilon_0+U$. The ground state is $|\uparrow\downarrow\rangle$ for $\epsilon_0 < -U$, the degenerate doublet $|\uparrow\rangle$, $|\downarrow\rangle$ for $-U < \epsilon_0 < 0$ and the empty state $|0\rangle$ for $\epsilon_0 > 0$. Thus, the QD can carry an S=1/2 local moment only for $-U < \epsilon_0 < 0$. Note that $\epsilon_0 = -\frac{U}{2}$ corresponds to the particle–hole symmetry point.

3.3 Equivalence with the Kondo problem

In the case of the local moment ($-U < \epsilon_0 < 0$), performing the Schrieffer-Wolff unitary transformation [38] on eq.3.4, shows that the Anderson Hamiltonian was equivalent to the Kondo one, and J can be expressed in terms of the Anderson parameters such that [38]:

$$J = 2 \mid v_k \mid^2 \frac{U}{\epsilon_0(\epsilon_0 + U)} \tag{3.5}$$

v_k can be expressed in terms of the coupling constant Γ and the density of states N_0, such that $\mid v_k \mid^2 = \frac{\Gamma}{\pi N_0}$. The expression of J is given as follow:

$$J = \frac{2\Gamma U}{\pi N_0 \epsilon_0(\epsilon_0 + U)} \tag{3.6}$$

where Γ is the width of the impurity energy level, and U the Coulomb repulsion between two electrons at the site of the impurity. For $-U < \epsilon_0 < 0$, J is negative confirming the antiferromagnetic nature of the exchange between the conduction electron and the impurity.

From eq.3.3 and 3.6, the Kondo temperature, T_K is expressed in terms of the parameters of the Anderson model [31]:

$$k_B T_K = \frac{\sqrt{U\Gamma}}{2} e^{\frac{\pi}{2}\epsilon_0 \frac{(\epsilon_0+U)}{(\Gamma U)}} \tag{3.7}$$

Note that the minimum value of T_K is obtained at the electron/hole symmetry point, $\epsilon_0 = -U/2$. The maximum T_K is found on the edges of the $-U < \epsilon_0 < 0$ zone.

3.4 Kondo effect in quantum dot

A simple Kondo system can be realized with a quantum dot connected to metallic leads via two tunnel barriers. The Kondo effect was predicted to occur in QDs in 1988 [39, 40], and then experimentally observed in semiconductor heterostructures [41], carbon nanotubes [42], individual molecules [43], and semiconductor nanowires [44] QDs.

The first observation of the Kondo effect in quantum dots was made in GaAs-based two-dimensional structures. The Kondo effect has now been seen in quantum dots based on a wide variety of nanomaterials such as carbon nanotubes, C_{60} molecules, organic molecules, and semiconductor nanowires.

We have seen in the previous section 1.2.2, that depending on the coupling between a quantum dot and source-drain electrodes, the electronic transport through the QD can be either in the Coulomb blockade or Kondo regime. When the electrical contacts are sufficiently transparent, and the QD is occupied by an odd number of electrons i.e. its highest energy level carries a spin 1/2 magnetic moment, higher-order co-tunneling process are possible in which the transfer of an electron between the leads is accompanied by the simultaneous flip of the electron's spin of the dot (See fig.3.2). The coherent superposition of many such co-tunneling events results in the screening of the local spin, which leads to the appearance of a peak in the density of states at the Fermi level of the electrodes, called Kondo resonance [31]. To probe transport through a quantum dot, all the electrons have to travel through this single magnetic site. In this case, the Kondo resonance makes it easier for states belonging to the two opposite electrodes to mix. This mixing increases the conductance. In another word, even in the Coulomb blockade regime, the Kondo effect makes it possible for current to flow through the QD. The great advantage of using quantum dots to study the Kondo effect is that their parameters can be calculated and tuned easily.

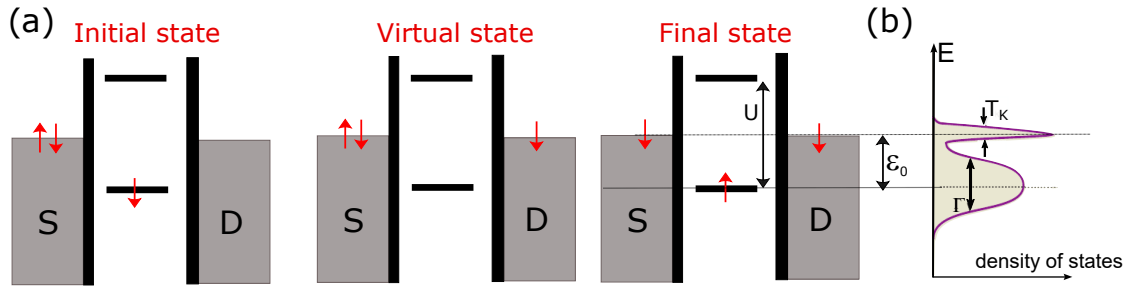

Figure 3.2: (a) Kondo screening mechanism in a QD. At the end of the co-tunneling process, the spin of the QD is flipped. (b) A resonance of width $k_B T_K$ develops in the density of states of the quantum dot at the Fermi level of the electrodes due to the Kondo effect.

By measuring the stability diagram of a QD, if the temperature is below the Kondo temperature T_K, Coulombs diamonds with an odd number of electrons exhibit a strong conductance increase at zero bias: the so-called Kondo ridge. From the width of the Kondo peak in bias voltage, we can extract the Kondo temperature. The zero-bias conductance peak whose amplitude depends on the

barrier's transmissions [45]:

$$G = \frac{2e^2}{h} \frac{4\Gamma_R \Gamma_L}{(\Gamma_R + \Gamma_L)^2} \sum_n \frac{\sin^2 \delta_n}{2} \tag{3.8}$$

where δ_n is the scattering phase shift of each channel participating to transport. According to the Friedel sum rule, $\delta_n = \pi \langle N_n \rangle$ with N_n the average occupation of the state n. In an ordinary spin-1/2 Kondo effect, there are two spin states and one electron, such that $\langle N_n \rangle = 1/2$. eq.3.8 is reduced to:

$$G = \frac{2e^2}{h} \frac{4\Gamma_R \Gamma_L}{(\Gamma_R + \Gamma_L)^2} \tag{3.9}$$

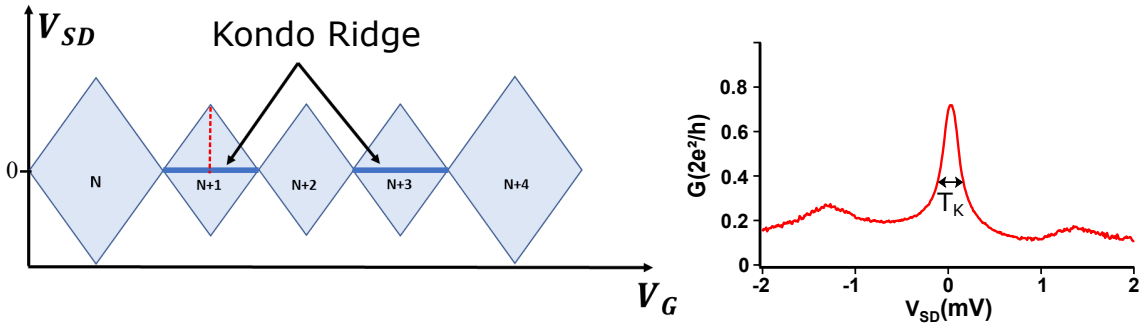

Figure 3.3: Left: Stability diagram of Four-fold degenerate CNT QD as a function of V_{SD} and V_G of a quantum dot in the Kondo regime. Blue regions correspond to low conductance due to Coulomb blockade, and white corresponds to high conductance. The Kondo ridges appear at every diamond that corresponds to an odd number of electrons on the dot. Right: Vertical cut at the center of the Kondo ridge (indicated in red) showing the peak in conductance at zero bias. From the half-width at half maximum of the Kondo peak one can extract the Kondo temperature T_K.

3.5 Specificity of a carbon nanotube Quantum dots

The Kondo effect requires the presence of unpaired spin in the highest occupied energy level of a QD. However, the role of the spin could be replaced by other degrees of freedom, such as an orbital quantum number [46, 47]. The four-fold degeneracy of the carbon nanotube enables the observation of different types of Kondo effect. This degeneracy is generally broken with an energy splitting equal to δE. If $\delta E \gg U, \Gamma$, the CNT is considered as a single level QD. Then the usual spin-1/2 SU(2) Kondo effect is observed. If $\delta E = 0$, i.e. orbital and spin degeneracies are present simultaneously, this leads to SU(4) Kondo effect of higher symmetry [49, 50]. Orbital Kondo effect has been also observed in CNT QD [48]. All these situations are summarized in fig.3.4.

3.5.1 SU(2) Kondo effect in CNT QD

Let us consider the case of a CNT QD connected to two metallic leads, where orbital degeneracy is broken by δE, such that $\delta E \gg U, \Gamma$. In this case, only one level, which is spin degenerate,

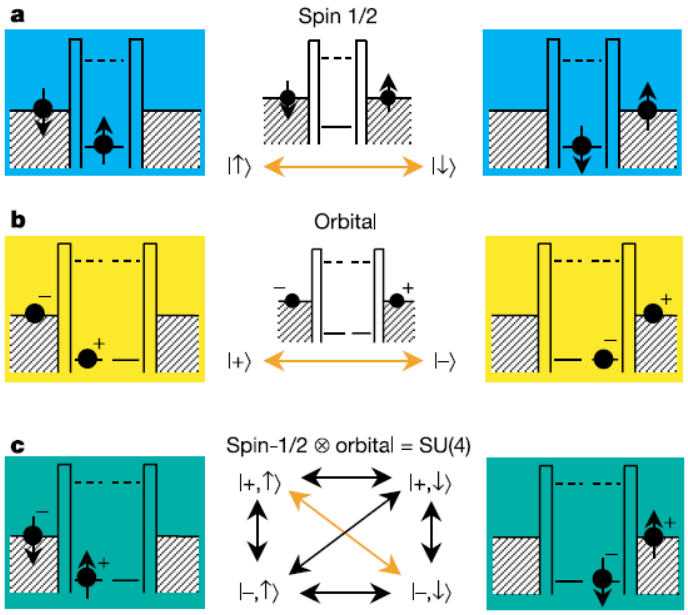

Figure 3.4: Spin, orbital and SU(4) Kondo effect in a quantum dot (QD) with an odd number of electrons. (a) Schematic illustration of a spin-flip co-tunneling process connecting the two states spin up $|\uparrow\rangle$ and spin down $|\downarrow\rangle$ from a single orbital state. (b) Co-tunneling process for spinless electrons for two degenerate orbital states, labeled $|+\rangle$ and $|-\rangle$. The depicted process flips the orbital quantum number from $|+\rangle$ to $|-\rangle$ and vice versa. The coherent superposition of orbital-flip processes leads to the screening of the local orbital quantum number. (c) QD with two spin-degenerate orbitals leading to an overall fourfold degeneracy. Spin and/or orbital states can flip by one-step co-tunneling processes (all possible processes are indicated by black arrows). These processes lead to the entanglement of spin and orbital states, resulting in an enhanced SU(4) Kondo effect. Taken from [48].

participates in the transport. Thus, we can assume the Anderson model to describe our system. A CNT oddly occupied likely gives rise to the Kondo effect. The Kondo effect, creates a strongly correlated state between the CNT QD and both reservoirs, opening a well-transmitted channel only if the temperature is smaller than the Kondo temperature T_K. T_K can be well approximated by the expression predicted by the Bethe Ansatz [57, 58]:

$$T_K = \sqrt{U\Gamma/2}\exp\left[-\frac{\pi}{8U\Gamma}|4\epsilon^2 - U^2|\right] \tag{3.10}$$

where U is the charging energy of the CNT quantum dot, $\Gamma = \Gamma_L + \Gamma_R$ is the coupling to the electrodes, and ϵ is the energy level of the dot relative to the Fermi energy of the reservoirs. Typically, in carbon nanotube quantum dots, the Kondo temperature reaches 1-2K [61, 116, 62], values like the one obtained in InAs nanowires [55, 63].

The larger is the coupling Γ, the larger is T_K: at a given temperature, as Γ increases, a stronger

Kondo screening is expected.

A typical stability diagram of a carbon nanotube in the Kondo SU(2) regime is shown in fig.3.5. Two Kondo ridges (bright yellow lines at $V_S = 0$) for odd diamonds are observed. The maximum amplitude of the Kondo enhanced conductance peak in case of SU(2) Kondo effect is given by eq.3.8. For spin-1/2 Kondo effect, the expression of conductance is recalled (see section 1.4):

$$G = \frac{2e^2}{h} \frac{4\Gamma_R \Gamma_L}{(\Gamma_R + \Gamma_L)^2} \tag{3.11}$$

The maximum conductance reached in the spin-1/2 Kondo effect with fully symmetric contacts ($\Gamma_R = \Gamma_L$) is $2e^2/h$. In another word, the Kondo effect opens a single spin degenerate perfectly transmitted channel.

Temperature dependence

Exciting electrons around the Fermi energy, a finite temperature of the order of T_K prevents electrons from participating in the Kondo singlet, and thus alters the Kondo resonance. Consequently, the zero-bias peak in conductance decreases as a function of temperature. The temperature dependence of the conductance can be described by the phenomenological expression

$$\frac{dI}{dV}(T) = \frac{G_0}{(1 + (2^{1/s} - 1)(\frac{T}{T_K})^2)^s} \tag{3.12}$$

With s a constant which depends on Kondo type correlations. This empirical formula derives from a fit to NRG calculations. For a spin-1/2 Kondo effect $s = 0.22$ [63, 64]. All physical quantities are then universal functions of dimensionless parameters, $k_B T_K$ being the scaling energy. Conductance, current and noise spectral density are functions of $\frac{T}{T_K}$, $\frac{eV_{SD}}{k_B T_K}$, $\frac{g\mu_B B}{k_B T_K}$, respectively.

Magnetic field dependence

The Kondo effect is a many-body effect, originates from local spin fluctuations, to which magnetic field couples strongly. When applying a magnetic field, the spin degeneracy is lifted into two levels corresponding to spin $\uparrow$ and spin $\downarrow$. The Kondo zero-bias conductance peak is expected to split into two peaks of lower conductance. The position of those peaks is related to the Zeeman energy so that $eV_{SD} = \pm g\mu_B B$, where is μ_B Bohr magneton and g is Landé factor.

In carbon nanotubes $g \approx 2$ [65, 16]. CNT possesses a large g factor compared for example with GaAs-based dots of g=0.1 to 0.44. Magnetic field parallel to the tube axis does strongly affect orbital states, so we apply field perpendicular rather than parallel to the tube axis to ensure that only the Zeeman effect is dominant. Fig.3.6 shows the conductance measurements in magnetic fields of a CNT QD, the split of the Kondo resonances occurs as a function of the magnetic field. As B increases, the Kondo resonance splits into two inelastic cotunneling peaks, that are still Kondo enhanced but weakened by the magnetic field.

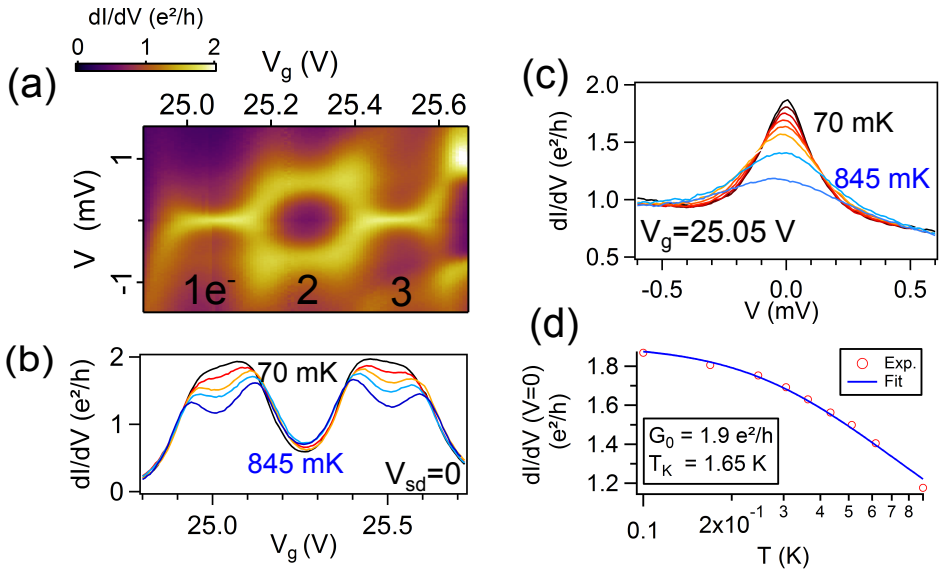

Figure 3.5: Temperature dependence of a spin-1/2 Kondo resonance in a carbon nanotube quantum dot contacted with Pd contacts. (a) Stability diagram (differential conductance as a function of V and V_g) of the nanotube, exhibiting Kondo ridges for N=1 and N=3. For N=2, inelastic cotunneling peaks are visible. (b) Conductance at zero bias as a function of V_g for various temperatures from 70 mK to 0.85 K. At the lowest temperature, the conductance almost reaches the maximum value of $2e^2/h$, meaning that the contacts are almost symmetric. (c) Temperature dependence of the Kondo peak at the center of the N=1 diamond. (d) Fit of the conductance to extract the Kondo temperature with eq.3.3, giving $T_K = 1.65K$. From [60].

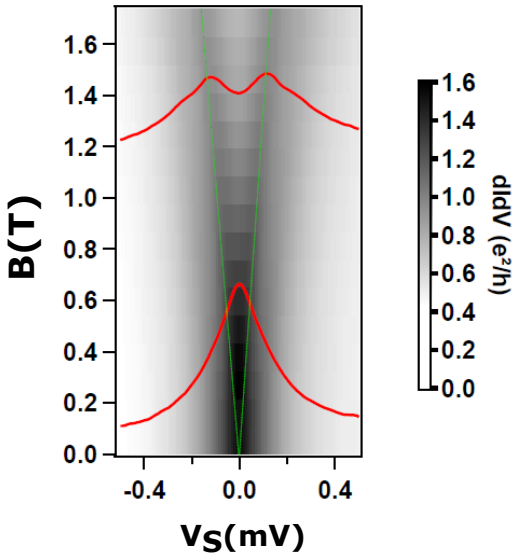

Figure 3.6: Perpendicular to the plane magnetic field splitting of the zero-bias peak at the center of the Kondo ridge. The exchange energy is $E = 2\mu_B B$. Red curves are traces taken for B = 0.108T and B = 1.302T. Green dashed curves are the expected lines of the position of the splitted peaks maximum for a $g = 2$ Landé factor. From [59].

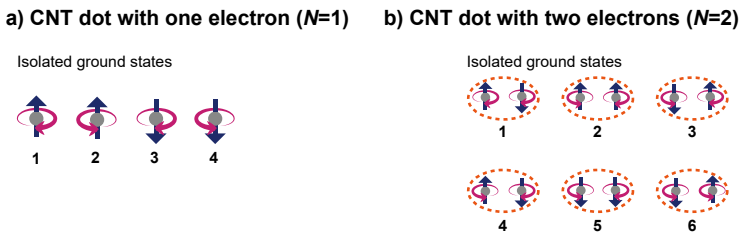

Figure 3.7: ((a) Representation of the four degenerate ground states for a dot containing one particle (N=1 and N=3). (b) Representation of the six degenerate ground states for a dot with two particles (N=2).

Effect of the contact asymmetry

Until now we have discussed the Kondo effect considering a CNT QD with symmetric contacts. In that case, the transmitting channel opened by the Kondo effect involves both reservoirs. However, in the experiment, this is in general not the case and we have to consider the contact asymmetry $a = \Gamma_L/\Gamma_R$. For asymmetric contact, the Kondo singlet is mainly formed between the dot and the best coupled reservoir. From eq.3.9, the conductance is reduced by a factor $\frac{4\Gamma_R\Gamma_L}{(\Gamma_R+\Gamma_L)^2}$ compared to the symmetric case. Then, for the same applied bias voltage, the current in asymmetric contact is lower than that in the symmetric case. The decoherence rate is shown to be proportional to the current, thus the decoherence is reduced as well. For this reason, we can say that the asymmetry tends to stabilize the Kondo singlet.

3.5.2 SU(4) Kondo effect in CNT QD

Carbon nanotube is naturally four-fold degenerate, its electrons possess spin and orbital (valley) degrees of freedom. The orbital degeneracy of a CNT plays the role of a pseudospin. Thus, SU(4) Kondo effect can occur in CNT QD, which requires the screening of the orbital pseudospin, together with the real spin at low temperatures. This increased degeneracy yields an enhancement of T_K [48, 49]. The SU(4) can only be observed when the symmetry of the four-fold degeneracy of CNT is well conserved during tunneling. For spin degeneracy this is the case, however, for orbital degeneracy, this conservation is not obvious, as it is not defined in the metallic electrode. If one considers that the leads to the dot are formed within the same nanotube, thus both the leads and QD have the same orbital symmetry, which should be conserved in tunneling processes [50].

Another condition for the occurrence of SU(4) Kondo effect, is that Kondo temperature should be larger than the zero-field splitting, either due to spin-orbit or valley-mixing ($T_K > \Delta_{SO}, \Delta_{KK'}$). In the upcoming section, we will discuss the possibility of breaking SU(4) Kondo effect by spin-orbit coupling and/or level mixing [51, 52].

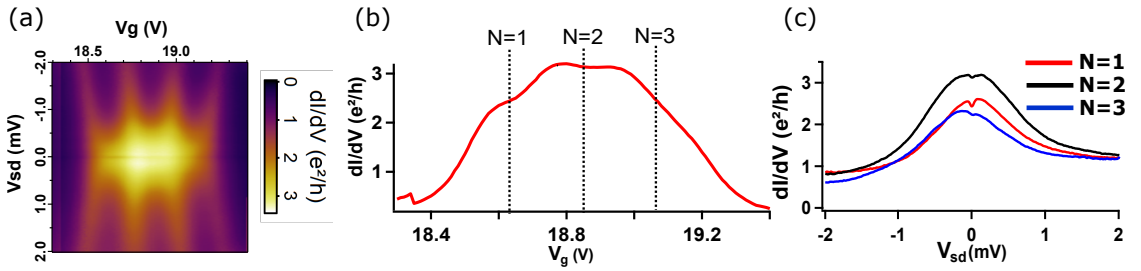

Figure 3.8: SU(4) Kondo effect in CNT QD with Pd contacts. (a) Differential conductance in the Kondo SU(4) regime. On the color plots, we can see that the Kondo ridge spreads all over the three diamonds N=1, 2, and 3. (b) Horizontal cut at Vs = 0, showing that the conductance goes up to 3.1 e^2/h at N=2. (b) Kondo resonance for the three occupancies [60].

In SU(4) Kondo effect, the Kondo ridges appear both at the odd numbers diamonds (N=1,3) and half-filled diamonds (N=2). For N=1 or 3 there are 4 degenerate ground state and six degenerate ground state for N=2. All those states are illustrated in fig.3.7. The N=1 and N=3 are equivalent due to electron-hole symmetry and have the same conductance of $2e^2/h$ (we are considering here the case of symmetric tunnel barriers). This value is calculated using eq.3.8 with $\langle N_n \rangle = 1/4$ for N=1 or $\langle N_n \rangle = 3/4$ for N=3). For N=2 diamond we have two electrons in four states, giving $\langle N_n \rangle = 3/4$, thus the maximum conductance reached for fully symmetric contacts is $4e^2/h$.

Fig.3.8 shows the stability diagram in a SU(4) Kondo regions. The outlines of the Coulomb diamonds are visible, hidden by the Kondo ridge that is very large and spreads all over the three diamonds N=1, 2, and 3. Kondo resonance at each occupancy (See fig.3.8.c) shows that the width of the Kondo peak is larger at N=2 (≈1.3 meV) than at N=1 and 3 (≈1 meV). The Kondo temperature is roughly estimated from the half-width at half maximum of the Kondo peak: 7K for N=2 and 6K for N=1 or 3. These values of Kondo temperature are very large compared to the one typically obtained in a nanotube for SU(2) Kondo effect (1-2K) as predicted by theory [48, 49].

Breaking of the SU(4) symmetry

The breaking of SU(4) symmetry originates from the breaking of the four-fold degeneracy of CNT QD. The orbital degeneracy could be broken due to spin-orbit, boundary conditions, or disorder.

Effect of spin-orbit coupling Spin–orbit coupling can be present in carbon nanotubes owing to their curvature and cylindrical topology [54]. If the spin-orbit coupling energy $\Delta_{SO} \neq 0$ and $k_B T_K > \Delta_{SO}$, the spin and orbital degree of freedom are coupled and the four degenerated states of CNT become two degenerate Kramers doublets [53]: (K↑, K↓) and (K↑, K'↓) with entangled spin and orbital degrees of freedom. In this case SU(4) Kondo effect is not possible anymore, however, the Kramers degeneracy can give rise to SU(2) Kondo effect.

Effect of orbital mixing The four-fold degeneracy of CNT can also be broken by orbital mixing attributed to the presence of weak disorder. The observation of orbital mixing can be related to the chirality of the CNT, such that A armchair nanotubes undergo orbital mixing, however zigzag nanotubes do not [56]. Due to orbital mixing, the K and K' orbital levels undergo level anticrossing

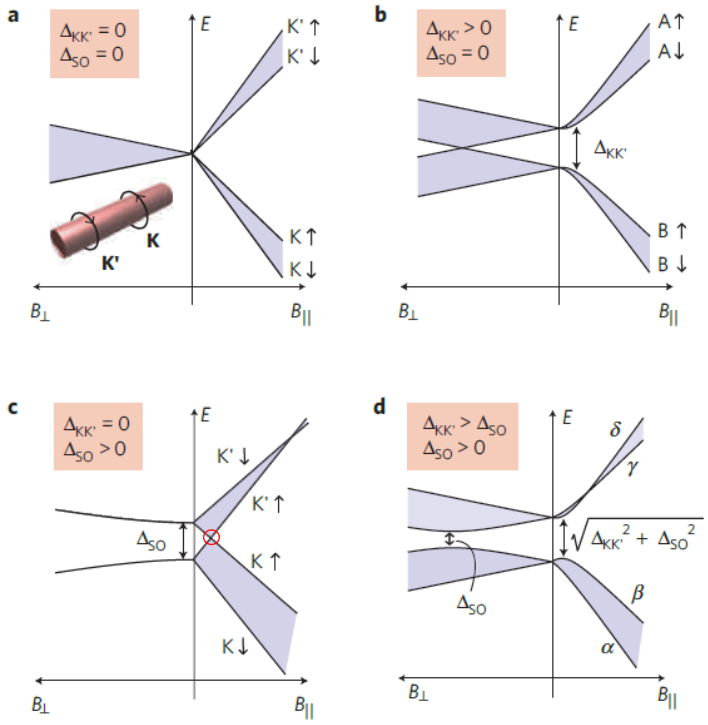

Figure 3.9: Calculated single-particle energy spectrum as a function of the magnetic field applied perpendicular (B⊥) and parallel (B//) to the CNT axis. (a) Perfect four-fold degeneracy. (b) With the presence of $\Delta_{KK'} > 0$, (c) $\Delta_{SO} > 0$, and (d) both $\Delta_{KK'} > 0$ and $\Delta_{SO} > 0$. Adapted from [55].

and the four-fold degenerated state of CNT becomes two spin degenerated pairs: (A↑, B↓) and (C↑, D↓), separated by $\Delta_{KK'}$, where A, B, C, and D are combinations of orbital states K and K'). As the split levels are spin degenerate, standard spin 1/2 SU(2) Kondo effect is possible.

Breaking of the four-fold degeneracy of CNT QD can be due to both spin-orbit coupling and orbital mixing. fig.3.9 shows the calculated single-particle energy-level spectra, considering the effect of Δ_{SO} and $\Delta_{KK'}$.

Ferrier et al. [67] show that it is possible to induce a crossover between SU(4) and SU(2) symmetry of the ground state at half-filling (N=2, two electrons in the dot) by tuning the orbital and spin degeneracy with a magnetic field. A magnetic field making an angle θ with the nanotube axis is applied. The behavior of each ground state (N=1 and N=2) is studied under the effect of a magnetic field and will be explained in what follows

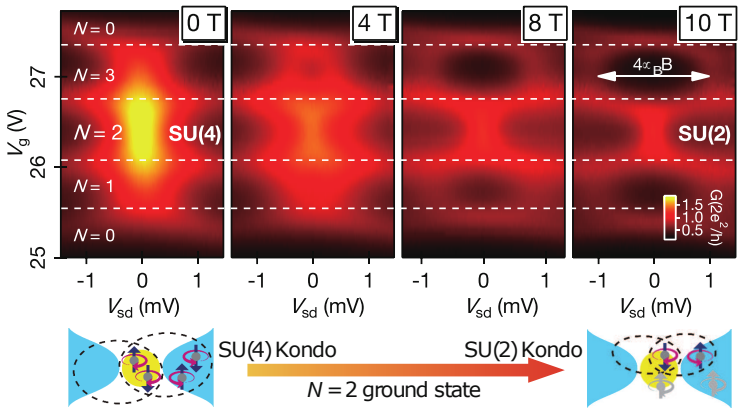

Figure 3.10: Stability diagrams for B=0, 4, 8, and 10 T at T=16 mK as contour plots of the conductance G as a function of V_g and V_{sd}. The Kondo resonance produces the bright broad vertical lines at $V_{sd} = 0$. This ridge disappears at high field for N=1 and 3. It is split into two satellite peaks at high V_{sd} separated by $\Delta V_{sd} \approx 4\mu_B B$. At N=2, G decreases but it remains maximum at $V_{sd} = 0$. From [67].

N=1 ground state, Dot containing one electron At zero magnetic field, four states are degenerate forming an SU(4) Kondo state. When the magnetic field is applied the spin and orbital degeneracy is lifted and the Kondo effect disappears.

N=2 ground state, Dot containing two electrons For N=2, at zero magnetic fields, six states are degenerate, this leads to the formation of SU(4) Kondo state. As B increases, the orbital and spin degeneracy is lifted. However, the ground state remains doubly degenerate for finite B, and can give rise to SU(2) Kondo effect.

The stability diagram of CNT with Pd/Al contacts is shown in fig.3.10. The measurement is done for B=0, 4, 8, and 10 T. The number N=0, 1, 2, and 3 indicates the number of electrons in the last occupied shell. At B=0 T, the Kondo resonance is seen for every filling as expected for the SU(4) Kondo effect. When the field increases from 0 to 10 T, ridges at N=1 and N=3 progressively disappear whereas the N=2 ridge remains until a very high field. But with reduced intensity, at B=0 the maximum conductance $G = 1.85G_Q$ ($G_Q = 2e^2/h$) which is close to $2G_Q$, the expected value for the N=2 unitary SU(4) state. As B increases, G decreases toward G_Q, the value expected for the SU(2) Kondo effect.

SU(2) orbital Kondo effect Jarrillo-Herrero et al. [48] shows that orbital Kondo effect can occur in carbon nanotubes. Applying a parallel magnetic field breaks the four-fold degeneracy, thus no Kondo effect is observed. However, from fig.3.9.c the state (K,↑) and (K',↑) undergoes level-crossing at $B = B_0$ (indicated in red circle). Then, the orbital degree of freedom is degenerated, leading to the reappearance of a Kondo resonance due to pure orbital SU(2) Kondo effect.

3.6 Conclusion

In this chapter, we presented the physics of an important many-body effect in condensed matter: the Kondo effect. This effect was initially observed in alloys with magnetic impurities, but it can occur also in a single impurity constituted by a quantum dot described by the Anderson model. The electrons at the Fermi energy of the reservoirs screens the magnetic moment of the impurity, giving rise to a resonance in the density of states of the quantum dot: the Kondo resonance. Then we focus on the Kondo effect in Carbon nanotubes quantum dot. The four-fold degeneracy of a carbon nanotube QD makes it a very interesting system to study the Kondo effect. In particular, it can sustain different Kondo effects: spin-1/2 SU(2), SU(4), and orbital Kondo effect.

Chapter 4

Introduction to superconductivity

In this chapter we will present the basics notions to understand the Josephson effect in nanoscale junction: the superconducting proximity effect, Josephson effect in a QD, physics of Andreev bound states, and the effect of Kondo correlations.

4.1 Superconductivity

In this section we will discuss the physics of conventional superconductors, where the electrons form coherent bound states called Cooper pairs, which dramatically change the macroscopic properties of the system, giving rise to perfect conductivity and perfect diamagnetism.

4.1.1 Phenomenology

In metals, the resistivity is expected to decrease with temperature, due to the reduction of electron-electron and electron-phonon interactions until it reaches a minimum finite value at the lowest temperature because of impurity scattering. In 1908, Heike Kamerlingh Onnes was the first to liquefy helium. A few years later in 1911, Onnes was studying the transport properties of mercury (Hg) at low temperatures. He found that below the liquefying temperature of helium, at around 4.2 K, the resistivity of Hg suddenly drops to zero. His discovery was the opening of a new chapter in low-temperature physics: Superconductivity. Nowadays Hg and many other metals (aluminum, lead, tin...) are known to be superconductors whose electrical resistivity completely vanishes when cooled down below their critical temperature T_c.

Besides having zero resistance, another interesting propriety of superconductors is expelling magnetic fields. In 1933, Meissner discovers the so-called Meissner effect: the magnetic flux density B is expelled below the superconducting transition temperature Tc, i.e. inside a superconductor material the magnetic field vanishes within a length λ, called the penetration length. This effect reveals the perfect diamagnetic properties of a superconductor. Because the current itself generates a magnetic field, the existence of a critical magnetic field B_c implies the existence of a maximum current which can be sustained by a superconductor, called the critical current I_c. The measurements of thermodynamic quantities, such as the low-temperature specific heat show an exponential dependence well below T_c. This suggests the presence of an energy gap Δ in the density of state of a superconductor between the ground state and quasi-particle excitation.

Depending on their magnetic field behavior superconductors can be classified into two categories: type I and type II superconductors. The type-I category of superconductors is mainly comprised of metals and metalloids (Pb, Al, Hg, Sn, In). However, the Type 2 category of superconductors is comprised of metallic compounds and alloys ($YBa_2Cu_3O_7, (La, Sr)CuO_2, CuMgO_2$), except for the elements vanadium, technetium, and niobium. Type-II tend to have higher transition temperature T_c than type-I superconductors (e.g $T_c(Pb) = 7.2K$, $T_c(YBa_2Cu_3O_7) = 92K$). In Type I superconductor the magnetic field is completely expelled from the interior for $H < H_C$. Above that field, a type I superconductor is no longer in its superconducting state. A Type II superconductors have two values of critical magnetic field, for $H < H_{C1}$ the magnetic field is completely expelled as type-I behavior. For $H_{C1} < H < H_{C2}$, there is a partial field penetration in the form of vortex lines of magnetic flux. Each vortex contains one flux quantum $\Phi_0 = \frac{h}{2e}$. Where the vortex appears the superconducting order parameter drops to zero. In this region, the metal is no longer a superconductor. Whereas the rest of the metal stays superconducting. When the field reaches the second critical field H_{c2} the metal stops to be superconducting.

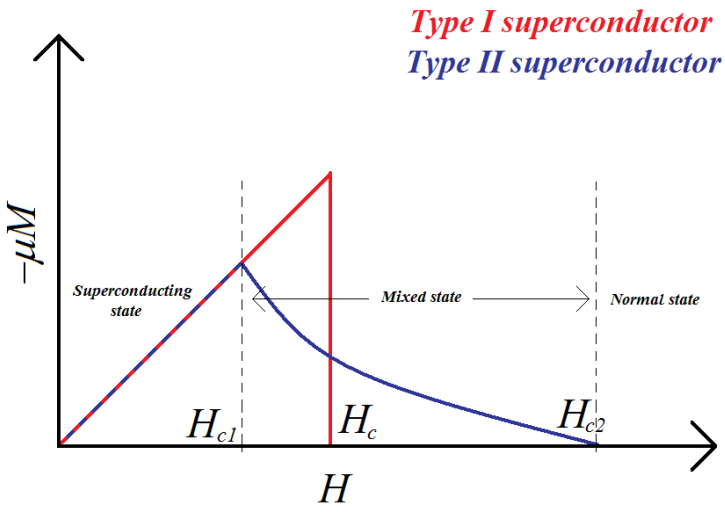

Figure 4.1: For a type I superconductor, magnetic flux is expelled, producing a magnetization (M) that increases with magnetic field H, when the field reaches the critical value H_c, the magnetization falls to zero as in normal metal. A type II has two critical magnetic fields (H_{c1} and H_{c2}), below H_{c1} type II behaves as I, and above H_{c2} it becomes normal.

Interaction between electrons and lattice atoms is responsible for the existence of a superconducting state. The electron-electron coupling is weak and can be destroyed by the thermal motion of the lattice. For this reason, superconductivity exists only at low temperatures. The attractive electron-electron interaction mediated by the phonons gives rise to Cooper pairs. A Cooper pair is a bound state formed by two electrons of opposite spins and momenta, of pairing energy Δ and spatial extension $\xi_0 = \frac{\hbar v_f}{\pi \Delta}$. The net spin of a Cooper pair is zero, consequently, these Cooper pairs form a coherent macroscopic ground state that obeys Bose-Einstein statistics.
Conventional and unconventional superconductors differ by the pairing mechanism. In conventional

superconductors, the pairing is due to electron-phonon attractive interaction. In unconventional superconductors, the Cooper pairs are not bound together by phonon exchange but instead by exchange of some other kind, e. g. spin fluctuations [68], magnetic fluctuations [69] .

In what follow we limit ourselves to the case of conventional superconductors. According to Ginzburg-landau theory, at zero magnetic field superconductivity is a second-order phase transition of the normal state. The superconducting state can be described with a single macroscopic wave function:

$$\psi = \mid \psi \mid \exp(i\varphi(r)) \tag{4.1}$$

ψ is the superconducting order parameter, with $\mid \psi \mid^2$ represents the density of Cooper pairs, and φ is the superconducting phase. For a complex order parameter ψ the Landau expansion of the free energy would give the expression of current in a superconductor as a function of potential vector $\vec{A}$, and the order parameter ψ:

$$I = -\frac{e\hbar}{m} \mid \psi \mid^2 (\vec{\nabla}\varphi - \frac{2e}{\hbar c}\vec{A}) \tag{4.2}$$

This relation emphasizes that a dissipation-less current is not induced by voltage bias but by a gradient of the superconducting phase φ.

4.1.2 BCS theory

In 1957 John Bardeen, Leon Cooper, and Bob Schrieffer developed a microscopic theory of superconductivity, the BCS theory [70]. The main point of the BCS theory is that the formation of Cooper pairs originates from a small attractive electron-electron interaction mediated by phonons. The BCS theory describes only the conventional superconductor, where phonons are responsible for the formation of bound electron pairs.

Ground state In a BCS mean-field approximation [71, 72], the effective Hamiltonian can be written as:

$$\mathcal{H} = \sum_{k,\sigma} \xi_{k\sigma} c^\dagger_{k\sigma} c_{k\sigma} + \sum_k \Delta_k c^\dagger_{k\uparrow} c^\dagger_{-k\downarrow} + \Delta^*_k c_{-k\downarrow} c_{k\uparrow} \tag{4.3}$$

where $c_{k\sigma}$ ($c^\dagger_{k\sigma}$) is the annihilation (creation) field operator of an electron of spin σ and vector momentum k. With $\xi_{k\sigma}$ being the kinetic energy and $\Delta_k = -\sum_{k'} V_{kk'}(c_{-k'\downarrow} c_{k'\uparrow})$, with $V_{kk'}$ the paring potential. In order to find solutions of BCS theory in a homogeneous superconductor, this Hamiltonian can be diagonalized using Bogoliubov transformation:

$$\gamma_{k,\uparrow} = u_k c_{k\uparrow} - v_k c^\dagger_{-k\downarrow} \qquad\qquad \gamma^\dagger_{-k,\downarrow} = u^*_k c^\dagger_{-k\downarrow} + v^*_k c_{k\uparrow} \tag{4.4}$$

with $\mid u_k \mid^2 + \mid v_k \mid^2 = 1$, is the normalization condition of Bogoliubov transformation. The diagonalized Hamiltonian takes the following form:

$$\mathcal{H} = \sum_{k,\sigma} E_k \gamma^\dagger_{k,\sigma} \gamma_{k,\sigma} \tag{4.5}$$

where $\gamma_{k,\sigma}$ and $\gamma^\dagger_{k,\sigma}$, are the fermionic annihilation and creation operator, usually called *Bogoliubons*.

From eq.4.4, the Bogoliubon appears to be a mixture of electrons and holes excitation of excitation energy $E_k = \sqrt{\xi_k^2 + \Delta^2}$. Solving the diagonalized Hamiltonian gives the usual BCS ground state:

$$|\psi_{BCS}\rangle = \prod_k (\mid u_k \mid + \mid v_k \mid e^{i\varphi} c^\dagger_{k,\uparrow} c^\dagger_{-k,\downarrow}) \mid 0\rangle \tag{4.6}$$

The probability of the pair (k↑,-k↓) being occupied is $\mid v_k \mid^2$, whereas the probability that it is unoccupied $\mid u_k \mid^2$. When the pair is occupied, its phase is the macroscopic superconducting phase φ.

Superconducting density of state The superconducting density of state $N_s(E)$ can be derived by equating $N_s(E)dE = \frac{N_n(\xi)}{2} d\xi$, where the normal density of states $N_n(\xi)$ can be considered constant and equal to the one at the Fermi level $N_n(\xi) = N(0)$. This leads directly to the simple result:

$$N_s(E) = N(0) \begin{cases} \frac{|E|}{\sqrt{E^2 - \Delta^2}} & \mid E \mid > \Delta \\ \\ 0 & \mid E \mid < \Delta \end{cases} \tag{4.7}$$

The density of state is sketch in fig.4.2, the superconducting density of state exhibits a gap Δ, such that no state is available around the Fermi energy. The value of the superconducting gap is shown to be proportional to T_c: Δ=1.76 $k_B T_c$

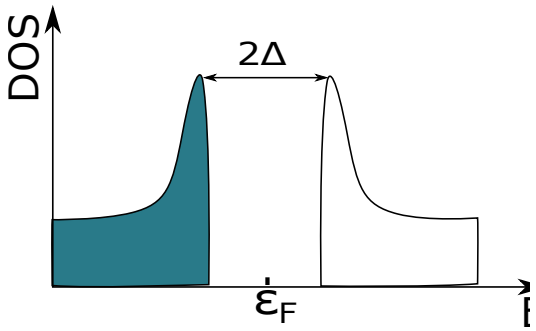

Figure 4.2: The BCS density of state of a superconductor is gapped around Fermi level. The states below the Fermi level (colored region) are filled and the states above are empty.

The order parameter introduced in the context of Ginzburg-Landau theory can be associated, under certain conditions, to the superconducting gap $\psi = \Delta e^{i\varphi(r)}$

4.2 Superconducting proximity effect

When a superconducting material brought into contact with non-superconducting one (normal or insulator), the superconducting correlations can survive in the normal (insulator) part, and can even carry a supercurrent when contacted between two superconductors: this the so called the superconducting proximity effect. The key underlying phenomenon of this effect is the Andreev reflection.

4.2.1 Andreev transport

Andreev reflection Let us consider an electron in a normal metal at energy $E_f + \epsilon$ with $\epsilon < \Delta$, wavevector $k_e = k_F + q$ and phase ϕ_e, arriving on NS interface. Due to the superconducting gap in the density of states of the superconductor, no available states are present in the superconductor at energies below the gap. Thus, the incoming electron is reflected as a hole of energy $E_f - \epsilon$ and opposite spin: this is the Andreev reflection. During Andreev reflection a charge of 2e is transferred in the superconductor at the Fermi energy, in the form of a Cooper pair. The phase acquired by the hole compared to the one of the electrons after the reflection is:

$$\phi_h = \phi_e + \varphi + \arccos\left(\frac{\epsilon}{\Delta}\right) \tag{4.8}$$

with φ the superconducting phase in the superconductor and Δ the superconducting energy gap

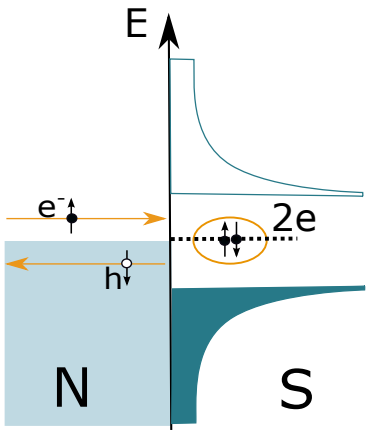

Figure 4.3: Andreev reflection process at a N/S interface. An incoming electron e with energy $E_f + \epsilon$, wavevector $k_e = k_F + q$ and phase ϕ_e is reflected backward into a hole with energy $E_h - \epsilon$, wavevector $-k_F + q$ and phase ϕ_e.

Andreev bound state Let us consider the case where a normal part of length L is enclosed between two superconductors. The reflected hole at the first NS interface can propagate and reach the second NS interface where it will be reflected backward as electron, closing the cycle (see fig.4.4.a). If the length of the normal part is small enough to ensure coherence along the whole path, a Cooper pair is transferred coherently from one superconducting contact to the other, and a non-dissipative current flow through the junction. When several Andreev reflections occurs, an entangled e-h pair is confined in the normal part forming a bound state called the Andreev bound state (ABS). These states carry supercurrent , and their energies depend periodically on the superconducting phase difference $\varphi = \varphi_L - \varphi_R$ such that:

$$2n\pi = \varphi + 2\arccos\left(\frac{\epsilon}{\Delta}\right) + \frac{2\epsilon}{\hbar v_f} L \tag{4.9}$$

This gives the following energy spectrum of Andreev bound state:

$$\epsilon = \Delta \cos\left(\frac{\varphi}{2} - n\pi - \frac{\epsilon}{\hbar v_f} L\right) \tag{4.10}$$

where φ is the phase difference between the superconducting electrodes. This equation admits multiple solutions which correspond to Andreev states inside the superconducting gap. In the case of perfectly transmitted short junction $L \ll \xi_0$, with ξ_0 being the superconducting coherence length, only two bound states are found at energies:

$$\epsilon = \pm\Delta \cos\left(\frac{\varphi}{2}\right) \tag{4.11}$$

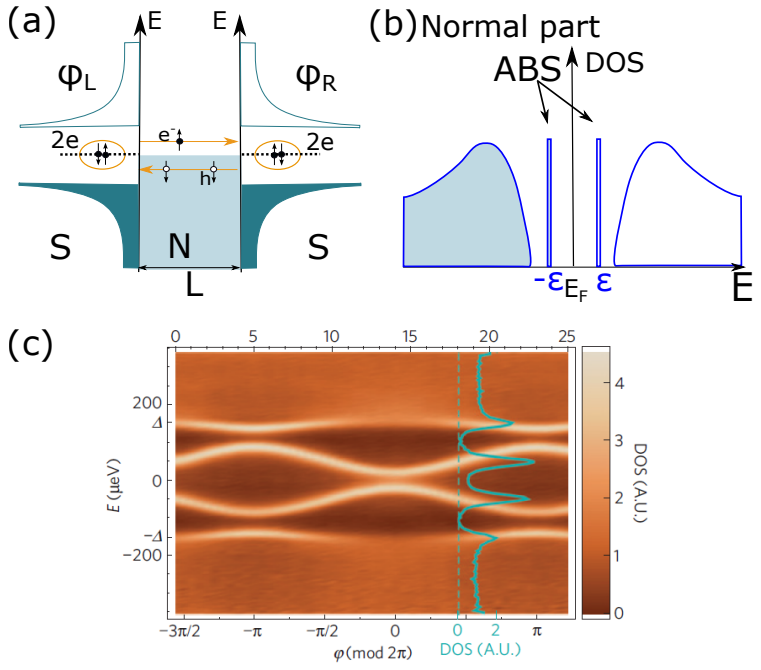

Figure 4.4: Principle of Andreev Bound States (ABS). (a) Andreev reflections in a SNS junction, leading to the formation of Andreev bound states (ABS) in the normal part. (b) The local DOS in the normal part exhibits a set of resonances in the gap at the energies of the ABS. The energies of the ABS depend periodically on the superconducting phase difference. (c) Observation of individually resolved Andreev bound states in a tunneling spectroscopy experiment. In this experiment, a carbon nanotube plays the role of the coherent conductor. Taken from [88].

4.2.2 Josephson effect

In 1962, David Josephson made two remarkable predictions [73], the DC and the AC Josephson effect in a Josephson junction. A Josephson junction is a combination of two superconducting material separated by a thin insulating layer of length L.

In 1966, de Gennes shows that the effect extends beyond Josephson's predictions and can exist if superconductors are connected by a "weak link" [74] such as normal metal, point contacts,

graphene, carbon nanotubes, semiconducting nanowires, and thin ferromagnetic layers. If the non-superconducting part is an insulator, the junction is called an SIS junction, and SNS junction in case of a normal metal, SFS Junction in case of a ferromagnetic layer [72].

In the non-superconducting part (N or I), there is no superconducting correlation. However, due to the superconducting proximity effect, at the interface with the superconducting part, some Cooper pairs can penetrate in the non-superconducting part. If the length of the N or I part is small enough such that the coherence of the pair is conserved during the crossing of the N or I part, the superconducting wave functions of the two contacts overlap allowing tunneling of Cooper pairs from one contact to the other when a finite superconducting phase difference exists between the two superconductors (See fig.4.7). We can distinguish two regimes, with respect to the superconducting coherence length ξ_0: $L < \xi_0$ corresponds to the short junction regime, $L > \xi_0$ to the long junction regime.

Dc Josephson effect

The DC effect refers to the flowing of supercurrent between two superconductors due to tunneling of Cooper pairs from one superconductor towards the other. The maximum of this supercurrent is called the critical current of the junction. The existence of this supercurrent relies on the formation of Andreev bound states in the non-superconducting part.

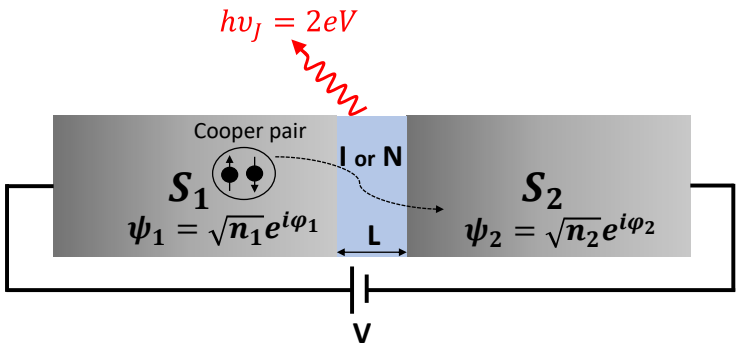

Figure 4.5: Sketch of a Josephson junction consisting of two superconductors separated by a non-superconducting part: I for insulator and N for normal. The two superconductors have different superconducting phases, such that there is a phase difference φ=$\varphi_2 - \varphi_1$ across the junction. At zero bias voltage, a supercurrent can flow through the junction due to the tunneling of a Cooper pair. When a constant voltage V is applied between the two superconductors, the Junction emits radiation such that $h\nu_J = 2eV$.

In the case of SIS Junction, Josephson predicted that a supercurrent can flows across the junction in the absence of any applied voltage given as:

$$I(\varphi) = I_c \sin(\varphi) \tag{4.12}$$

where I_c is the Josephson critical current, and φ=φ_2-φ_1 is the superconducting phase difference

across the junction(see fig.4.5).
In case of "weak link", the supercurrent is a function of φ, such that $I(\varphi) = I_c f(\varphi)$.

Ac Josephson effect

When a bias voltage V is applied between the two superconductors, the phase evolves in time according to:

$$\frac{d\varphi}{dt} = \frac{2eV}{\hbar} \tag{4.13}$$

Thus, an alternating supercurrent at the Josephson frequency $\nu_J = 2eV/h$ and its harmonics is flowing through the junction, this is the AC Josephson effect. The oscillating Josephson current is given by the Fourier series of eq.4.12 of period 2π:

$$I(t) = \sum_{n=1}^{\infty} I_{c,n} \sin(2\pi\nu_J n t) \tag{4.14}$$

The oscillating phase accelerates the tunneling of Cooper pairs with energy gain $2eV$. As the Cooper pairs are not allowed to alter their energy while tunneling, a photon at frequency $h\nu_J = 2eV$ is emitted. ν_J is related to twice the electronic charge since the two electrodes exchange cooper pair rather than a single electron. Those photons can be absorbed by the environment and can be probed as photo-assisted tunneling steps in the I(V) characteristic of a nearby detector.

The AC Josephson emission has been first detected in tunnel Josephson junctions by Giaever [75] and Yanson et al.[76]. Thanks to the metrological precision of the AC Josephson effect, a superconducting tunnel junction can be used as GHz radiation emitter [77] or to define the voltage standard [78]. In Josephson junctions involving a non-superconducting but non-insulating material, measuring the AC-Josephson effect allows us to probe the Andreev Bound States (ABS) spectrum at a finite frequency and out-of-equilibrium [79, 80]. For instance, its measurement demonstrated the topologically protected crossing of ABS in HgTe [81, 82], InAs nanowires [83] and Dirac semi-metals [90], that was not accessible through DC measurement because of quasiparticle poisoning.

Shapiro steps To probe the ac components of the current, one can apply an external microwave signal of frequency ω. Let us consider both a DC and an AC voltage across the junction.

$$V = V_0 + V\cos(wt) \tag{4.15}$$

From eq.4.13 the phase difference takes the form

$$\varphi(t) = \varphi_0 + \frac{2eV_0}{\hbar}t + \frac{2eV}{\hbar\omega}\sin(\omega t) \tag{4.16}$$

From eq.4.16 the current across the junction can be expressed as a function of Bessel functions J_n such that:

$$I(t) = Ic\sum_{-\infty}^{+\infty} J_n(\frac{2eV}{\hbar\omega})\sin(\omega_0 t + (n+m)\omega t + \varphi_0) \tag{4.17}$$

For an applied DC voltage $V = \frac{n\hbar\omega}{2e}$, the DC component of the current is:

$$I(t) = I_c J_n(\frac{2eV}{\hbar\omega})\sin(\varphi_0) \tag{4.18}$$

Thus, when the DC voltage is an integer multiple of $\frac{\hbar\omega}{2e}$ the DC supercurrent suddenly jumps to the value given by eq.4.18. In the case of a DC current bias of the junction, together with irradiation, a simple ladder behavior appears in the I(V) characteristics. These are called Shapiro steps, known also as inverse of the AC Josephson effect.

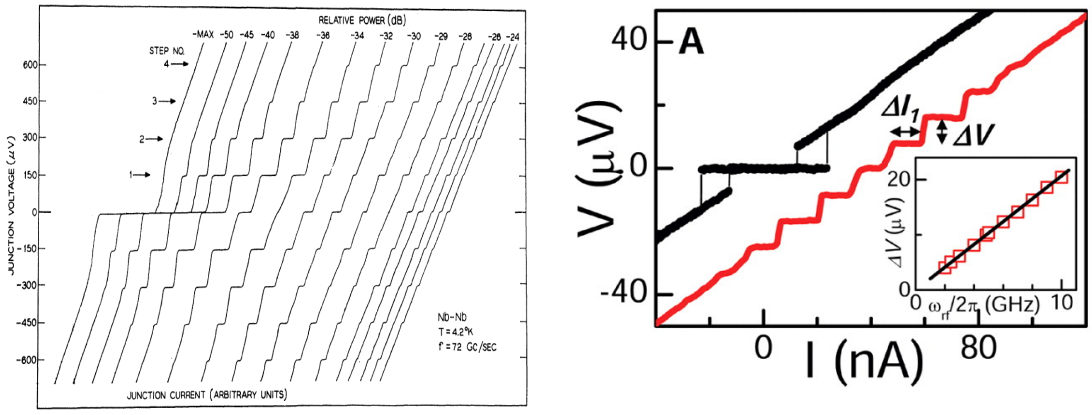

Figure 4.6: Shapiro steps measured in Left: Nb-Nb point-contact Josephson junction. Right: InAs nanowire. The applied microwave radiation results in voltage plateaus (Shapiro steps) at integer multiples of V.From [84] and [85].

4.2.3 Current-phase relation

From the DC Josephson relations, we deduce that the supercurrent flowing between two superconductors depends on the superconducting phase difference φ, which is analog to the corresponding relation between current and the phase gradient eq.4.2. Applying a time reversal transformation changes the direction of the current and the sign of the phase, this implies that the current needs to be an odd, 2π periodic function of the superconducting phase difference φ [86]. The exact relation between the supercurrent and the superconducting phase is called the current-phase relation, which depends strongly on the strength and of the nature of the coupling between the two superconducting reservoirs.

Case of SNS Junction

For a SNS structure with N transport channels of transmissions T_n, the ABS energy for a single conduction channel in the limit $L \ll \xi_0$ is given by [87]:

$$\epsilon = \pm\Delta\sqrt{1 - T_n \sin^2(\frac{\varphi}{2})} \tag{4.19}$$

Each one of the two Andreev bound states of a channel carries a supercurrent proportional to the derivative of the Andreev Bound states energy with respect to the phase:

$$I(\varphi) = \frac{2e}{\hbar}\sum_n \frac{\partial\epsilon_n}{\partial\varphi} \tag{4.20}$$

This yields a current-phase relation (CPR) for an SNS junction at very low temperature:

$$I(\varphi) = \frac{e\Delta}{2\hbar} \sum_n \frac{T_n \sin(\varphi)}{\sqrt{1 - T_n \sin^2(\frac{\varphi}{2})}} \tag{4.21}$$

For an arbitrary transmission, the current-phase relation contains harmonics, the extreme limit being $T \approx 1$, yielding a singularity at $\varphi = \pi$: the current-phase relation is then strongly anharmonic, close to a saw-tooth (represented on fig.4.7.a in blue). However, as soon as there is a finite temperature, the highest harmonics are suppressed first, such that the current-phase relation tends to be sinusoidal.

Case of a tunnel junction

In the case of tunnel junction, where the channels are weakly transmitted $T_n \ll 1$, the current-phase relation is nearly harmonic $I = I_c \sin(\varphi)$ (See fig.4.7, represented in pink). The value of critical current is I_c given by the Ambegaokar-Baratoff formula [89]:

$$I_c R_n = \frac{\pi}{2e} \Delta(T) \tanh\left(\frac{\Delta(T)}{2k_B T}\right) \tag{4.22}$$

where R_n denotes the tunneling resistance of the electrons in the absence of the pair interaction.

At temperatures far below T_c, Δ is nearly constant. For T $\to$ 0, $tanh(\Delta/2k_BT) \approx 1$ then eq.4.22 becomes:

$$I_c R_n = \frac{\pi}{2e} \Delta \tag{4.23}$$

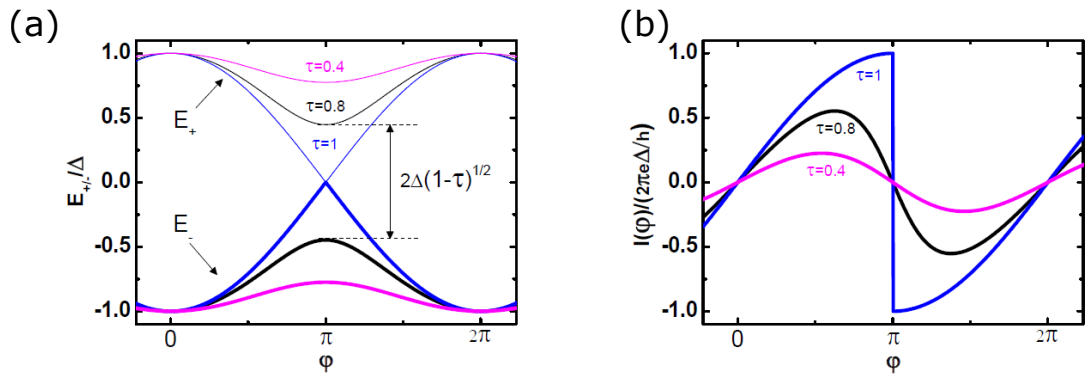

Figure 4.7: (a) Andreev bound states energy spectrum for a single channel with three different transmissions τ= 0.4, 0.8, 1. (b) Current phase relations associated to the previous spectrum at zero temperature. Taken from [59].

4.3 Conclusion

Through this chapter, we have presented a brief introduction to superconductivity. Superconducting correlations result from the attractive interactions between conduction electrons in a metal mediated

by phonon, forming Cooper pairs. At $T < T_C$, the metal becomes a superconductor, as a result, a non-dissipative current "supercurrent" induced by the superconducting phase φ flow through the metal. We have seen that a weak link connected to superconducting electrodes can support a supercurrent due to the superconducting proximity effect. This supercurrent is a periodic function of φ. The exact relation between the current and the phase is called the current-phase relation (CPR).

Chapter 5

DC Josephson effect in a quantum dot

As we discussed in section 1.2.2, when a quantum dot (QD) is coupled to normal electrodes, the tunneling of electrons can lead to three different transport regimes depending on the ratio between the charging energy U and the coupling constant Γ. When a QD is coupled to superconducting electrodes, an additional energy scale will highly affect the electronic transport: the superconducting gap Δ. Depending on the relative value between the dot's parameters (Γ and U) and Δ, three different coupling regimes are observed, the strong coupling regime, weak coupling regime, and intermediate regime [91]. Superconducting-Quantum dot-Superconducting (S-QD-S) system has been realized in different nano-structures: Carbon nanotubes [92, 28, 117], InAs nanowires [93, 94], and graphene [95]. Carbon nanotubes are not intrinsically superconducting, however, when connected between two superconducting electrodes they can carry a supercurrent [107, 108] due to the superconducting proximity effect. In this chapter, we review the basics properties of the S-QD-S system.

5.1 Strong Coupling regime

In the strong coupling regime, the charging energy of the Cooper pair and the superconducting gap is small compared to the coupling constant. Resonant Cooper pair tunneling occurs when aligning the energy level in the dot with the Fermi level in the leads. The supercurrent flowing through the dot is maximum when the dot level is aligned with the Fermi energy of the leads (ON state in fig.5.1) and zero when driven out-of-resonance (OFF state in fig.5.1)

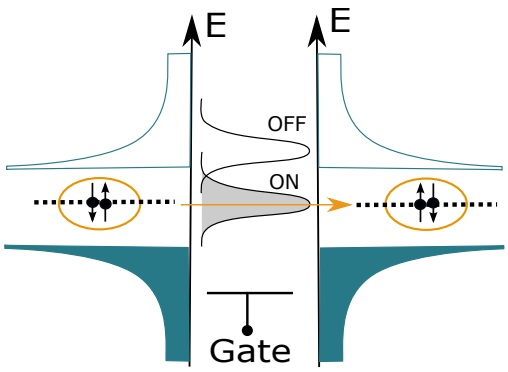

Figure 5.1: Energy level diagram of the quantum dot in the strong coupling regime. Depending on gate voltage, the dot can be in an ON state, where supercurrent is maximal due to resonant Cooper pair tunneling. When the energy level of the dot is put away from Fermi energy, the system is in an OFF state, and the supercurrent is suppressed.

5.2 Weak Coupling regime

The weak coupling regime refers to the case $\Gamma \ll U, \Delta$. In this regime, the tunneling of Cooper pairs is suppressed by Coulomb repulsion, and the transport is dominated by single quasi-particle tunneling. This tunneling happens for bias voltage high enough to overcome the superconducting gap $eV_{SD} > 2\Delta$ and depends on the position of the energy levels in the QD, controlled by the gate voltage.

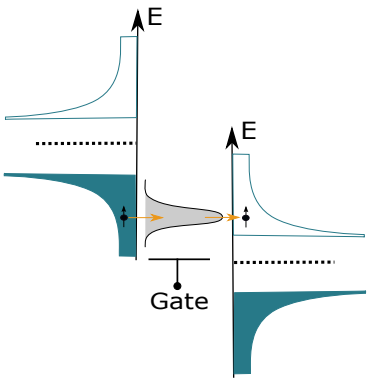

Figure 5.2: Energy level diagram of a quantum dot in the weak coupling regime. The tunneling of Cooper pairs is suppressed. One needs to provide at least energy $eV_SD = \Delta$ for the quasiparticles tunneling to take place.

5.3 Intermediate Coupling regime

The intermediate regime is very interesting. In this regime, U is sufficiently high to give rise to Coulomb blockade, and Γ is high enough to allow the co-tunneling process. Rather than tunneling as one entity, the Cooper pair breaks and the two electrons co-tunnel coherently (during typically the time $\hbar/\Gamma$, the cooper pairs can reform in the second leads if $\Gamma > \Delta$).

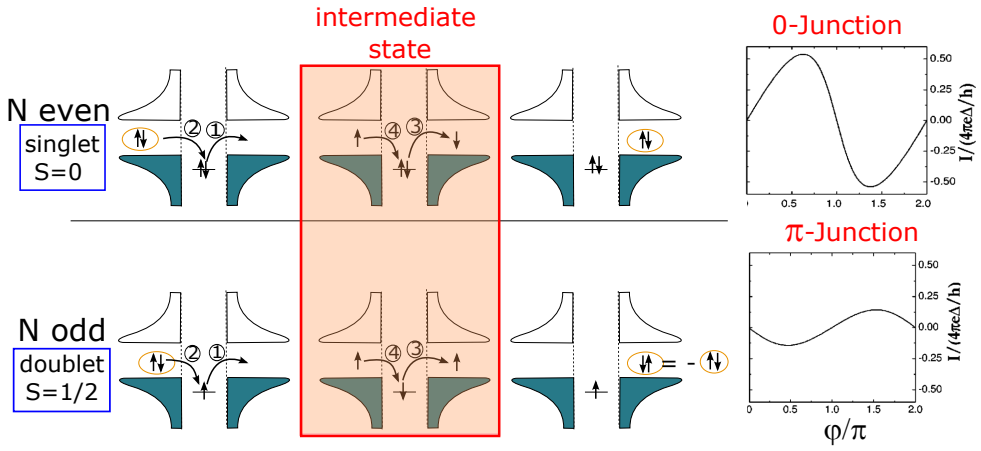

Figure 5.3: Fourth order tunneling processes of a cooper pair in the intermediate regime. Left: For a total spin S=0 on the dot, the cooper pair is transported with the same spin order, supercurrent is important. For a total spin S=1/2, the cooper pairs spin order is reversed a π phase shift is induced. Right: Corresponding calculated current-phase relation for 0-Junction and π-Junction. Taken from [100].

In this range, the amplitude and the sign of the supercurrent highly depend on the dot's occupancy, and two cases can be distinguished. When a QD is occupied by an even number of electrons, the dot is in a singlet state (S=0). The Cooper pairs tunnels through the QD preserving its spin order and the supercurrent is high (See fig.5.3). The Josephson coupling is positive this is known as the 0-junction. Whereas when the occupation number is odd the QD is in a doublet state. There is only one spin in the highest occupied state, spin up or spin down electron. At the end of the co-tunneling process, the dot's spin is left unchanged, and a Cooper pair is transported with inverted spin ordering as illustrated in fig.5.3. In this situation, the fourth-order tunneling process is accompanied by a spin-flip, which strongly affects the supercurrent [96]. The Josephson coupling is said to be negative, the supercurrent amplitude is weakened compared to the 0 junction case [97] and the current-phase relation (CPR) is dephased by π [98, 99]: $I(\varphi) = I_c \sin(\varphi + \pi)$: this is the π-Junction

5.4 Competition with Kondo effect

The Kondo effect occurs in an oddly occupied QD coupled to two electrodes made up of normal metal (See chapter 3). The screening of the magnetic impurity by the conduction electron of the

two electrodes provides a perfectly transmitting channel for transport. Let us consider the case where the electrodes become superconducting. In this case, the Kondo effect may compete with other quantum many-body phenomena: superconductivity.

Would the Kondo correlations survive in the presence of Cooper pairs and the superconducting gap at the Fermi level? And what will happen to the Josephson current for such a junction?

We have seen that the tunneling of Coopers pair between two superconducting contacts coupled through a QD, depends on the parity of the dot, a QD with an even(odd) number of electron leads to 0-junction(π-junction)). However, in the presence of the Kondo correlation, the Kondo singlet state competes with the pairing energy Δ of the Cooper pairs. The Kondo-superconductivity interplay has been extensively studied theoretically [99, 100, 101, 49, 102, 103]:

The resulting physics of the system is controlled by the ratio of T_K/Δ:

- If $k_B T_K/\Delta \ll 1$, Kondo correlation cannot develop due to the lack of electrons at the Fermi level of the contacts as shown in fig.5.4.a there is no co-tunneling process. Thus, the magnetic spin remains unscreened. In this case, the Josephson coupling is negative: this is a π-junction

- If $k_B T_K/\Delta \gg 1$, the quasi-particle density of state of the superconductors overlap with that of the Kondo resonance (see fig.5.4.b). The cotunneling processes are enhanced, making the transfer of Cooper pairs easier, and favoring the formation of a Kondo/BCS singlet state. The two phenomena cooperate to enhance the supercurrent. In this case, the Josephson coupling is expected to be positive, this leads to a 0-junction.

- If $k_B T_K/\Delta \approx 1$, then one enters the intermediate regime. In this case, the magnetic state of the dot depends on the phase difference between the two superconductors. In this limit, a transition between the singlet and doublet state can be observed driven by the ratio $k_B T_K/\Delta$ as predicted by Glazman [99], and observed experimentally [104, 105].

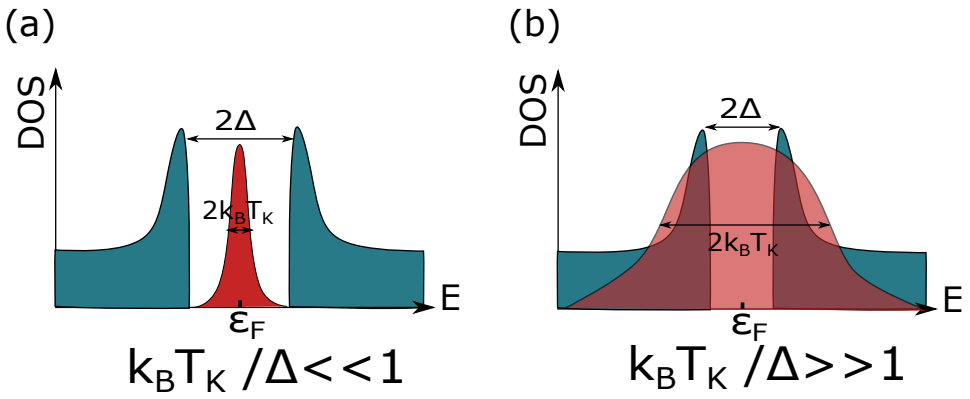

Figure 5.4: Density of state of the superconducting contacts together with the Kondo resonance in its normal state. (a) For $k_B T_k/\Delta \ll 1$, the electrons that could participate in the screening are not available because of the superconducting gap. (b) For $k_B T_k/\Delta \gg 1$, both the Kondo effect and superconductivity can exist leading to an enhanced supercurrent.

5.5 Induced 0-π transition

In the strong coupling regime, the superconductor wave function spreads over the dot, inducing a BCS-singlet ground state i.e. a 0-junction. When the QD enters the Coulomb blockade regime, the dot is occupied by a fixed number of electrons, alternating even or odd. Thus a 0-π transition is achieved by modifying the parity of the electronic charge on the dot using electrostatic gates. In the intermediate regime, where Kondo correlation is present, a 0-π transition is possible depending on the ratio between Δ and T_K, the latter can be tuned using a gate voltage via the position of the energy level. Thus, a first-order quantum transition between 0 and π junction is achieved by tuning the microscopic parameters of the quantum dot. These parameters are the broadening Γ of the energy levels in the dot due to the coupling to the reservoirs, the superconducting gap Δ of the contacts, the dot's charging energy U, and it's level energy ϵ. Note that, the ground state of the system (singlet or doublet) depends strongly on the superconducting phase φ.

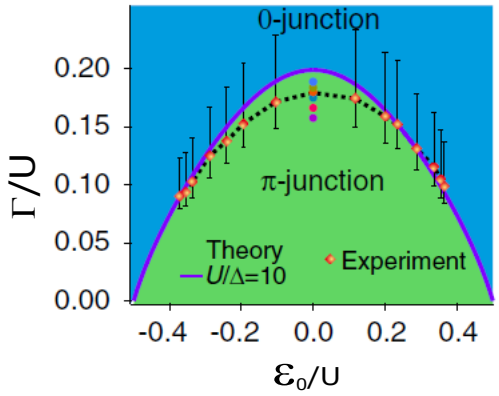

Figure 5.5: Phase diagram of the 0-π transition of a carbon nanotube in the Kondo regime, as a function of the dot energy ϵ_0/U and the level width Γ/U. Taken from [62].

The phase diagram of the 0-π transition of a quantum dot (in this precise case a carbon nanotube quantum dot) is presented in fig.5.5. In the center of the Coulomb diamonds, the charging energy U is high, the doublet state is more likely to appear due to Coulomb blockade. As we go towards the edges of the diamond, U starts to decrease, favoring the formation of a singlet state. As Γ increases, co-tunneling processes allow some current to flow in the Coulomb blockade regime, this will reduce the range for π behavior. When Γ is high compared to U, co-tunneling processes become more important, there is no π-junction behavior, and a 0 junction is maintained.

The transition from a 0 to a π junction can be achieved by tuning the dot's parity with a gate voltage, this is called a gate-controlled 0-π transition. It has been experimentally observed in an InAs nanowire QDs [93] and in a CNT QDs [92, 62, 105]. In both experiments, the QD is inserted in a superconducting loop so that the phase is controlled by a magnetic field, allowing the measurement of the current-phase relation. Jorgensen et al. [118] measured as well this gate-

controlled 0-π transition in a CNT but without control of the phase, the measurement is shown in fig.5.6.

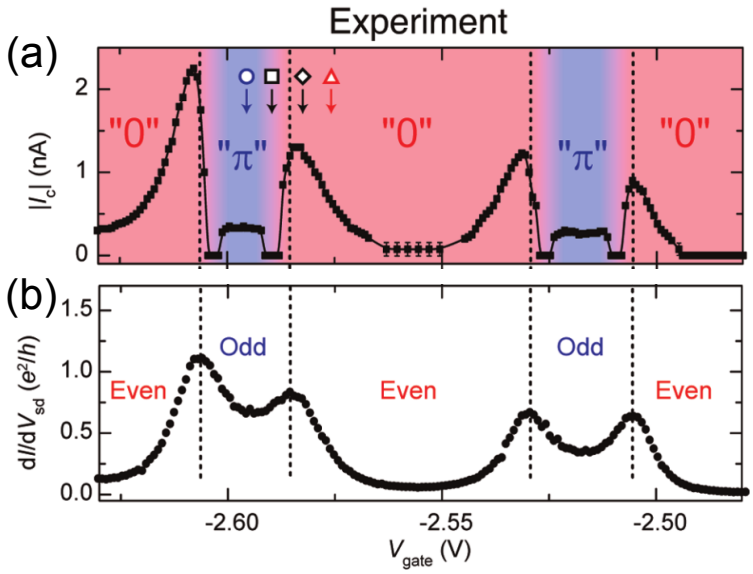

Figure 5.6: Measurement of the critical current amplitude in a carbon nanotube quantum dot contacted with superconducting electrodes. When the gate voltage is tuned, the critical current amplitude alternate positive and negative, indicating a 0 to π transition. Adapted from [118].

More recently, Delagrange et al. [123] measured the current phase relation of a CNT QD embedded in a superconducting loop with two Josephson junctions forming an asymmetric SQUID. To phase bias the CNT Junction, a magnetic flux is applied with a magnetic field perpendicular to the SQUID. The modulation of the switching current δI_s versus magnetic field B, proportional to the CPR of the carbon nanotube, is measured for various V_g in an oddly occupied diamond and is represented on fig.5.7.a. Close to the particle/hole symmetry point the system acts as a π-junction. Away from this point, the system exhibits a 0-junction behavior. This is compatible with 0-π transitions at $T_K \approx \Delta$ of fig.5.5, driven by the interplay between the Kondo effect and the superconductivity. In between, the phase dependence at different gate voltages shows that the CPR is anharmonic: A distortion appears first around π and develops as T_K decreases. The CPR is composite, with a part of type 0 around $\varphi = 0$ and a π junction behavior around $\varphi = \pi$. The CPR switched completely to the π-junction in the center of the Coulomb diamond where T_K is minimum. The transition from one part to the other is achieved by varying the superconducting phase. The critical phase φ_C is the phase at which, the system undergoes the transition from 0 to π for a fixed gate voltage. The CPR has 0-behavior for $\varphi \in [0, \varphi_C]$ and π-behavior for $\varphi \in [\varphi_C, \pi]$. The critical phase is extracted for several different diamonds, giving a phase diagram of the transition. It shows that it exhibits a universal behavior, independent of the values of the parameters of the quantum dot (see fig.5.7.c). This experiment demonstrates experimentally that the $0 - \pi$ transition can be controlled not only by the gate voltage but also by the superconducting phase.

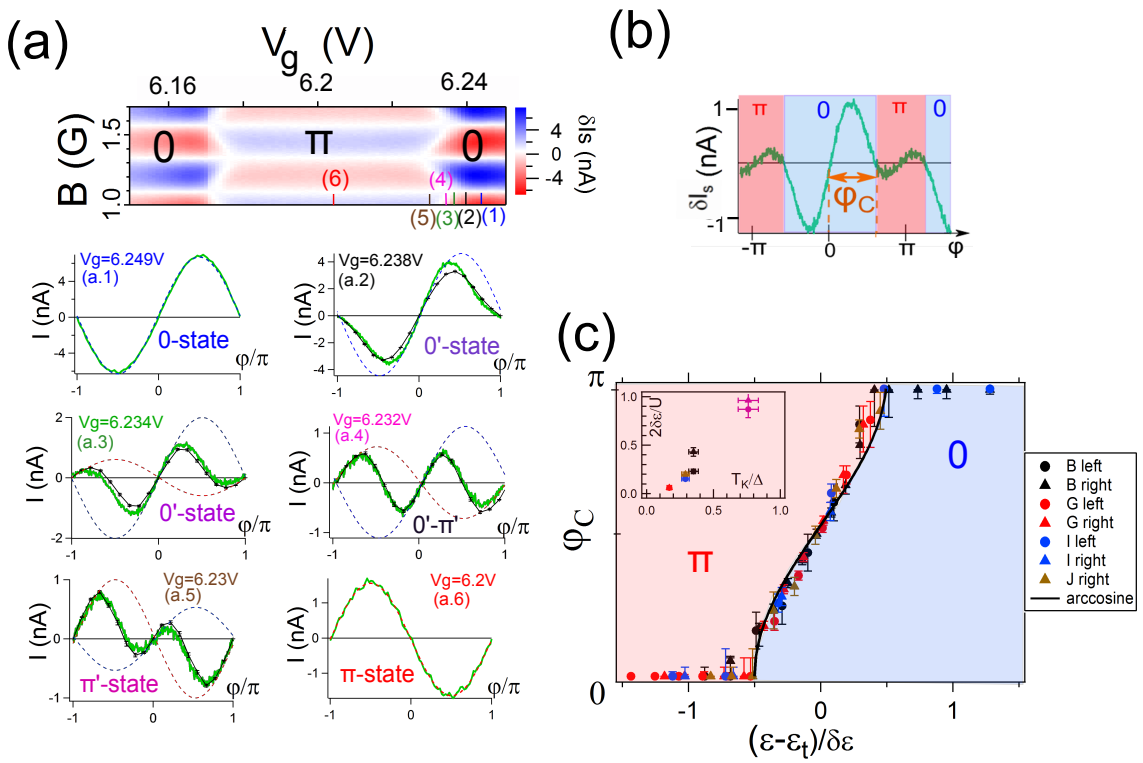

Figure 5.7: (a) Modulation of the switching current of the SQUID δI_s, proportional to the CPR, as a function of the magnetic field B and the gate voltage V_g for an oddly occupied diamond. Vertical cuts at the 0-π transition, showing the whole transition. The dashed lines are guides to the eyes and represent the contributions of the singlet (0-junction, in blue) and the doublet state (π-junction, in red). (b) Definition of the critical phase φ_C at which the system undergoes 0 to π transition. (c) Critical phase φ_C plotted as a function of ϵ_d, yielding a phase diagram of the 'φ-controlled transition, where δE the width of the transition. Taken from [60].

5.6 Conclusion

In a QD between two superconductors, the tunneling of Cooper pairs across the QD is highly affected by the ration Γ/Δ and the CPR is strongly dependent on the parity of the number of electrons on the QD: for even occupancies, the supercurrent is positive and high: this is a 0-junction. However, for odd occupancies, the supercurrent undergoes a sign reversal: this is a π-junction. In the last section, we study the competition between the Kondo singlet ground state with characteristic energy $k_B T_K$ and the spin singlet ground state of superconductivity composed of Cooper pairs with pairing energy Δ and phase φ. If the Kondo effect is strong enough compared to superconductivity ($T_K > \Delta$), a BCS-Kondo singlet state is formed that restore a 0-junction. If $T_K \approx \Delta$, the system undergoes a 0-π transition driven by φ, where the dot's spin is respectively screened or unscreened. The transition for 0 to π can also be induced by tuning the dot's parameters, or the gate voltage.

Chapter 6

AC Josephson effect in carbon nanotube quantum dot

In this chapter, we focus on the dynamics of QD Josephson junctions by measuring the Ac Josephson effect in a CNT QD, in the regime where both superconducting proximity effect and Kondo effect are present. The first section will be dedicated to describing the principle of the measurement along with the experimental setup. Then we will present the experimental results and interpretations.

6.1 Measurement of AC Josephson effect

6.1.1 Experimental setup

In order to measure the AC emission of a CNT QD connected with superconducting electrodes, one can use high frequency electronics (for frequencies below 10GHz at cryogenic temperature) or an on-chip quantum detector. In this experiment, we have chosen to use a superconducting tunnel junction (SIS junction) as a quantum noise detector. The source of emission (CNT) is coupled on-chip to an SIS Josephson junction via a resonant circuit. The source and the detector are directly connected to the end of the central line of a coplanar waveguide resonator, whose other end is grounded so that they are coupled at the resonance frequencies of the circuit. The resonance is expected at $\nu_0 = 12GHz$, $\nu_0 = 31GHz$ and $\nu_0 = 51GHz$. The fabrication of the sample is explained in detail in Chapter 2. The experimental setup is represented in fig.6.1.

SIS Junction has been used as a quantum detector to measure the noise of a carbon nanotube quantum dot in the Coulomb blockade regime [109], the noise of a Josephson junction [110], the asymmetrized noise of a two-level system [111], and high frequency emission of CNT QD in the Kondo regime [123] or InAs nanowires [83].

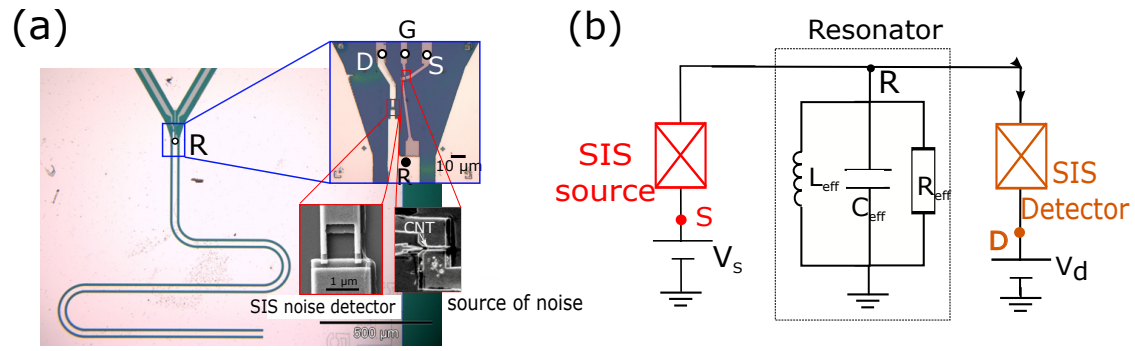

Figure 6.1: (a) The carbon nanotube Josephson junction is coupled to a quantum detector SIS junction via a coplanar waveguide resonator. (b) The equivalent electronic circuit is the coplanar waveguide is equivalent at resonance to an RLC circuit.

Josephson Junction as quantum detector

For an SIS junction, the noise detection is based on the measurement of photo-assisted tunneling (PAT) current of quasi-particles in the junction. In this experiment, instead of using a simple SIS junction, we use two identical SIS junctions in a SQUID geometry. In such geometry the critical current is equal to $I_c = 2I_0 \cos\left(2\pi\frac{\Phi}{\Phi_0}\right)$, with Φ is the magnetic flux applied and $\Phi_0 = \frac{h}{2e}$ the flux quantum and I_0 the critical current of a single junction. This implies that applying a magnetic flux of $\Phi = (2n+1)\frac{\Phi_0}{4}$ with n is an integer, leads to the suppression of supercurrent features and AC Josephson radiation generated by the detector, that could disturb the measured signal coming from the CNT.

In an SIS Junction, due to the presence of a superconducting gap around the Fermi energy, there are no quasiparticles current when $V_d < 2\Delta/e$, only current due to Cooper pair tunneling: supercurrent flows across the junction. When the junction is biased such that $V_d > 2\Delta/e$, quasiparticles current flows as for the normal tunnel junction case due to elastic tunneling of quasiparticles. The typical I(V) characteristic of an SIS junction is shown in fig.6.2.

However, when the SIS detector absorbs or emits a photon at energy hν, this will alter its I-V characteristics as follow:

- If the junction is biased below the gap i.e. $\mid V_d \mid < 2\Delta/e$, a photo-assisted tunneling current of quasi-particle is possible provided that a photon of energy $h\nu > 2\Delta - \mid eV_d \mid$ is absorbed. Thus, a current step of width hν/e appears in the I(V) characteristics with a height proportional to the amplitude of the absorbed radiation.
- If the junction is biased above the gap i.e. $\mid V_d \mid > 2\Delta/e$, in addition to the finite quasiparticle current due to elastic tunneling processes, quasiparticles can inelastically tunnel and emit photons at energy $h\nu < 2\Delta - \mid eV_d \mid$. These inelastic events happen only if these photons are absorbed by the environment. This process leads to the decrease of quasiparticles current and a negative step I(V) is observed.

Here we are interested in PAT below the gap, i.e. related to the emission by the CNT junction. The expression of I_{PAT} will be derived in both cases in the following section.

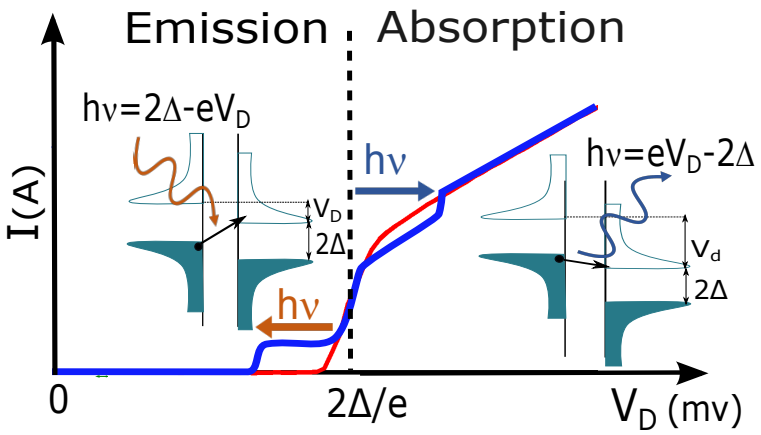

Figure 6.2: Red curve: Typical current-voltage characteristic of an SIS junction. Blue: calculated I(V) of the detector under irradiation giving rise to photo-assisted tunneling current I_{PAT} steps. Below the gap, the detector is emission sensitive. Above the gap, the detector is mainly absorption sensitive. Taken from [110].

Expression of the photo-assisted tunneling current with P(E) theory

In what follow we derive the I(V) characteristic of a tunnel junction in the absence and presence of an electro-magnetic environment based on derivation done by Ingold and Nazarov which address the charge tunneling rates in ultrasmall junctions [112]. Changes due to the environment are calculated within the same P(E) formalism and an interpretation is given in terms of photo-assisted tunneling induced by the noisy environment.

Tunneling rate formula P(E) is the probability for the junction to absorb or emit the energy $\mid E \mid$ in the environment. If $E > 0$, the energy is absorbed by the environment, if $E < 0$ it is emitted. Starting from the definition of P(E), and using the Fermi Golden rule, one expresses the forward tunneling rate in a normal tunnel junction by :

$$\vec{\Gamma}(V_d) = \frac{1}{e^2 R_T} \int_{-\infty}^{+\infty} dE dE' f(E)(1 - f(E' + eV_d))P(E - E') \tag{6.1}$$

Where V_d is bias voltage of the junction, $f(E) = [1+e^{\beta E}]^{-1}$ is the Fermi function with $\beta = 1/k_B T$, $1/R_T$ is the tunneling conductance, and $P(E - E')$ is the probability for the electromagnetic environment to absorb the energy $E - E'$. In absence of an environment, it is not possible to exchange any energy, this probability is reduced to the Dirac function: $P(E - E') = \delta(E - E')$.

However, we are interested in the tunneling rate of a superconducting tunnel junction, thus we must include the superconducting density of states (eq.4.7) in eq.6.1.

That gives for the forward tunneling rate in a superconducting tunnel junction :

$$\vec{\Gamma}(V_d) = \frac{1}{e^2 R_T}\int_{-\infty}^{+\infty} dE dE' \frac{N_s(E)N_s(E'+eV_d)}{{N_0}^2} f(E)(1-f(E'+eV_d))P(E-E') \tag{6.2}$$

P(E) and I(V) characteristic The current response I(V) of a superconducting tunnel junction to a voltage bias V_d in presence of an environment having a probability P(E) to exchange energy E can be computed from the forward and backward tunneling rate

$$I_{qp}(Vd) = \vec{\Gamma}(V_d) - \overleftarrow{\Gamma}(V_d) \tag{6.3}$$

knowing that $\overleftarrow{\Gamma}(V_d) = \vec{\Gamma}(-V_d)$, due to voltage bias symmetry. eq.6.3 can be written as:

$$I_{qp}(V_d) = \vec{\Gamma}(V_d) - \vec{\Gamma}(-V_d) = \frac{1}{e^2 R_T}\int_{-\infty}^{+\infty} dE dE' \frac{N_s(E)N_s(E'+eV_d)}{{N_0}^2}[f(E)(1-f(E'))P(E-E'+eV_d) - f(E')(1-f(E))P(E'-E-eV_d)] \tag{6.4}$$

To write $I_{qp}(V_d)$ in more convenient way, we include in eq.6.4 the two following properties:

- $P(-E) = e^{-\beta E}P(E)$, the detailed balance relation of P(E)
- $f(E)[1-f(E+x)] = \frac{f(E)-f(E+x)}{1-e^{\beta x}}$

After doing the calculation, eq.6.4 may be rewritten as:

$$I_{qp}(V_d) = \int_{-\infty}^{+\infty} dE \frac{1-e^{-\beta eV}}{1-e^{-\beta E}} \times P(E-eV_d) I^0_{qp}(E/e) \tag{6.5}$$

Where $I^0_{qp}(V_d)$ is the I(V) characteristic of a voltage biased SIS junction in absence of environment:

$$I^0_{qp}(V_d) = \frac{1}{eR_T}\int_{-\infty}^{+\infty} dE \frac{N_s(E)N_s(E+eV_d)}{{N_0}^2}[f(E)-f(E+eV_d)] \tag{6.6}$$

Photo-assisted tunneling current as a probe of voltage noise The photo-assisted tunneling current can be interpreted as the difference between the quasi-particle current with and without environment $I_{PAT}(V_d) = I_{qp}(V_d) - I^0_{qp}(V_d)$. In what follow we will derive the expression of P(E) in terms of the voltage fluctuation across the detector. All the information about the environment is contained in the auto-correlation of the phase operators : $J(t) = \langle[\delta\hat{\phi}(t) - \delta\hat{\phi}(0)]\hat{\phi}(0)\rangle$. $\delta\hat{\phi}(t) = \int_{-\infty}^{t} dt' \delta\hat{V}(t')$, are the conjugate phases of the voltage fluctuations $\delta\hat{V}(t')$ across the detector[characterized by the spectral density $S_v(\omega)$] [113].

From [112] we can deduce that P(E) is the Fourier transform of $e^{J(t)}$:

$$P(E) = \frac{1}{h}\int_{-\infty}^{+\infty} dt \exp\left(J(t) + \frac{i}{\hbar}Et\right) \tag{6.7}$$

In the case of low noise amplitude, one has $exp(J(t)) \approx 1 + J(t)$. Once introduced into Eq.6.7, one obtains a simplified version of the probability P(E) in terms of $S_V(\nu)$, the non-symmetrized spectral density of excess voltage fluctuations at frequency ν across the detector [113]:

$$\begin{aligned} P(E) &= \frac{1}{h}\int_{-\infty}^{+\infty} d\tau(1+J(\tau))exp(\frac{i}{\hbar}E\tau) \\ &= \left[1 - \frac{e^2}{h^2}\int_{-\infty}^{+\infty} d\nu \frac{S_V(\nu)}{\nu^2}\right]\delta(E) + \frac{e^2}{h^2}\frac{S_V(E/h)}{E^2} \end{aligned} \tag{6.8}$$

By inserting the new expression of P(E) in eq.6.5, one obtains the expression for the total current $I_{qp}(V_d)$ flowing through the junction in the presence of the environment. By subtracting the value of the current without environment $I^0_{qp}(V_d)$ we obtain the expression of the photo-assisted tunneling $I_{PAT}(V_d)$ current through the detector [110]:

$$\begin{aligned} I_{PAT}(V_d) &= I_{qp}(V_d) - I^0_{qp}(V_d) \\ &= \int_0^{\infty} d\nu \left(\frac{e}{h\nu}\right)^2 S_V(-\nu) I^0_{qp}\left(V_d + \frac{h\nu}{e}\right) \\ &+ \int_0^{eV_d} d\nu \left(\frac{e}{h\nu}\right)^2 S_V(\nu) I^0_{qp}\left(V_d - \frac{h\nu}{e}\right) \\ &- \int_{-\infty}^{+\infty} d\nu \left(\frac{e}{h\nu}\right)^2 S_V(\nu) I^0_{qp}(V_d) \end{aligned} \tag{6.9}$$

As shown in fig.6.2, depending on the value of V_d, the SIS junction could be either in absorption or emission mode.

I_{PAT} due to emission noise If the detector is biased below the gap, $V_d < 2\Delta/e$: $I^0_{qp}(V_d - \frac{h\nu}{e}) = I^0_{qp}(V_d) = 0$. Thus, only the first term of eq.6.9 contributes: we are then measuring the emission of the source absorbed by the detector.

$$I_{PAT}(V_d) = \int_0^{\infty} d\nu \left(\frac{e}{h\nu}\right)^2 S_V(-\nu) I^0_{qp}\left(V_d + \frac{h\nu}{e}\right) \tag{6.10}$$

I_{PAT} manifest itself as a small steps step at $2\Delta > eV_d > 2\Delta - h\nu_0$.

I_{PAT} due to absorption noise If the detector is biased above the gap, $V_d > 2\Delta/e$, all the terms contribute but with a stronger weight for the absorption by the source.

Coupling to the resonance circuit

In this experiment the noise source (CNT QD) is coupled to the detector (SIS Josephson junction) via an on-chip coupling circuit characterized by the transimpedance $Z_t(\nu)$. This transimpedance quantifies the link between voltage noise $S_V(\nu)$ appearing across the detector and current noise $S_I(\nu)$ generated by the source such that [113]:

$$S_V(\nu) = \mid Z_t(\nu) \mid^2 S_I(\nu) \tag{6.11}$$

In this experiment the coupling is chosen to be resonant, such that the detection occurs only at the resonance frequency of the coupling circuit. This make it easier to analyze the signal coming from the detector. Another advantage of using a resonant coupling is that its high transimpedance make it possible to collect a reasonable amount of photo-assisted tunneling current through the detector.

The transimpedance of a resonant coupling is: $Z_t(\nu) = \sum_n Z_t^n(\nu - \nu_n)$ with $Z_t^n(\nu - \nu_n)$ a resonance centered around the frequency ν_n, n^{th} harmonic of the resonator. Using eq.6.11 and the definition of transimpedance of a resonant coupling, the expression of photo-assisted tunneling current related to the emission of the source can be written as:

$$I_{PAT}(V_d) = \int_0^\infty d\nu \left(\frac{e}{h\nu}\right)^2 S_I(-\nu) \sum_n |\ Z_t^n(\nu - \nu_n)\ |^2 I_{qp}^0\left(V_d + \frac{h\nu}{e}\right) \tag{6.12}$$

We used a coplanar waveguide geometry, with a transmission line placed between two larges ground plane. One extremity of the transmission line is grounded while the source and the detector is connected to the other extremity (See fig.6.1).

The length of the resonator L corresponds to the quarter of the wavelength, giving resonance frequencies such that $L = \lambda_n(\frac{1}{4} + \frac{n}{2})$ with n being an integer. The dimensions of the resonator made of Aluminum of thickness 200 nm on an undoped silicon wafer are shown in fig.6.3. The length of the resonator is L=3mm, such that the resonance frequencies are at 12.5 GHz and the odd harmonics. For an SIS junction with alternating current $I = I_c \sin\left(\frac{2eV_s t}{\hbar}\right)$. The associated current spectral density is $S_I(\nu, V_s) = \frac{I_c^2}{4}\left(\delta\left(\nu - \frac{2eV_s}{h}\right) + \delta\left(\nu + \frac{2eV_s}{h}\right)\right)$. We assume here a quasi-monochromatic Josephson emission. This gives the emission contribution to the photo-assisted tunneling current [114]:

$$I_{PAT} = \frac{1}{(2V_{SD})^2}\frac{I_C^2}{4}|Z_t(2eV_{SD}/h)|^2 I_{qp}^0(V_d + 2V_{SD}). \tag{6.13}$$

with $I_{qp}^0(V_D)$ the IV characteristic of the detector without irradiation.

The usual way for characterizing a resonator, *i.e.* determining its resonance frequencies and quality factors, is to measure the frequency dependent reflection coefficient with high frequency electronics. But here, the sample is designed to be addressed by DC measurements, AC signal being confined on-chip. The best way to characterize the resonator (and the detector) is to use an on-chip AC source. A very convenient one is given by the AC Josephson effect of a Josephson junction: when biased by the voltage V_s, there is an AC current $I(t) = I_C \sin\left(\frac{2eV_s}{\hbar}t\right)$ in the junction. Using eq.6.13 and 4.23, and knowing the $I(V)$ characteristic in absence of environment I_{qp}^0, the measurement of I_{PAT} at a fixed $eV_d < 2\Delta - h\nu_0$ gives access to $|Z_t(\nu)|$ at each resonant frequency.

The measurement is presented on fig.6.3. In the case of the Josephson emission with finite bandwidth, the resonance peak seen in the PAT current results from the convolution of the transimpedance and the finite bandwidth emission. To calculate the quality factor of the resonator, it can be modelized by the RLC circuit presented in fig.6.1.b. The effective capacitance, inductance and resistance modeling the resonator is given by [115]:

$$L_{eff} = \frac{2L_l L}{\pi^2}, \qquad C_{eff} = \frac{C_l L}{2}, \qquad R_{eff} = \frac{Z_0}{\alpha L} \tag{6.14}$$

L_l and C_l are respectively the inductance and capacitance per unit of length, L the length of the line and α a coefficient that quantifies the losses in the system. The length of our resonator L=3mm, the $Z_0 = \sqrt{\frac{L_l}{C_l}} = 46\Omega$ and $\nu_0 = \frac{1}{2\pi\sqrt{L_{eff}C_{eff}}} = 10GHz$, yielding:

$$L_l = 7.7 \times 10^{-7} H/m, \qquad L_{eff} = 0.46nH \tag{6.15}$$

$$C_l = 3.62 \times 10^{-10} F/m, \qquad C_{eff} = 0.54pF \tag{6.16}$$

The Quality factor is given by:

$$Q = 2\pi\nu_0 R_{tot} C_{eff} \tag{6.17}$$

with $R_{tot} = (R_{eff}^{-1} + R_D^{-1} + R_S^{-1})^{-1}$, R_{eff} represents the internal losses of the resonator, R_D the resistance of the detector and R_S of the source. we can assume that R_{tot} is dominated in any case by R_D and R_S and not by the intrinsic losses of the resonator. For our sample, we have $R_S = 7K\Omega$ and $R_D = 6K\Omega$. This gives $R_{tot} = 3.2k\Omega$ and a quality factor Q=100. However, the width of the resonance peaks shown in fig.6.3 gives a very low-quality factor Q=2 for 12 GHz. This could be due to the fact that the detector and the source are directly coupled to the transmission line, inducing extra losses. But we think that the main reason is the noise in the voltage bias line.

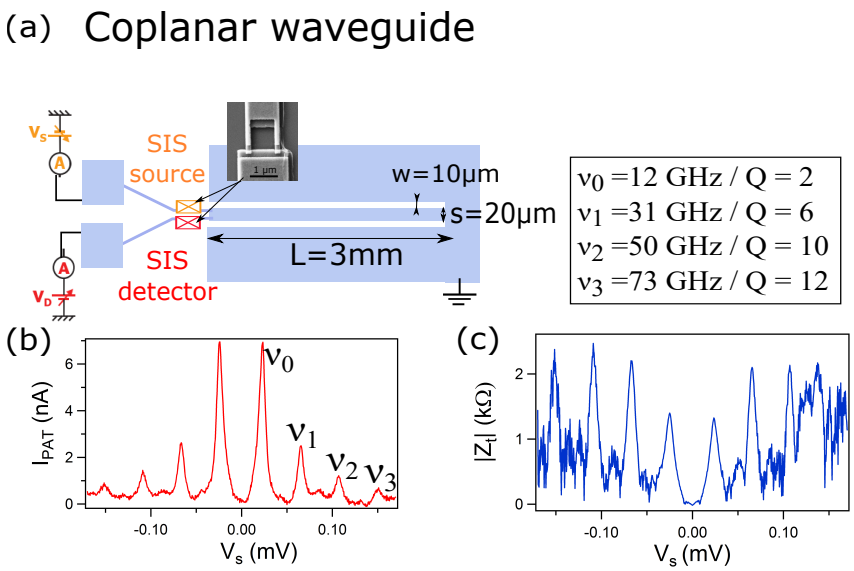

Figure 6.3: (a)Design of the coplanar waveguide resonator used in this experiment, showing the coupling between the source and the detector. (b) Photo-assisted quasiparticle current measured in the detector biased at $2\Delta - h\nu_0 < eV_d < 2\Delta$ as a function of the bias V_S of the source of AC Josephson effect. The frequency of the emission is given by the Josephson frequency $\nu = \frac{2eV_s}{h}$. (b) Trans-impedance $Z_t(\nu)$ extracted from I_{PAT} using formula 6.13. The corresponding resonance frequencies and quality factors are given. In this sample, the detector is a SQUID of normal resistance around 5 kΩ and the source a simple junction of normal resistance 12 kΩ.

From fig.6.3 we realize that the width of the resonance is the same (around 6 GHz), whatever the frequency of the resonance or the design of the resonator. This constant width may be due to the non-monochromaticity of our source (the SIS junction) instead of the resonant circuit itself. This non-monochromaticity may originate from fluctuations of the biasing voltage V_{SD}, and thus may be improved by better filtering. In the following section, we will present a new biasing circuit that aims to reduce the voltage noise, thus improving the monochromaticity of our source of emission.

Low noise voltage biasing In order to emit radiation that can be detected by the on-chip detector the source must be biased according to:

$$2eV = h\nu_J \tag{6.18}$$

with ν_J is the resonance frequency of the coupling circuit. This relation implies that the voltage noise δV of the biasing line must be much lower than the band width $\delta\nu$ of the emission:

$$\delta V \ll \frac{h\delta\nu}{2e} \tag{6.19}$$

The bandwidth of the detection is fixed by the quality factor of the resonant circuit and is equal to: $\delta\nu = \frac{\nu_0}{Q} = \frac{10}{100} = 0.1$ GHz, it corresponds to $\delta V = 20$nV.

Thermal noise on the biasing line To reduce the voltage noise on the sample, the sample is biased at low temperature through a biasing circuit placed near the sample inside the cryostat as shown in fig.6.4. The sample is biased through a 110Ω with a 100nF in parallel to form an RC filtering stage. A 1kΩ resistance is used to detect the current through the source. A 10nF capacitance is also used to filter the noise of this resistance.

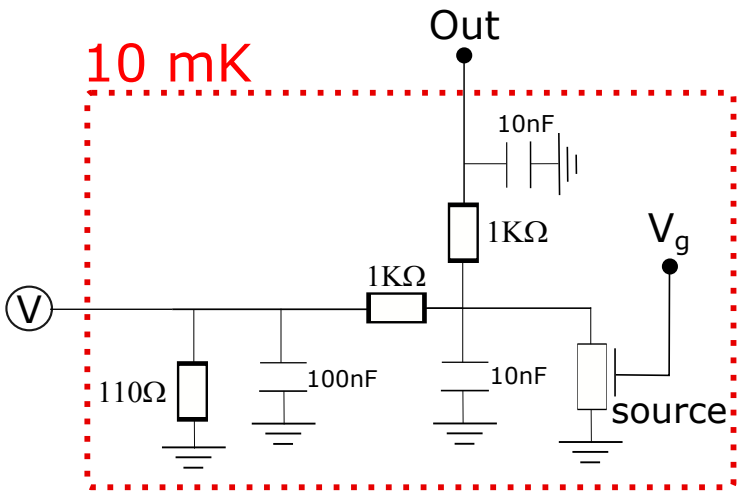

Figure 6.4: Low temperature biasing circuit.

The thermal noise of an R-C filtering stage due to resistance is given by:

$$\delta V^2 = 4k_B T R \Delta f \tag{6.20}$$

with Δf the bandwidth of with cut-off filter frequency $1/2\pi RC$. The voltage noise then takes a very simple form:

$$\delta V^2 = \frac{1}{2\pi}\int_0^{+\infty} \frac{4k_B T R}{1+R^2C^2\omega^2} d\omega = \frac{k_B T}{C} \tag{6.21}$$

The value of the voltage noise depends on two factors:

- T, the temperature of the resistance. Decreasing T will lower the value of δV. Thus, when placing the biasing circuit at 10 mK, one expects to lower the voltage noise.
- C, the value of capacitance placed in parallel with the resistor. δV is inversely proportional to the capacitance. So, to minimize the value of δV one must choose a suitable value of C.

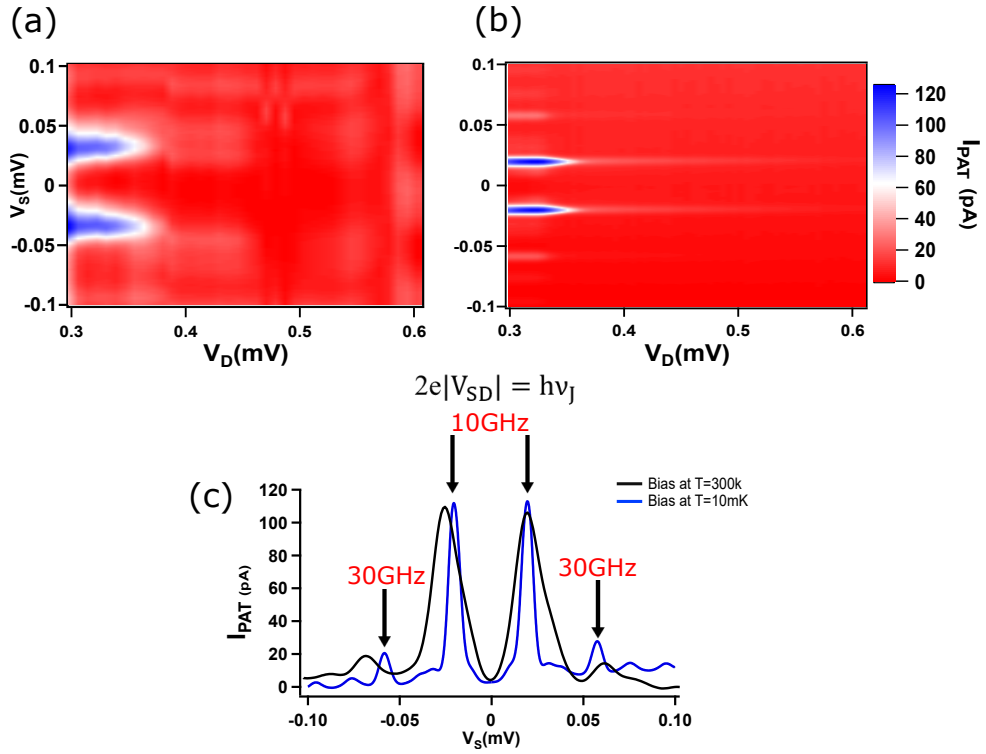

Figure 6.5: Color plot of the Photo assisted tunneling current across the detector as a function of source-drain voltage V_s and detector bias voltage V_d.(a) The bias circuit is at room temperature T=300K. (b) The bias circuit is placed near the sample at T=10 mK. (C) Vertical cut at $V_d = 0.33mV$ showing the PAT current peaks that correspond to a resonance frequency of 10 GHz and 30 GHz.

With T = 10mK and C= 100nF will give a very good value $\approx 2.9nV < 20nV$. Because we need to measure the current, we add the 1kΩ, and filter them with the 10 nF, this leads to voltage fluctuation around 10nV. To test the efficiency of our biasing circuit, we measure the radiation of a

Josephson junction coupled to another Josephson junction that plays the role of a detector through the same resonant circuit explained previously. We measure the photo-assisted tunneling current I_{pat} of the source first with a biasing circuit at room temperature, then we use the biasing circuit at 10 mK and compare the results. fig.6.5 shows the PAT current in two different biasing conditions.

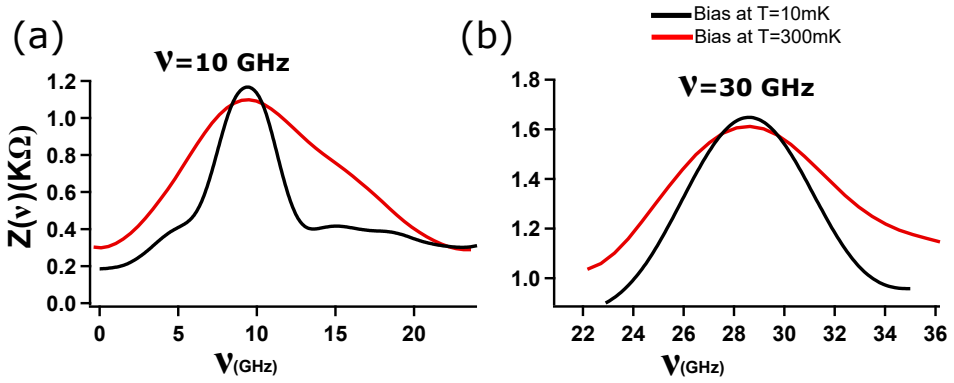

Figure 6.6: Trans-impedance $Z_t(\nu)$ extracted from I_{PAT} using formula 6.13. (a) For ν=10 GHz. (b) For ν=30 GHz.

A vertical cut at a given value of detector bias V_d shows two peaks in PAT current, at ν=10 GHz and ν=30 GHz in both biasing conditions. However, for the cold bias circuit, the signal is sharper, and the peaks are narrower. From these curves, using eq.6.13 and knowing experimentally the value of I_C and I_{qp}^0, we can calculate the transimpedance $Z_t(\nu)$ (See fig.6.6) and extract the quality factor from the full width at half maximum (FWHM) of the resonance peaks. The result of the calculation is summarized in table6.1. Comparing the obtained value for Q with the one expected from the dissipation introduced by the source and detector conductance shows that the improvement of Q is not satisfactory. Some improvement still needs to be done.

	ν=10GHz	ν=30GHz
Bias at T=300 K	1	2.2
Bias at T=10 mK	2.5	4

Table 6.1: Calculated quality factor from FWHM of resonance peaks of fig.6.6.

6.2 Conclusion

In this section, we have shown that an SIS junction can be used as a quantum detector. Depending on the value of bias voltage with respect to Δ, the SIS junction can distinguish between emission and absorption processes. The response of the detector due to the presence of a noisy environment is calculated based on the P(E) theory. The inelastic tunneling of a quasi-particle enhanced by the environment is given in terms of photo-assisted tunneling current. In our experiment, we used an SIS quantum detector coupled to carbon nanotube-based Josephson Junction (source of emission) through a resonant circuit. The measurement of the photo-assisted current of the detector gives

direct access to the signal emitted by the carbon nanotube. The AC emission manifests itself as steps in the I(V) characteristic of the detector. In order to calibrate our coupling circuit, an SIS junction is used as a source of emission coupled to an SIS detector. The measurement of the photo-assisted tunneling current across the detector allows the extraction of the quality factor and the transimpedance of the resonant circuit. Finally, we have shown that by reducing the voltage noise using a new biasing circuit at low temperature, we manage to reduce the bandwidth of the emission of the source junction to improve the frequency resolution of the detection.

6.3 Characterization of the sample in the normal state

In this section, we present the experimental results of the CNT sample shown in fig.6.1 in the normal and superconducting state.

As detailed in chapter 1, a QD is characterized by a set of parameters: the charging energy U, the coupling constant Γ, and the contact asymmetry $\frac{\Gamma_R}{\Gamma_L}$. Depending on the values of the coupling Γ between the dot and the reservoirs and the charging energy U, the transport regime goes from pure Coulomb blockade to Kondo effect, and finally Fabry-Pérot regime. To characterize the measured sample and determine the parameters of a CNT QD, the sample is first measured in the normal state.

6.3.1 Differential conductance in the normal state

In previous work [60], a similar measurement was done for CNT samples, denoted S-NbAl, where the contracts were made of Pd(8 nm)/Nb(11 nm)/Al(50 nm) of superconducting gap $\Delta_{pd/Nb/Al} = 150\mu eV$. The presence of a thin layer of Pd provides good contact on the CNTs, however, it reduces the superconducting gap compared to that of Al or Nb.

For a sample contacted using Nb, one needs to apply a high magnetic field around 1T to suppress superconductivity. Applying a high magnetic field affects the normal state of the CNT QD, preventing a reliable extraction of all the parameters of the dot. For this reason, in the present work, the CNT sample was contacted with Pd/Al of superconducting gap $\Delta_{pd/Al} = 50 \pm 5\mu eV$.

Superconductivity in the Pd/Al contact is suppressed by a low magnetic field of 0.1T, without affecting the normal state of the CNT quantum dot, thus allowing a good determination of the parameters of the dots. The differential conductance of the CNT dI/dV_{SD} as a function of the bias voltage V_{SD} and the gate voltage V_g in the normal state is measured using the lock-in-amplifier technique at 50 mK as described in chapter 2 section 2.1.6. The resulting stability diagram is represented in fig.6.7.

The stability diagram of the QD exhibits Coulomb blockade diamonds with the four-fold degeneracy found for clean CNT quantum dots(three small diamonds followed by a larger one). For the diamonds with an odd number of electrons, the Kondo effect manifests through a high conductance region at zero bias, the Kondo ridge. We focus here on two Kondo ridges A and B, with N=1 and N=3, respectively. A vertical cut in the center of the Kondo ridge, particle-hole symmetry point (red curves in Fig6.7) shows a peak in conductance at zero-bias voltage. The conductance reaches high value, $0.7\frac{2e^2}{h}$, $0.8\frac{2e^2}{h}$, $0.9\frac{2e^2}{h}$ for Kondo A, B and region C respectively. The maximum conductance reached is lower than $2e^2/h$, indicating a not perfectly transmitted channel and thus an asymmetric coupling between left and right reservoirs. On fig.6.7 we also show another gate region (21-23V), called hereafter region C, with a conductance close to the conductance quantum but without Kondo features.

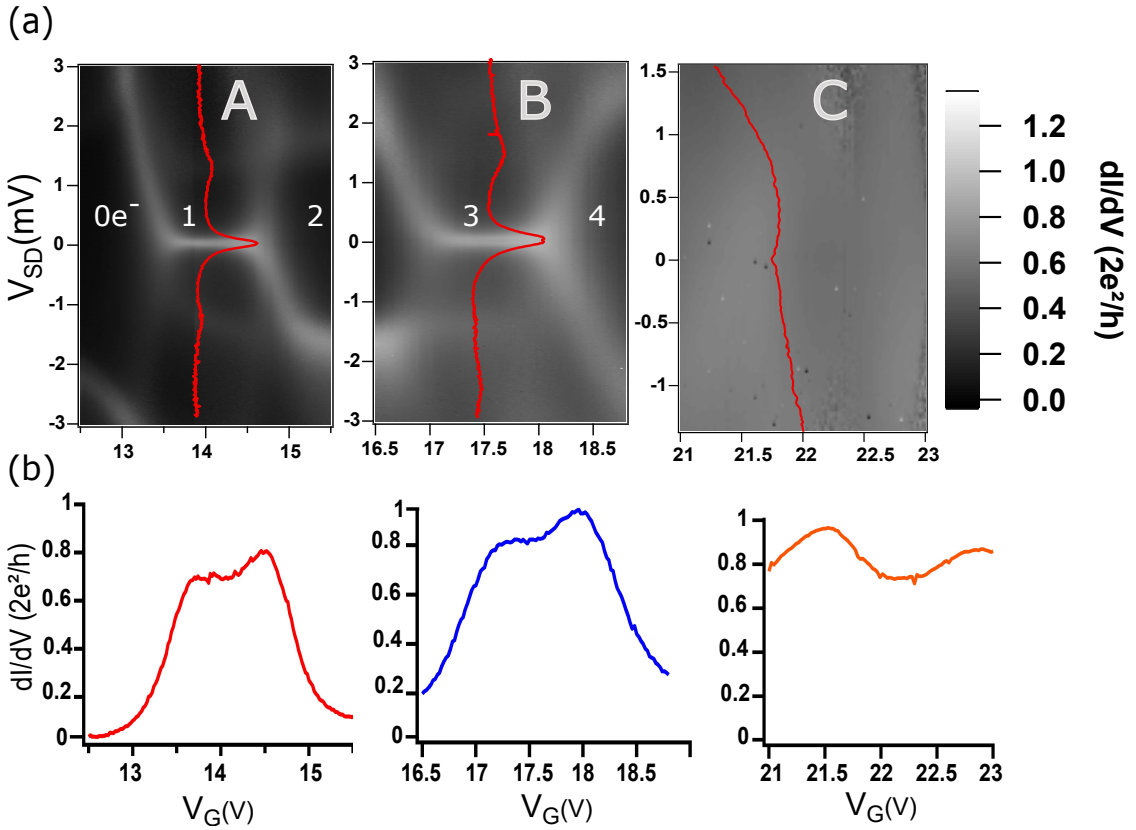

Figure 6.7: Normal state stability diagram of the carbon nanotube quantum dot. (a) Differential conductance dI/dV_{SD} versus bias voltage V_{SD} and gate voltage V_g. The nanotube exhibits strong evidence for the Coulomb blockade and SU(2) Kondo effect. For an odd number of electrons occupying the QD, two Kondo ridges for occupancies 1 and 3, labels A and B are observed. The dI/dV_{SD} curves (red curves) are taken at gate voltages 14V, 17.5V, and 21.5V. (b) Conductance at V_{SD}= 0 of Kondo ridges A and B, and for zone C.

6.3.2 Determination of the QD's parameters

Determination of the Kondo temperature

As explained in section 1.3.1.1, The temperature dependence of the conductance can be described by the phenomenological expression

$$\frac{dI}{dV}(T) = \frac{G_0}{(1 + (2^{1/s} - 1)(\frac{T}{T_K})^2)^s} \tag{6.22}$$

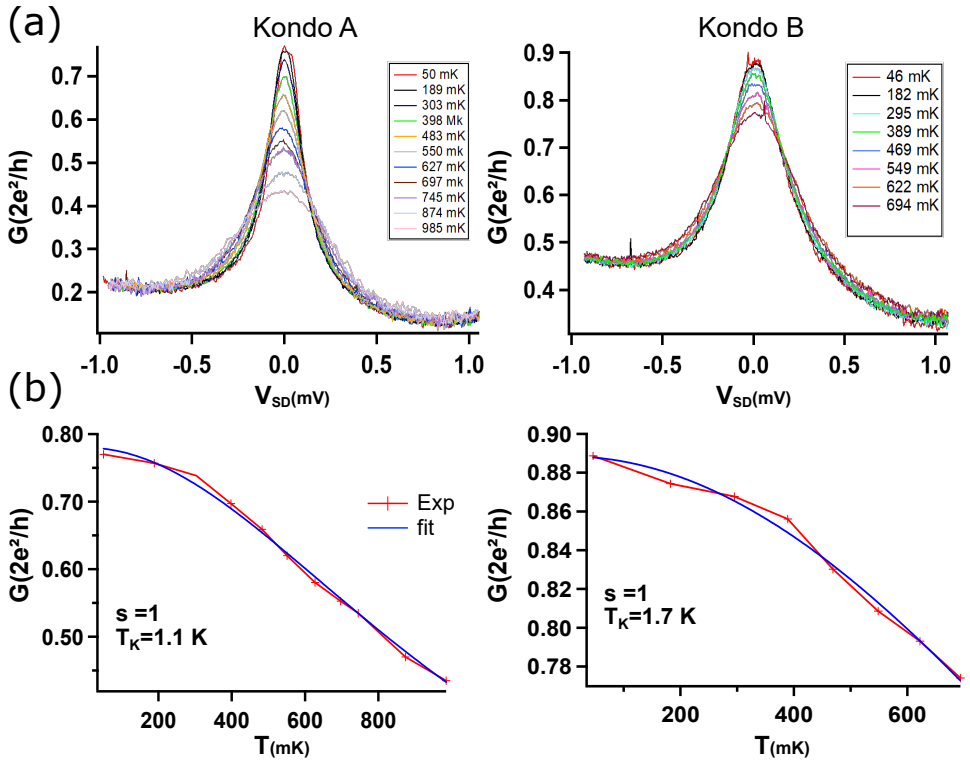

Figure 6.8: (a) Temperature dependence of the conductance peak at the center of the Kondo ridges for various temperatures from 50 mK to 1 K, and from 50 mK to 0.7 K for Kondo A and B respectively. (b) Temperature dependence of the Conductance of the CNT quantum for zone A and B. The agreement with the NRG calculation (s=0.22) is not extremely good. Consequently, the data is fitted with s=1 and we took for the Kondo temperature the value of temperature where $G(T = T_K) = G_0/2$. The parameter extracted from the fit is shown in the legend of the figure.

The temperature dependence of the Kondo resonance at zero-bias voltage for both ridges A and B is represented in fig.6.8.a. Fitting the conductance at zero-bias as a function of temperature with eq.6.22 allows one to extract the Kondo temperature (fig.6.8). The agreement of this formula with our data is not completely satisfactory. We define T_K as the value of T where the conductance is divided by a factor 2 i.e. $G(T = T_K) = G_0/2$, with $G_0 = G(T = 50mK)$. Note that this definition is independent of the parameter s. The value extracted this way is consistent with the width of the zero-bias conductance peak as a function of bias voltage V_{SD}.

Determination of the charging energy and coupling constant

From the size of Coulombs diamonds, we can determine the charging energy of diamonds with odd electronic occupancies (N=1 and N=3). First, the lever arm α between V_g and the energy ϵ_d (see fig.6.7) are extracted from the ratio between the height and width of N=2 diamonds. Then, measuring the width $\Delta V_{g(1,3)}$ of N=1 and N=3 diamonds, and knowing that $U_{1,2} = \alpha \Delta V_{g(1,3)}$ we

obtain: $U_1 = 3.9meV$ and $U_3 = 4meV$ for diamonds with Kondo ridges A and B respectively.

To confirm this value of the charging energy and extract the coupling constant, the Kondo temperature T_K can be well approximated by the expression predicted by the Bethe Ansatz [57, 58]:

$$T_K = \sqrt{U\Gamma/2}\exp\left[-\frac{\pi}{8U\Gamma}|4\epsilon^2 - U^2|\right] \tag{6.23}$$

where ϵ is the energy shift measured from the center of the Kondo ridge. The gate dependence of the Kondo temperature (fig. 6.9.b) is then extracted from the evolution versus gate of the width of the zero-bias peak. By fitting these data by formula 6.23, we can then extract the parameters of the quantum dot. The charging energy agrees with the one extracted from the stability diagram.

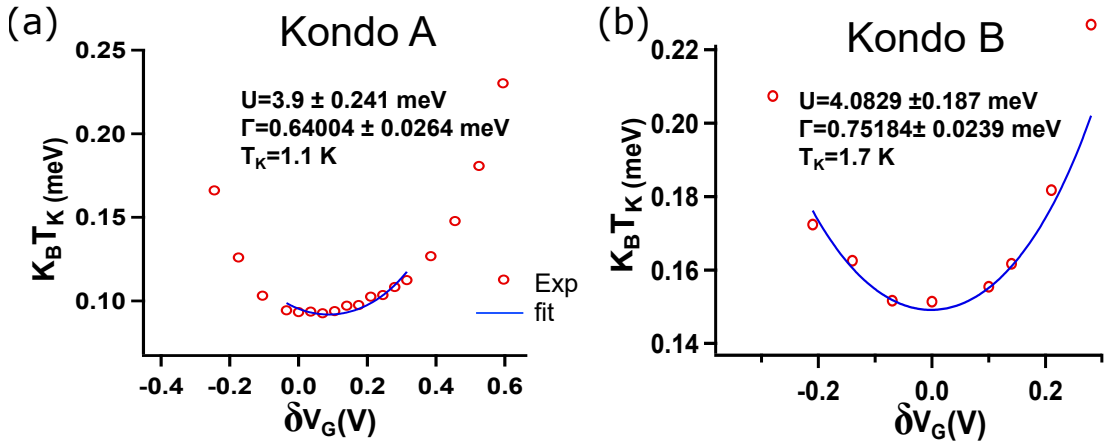

Figure 6.9: Gate dependence of the Kondo temperature extracted from the evolution of the width of the zero-bias conductance peak for Kondo ridges A and B. The parameter extracted from the fit is shown in the legend of the figure.

The different parameters of the QD, described with the Anderson impurity model, are extracted for the Kondo ridges A and B are summarized in Table 6.2). The charging energy U is deduced from the size of the Coulomb diamond, the coupling to the reservoirs $\Gamma = \Gamma_L + \Gamma_R$ from the gate dependence of the Kondo temperature, and the asymmetry $a = \Gamma_L/\Gamma_R$ of the contact from the value of the conductance at the particle-hole symmetry point. Since $\Gamma_R/\Gamma_L \neq 1$, the contacts are not fully symmetric.

	T_K(K)	T_K(μeV)	U (meV)	Γ(meV)	a	Δ(meV)	T_K/Δ
Kondo A	1.1	97.9	3.9	0.62	3.3	0.05	1.958
Kondo B	1.7	146.5	4	0.75	2.5	0.05	2.93

Table 6.2: Parameters of the carbon nanotube quantum dot on the Kondo regions A and B.

Calculating the ratio T_K/Δ, we find that it is always higher than one ($T_K/\Delta > 1.9$ for Kondo ridge A and > 2.9 for region B). This means that the Kondo effect is strong enough to screen

the magnetic impurity of the QD. Thus, the QD Q should stay in the singlet state, leading to a 0-junction behavior. This is confirmed by NRG calculation (see section 6.5).

6.4 Superconducting state

By switching off the magnetic field, the electrodes become superconducting. In what follows we will present first the extraction of the supercurrent using the resistive and capacitively shunted junction (RCSJ) model. Then the measurement of the differential conductance dI/dV_{SD} as a function of the bias voltage and the gate voltage in the superconducting state. Finally, I will present the AC emission measurement.

6.4.1 DC supercurrent

The supercurrent branch is more reliably measured in a current bias scheme where the differential resistance dV/dI is measured as a function of bias current I_{SD} and gate voltage V_G. We now current bias the device to obtain the value of the critical current. We simultaneously use AC and DC bias while measuring the resulting voltage drop across the CNT. From the AC part, we obtain data on the differential resistance.

The color plot shown in fig.6.10.a represents the differential resistance of the sample as a function of the bias current. In part b of the figure are represented vertical cuts of the color plot at three gates voltages in the three different regions, from which the critical current will be extracted.

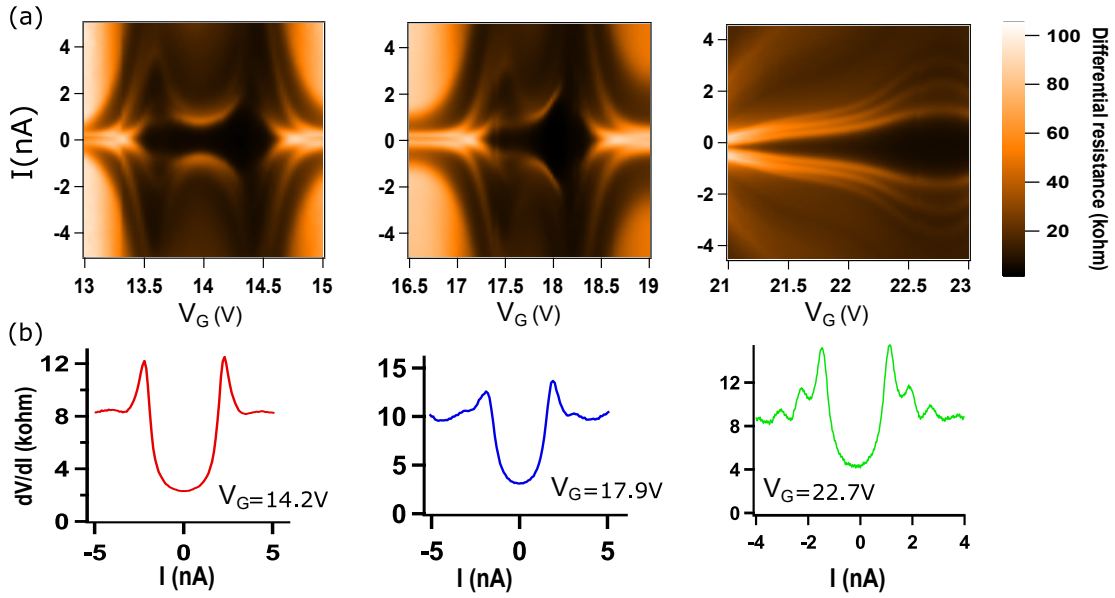

Figure 6.10: (a) Differential resistance of the CNT as a function of the biasing current, in the same region of gate voltage as fig.6.7. (b) Vertical cuts of the color plot at three gate voltages.

By numerical integration of the color plots, we get I-V curves that show a supercurrent branch and a smooth transition to a resistive branch with higher resistance. The transition between the two regimes is not hysteretic, and the supercurrent part exhibits a nonzero resistance R_S at low bias even. This behavior is common in mesoscopic Josephson junctions that have a high normal state resistance of the order of the resistance quantum h/e^2.

When a Josephson junction is current biased, currents smaller than the critical current I_c can flows as supercurrent across the junction. Supercurrent is described in terms of the Josephson equation:

$$I_J = I_c \sin(\varphi) \tag{6.24}$$

However, at finite voltages, a quasi-particle current $I_q(V)$ also flows across the Josephson junction. At not too large voltages the $I_q(V)$ is treated in terms of an ohmic resistance R

$$I_q = \frac{V}{R} \tag{6.25}$$

In general, a Josephson junction has a finite capacitance C. This result a displacement current I_d across the junction due to its capacitance given by:

$$I_d = C\frac{dV}{dt} \tag{6.26}$$

The total current I across the junction is the sum of the Josephson current I_J, the quasiparticle current I_q, and the displacement current I_d

$$I = I_J + J_q + I_d = I_c \sin(\varphi) + \frac{V}{R} + C\frac{dV}{dt} \tag{6.27}$$

Thus, a Josephson junction can be modeled by means of a parallel connection of an ohmic resistance R, a capacitor, and the Josephson element as shown in fig.6.11. Because of this circuit the model is referred to resistive and capacitively shunted junction (RCSJ) model.

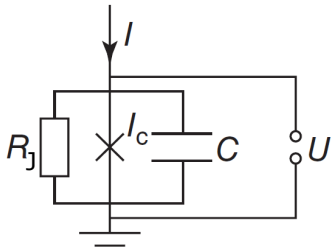

Figure 6.11: Equivalent circuit of a Josephson junction according to the RCSJ model. The Josephson element is indicated by a cross.

Due to the effect of the electromagnetic environment, the supercurrent gives rise to a dissipative branch close to zero bias voltage. In order to extract more reliably the supercurrent of our device, we

use the (RCSJ) model [117, 118]. This model includes the effect of the dissipative electromagnetic environment.

The input parameters are the value of the external resistor R and temperature T. The critical current I_c and the junction resistance R_J can then be extracted for every measured gate voltage, from a fit to :

$$I(V_{bias}) = \left\{ I_c Im \left[\frac{I_{1-i\eta}(I_c\hbar/2ek_BT)}{I_{-i\eta}(I_c\hbar/2ek_BT)} \right] + \frac{V_{bias}}{R_j} \right\} \frac{R_j}{R_j + R} \tag{6.28}$$

where $\eta = \hbar V_{bias}/2eRk_BT$ and $I_\alpha(x)$ is the modified Bessel function of complex order α [118]. The value of the critical current and the junction conductance $1/R_J$ are plotted on fig.6.12. The parameters used for the fit are $R = 0.9\text{k}\Omega$ and $T = 100\text{mK}$.

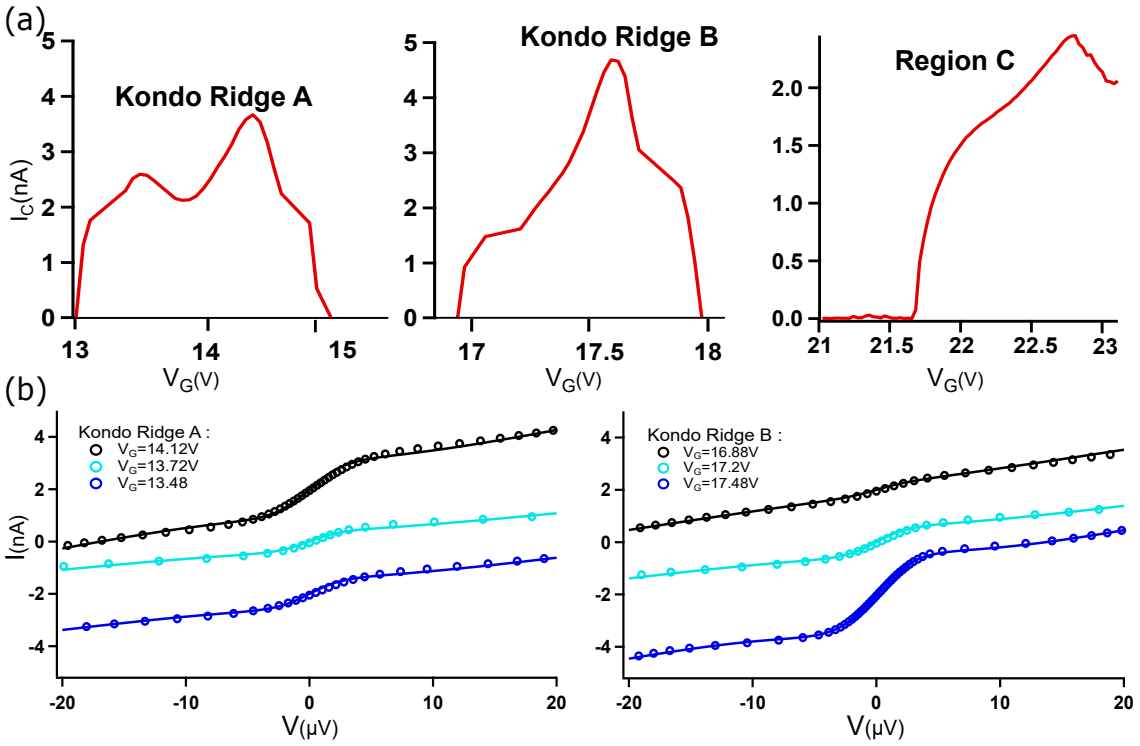

Figure 6.12: (a) Gate dependence of the extracted critical current for Kondo ridge A and B and regions C. The parameters of the fit are $R = 0.9\text{k}\Omega$ and $T = 100\text{mK}$. (b) Data and theoretical curves fitted with eq.6.28 for three gate voltages of the Kondo ridge A (left) and the Kondo ridge B (right).

The fact that the supercurrent in the Kondo regions A and B remains relatively large is a good indicator that the QD stays in the singlet state, leading to a 0-junction behavior. This is expected from the ratio T_K/Δ, which is always higher than one for both Kondo ridges.

6.4.2 Differential conductance in the superconducting state

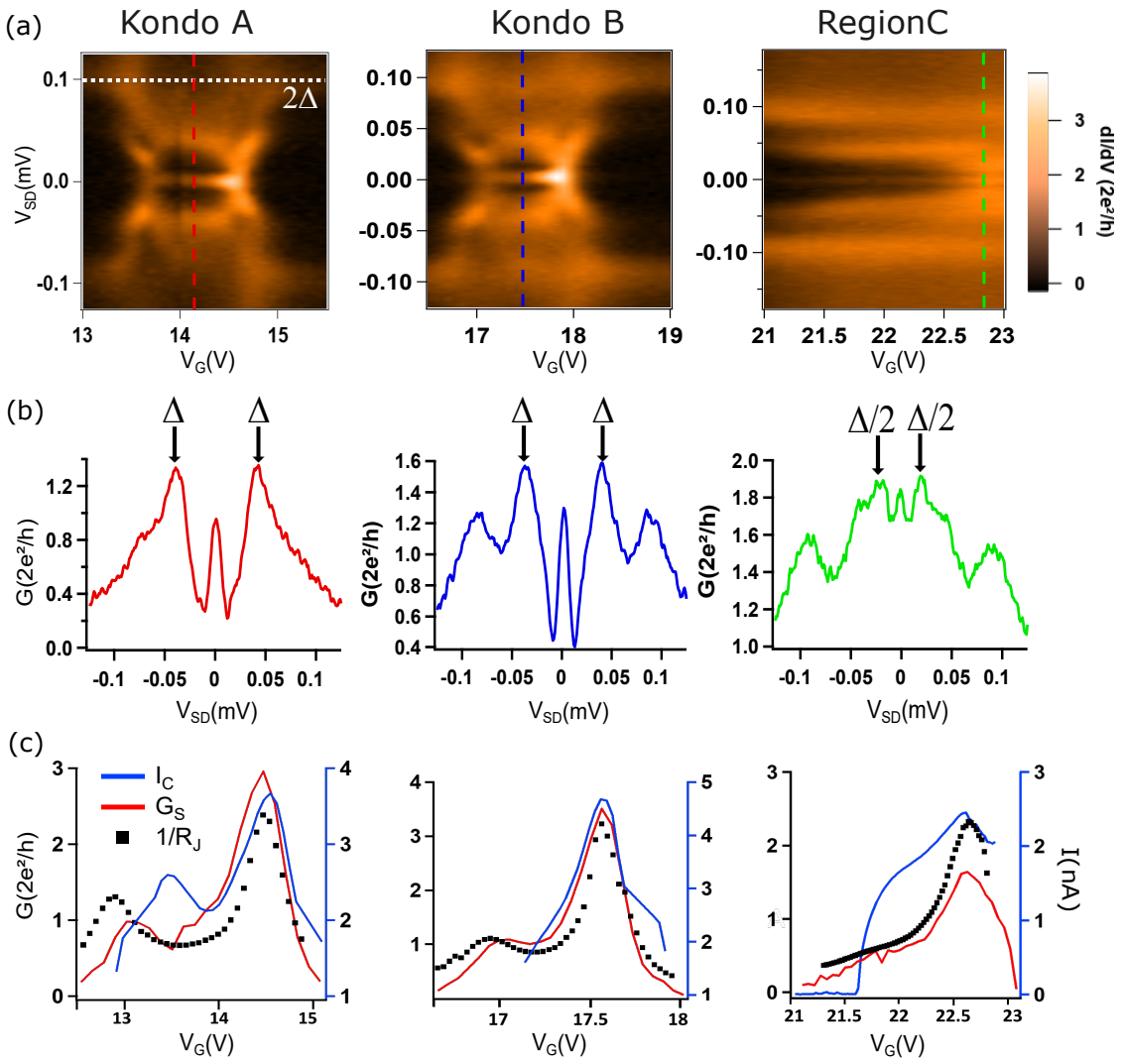

Figure 6.13: (a) Differential conductance dI/dV as a function of bias voltage V_{SD} and gate voltage V_G for Kondo A and B and region C. (b) Vertical cuts of the three color plots given above at the gate voltages indicated by the dashed color lines. (c) Gate dependence of the critical current I_C, the inverse of the resistance R_J extracted from the RCSJ model, and the conductance in the superconducting state G_s (Horizontal cut at $V_{SD} = 0$ of color plot in (a)). $1/R_J$ and G_S, exhibit very similar values and behavior.

Figure.6.13.a shows the differential conductance dI/dV as a function of the bias voltage and the gate voltage in the superconducting state. The horizontal lines around $V_{SD} = \pm 0.1$mV corresponds to the superconducting gap of 2Δ due to the onset of quasiparticle tunneling between source and drain electrodes, leading to $\Delta = 50\mu$eV. A zero-bias peak of conductance in regions of high normal state conductance of (fig.6.7) is observed due to the supercurrent branch enhanced by the Kondo effect for zone A and B. Out of the zero bias, one also sees traces (conductance bumps) of the multiple Andreev reflections (MAR) processes at fixed voltages $2\Delta/n$ with $n = \pm 1, \pm 2, \pm 3$,....We can notice that the 3 regions A, B, and C exhibit a gate modulated supercurrent and a conductance, $1/R_J$, which is quite close to the experimentally measured dI/dV.

6.4.3 AC Josephson emission measurement

We now present the measurement of AC Josephson emission. In order to measure all the frequencies available (ν_0,ν_1,ν_2 etc.), we bias the detector to a voltage V_d below the gap (emission sensitive region of the detector) such that 2Δ-h$\nu_0 < eV_d < 2\Delta$, which is kept fixed during a measurement.
When biased by a voltage V_{SD}, the CNT emits a radiation at the frequency ν, given by the Josephson relation $h\nu = 2eV_{SD}$. The SIS detector absorbs the corresponding photons, and this will induce photo-assisted tunneling (PAT) current across it. In our setup, the coupling between the detector and the CNT quantum dot is efficient only at the resonance frequencies of the coupling circuit, which is designed to be 12.5GHz and odd harmonics. Assuming that the current through the CNT junctions oscillates at the Josephson frequency $h\nu = 2eV_{SD}$ with an amplitude I_C^{AC}, the I_{PAT} current through the detector reads, at a detector bias voltage V_D such that $2\Delta - h\nu < V_D < 2\Delta$:

$$I_{PAT} = \frac{1}{(2V_{SD})^2} \frac{(I_C^{AC})^2}{4} |Z_t(2eV_{SD}/h)|^2 I_{qp}^0(V_D + 2V_{SD}) \tag{6.29}$$

with $I_{qp}^0(V_D)$ the IV characteristic of the detector without irradiation and $Z_t(\nu)$ the impedance of the resonant coupling circuit at frequency ν. Consequently, the PAT current is sizeable only when the Josephson frequency matches one of the resonances frequencies of the coupling circuit. Experimentally the value of I_{PAT} is measured which allows us to extract the value of I_C^{AC} using equation 6.29.

We simultaneously measured the differential conductance of the CNT Josephson junction and the PAT current through the detector. We measure the derivative of the photo-assisted tunneling current (PAT) through the detector as a function of the gate V_G and bias voltage V_{SD} of the CNT quantum dot. The color plot of dI_{PAT}/dV_{SD} is represented in fig.6.14.a. By integrating this quantity with respect to V_{SD}, we obtain the photo-assisted tunneling current across the detector. The color plot of PAT current in the three interesting regions is shown in fig.6.14.b. Two peaks of photo-assisted tunneling current are observed at $\pm V_{SD}$ =22.4μeV. This value corresponds to Josephson frequencies ν_J =12 GHz. The signal at other harmonics frequency of the resonator is too small to be observed. This could be because at higher harmonics the frequency is greater than Δ(for ν=31GHz,$eV = 65\mu eV \gg \Delta = 50\mu eV$). Note that it has been possible to measure it for the Pd/Nb/Al sample (see section 6.4.3) with $\Delta = 150\mu eV$. For region C, the photo-assisted tunneling peaks appear for all gate voltage, however, for Kondo ridges A and B no emission was detected close to the particle-hole symmetry point. To understand the reason behind that, we will extract the value of the PAT current more accurately and compare it to the DC current.

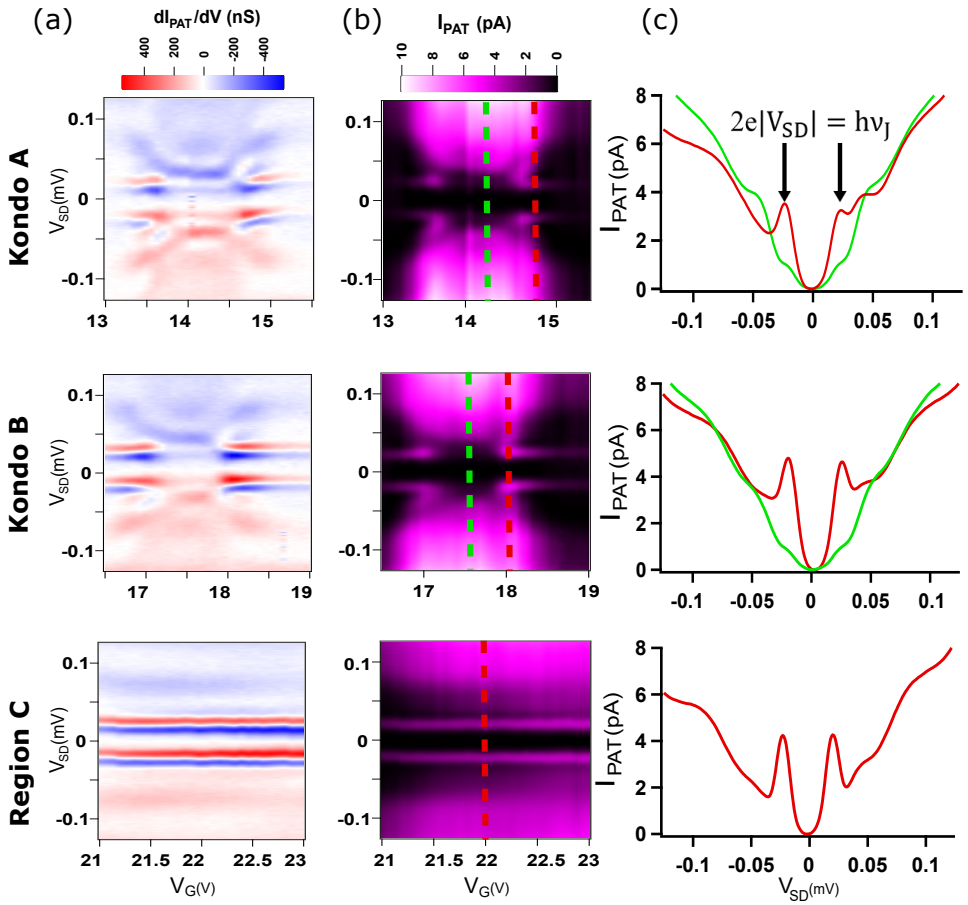

Figure 6.14: (a) Derivative of the photo-assisted tunneling current. (b) Quantity represented on (a) integrated over V_{SD}, yielding $I_{PAT}(V_{SD}, V_g)$. (c) Vertical cuts of the I_{PAT} color plot at the gate voltages indicated by the dashed color lines, two photo-assisted tunneling peaks at $V_{SD} = \pm 22.4 \mu eV$ is observed.

The Josephson emission is extracted from the amplitude of the PAT current through the detector as a function of the gate V_g and bias voltage V_{SD} of the CNT quantum dot. The emission of the carbon nanotube junction has two contributions. The first one is the AC Josephson effect of the CNT junction, at the Josephson frequency given by $h\nu = 2eV_{SD}$ and depending on the anharmonicity of the current-phase relation some harmonics. The second contribution is the shot-noise associated with MAR processes and quasiparticle tunneling. In the PAT response, we did not detect any signature of harmonics in the AC Josephson effect. Consequently, we separate the two processes by attributing the peak at the Josephson frequency to the AC Josephson effect and the remaining baseline to the shot-noise. This baseline is calculated by fitting the data away from the Josephson peak with a polynomial (Fig. 6.15.a). This allows to separate the contribution of the AC Josephson effect (fig.6.15.b) from the shot-noise (fig.6.15.c).

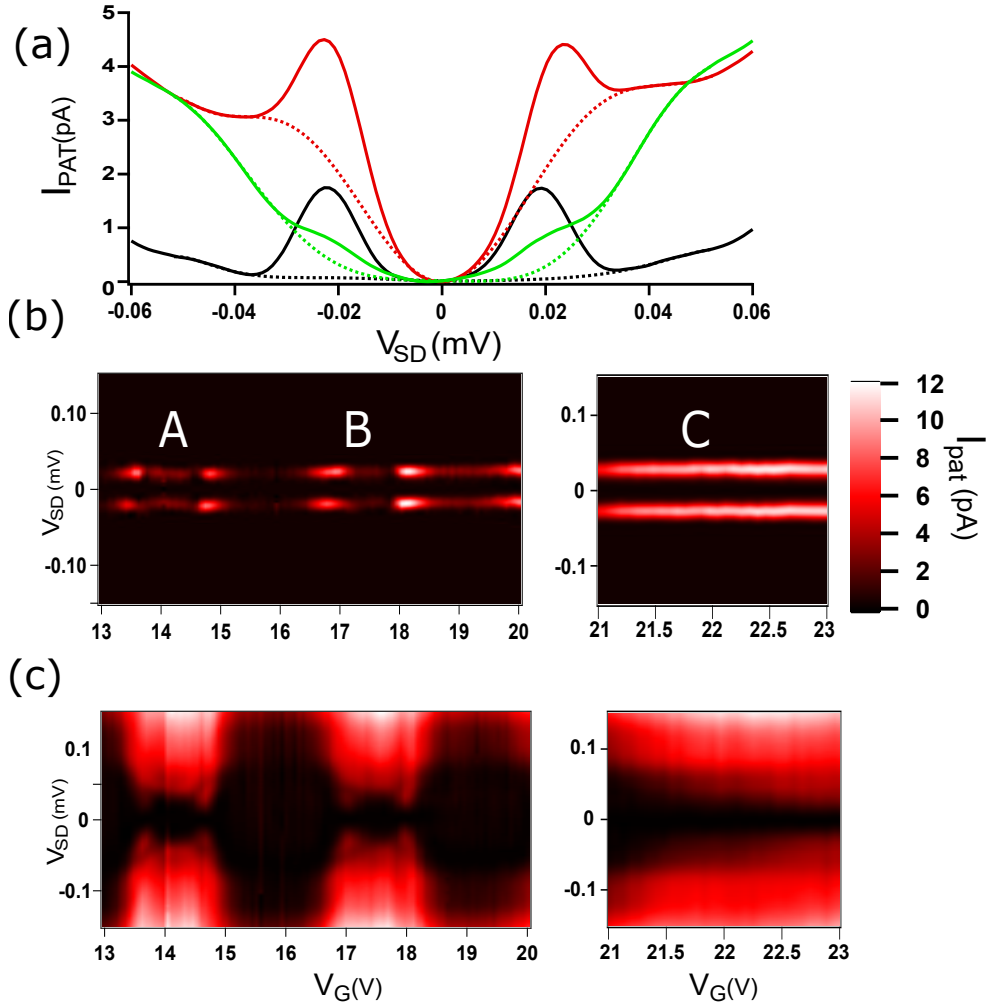

Figure 6.15: Extraction procedure of the AC Josephson emission. (a) The PAT signal of 6.14.b is separated in a baseline and a peak at the Josephson frequency. The baseline is obtained by fitting the data away from the Josephson peak with a polynomial. (b) Extracted PAT current related to the AC Josephson effect. It corresponds to the PAT current with the baseline subtracted for the region of interest. (c) Extracted PAT current corresponding to the MAR process is the same region as b. It corresponds to the baseline obtained by the procedure described in a.

Data for the Pd/Nb/Al sample

We show in this part the data on the CNT sample with Pd/Nb/Al measured during the thesis of Raphaëlle Delagrange [60].

In this CNT sample, the contacts are 400 nm apart and made of Pd(8nm)/Nb(11nm)/Al(50nm)

trilayer with an effective gap $\Delta = 150\mu eV$, higher than the one of the Pd/Al sample. For the Pd/Al/Nb contact one must apply a magnetic field of more than 1T to suppress superconductivity in the contacts. This strongly affects the Kondo resonance and thus prevents a reliable extraction of all the parameters of the dots.

In figure.6.16 we show the differential conductance of the CNT quantum dot with a 1T magnetic field applied, with two Kondo ridges D and E. The superconducting gap of the trilayer Pd/Al/Nb is higher than the one of the bilayers Pd/Al. This allows the detection of the Josephson emission at the first and third resonance frequency of the coupling circuit, i.e. 11GHz and 31GHz. As shown in fig.6.17 the photo-assisted tunneling current exhibits four peaks, symmetric in V_{SD}. They are centered around $V_{SD} = \pm 22\mu eV$ and $V_{SD} = \pm 64\mu eV$. These values correspond to Josephson frequencies $\nu_J = 11GHz$ and $\nu_J = 31GHz$.

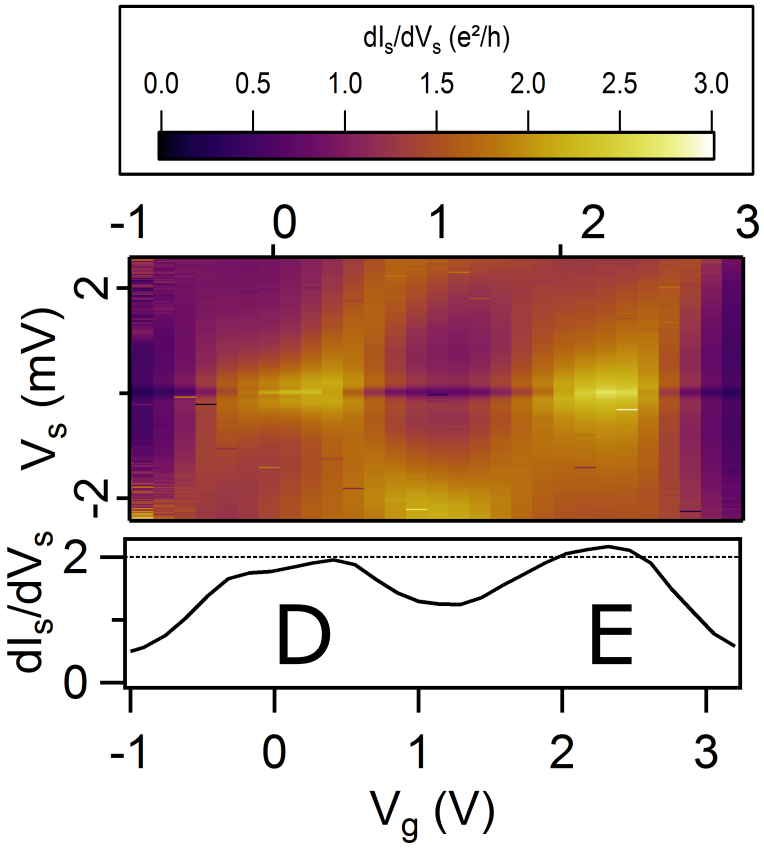

Figure 6.16: Differential conductance of Pd/Nb/Al sample in presence of a 1T magnetic field as a function of the bias and gate voltages. Horizontal cuts of these color plots are given for $V_s \approx -0.3$ mV, outside from the superconducting dip. Taken from [60].

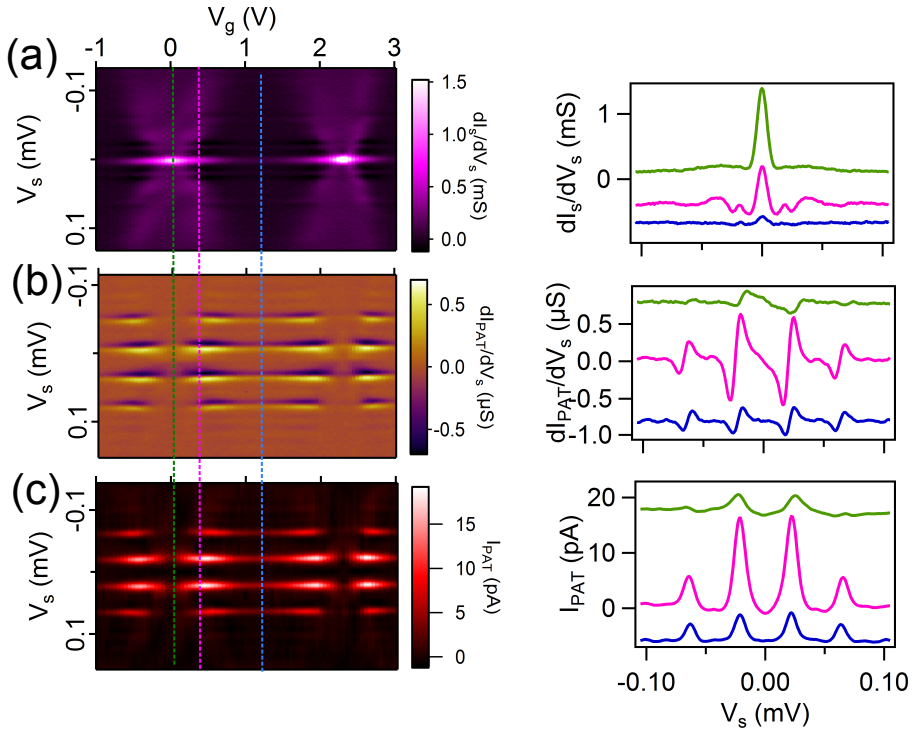

Figure 6.17: Measurement of S-NbAl sample. (a) Differential conductance of the CNT as a function of its bias voltage Vs in the superconducting state in the gate voltage region investigated above. (b) The derivative of the photo-assisted tunneling current. (c) Quantity represented on (b) integrated over Vs, yielding I_{PAT}(Vs, Vg). Vertical cuts of the three-color plots are given on the right at the gate voltages indicated by the dashed color lines. Taken from [60].

Data for the Pd/Al sample

In figure 6.18 we plot the amplitude of the dynamical critical current I_C^{AC} extracted using formula 6.13 from the peak in the PAT current for the Pd/Al sample. The main result of these measurements is that the dynamical critical current follows nicely the critical current I_C for the reference region C. However there is a strong reduction of I_C^{AC} close to the center of the Kondo region A and B, in a region where the critical current I_C is enhanced thanks to Kondo correlations. Using the same procedure as the one described for the Pd/Al samples, the critical current and the AC Josephson emission of Kondo ridges D and E of the Pd/Nb/A l are compared and exhibit the same qualitative behavior.

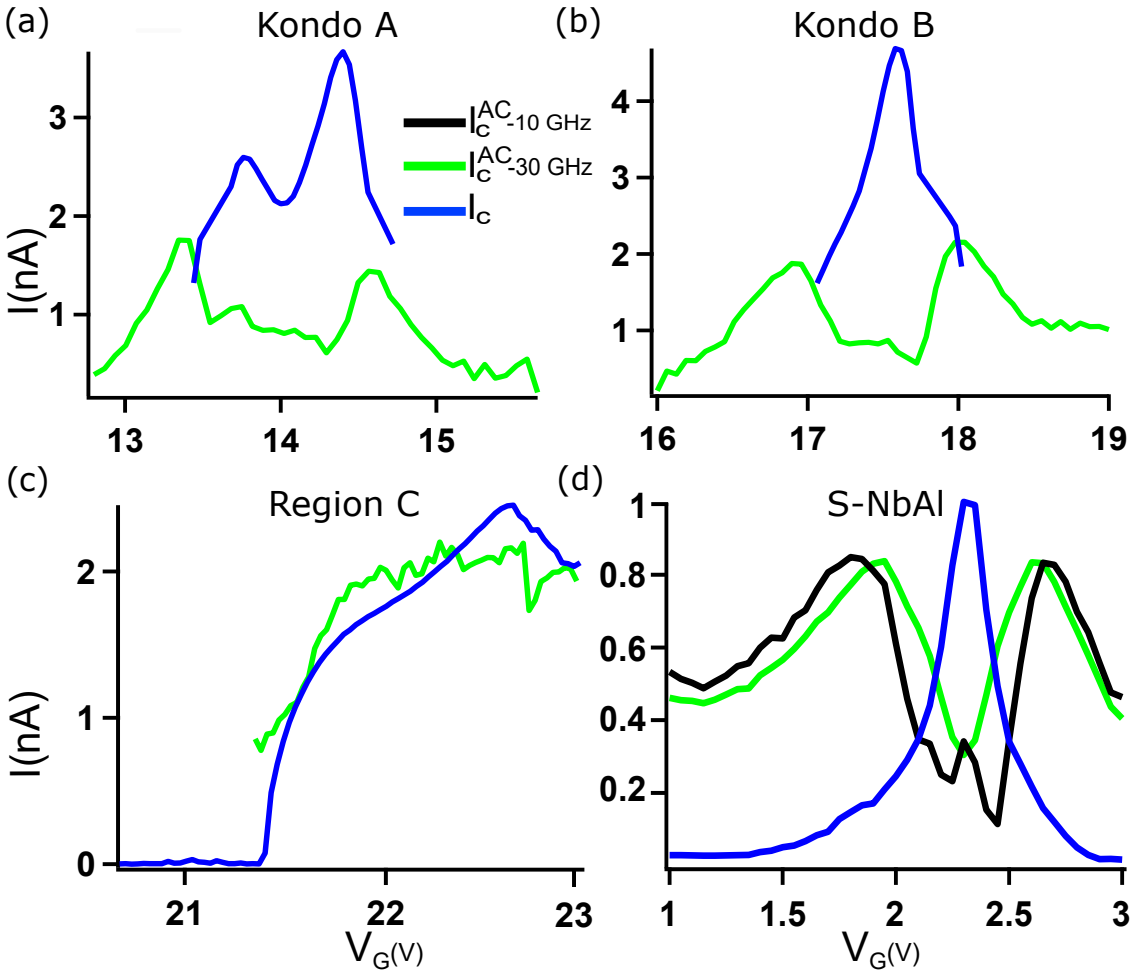

Figure 6.18: Comparison of the critical current I_C and the AC critical current I_C^{AC} (extracted from eq.6.13) for (a) Kondo A. (b) Kondo B. (c) Region C. (b) Same comparison for the sample with Pd/Nb/Al contact S-NbAl where two harmonics at 10 and 30 GHz were detected.

6.4.4 Possible Interpretations

The collapse of the AC Josephson emission in Kondo regions A and B suggests that the nanotube Josephson junction behaves like a π-junction, instead of the 0-junction expected from the DC critical current measurement. One may think about different scenarios.

An effect of decoherence?

The first one is the effect of decoherence. Indeed due to the finite bias V_{SD} applied on the junction, one may consider the voltage-induced spin relaxation [116, 119, 120, 121, 122], which is a dominant decoherence process when $eV_{SD}/k_BT_K \geq 1$. In the present experiment, at the resonance frequency,

one has $eV_{SD}/k_BT_K = 0.28$ for Kondo ridge A and 0.17 for ridge B, so that this effect should be small [123].

What about the dynamics of the Kondo effect?

Dynamical effects can also affect AC emission. Indeed, it has been shown that there is a frequency cut-off, of the order of k_BT_K/h, in the high frequency emission of a quantum dot in the normal state [123]. However, in the present experiment, the ratio of $h\nu/k_BT_K$ is always smaller than one (0.526 for Kondo ridge A and 0.34 for ridge B).

6.5 Numerical renormalization group calculation

To get a more quantitative understanding of the behavior of the quantum dot in region A and B we have performed numerical renormalization group (NRG) calculation [124, 125] of the Andreev bound state spectrum and supercurrent of the ground state using the parameters determined in the normal state (table 6.2). The NRG calculations were done in collaboration with Tomáš Novotný and Alžběta Kadlecová (University of Prague, Czech Republic).

6.5.1 Calculation of the Andreev spectrum of CNT QD

The NRG calculation gives the many-body state spectrum of our junction at the particle-hole symmetry point $\epsilon = 0$ (see fig.6.19.a), where the energy of the ground state is considered a reference state at zero energy, the solid line represent the first excited doublet state, which is detached from the continuum due to electron-electron interaction. The dashed line represents the first excited singlet state, which is overlapping with the continuum at $E_A = \Delta$. Note that, due to technical reasons, the NRG calculation does not give the energy of the singlet state for values higher than the gap Δ. The NRG calculation confirms that the ground state of the system is always the singlet state. This leads to a supercurrent in the nanoampere range as shown in fig.6.19.b, consistent with the experiment, with the phase behavior of a "0-junction". NRG calculation allows us also to evaluate the evolution of the detachment of the ABS from the continuum at $\varphi = 0$ for the first excited doublet state only, and the value of the ABS at $\varphi = \pi$ for both the first excited doublet and singlet state (see fig.6.20).

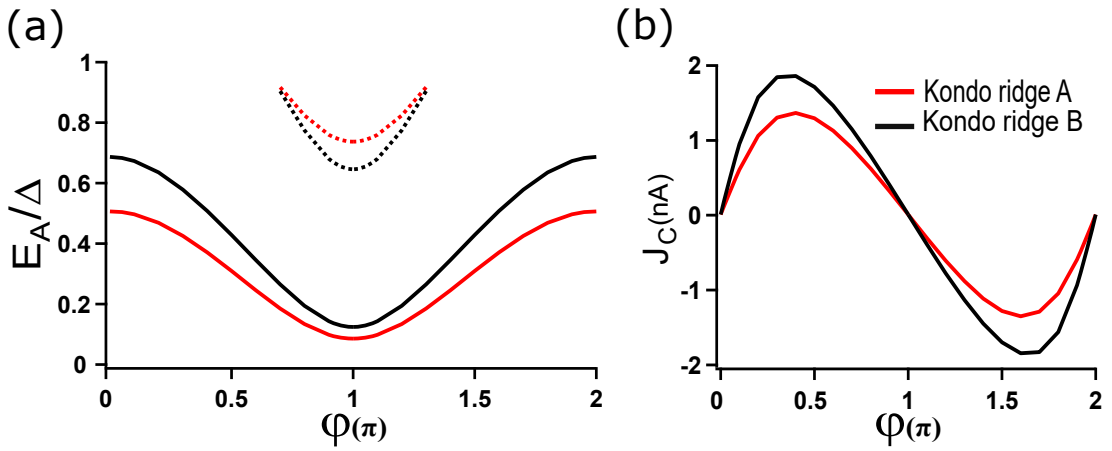

Figure 6.19: NRG calculation. (a) Andreev bound state spectrum (b) Supercurrent amplitude as a function of the superconducting phase difference φ at the particle-hole symmetry point obtained by NRG calculation with the parameters of the Kondo ridge A and B.

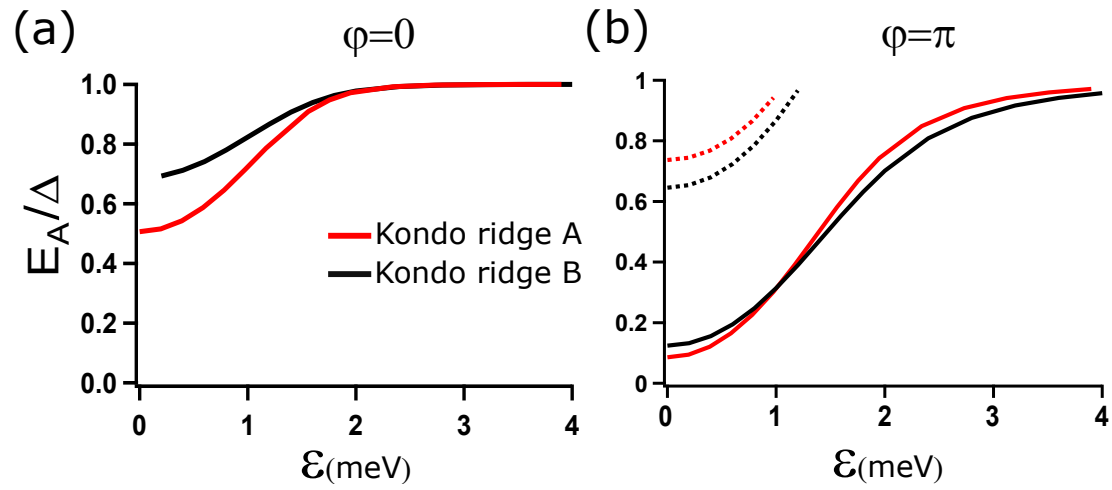

Figure 6.20: (a) NRG calculation of the ABS energy at $\varphi = 0$ for the first excited doublet state as a function of the energy level of the QD ϵ for the Kondo ridge A and B. This measures the detachment of the ABS from the continuum of excitation. (b) Same quantity at $\varphi = \pi$. Data for both first excited doublet and singlet state are presented.

6.5.2 Calculation of the current of singlet state and doublet state

The amplitude of the supercurrent of the singlet ground state is given by the NRG calculation. The amplitude of the doublet state can then be deduced from this latter value and the phase dependence

of the ABS. The idea is to calculate the ABS spectrum and the current of singlet state J_S as a function of φ for different values of ϵ such that $-U/2 < \epsilon < U/2$. Fig.6.21.a,b shows the ABS spectrum and the current of the singlet state at $\epsilon = 0$meV. The set of curves of $J_S(\varphi)$ allows us to plot J_S as a function of ϵ (Blue curve of fig.6.21.c). Then J_D is calculated using the following expression:

$$J_D = J_S + \frac{2e}{\hbar}\frac{\partial E_A}{\partial \varphi} \tag{6.30}$$

This calculation is done at each value of ϵ, the result is shown in fig.6.21.c (orange curve). Comparing J_S and J_D shows that the amplitude of the current in the doublet state is reduced compared to the singlet state, and the sign changes.

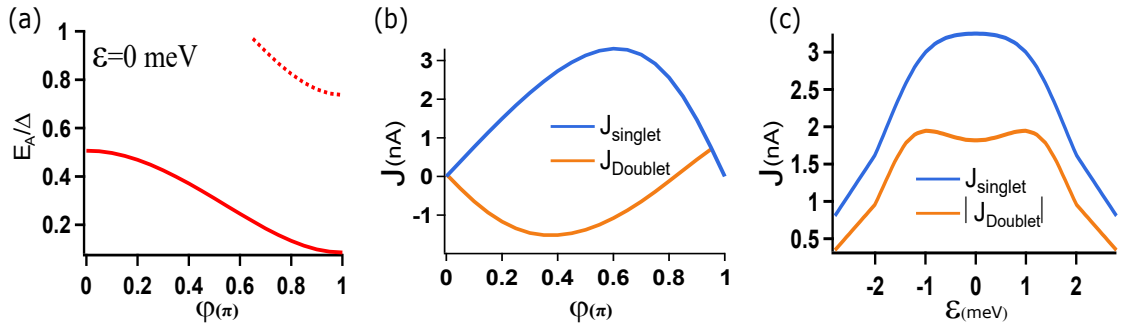

Figure 6.21: NRG calculation of at $\epsilon = 0$ meV (a) ABS spectrum and (b) Supercurrent of the singlet state and the doublet state at $\epsilon = 0$meV as a function of φ for Kondo ridge A, calculated using Eq.6.30(d) Calculated amplitude of the first harmonics of the current phase relation for zone A in the singlet and doublet state. Note that what is plotted is the absolute value of J_D.

6.6 Landau-Zener tunneling

The collapse of the AC emission corresponds to Kondo enhanced high critical current. For symmetric contacts, the Kondo effect opens a nearly perfectly transmitted channel (T≈1). The doublet Andreev bound states are very low in energy at $\varphi = \pi$. In this case, one may think about the transition to an excited level due to Landau Zener because of the phase evolution. This is what happens for a quantum channel junction with high transparencies [128] and involves a transition between singlet states, due to parity constrain [129]. Compared to a quantum channel with the same transmission in the normal state, a quantum dot Josephson junction, in the range of parameters explored here, has an excited singlet state with slightly higher energy and a doublet state detached from the continuum and with a decreased energy especially at phase $\varphi = \pi$ (see Fig.6.22).

Knowing the shape of the ABS one can calculate the value of the Landau Zener tunneling probability to the excited singlet state using the formula :

$$P_{LZ} = \exp\left[-\frac{\pi}{2}\frac{E_g^2}{eVD}\right] \tag{6.31}$$

with E_g the minimal value of the ABS, i.e. the ABS at phase value π and D the maximal value

of the ABS, i.e. its value at phase value equals 0. V is the applied voltage, which determined the phase evolution through the Josephson relation $d\varphi/dt = 2eV/\hbar$ [130].

For a quantum channel $E_g = 2\Delta\sqrt{1-T}$ and $D = 2\Delta$. With a conductance of 0.71 in unit of $2e^2/h$ this leads to $E_g = 1.07\Delta$ and $P_{LZ} = 0.16$. For the QD Josephson junction of similar conductance in the normal state, the NRG calculation, at the particle-hole symmetry point, gives $E_g = 0.74\Delta$ so that $P_{LZ} = 0.42$. This value is not extremely small but it does not change a lot when one goes away from the particle symmetry point. Hence at ϵ=1 meV, where we see in the experiment that the dynamical supercurrent increases, this Landau Zener probability is 0.24. Thus, the Landau-Zener tunneling mechanisms are not suitable to explain our experimental observation.

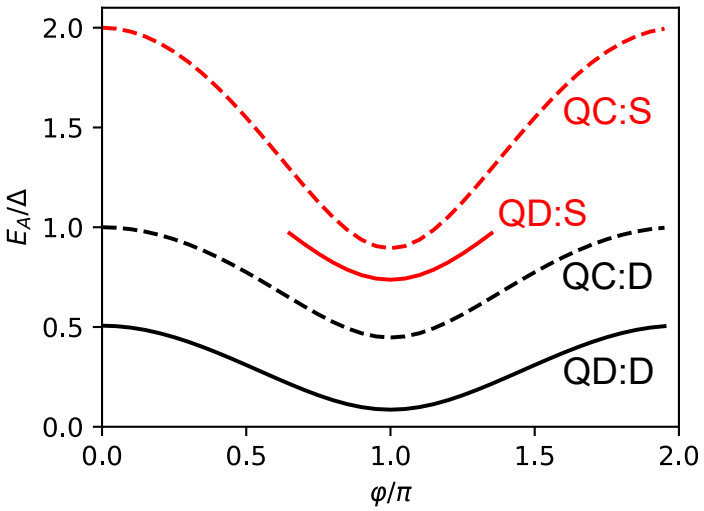

Figure 6.22: Comparison of the many-body spectrum for Kondo ridge A at the particle-hole symmetry point and a quantum channel with the same transmission in the normal state, as a the function of the phase difference φ. The energy difference between the singlet ground state and the spin degenerate doublet state is denoted in black, with a solid line and a legend QD:D for the quantum dot and a dashed line and a legend QC:D for the quantum channel. The energy difference between the singlet ground state and the excited singlet state is denoted in red, with a solid line and a legend QD:S for the quantum dot and a dashed line and a legend QC:S for the quantum channel.

6.7 A renormalized-quantum-point-contact-based prediction

Quantum dots in the Kondo regime have been sometimes treated like a single quantum channel [141, 142]. The idea is that Coulomb interaction U causes a renormalization of parameters (ABS energies, transmission), but does not produce qualitative differences. Of course, this only holds as long as the junction remains in the zero phase in the entire range of the superconducting phase difference φ, as is the case in our study. This section intends to show that even this crude approximation, which amounts to neglecting vertex corrections in the diagrammatic approach, predicts a drop in the AC current similar to the measured data.

The full transport theory for a short superconducting quantum channel (or quantum point contact) has been published in the nineteens by Averin and Bardas [128] and Cuevas, Martín-Rodero and Levy Yeyati [131]. These studies feature results for the real and the imaginary part of the first Fourier component I_1 of the AC current for several different values of transmission. We use their results (read off graphically) for applied bias voltage $V = \Delta/2$ to construct the $|I_1(D)|$ dependence, where D is the transmission of the channel. In full analogy to the quantum point contact, we consider the transmission of our setup to be given by the energy of the doublet Andreev bound states at $\varphi{=}\pi$, namely $D(\varepsilon) = 1 - \left(\frac{E_{ABS}(\varepsilon, \varphi{=}\pi)}{\Delta}\right)^2$. We obtain equilibrium values of $E_{ABS}(\varepsilon, \varphi = \pi)$ from the NRG. Results for both A and B Kondo ridges are similar and given in fig.6.23, showing a semi-quantitative agreement between the renormalized-quantum-point-contact based prediction and measured experimental data.

This approach is different from the microscopic considerations about Landau-Zener tunneling in that it is not limited to the adiabatic approximation, as refs. [128, 131] are working with a full numerical solution to the AC emission in the quantum point contact. Indeed, it is questionable whether the bias voltage $V = \Delta/2$ is small enough for ABS energies computed for zero bias to remain meaningful.

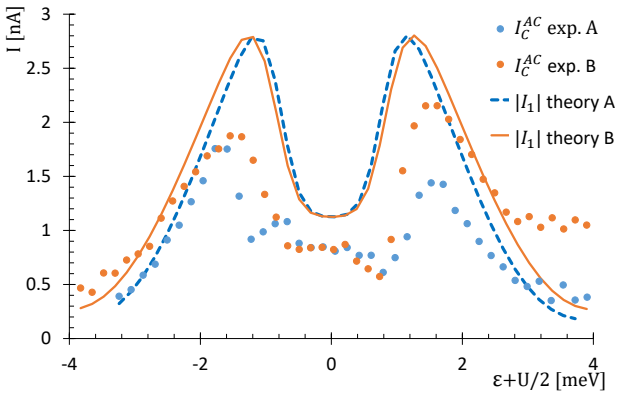

Figure 6.23: Gate dependence of the first Fourier component $|I_1|$ of the AC Josephson current. Bullets represent the experiment lines the theoretical prediction for a single quantum channel with a renormalized transmission. Transmission of the quantum dot has been evaluated from the energy of Andreev bound states at $\varphi = \pi$, obtained by the NRG. The dots represent experimental data for Kondo ridges A and B. The values of $|I_1|$ are based on [128, 131].

Being based on the case of a quantum channel this analysis needs to be taken cautiously in the case of a quantum dot where electron-electron interaction modifies the many-body spectrum. In particular, this analysis does not take into account the detachment of the first ABS from the continuum. Moreover, if one does the same analysis considering only the transition between singlet states, which preserves spin and parity, the effective transmission of the system is lower. This leads to a very small reduction of the dynamical supercurrent, not consistent with the experiment.

6.8 Evaluation of the quasiparticle dynamics in the QD junction

In a superconductor, the density of unpaired electrons (quasiparticles) should decrease exponentially as the temperature is lowered, then vanish when approaching zero temperature [72]. However, it has been shown that at temperatures much lower than the transition temperature T_C, the number of quasiparticles can saturate [132, 133]. In the presence of non-equilibrium quasiparticles, the performance of superconducting devices can be degraded. This has been seen in Single-Cooper-Pair transistors [135, 136] as the parity of the total number of electrons matters. Also, in superconducting qubits [137, 138], as quasiparticle tunneling imposes a sharp limit on the qubit operation time. The trapping of a single quasiparticle in such a superconducting device has been named as "poisoning", as it alters the expected behavior of the ground state of the system.

Chtchelkatchev et al.[139] show that Bogoliubov quasiparticles can be trapped in discrete Andreev levels of a superconducting junction. This trapping should induce an excitation from the even ground state, to an odd excited state, which in turn should manifest itself as a change of supercurrent. The poisoning process can occur by injecting electron form an auxiliary electrode [88] or could happen spontaneously. The first observation and characterization of single quasiparticles trapping in superconducting break junctions have been done by Zgirski et al. [140]. In their experiments, they show that in a superconducting point contacts quasiparticle could be trapped in one of the discrete subgap Andreev bound states. Those trapped quasiparticles are long-lived, with time scales up to hundreds of μs.

To see whether QP poisoning could explain the behavior of the AC Josephson emission seen experimentally, we study the dynamics of quasiparticle (QP) tunneling in the quantum dot. We evaluate here the quasiparticle dynamics, which may lead to the occupation of the doublet state, in the QD Josephson junction. We evaluate the different rates controlling the injection and escape of QP in the dot [143] because of the electromagnetic environment of the junction. This environment is, in the present experiment, constituted by the resonant coupling circuit of impedance Z_{env} and it is assumed to be in equilibrium at a temperature T_{env}, which can be, in general, different from the temperature of the QP in the continuum T_{QP}. T_{env} and T_{QP} can be significantly larger than the base temperature in our experiment ($\sim$ 50 mK) due to incomplete filtering of radiation, for that, we have used $T_{env} = 120mK$ and $T_{QP} = 60mK$. The numerical evaluation of this rate (and every other) for the different processes are illustrated in fig.6.24. The different rates are :

- Γ^a_{out}, the rate for a QP on the Andreev level to escape in the continuum at the energy E after absorbing energy $E - E_A$ from the environment. It reads : $\Gamma^a_{out} = \frac{8\Delta}{h}\int_\Delta^{+\infty} dED(E - E_A)g(E, E_A)f_{BE}(E-E_A)(1-f_{FD}(E))$. In this expression, $D(E)$ is related to the probability $P(E)$ for the environment to exchange the energy E, by $P(E) = D(E)f_{BE}(E)$. $D(E) = Re(Z_{env}(E)/E)/R_Q$, with $R_Q = h/4e^2$ and $f_{BE}(E)$ the Bose-Einstein distribution at energy E and temperature T_{env}. $g(E, E_A)$ is related to the matrix element of the current operator and we approximate it by $g(E, E_A) = \sqrt{(E^2 - \Delta^2)(\Delta^2 - E_A^2)}/[\Delta(E - E_A)]$. $f_{FD}(E)$ is the Fermi-Dirac function, describing the QP in the continuum at a temperature T_{QP}.

- $\Gamma^b_{out} = \frac{8\Delta}{h}\int_\Delta^{+\infty} dED(E + E_A)g(E, -E_A)(1 + f_{BE}(E + E_A))f_{FD}(E)$, the rate for two QP to recombine into a Cooper pair, one QP occupied the Andreev level and the other one was in

the continuum at energy E. The excess of energy $E + E_A$ is emitted in the environment.

- $\Gamma^a_{in} = \frac{8\Delta}{h} \int_{\Delta}^{+\infty} dED(E - E_A)g(E, E_A)(1 + f_{BE}(E - E_A))f_{FD}(E)$, the rate for a particle of energy E to enter the QD and occupy the doublet state, of energy E_A, after exchanging an energy $E - E_A$ with the environment.
- $\Gamma^b_{in} = \frac{8\Delta}{h} \int_{\Delta}^{+\infty} dED(E + E_A)g(E, -E_A)f_{BE}(E + E_A))(1 - f_{FD}(E))$, the rate for breaking a Cooper pair into one QP occupying the Andreev level and another one in the continuum at energy E, after absorbing the energy $E + E_A$ from the environment.

These rates can be evaluated numerically. We then deduce the probability to be in the doublet state $P_D = 2\Gamma_{in}/(3\Gamma_{in} + \Gamma_{out})$ as a function of the position of the Andreev level E_A. The result of the calculation is summarized in fig.6.25.

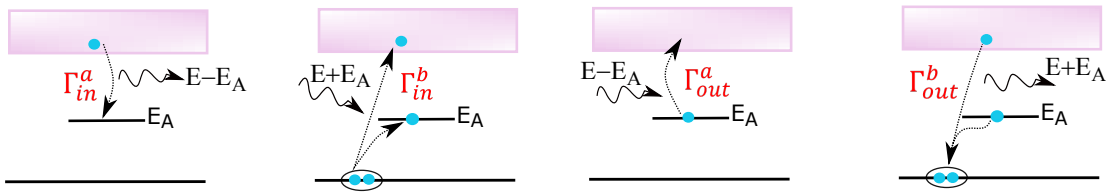

Figure 6.24: The dynamics of trapping and untrapping quasiparticles in the dot as described in the text.

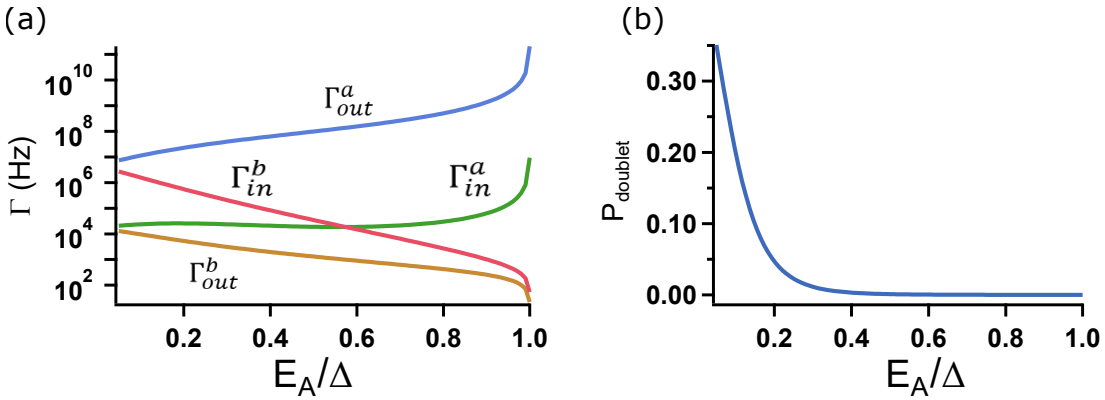

Figure 6.25: (a)Numerical evaluation of the rate of the QP injection and escape in the QD junction with $k_B T_{env} = 0.2\Delta$ and $k_B T_{qp} = 0.1\Delta$. (b) Probability for the junction to be in the doublet state as a function of the energy E_A of the Andreev level.

Figure.6.25.b shows that for the energy of the Andreev level higher than 0.2Δ, the probability for the QD to be in the doublet state is extremely small (below 0.05) in a DC current configuration

with a current biasing changing in the kHz range. However, the situation is very different when we measure the AC emission.

Indeed, due to the applied bias, the injection rate of QP can be significantly higher. Moreover, close to the particle-hole symmetry point, the double state is detached from the continuum due to electron-electron interaction. This keeps the escape rate of quasi-particle relatively low. Consequently, the probability for the QD to be in the doublet state is expected to be higher in a voltage bias situation. This leads to a decrease of I_{AC}^{C} since the critical current of the doublet state is lower than the one of the singlet ground state. Despite a higher gap value, the samples with Pd/Nb/Al contacts exhibit the same phenomenon (fig.6.18). This can be related to the existence of a soft gap for these samples [126], inducing a small but finite QP density at an energy below the gap.

Going away from the electron-hole symmetry point, by changing the value of ϵ, the gap between the doublet state and the continuum of excitation above Δ is reduced significantly (see fig.6.20.b). The probability for the QP present on the dot to escape increases then due to Demkov-Osherov tunneling processes between the doublet state and the continuum due to the phase evolution of the junction [127, 144]. Figure 6.26c represents the probability to escape to the continuum. This data has been derived by using the result of [127]. Note that this latter article was devoted to the topological superconductor. Consequently, the result of this article may need to be adapted to the case of a QD. Concurrently the minimum value of the energy of the doublet ABS, at $\varphi = \pi$, increases. This reduces the rate of QP injection in the QD. These two effects thus restore a high probability for the QD to be in the singlet ground state and increase its effective supercurrent. This is what is measured in the data.

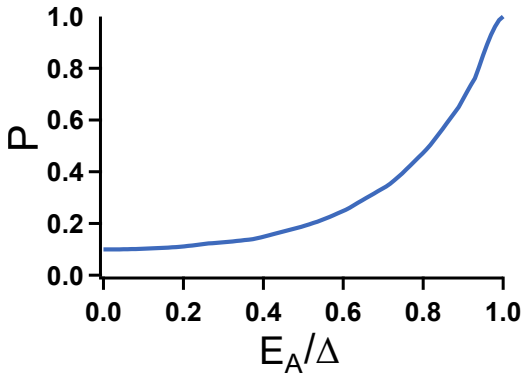

Figure 6.26: Probability for a QP present in the quantum dot to escape after tunneling into the continuum due to Demkov-Osherov tunneling. This curve is calculated at a voltage eV=$\Delta/2$ and use the result derived in reference [127].

From the amplitude of the AC emission measured in the experiment, it is possible to extract the probability P_D to be in the doublet state assuming that the dynamical Josephson current is given by $I_{AC}^{C} = P_D J_D + (1 - P_D) J_S$. J_S and J_D are given in fig.6.21.d.

In the following, we will call coherent, a situation where the QP injection is correlated with the value of the superconducting phase. When this is not the case we deal with an incoherent case. In

an incoherent calculation, only the amplitude of the singlet and doublet supercurrent is considered. With a probability one to be in the doublet state close to the particle-hole symmetry point, one can qualitatively reproduce the reduction of the supercurrent. In a coherent scenario, the sign of the supercurrent (positive for the singlet and negative for the doublet) must be considered. This leads to a quantitative agreement with the data, with a finite probability to be in the doublet state but puts strong constraints on the model used to describe the dynamics of the junction.

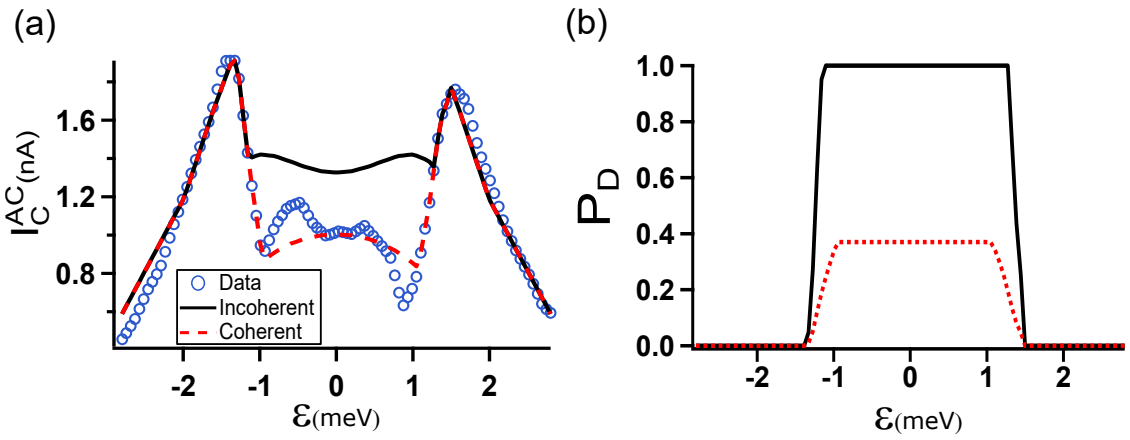

Figure 6.27: (a) Comparison between the data for Kondo ridge A (blue circles) and the calculated amplitude of the AC supercurrent I_C^{AC} introducing a finite probability for the system to be in the doublet state. In the incoherent calculation (black solid line), only the amplitude of the singlet and doublet supercurrent is considered. In the coherent scenario (red dashed line) the sign of this current is also considered. (b) Probability for the system to be in the doublet state in the incoherent (black solid line) and coherent regime (red dashed line).

6.9 Conclusion

In this section, we have measured the dynamics of a carbon nanotube Josephson junction by probing its Josephson emission. We show that this emission is strikingly reduced in the gate region where the critical current is enhanced due to the interplay of the Kondo effect and superconducting proximity effect. Using the NRG technique, we were able to calculate the many-body state spectrum of our system. This helps us to evaluate the probability of the QD to be in a doublet state due to quasiparticle injection. The calculated data reproduces nicely (qualitatively and quantitatively) our experimental data. The measurement of the AC Josephson effect in the Kondo regime shows that it is possible to tune the quantum state of a quantum dot Josephson junction between a spin singlet and doublet state. This 0-π transition can be attributed to the dynamics of quasiparticle in the quantum dot which changes its state, from singlet to doublet. This points towards the importance of considering the electron-electron interaction in the dynamic of a QD Josephson junction.

Chapter 7

On-chip resonant circuit and measurement of electronic temperature

In this chapter, we present two different experiments that aim to improve our detection methods at low temperature.

7.1 High Kinetic Inductance Microwave Resonator Made with Tungsten Nanowires

High kinetic inductance superconducting materials have a growing impact on the superconducting circuits community. Operated in the microwave frequency domain, they allow to engineer high impedance circuits which have been shown to provide an efficient way to increase the lifetime of superconducting quantum bits [145, 146, 147, 148], couple electron charge and spin to microwave photons [149, 150], study the coherent quantum phase slip [151] or generate a high impedance environment in dynamical Coulomb blockade experiments [152, 153].

Until now, these materials consisted of arrays of Josephson junctions, disordered thin films of metallic compounds (NbN, TiN...), granular aluminum, or superconducting semiconductors. Their use in superconducting circuits usually requires a final sharpening step using electron-beam lithography which has so far reduced their range of application. In this experiment, we will show you that it's possible to fabricate very thin (5nm), narrow (35nm) and long (400µm) tungsten (W) nanowire made by helium beam assisted deposition, demonstrating a very high kinetic inductance, 250 times larger than the geometrical one. We fabricated and characterized a hybrid microwave resonator where the inductive part is set by a superconducting tungsten nanowire. Thanks to the large kinetic inductance of the nanowire, the resonator is nonlinear (120 Hz/photon) and exhibits a reasonably high quality factor (4000).

Focused ion beam (FIB) is a recent and powerful multitask micro/nano-fabrication tools. It is

composed of a focused ion beam column and can be equipped with precursor-based gas injection systems (GIS). FIB provides precise and direct write lithography, imaging, deposition, sputtering, chemical analysis of the matter at ultra-high resolution, machining, and manipulation. The two more frequently used ions in a FIB system are gallium ions and helium ions.

Until now, tungsten superconducting nanowires have been deposited using Ga^+ ions in a Focused Ion Beam (FIB) [155, 12, 156] or electrons in an electron scanning microscope (SEM) [154]. However, in this experiment, we will study the properties of W nanowires deposited by a focused helium ion beam from gas field-ion sources [163]. Since He-FIB exhibits a lower proximity effect compared to electron beam this could allow fabricating extremely narrow nanowires with potentially better superconducting properties. When compared to Ga-FIB, He-FIB provides higher resolution, less damage and lower contamination, and no Ga implantation. W nanowires have many potential applications in the field of mesoscopic devices. It has already been used to connect nanoscale samples such as fullerenes [12], graphene [157], mesoscopic metallic samples [158], Bi nanowires [159, 160] or study superconductivity in low dimension [161, 162]. This work has been done in collaboration with Julien Basset, where I was mainly involved in the fabrication process and DC characterization of the tungsten nanowires.

7.1.1 Fabrication

To fabricate the hybrid resonator, first 110 nm of Nb is sputtered on a high resistivity silicon substrate with 500 nm thick thermal oxide. Then optical lithography is performed to define a positive mask on top of Nb, followed by reactive ion etching with SF_6. Two different designs are prepared, a coplanar waveguide (CPW) resonator (fig. 7.1.a-b) and a lumped element resonator (fig. 7.1.d). The W nanowire is then deposited to form a resonator: a long wire grounded on one side and capacitively coupled to a transmission line for the $\lambda/4$ CPW resonator and in parallel with an interdigitated capacitor in the lumped geometry (fig. 7.1.c-d). The W nanowires are deposited using helium beam assisted deposition. The W precursor (tungsten hexacarbonyl $W(CO)_6$) is injected by a gas injection system (GIS) and exposed in the region of interest. Upon interacting with helium ions coming from an ultra-high brightness gas field ionization source (GFIS) that is subjected to a high voltage (30 kV), the ($W(CO)_6$) molecule will be decomposed locally and deposit an almost-pure and thin layer of Tungsten onto the surface. During nano deposition, we use a He-beam current ranging from 10 to 30 pA. The target pressure in the chamber is $4 \cdot 10^{-6}$ Torr. The patterning geometry and parameters are controlled by the nanofabrication system NPVE from Fibics. For the lumped element resonator, a W nanowire of 9.8μm was realized whereas for the CPW $\lambda/4$ resonator a length of 390μm was used. Fabricating such a long nanowire is possible thanks to the very high stability of the He-FIB and He-IBID process compared to previous experiments with Ga-FIB [12]. For more details about the fabrication process and growth condition see [164]

Sample	Current(pA)	Dose	Length(μm)	Thickness (nm)	Width (nm)
NW1	20	0.178nC/μm	5.9	40	50
NW2	20	0.06nC/μm	5.9	5.5	35
NW3	10	3nC/μm^2	5.9	20	70
Resonator "Lumped"	20	0.16nC/μm	9.8	30	35
Resonator "$\lambda/4$"	27	3nC/μm^2	390	12	75
Resonator "*Lumped2* "	27	3nC/μm^2	30	25	80

Sample	Resistance (kΩ)	$R_\square$ (Ω)	ρ ($\mu\Omega$.cm)	$\xi(2K)$ (nm)	$\lambda(0K)$ (nm)
NW1	7.75	65.7	266	6.7	674
NW2	25.15	149.2	80.6	7.6	400
NW3	9.1	108.0	216.0	7	449

Table 7.1: Growth parameters, dimensions, and transport properties of the fabricated W nanowires. With the indicated parameters the time needed to write the W part of the resonator "Lumped" is 88 seconds, whereas for the "$\lambda/4$" type it is 40 minutes.

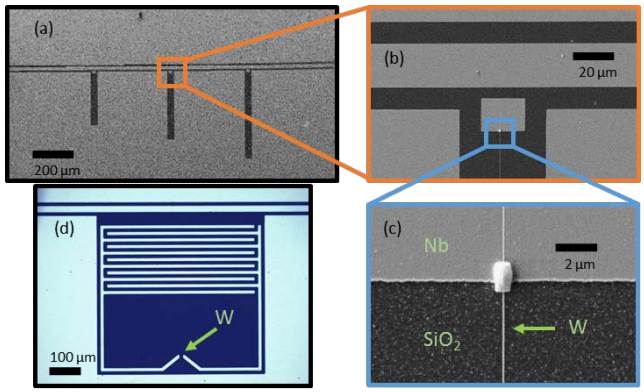

Figure 7.1: (a) SEM image of a CPW sample. The transmission line runs horizontally with three $\lambda/4$ resonators hanging vertically. (b) SEM image of the coupling area between CPW resonator and transmission line. (c) SEM image of a W nanowire connected to Nb with a thick W patch at the junction. (d) Optical microscope picture of the lumped resonator. The arrow points to the nanowire placed horizontally.

7.1.2 DC Characterization of the nanowires

In order to measure the critical temperature T_C, critical magnetic field, and the critical current of the W nanowires, three nanowires (NW1,NW2, and NW3) of 5.9µm length were grown with different growth conditions (See table 7.1) on a sample dedicated to electrical DC measurements. The sample is cooled down to 1.8K in a Physical Property Measurement System (PPMS) from Quantum Design company, where a magnetic field up to 9T can be applied. The resistance measurement was done in a two-probe configuration and a contact resistance was substracted from the raw data.

Fig.7.2 shows the evolution of the differential resistance as function of temperature (fig.7.2.a) and magnetic field (fig.7.2.b) for the three measured nanowires. From 300K, when the temperature is lowered, the resistance increases slightly ($\approx 5\%$) to finally show a superconducting transition around $T_c \in [5-6.5]$K. Then we fix the temperature below the transition point at T=2 K while

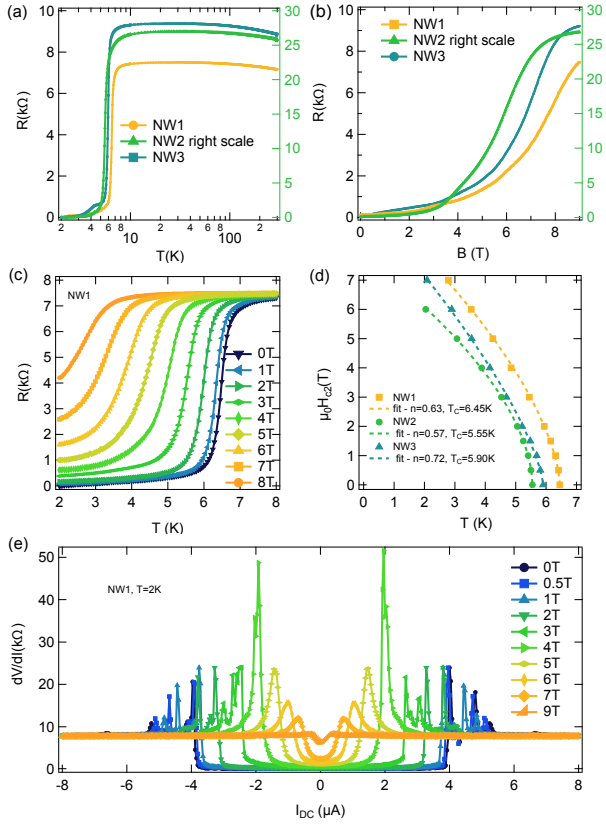

Figure 7.2: (a) Resistance of W nanowires referenced in table 1.1 *vs* temperature T and (b) perpendicular magnetic field B. (c) Resistance of sample NW1 *vs* T for different B. (d) Critical field H_{C2} *vs* T of the wires with the corresponding fit. Fitting parameters are indicated in the legend. (e) Differential resistance *vs* current of sample NW1 for different magnetic fields.

varying the perpendicular magnetic field from 0T to 9T. The nanowires are superconducting with a resistance that develops a magnetic field behavior consistent with a type 2 superconductor. Defining Hc_2 as the magnetic field for which the nanowire recovers half of its normal state resistance, we see that all wires exhibit an H_{c2} larger than 5 T.

Then we study the effect of temperature T on the value of Hc_2. Fig.7.2, shows the temperature dependence of the resistance at different magnetic field only for NW1. The temperature dependence of Hc_2 of the three nanowires is shown in fig.7.2.d, superconducting transitions shifts to lower T with magnetic field. The data can be fitted to a power dependence eq. which is valid close to T_c given by$\sim$:

$$H_{c2}(T) \propto (\frac{1-T}{T_c})^n \tag{7.1}$$

with n is the power index reflecting the dimensionality of the superconductivity. For a purely $2D$ superconductor $n = 1$ is expected for perpendicular magnetic fields and $n = 0.5$ for parallel magnetic

fields. Using eq.7.1 we found that n=0.57, 0.63 and 0.72 for NW2, NW1 and NW3 respectively. Finding an intermediate value of n points towards reduced dimensionality of superconductivity in the W nanowires [165, 166, 167].

To extract the value of critical current I_C, we measured the differential resistance dV/dI as the function of biased current I_{DC}. Fig.7.2.e shows dV/dI for NW1 at $T = 2K$ for different magnetic fields. For NW1, the zero-field critical current is 4.0 μA, and it decreases with the increase of the magnetic field. At this temperature, the curves are non-hysteretic. For nanowires NW2 and NW3, the zero-field critical currents are 1.3 and 3.8 μA respectively. To further study the behavior of critical current with temperature, NW2 was cooled down to 10 mk in a highly filtered dilution refrigerator. The differential resistance as a function of current is shown in fig.7.3. We observed an increase up to 12μA, with a thermal hysteresis behavior highlighting the increase of electron-phonon relaxation times at low temperature.

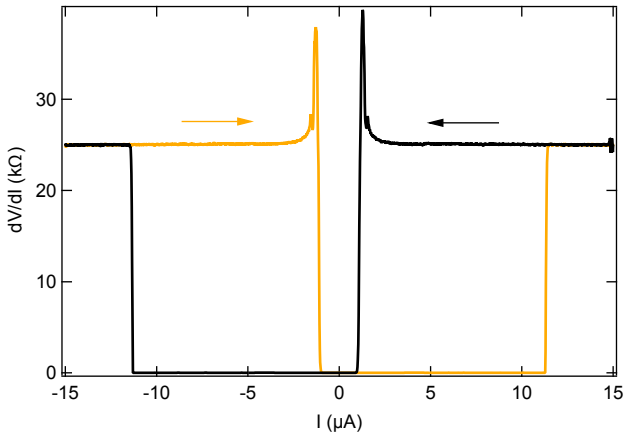

Figure 7.3: Differential resistance *vs* current of sample NW2 at very low temperature (T=10mK). The orange curve corresponds to an increase of the current whereas the black one is for decreasing current.

From the value of H_{C2} and T_C we extract the superconducting coherence lengths ξ and London penetration lengths λ, reported in table 1, assuming [72] $\mu_0 H_{C2}(T) = \Phi_0/2\pi\xi^2(T)$ and $\lambda(0) = 1.0510^{-3}\sqrt{\rho/T_c}$ with ρ the resistivity [168].

7.1.3 Microwave characterization of W nanowires

To probe the microwave properties of a resonator made with W nanowires, the two designs are shown in fig.7.1, the coplanar waveguide, and the lumped resonators are cooled down to 10 mK in a dry dilution fridge. The microwave signal is sent via attenuated and thermally anchored microwave lines. The transmitted wave is amplified and the complex transmission spectra S_{21} through the lines are measured with a vectorial network analyzer. The interference of the incident microwave signal and the one reflected from the resonator lead to a dip in S_{21}. This dip is accounted theoretically

by:

$$S_{21} = 1 - \frac{Q_t}{Q_c}\frac{1 - 2jQ_c u}{1 + 2jQ_t x} \tag{7.2}$$

with $x = (\omega - \omega_0)/\omega_0$ the fractional detuning of the readout angular frequency ω relative to the resonance frequency ω_0. $u = \frac{\delta\omega}{\omega_0}$ with $\delta\omega = \omega_1 - \omega_0$ is the frequency shift of the in-phase point on the resonance circle from ω_0 to ω_1 and represent the asymmetry. u is a dimensionless parameter considering the asymmetry in the transmission line and is essential to extract reliable quality factors in hanger-coupled resonators [169]. It reduces to 0 for a symmetric transmission line. The coupling quality factor Q_c quantifies the coupling between the transmission line and the resonator which has an intrinsic quality factor Q_i. These two terms are related to the total (or loaded) quality factor Q_t via $Q_t^{-1} = Q_i^{-1} + Q_c^{-1}$. Q_i which gives information on the quality of the resonator independently of the coupling to the measurement line and is a figure of merit of the material quality.

At low temperature, we found that the lumped resonator exhibits a resonance at f=4.46GHz (fig.7.5), whereas the CPW resonator has a resonance at f=4.05GHz (fig.7.4). In the following, using those values, we extract the kinetic inductance of the W nanowires.

The kinetic inductance can be estimated, at very low temperature, from $R_\square$ and T_C [175]:

$$L_{K,\square} \approx \frac{R_\square h}{2\pi^2 \Delta_0}. \tag{7.3}$$

where $\Delta_0 = 1.76 k_B T_c$. With $T_c \in [5 - 6.5]$K and the square resistances from table 7.1 we evaluate a kinetic inductance $L_{K,\square} \in [7 - 25]$ pH/$\square$.

Using a finite element simulation Sonnet® software we could extract for the lumped resonator, the parallel capacitance $C \approx 240$ fF, and the geometrical inductance of the wide Nb inductive part $L_{geo,D} \approx 0.935$ nH. From the value of the resonance frequency $f = 1/(2\pi\sqrt{(LC)})$ we deduce the kinetic inductance of the wire $L_K = 4.3$nH. The geometrical inductance of the nanowire alone is expected to be $L_{geo,W} \approx 17$ pH leading to the kinetic inductance fraction $\alpha = L_K/(L_{geo,W} + L_K) = 0.996$ and kinetic over geometrical inductance ratio $\beta = L_K/L_{geo,W} = 253$ so that the geometrical inductance can be neglected. We obtain a kinetic inductance per unit length $\mathcal{L}_K \approx 439\mu$H/m and a kinetic inductance per square $L_{K,\square} = 15.4$pH/$\square$ which falls in the expectation window calculated earlier.

For the coplanar waveguide resonator, we extracted the lineic capacitance to ground to $\mathcal{C} \approx$ 48pF/m and the lineic geometrical inductance of the wire $\mathcal{L}_{geo} \approx 1.7\mu$H/m. The lineic inductance was then deduced from the value of the resonance frequency $f = 1/(4\sqrt{(LC)}$ and the length of the line. We found $\mathcal{L} = \mathcal{L}_{geo} + \mathcal{L}_K \approx 512\mu$H/m. From these numbers we extracted a phase velocity $c = 1/\sqrt{\mathcal{L}\mathcal{C}} = 6.4 \times 10^6$ m/s and a characteristic impedance $Z_C = \sqrt{\mathcal{L}/\mathcal{C}} = 3.3$ kΩ. Such material is therefore highly suitable for dynamical Coulomb blockade experiments where the characteristic impedance Z_C must be comparable to the resistance quantum $R_Q = h/4e^2 \approx 6.5k\Omega$. More specifically, the coupling of *e.g.* a tunnel junction to a high impedance microwave resonator is characterized by the coupling parameter $\lambda = \sqrt{\pi Z_C/R_Q}$. With $\lambda \approx 1.26$ in our experiment we would be at the onset of the strong coupling regime $\lambda \geqslant 1$ where e.g. dc-driven single microwave photon generation could be achieved [176, 177].

Temperature dependence

In this section, we will study the effect of temperature on the value of resonance frequency and quality factor of a resonator made with W nanowires. Figure 7.5(a) shows the transmission spectra

of the lumped resonator at low power under various values of temperature ranging from 10 mK to 2.29K with fits using equation 7.2. At 10 mK, we found $\omega_0/2\pi = 4.4642$GHz and $Q_i = 3990$ at low power. Decreasing the temperature leads to an increase of the resonance frequency together with a sharpening of the resonance (fig. 7.5.b-c). Below $T = 0.9$K the resonance frequency is nearly constant and decreases strongly as one raises the temperature. Q_i evolves similarly with a maximum value reaching $Qi = 3990$ at 10mK.

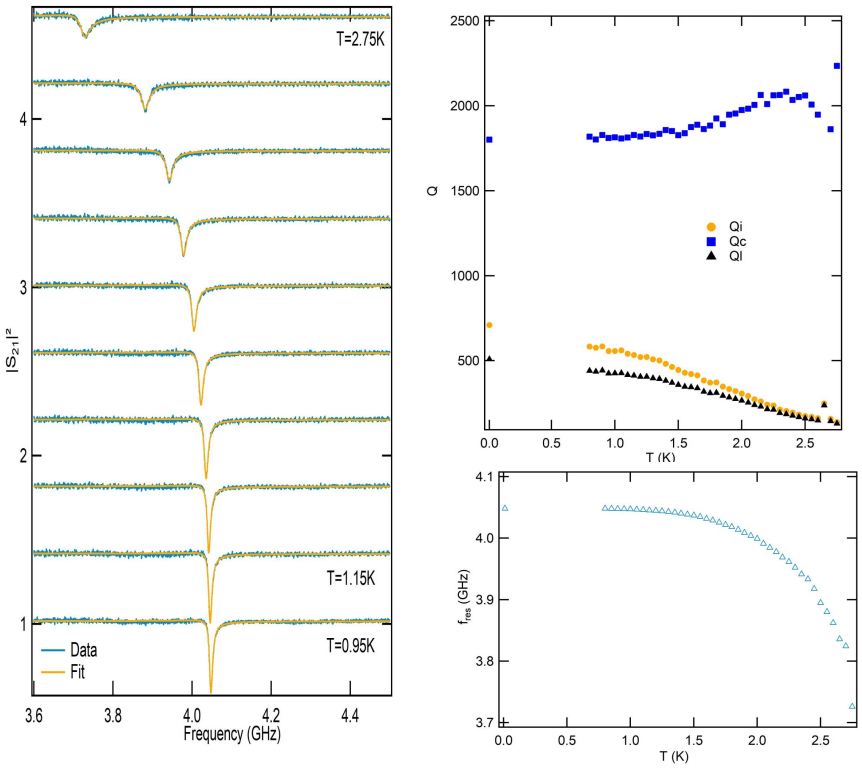

Figure 7.4: (a) Temperature dependence of the normalized transmission spectra of the CPW resonator. (b) Extracted quality factors *vs* temperature. (c) Temperature dependence of the resonance frequency.

The temperature dependence of the resonance frequency and the quality factor were both fitted by Mattis-Bardeen (MB) theory, which relates the temperature dependence of the resonance frequency and quality factor to the complex conductivity of the material $\sigma = \sigma_1 - i\sigma_2$ (See SM of [164]). This theory allows us to reasonably tackle the temperature dependence of the resonance frequency whereas discrepancies are found regarding the quality factors for which the MB theory predicts a diverging Q_i as the temperature is lowered. To reproduce our data, we introduce extra losses in the internal Q_i factor as: $Q_i^{-1} = Q_{MB}^{-1} + Q_{loss}^{-1}$. First, we fixed Q_{loss} at 3990 for all

the temperatures, see the yellow curve of fig.7.5.c. We see that the agreement in the intermediate temperature regime is unsatisfactory. Then we introduce a temperature dependence Q_{loss} given by $Q_{loss} = 3990(1 - T/3)$. The corresponding curve is shown in black in figure 7.5c demonstrating a reasonable agreement. This decay sheds light on the physics of losses into the resonator which increases as the temperature is raised. These extra losses need to be further understood and may be related to poisoning [170, 171, 172], TLS [173, 174] and/or mobile vortices [72].

The same data is measured for the CPW $\lambda/4$ resonator (See fig.7.4.a) it shows the same temperature dependence behavior of the resonance frequency and quality factor as the lumped resonator. This design exhibits a smaller quality factor $Q_i \approx 710$. In this geometry, the wire length was 390 μm long with a resonance frequency $\omega_0/2\pi = 4.05$ GHz.

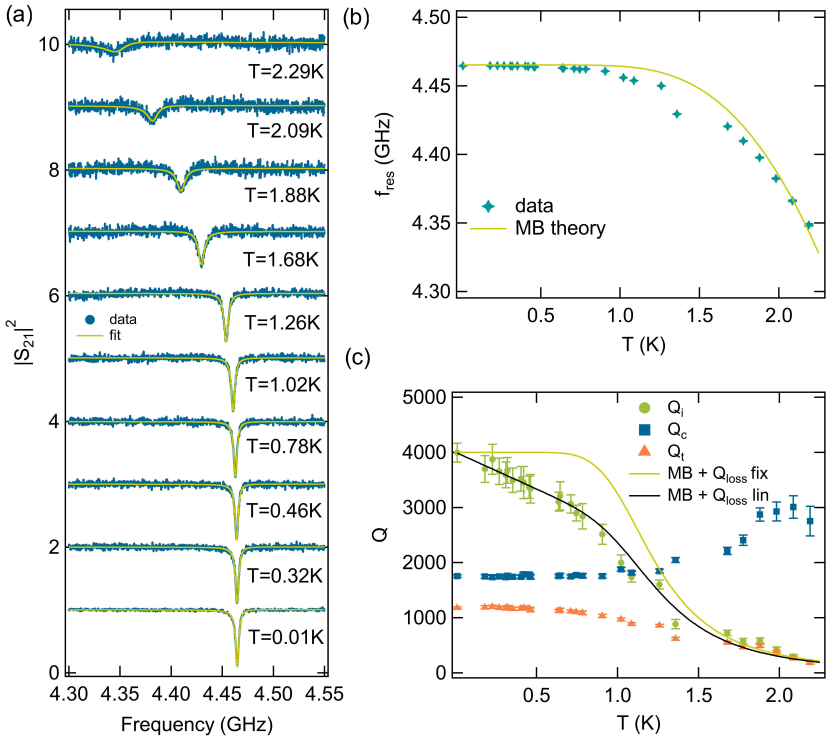

Figure 7.5: (a) Temperature dependence of the normalized transmission spectra of the lumped resonator. (b) Temperature dependence of the resonance frequency. (c) Extracted quality factors *vs* temperature.

Power dependance

Studying the power dependence of the normalized transmission spectra will introduce nonlinearity to the system due to the nonlinear kinetic inductance of the nanowires. To quantitatively tackle

this nonlinear effect, one needs to introduce into the fractional detuning parameter x of eq.7.2 the shift $\delta\omega$ of the resonance frequency due to the nonlinear kinetic inductance. The shifted resonance reads [178] $\omega_r = \omega_0 + \delta\omega = \omega_0 + Kn_{ph}$ where we have introduced the Kerr parameter K relating the frequency shift to n_{ph}, the number of photons stored in the resonator. By inserting new expression of ω_r into the fractional detuning we obtain:

$$x = \frac{\omega - \omega_0 - \delta\omega}{w_0 + \delta\omega} \approx x_0 - \delta x = x_0 - \frac{Kn_{ph}}{\omega_0} \tag{7.4}$$

with $x_0 = \frac{\omega - \omega_0}{w_0}$. Using the power conservation law relating the lost energy into the resonator P_{diss} with respect to the measurement lines accounted by the scattering parameters corresponding to wave reflection S_{11} and transmission S_{21}. In a hanger resonator the conservation law reads:

$$P_{diss} = P[1 - |S_{11}|^2 - |S_{21}|^2] \tag{7.5}$$

with $S_{11} = S_{21} - 1$. By replacing in this equation, the S_{21} formula, we find:

$$P_{diss} = P\left[\frac{2Q_t^2}{Q_i Q_c}\frac{1 + 4\frac{Q_c^2 Q_t}{Q_c - Q_t}ux}{1 + 4Q_t^2 x^2}\right]. \tag{7.6}$$

Inserting in eq.7.6 the definition of the internal quality factor $Q_i \approx n_{ph}\hbar\omega_0^2/P_{diss}$ gives access to the number of photons in the resonator as a function of the applied power:

$$n_{ph} = \frac{2Q_t^2 P}{Q_c \hbar\omega_0^2}\frac{1 + 4\frac{Q_c^2 Q_t}{Q_c - Q_t}ux}{1 + 4Q_t^2 x^2}. \tag{7.7}$$

Replacing the expression of n_{ph} given by 7.7 into eq.7.4 we get:

$$x = x_0 - \frac{Kn_{ph}}{\omega_0} = x_0 - K\frac{2Q_t^2 P}{Q_c \hbar\omega_0^3}\frac{1 + 4\frac{Q_c^2 Q_t}{Q_c - Q_t}ux}{1 + 4Q_t^2 x^2}. \tag{7.8}$$

From eq.7.8 we can define the non-linear parameter a_{NL} given by:

$$a_{NL} = -\frac{2KQ_t^3}{Q_c \hbar\omega_0^3}P \tag{7.9}$$

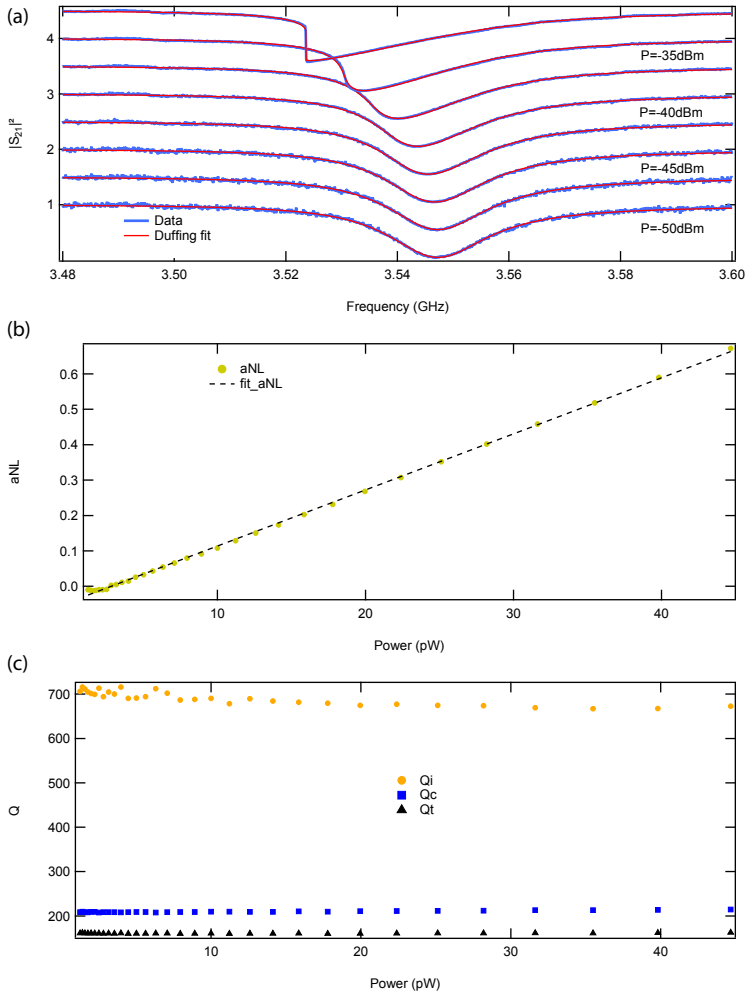

Figure 7.6: (a) Power dependence of the normalized transmission spectra near the microwave resonance of the lumped resonator at 1.5K. (b) Power dependence of the a_{NL} term allowing us to extract (see text) a Kerr parameter $K_{W,He} = 74$ Hz/photon at 3.5GHz. (c) Extracted quality factors as a function of the microwave power. The Q's seem to be rather stable with respect to Power with a maximum internal quality factor of 700.

Inserting eq.7.8 in the expression of S_{21}, allows us to plot as a function of the applied microwave power P, the nonlinear term a_{NL}, Q_i, Q_c and Q_t. fig.7.7.a and fig.7.6.a shows the power dependence of the transmission spectra of the lumped resonator at 10 mK and 1.5 K respectively. As one increases the microwave power, the peak shifts towards smaller frequency, slants and eventually becomes bistable at high power. By fitting the data with eq.7.2, considering $\delta\omega$, we extract the different quality factors for the resonators. At 10 mK, the quality factors (fig. 7.7.b) slightly increase from $Q_i = 3990$ to 4290 as the power is elevated up to 0.1 pW and remains stable at higher powers.

However, at 1.5K the quality factor seems to be rather stable with respect to the power (fig. 7.6.b). From the linear dependence of a_{NL} parameter with respect to microwave power P (See Figure.7.6), we extract a Kerr parameter. We find a non-linear Kerr parameter $K/2\pi = 200 \pm 120$ Hz/photon at 4.465 GHz (T=10mK), and $K_{W,He} = 74$ Hz/photon at 3.55 GHz(T=1.5K). As such the hybrid lumped resonator presented here is an interesting candidate to realize relatively high sensitivity photon detection experiments at a very moderate temperature such as the one of a pumped He bath.

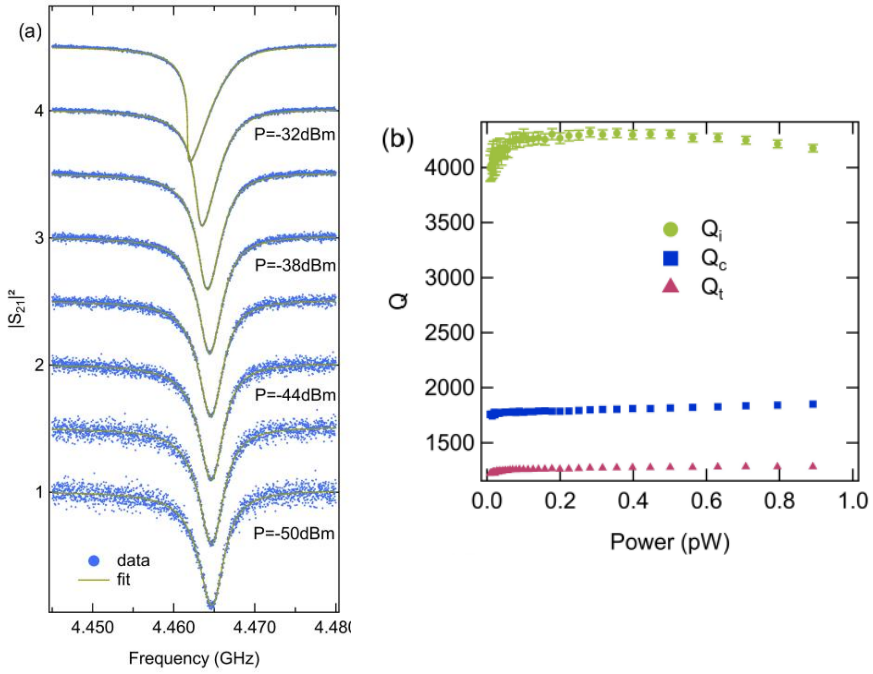

Figure 7.7: (a) Power dependence of the normalized transmission spectra of the lumped resonator at 10 mK.(b) Extracted quality factors *vs* microwave power.

Magnetic field dependence

Studying the physics of mesoscopic devices made with superconducting materials, requires most of the time applying a magnetic field. For example, for a carbon nanotube connected to superconducting contacts, a magnetic field should be applied in order to characterize the carbon nanotube in the normal state. This is the same in many other experiments where the spin degree of freedom is of interest. To implement such a resonators design made with W nanowires of high critical magnetic field in devices, we have to make sure that properties of the resonator are rather immune to the applied magnetic field. fig.7.8 shows the magnetic field dependence of the transmission spectra for the lumped resonator measured at $T = 1.55$K in a pumped He bath. At 0 magnetic field, the curve is fitted with the S_{21} formula and we found resonance frequency around 3.55GHz with an

internal Q_i factor of 700. We measured the microwave resonance up to 130 mT. The magnetic field dependence of the resonance frequency and quality factor is shown in fig.7.8.b. As expected, we observe a small change for Q_i ($< 10\%$) and f_{res} ($< 0.05\%$) for this range of magnetic field.

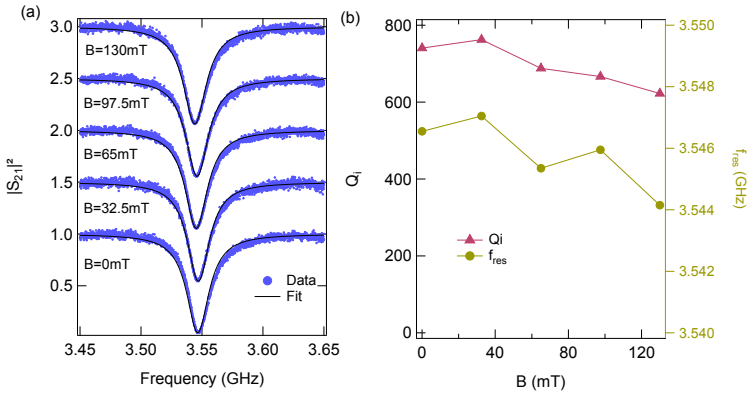

Figure 7.8: (a) In plane magnetic field dependence of the normalized transmission spectra of the lumped resonator at 1.55K with fits using the S_{21} formula. (b) Evolution of Q_i and f_{res} *vs* magnetic field.

7.1.4 Conclusion

In this section, we have presented a new hybrid microwave resonator made with a thin film of Nb and W nanowire grown with a He-beam induced deposition technique, which is a direct-write and resist-free process that does not involve any lithography steps. The nanowires exhibit high critical temperature T_C 5K, and critical magnetic field $B_C > 1T$. Two different designs were measured at low temperature, a lumped, and a coplanar waveguide resonator. The microwave characterization of the resonators reveals that the measured resonators exhibit internal quality factors up to $Qi = 4290$ at 4.46 GHz for $T = 10$ mK. We measure a large kinetic inductance for the W nanowire of $L_K = 15.4$ pH/□.

The magnetic field dependence shows that the resonators are immune to an in-plane magnetic field up to 130 mT. As such, this hybrid resonator could be interesting to study mesoscopic devices where the spin degree of freedom needs to be addressed. All those properties make W nanowires made with the He-FIB a good candidate for engineering a compact non-linear high impedance superconducting element for quantum electronics.

7.2 Single electron transistor thermometer

In this section, we will present measurements of electronic temperature using a micrometer scale mesoscopic circuit, a single electron transistor. When quantum properties of the atomic device can be observed at room temperature, devices of micrometer size require helium temperatures (4.2K) or even sub-kelvin temperatures. Performing transport measurement at the millikelvin range is possible, with the development of helium-based refrigeration technique, the temperature can be lowered down to 5-10 mK range at the mixing chamber (MC)(To know more about dilution fridges check chapter 2 section 2.1.4). However, due to thermal contact between the circuit and measurement lines, electrical noise, microwave heating, the electronic temperature is usually above this value.

7.2.1 Single electron transistor

In 1985 Dmitri Averin and Konstantin Likharev [179], proposed the idea of a new mesoscopic device called a single-electron transistor(SET). A few years later Theodore Fulton and Gerald Dolan [180] fabricated and demonstrated how such a device works. A single electron transistor is a three-terminal device based on the Coulomb blockade effect. In such a device two electrodes, source and drain are connected through a tunnel barrier to a metallic island. For the current to flow, electrons are forced to tunnel from(to) the island to the (from) source-drain electrode. The two tunnel junctions are modeled by a capacitor (C_D and C_S) and resistor (R_D and R_S) in parallel. A third electrode, the gate, which is capacitively coupled (C_G) to the island, is used to control N_g, the number of electron on it, such that, $N_g = \frac{C_g V_g}{e}$. (see Fig 7.9(a))

Fabrication

To fabricate a single electron transistor made up of Aluminum as metal and Aluminum oxide as an insulator, we use the resist recipe and lithography technique explained in the fabrication chapter. First, 50 nm of Aluminum is evaporated with an angle 15° to form the source, drain, gate electrodes, and the transistor. The tunnel junctions are then formed by introducing 7 mbar of oxygen into the chamber for almost 20 mins so that the first Al layer becomes coated by a thin layer of Al_2O_3. Finally, a second layer of aluminum (100nm) deposited at an angle -15° (see figure7.9(b)). The sample is cooled down in a dry fridge of base temperature 10 mK and measured through low pass filtered lines. The inner part of these lines is made up of manganin wire (Lakeshore manganin 36AWG), placed inside a Cupronickel (CuNi) tube with a diameter 0.5mm x 0.8mm. The total capacitance to the ground of the wire is 7 nF. The differential conductance of the set is probed with a lock-in technique.

Charging energy

When the temperature is lowered, such that $k_B T < E_C$, where E_C is the charging energy, the number of charges on the island is quantized. To add one electron on the SET, one should pay the charging energy of the SET given by, $E_C = \frac{e}{2C_\Sigma}$,with C_Σ the total capacitance of the island $C_\Sigma = C_S + C_D + C_g$.

Charge quantization results in periodic peaks of the SET conductance G_{SET} when sweeping gate voltage V_g. In the presence of dc bias voltage (V_{SD}), the peaks develop into periodic 'Coulomb diamond' patterns. The plot obtained is known as the stability diagram (See Fig 7.10). The

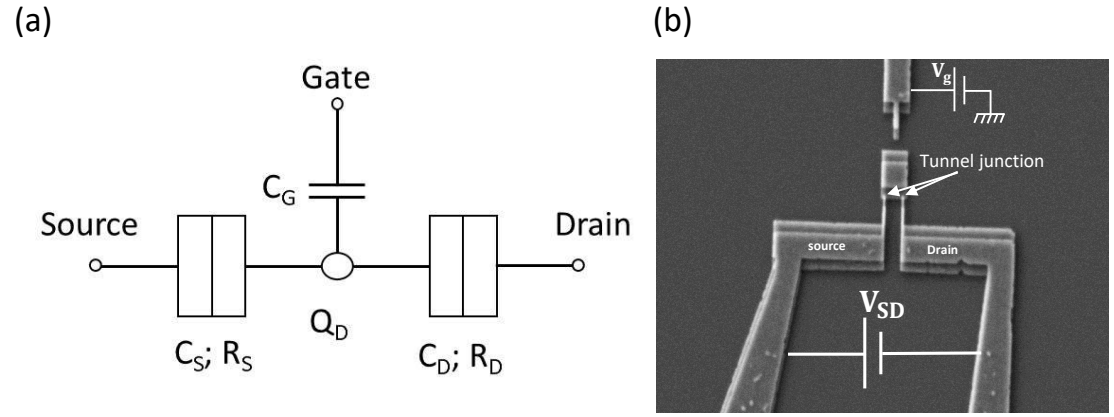

Figure 7.9: (a) Schema of the equivalent circuit of a single electron transistor. (b)Scanning electron microscope image of the measured SET, the island, and the three electrodes are made of Al, the tunnel barrier is made up of Al/Al_2O_3/Al using angle evaporation technique. A small magnetic field is applied to suppress superconductivity of Al.

stability diagram is composed of consecutive diamonds of the same size for each integer value of N_g. The width of the Coulomb diamond along the gate axis is $\frac{e}{C_g}$ and the diamond extends to $\pm \frac{e}{C_\Sigma}$ in bias voltage V_{SD}, thus the total high of the diamond is $4E_C$ as shown in Fig 7.10. Inside the diamonds tunneling is forbidden by the Coulomb blockade and conductance reads zero. The diamonds touch each other at the so-called 'charge degeneracy point', where two charge states have the same energy. Due to this degeneracy, the Coulomb blockade is lifted and electrons tunnel through the SET. The Color plot in Fig 7.10 represent the differential conductance $\frac{dI}{dV_{SD}}$ as function of V_g and V_{SD} measured at B=2T. The value of E_C is extracted using fig 7.10 by measuring the width of the diamonds in the bias voltage axis, the value found is E_C=22$\pm$2 μeV.

Coulomb blockade oscillations

When sweeping the gate voltage at zero bias voltage, the charge degeneracy point is crossed, a zero-bias conductance peak is observed. Thus, a periodic pattern of equidistant conductance peaks is obtained. In Fig 7.11, 4 coulombs peak are observed spreading over 14 mV in gate voltage.

The width of these conductance peaks at zero dc bias voltage constitutes a well-known primary thermometer. For a metallic island, with a continuous density of states and connected through tunnel contact, the SET conductance reads [181]

$$G_{SET}(\delta V_g) = \frac{G_\infty}{2} \frac{2E_C(\delta V_g/\beta)/k_B T}{\sinh(2E_C(\delta V_g/\beta)/k_B T)}. \tag{7.10}$$

Where $G_\infty = \frac{G_S G_D}{G_D + G_S}$ is the high voltage differential conductance of the SET given by Ohm's law, with G_S and G_D the conductance of source and drain electrode respectively. β=e/C_g the gate voltage period and δV_g the gate voltage difference to charge degeneracy. From 7.11 one find β=e/C_g=3.22 mV. Knowing the value of β and E_C, one can fit each peaks conductance in figure 7.11 with equation 7.10 and extract the value of electronic temperature.

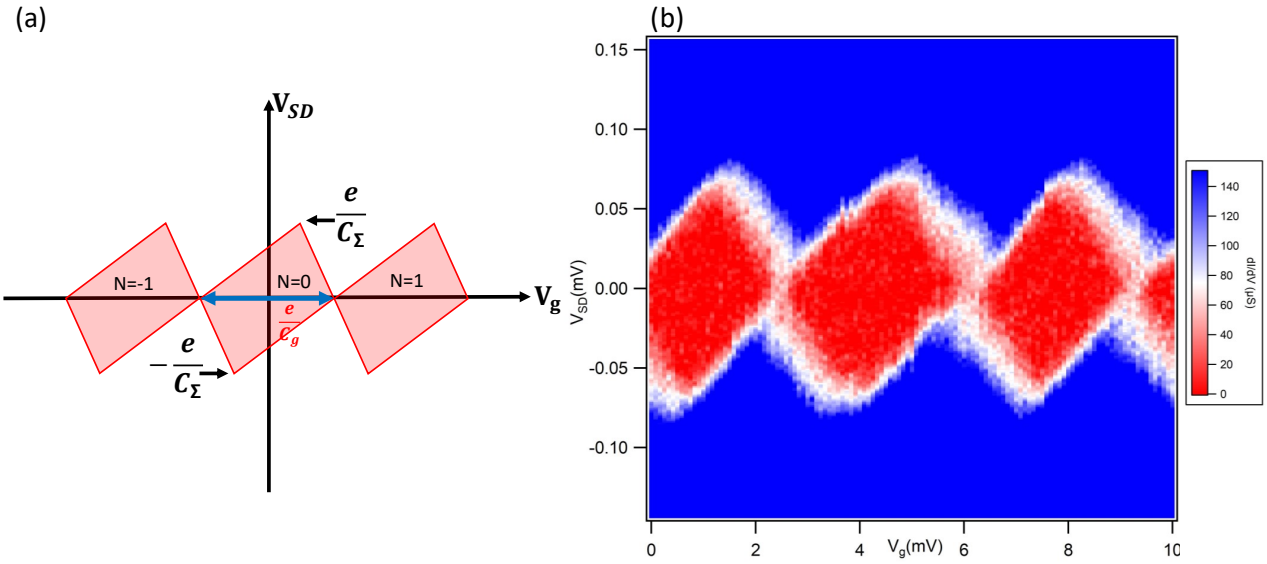

Figure 7.10: Coulomb blockade stability diagram. (a): Schematic representation of stability diagram of a single electron transistor, the red region corresponds to $\frac{dI}{dV_{SD}} = 0$ showing Coulomb blockade region. (b): Color plot of the conductance of the SET as a function of the gate voltage V_g and source-drain voltage V_{SD}.

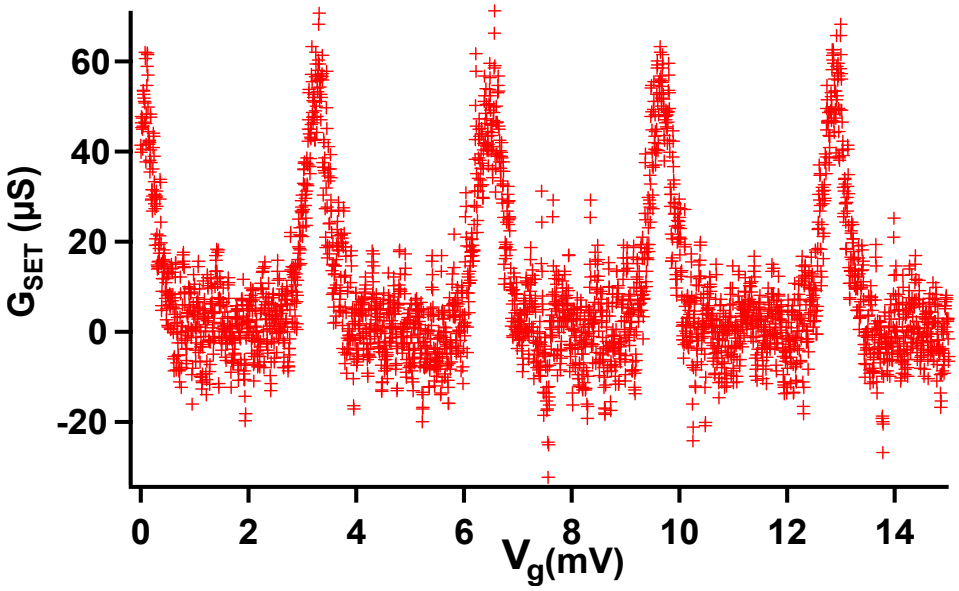

Figure 7.11: Coulomb blockade oscillations at zero bias voltage. Conductance of the SET G_{SET} versus the gate voltage V_g.

Each peak of 7.11 is fitted using eq. 7.10, and the value of the electronic temperature is obtained for several conductance peak (Fig7.12).

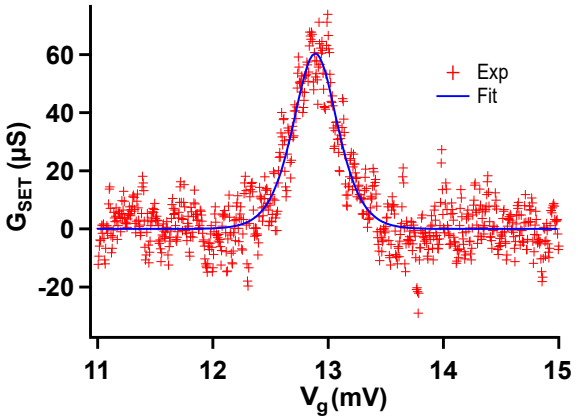

Figure 7.12: Measured conductance G_{SET} versus the gate voltage V_g. The points represented the measured values, eq 7.10 fits well the peak (bleu curve), giving $G_\infty = 116\mu S$ and $\frac{2E_C}{\Delta k_B T} = 9.3 \times 10^3 V^{-1}$, which gives $T_{electronic} = 23mK$ for this peak.

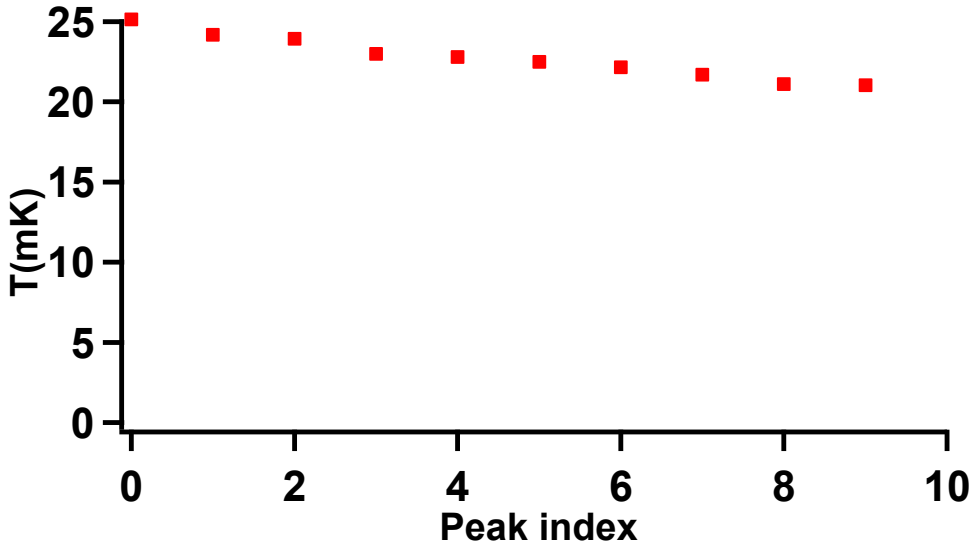

Figure 7.13: Electronic temperature extracted from fitting of the averaged peaks using eq. 7.10 versus the index of the peak. We find $T_{electronic} = 23 \pm 2$ mK.

7.2.2 Conclusion

Even though the base temperature of our dry refrigerator reads 10 mK, the electronic temperature measured with a coulomb blockade thermometer, single electron transistor found to be slightly higher $T_{electronic}$ = 23±2 mK. For a wet dilution fridge, due to space limitation, the filtering is less efficient, one have T_{MC} =50 mK and $T_{electronics}$ =80 mK. This implies that the condition of filtering in the dry fridge is better, since the difference in temperature between the mixing chamber and that felt by electron is lower.

Additional thermalization and cooling techniques will lead to lower electronic temperature. The lowest electronic temperature reported is 3.7 mK [182]. Also 6 mk electronic temperature has been reported in a medium-sized dilution refrigerator using three different methods, Coulomb blockade thermometer, quantum shot noise thermometer, and dynamical Coulomb blockade thermometer [183].

Conclusion

To conclude, during this thesis we have probed the dynamics of a quantum dot Josephson junction by measuring its Josephson emission. To do this we use the AC Josephson effect to probe the quantum state of a quantum dot Josephson junction between a singlet state and a doublet state. The sample which is a carbon nanotube-based-Josephson junction is first measured in the normal state, where we were able to extract all the relevant parameters. Then we probe the dynamics of our system by measuring its AC Josephson emission. We show that this emission is strikingly reduced in the gate region where the critical current is enhanced due to the interplay of the Kondo effect and superconducting proximity effect. By performing numerical renormalization group calculation of the energy spectrum and supercurrent of the ground state using the parameters determined in the normal state, we were able to calculate the many-body spectrum of our system. This helps us to evaluate the probability of the QD to be in a doublet state due to quasi-particle dynamics. We found that this probability is low in DC current configuration. However, when we apply a voltage bias to probe the AC Josephson effect, we found that the probability for the QD to be in doublet state is high. This leads to a decrease of I_{AC}^{C} since the critical current of the doublet state is lower than the one of the singlet ground state. Thus, we can attribute the collapse of AC Josephson emission to the dynamics of quasiparticles in the quantum dot which induce a transition between a singlet ground state and a doublet excited state. This points towards the importance of understanding the role of electron-electron interaction and non-equilibrium conditions in the dynamics of a QD Josephson junction. This topic requires more theoretical studies. We have seen that the asymmetry of the contacts affects the physics of our system. For that, we started working on a new carbon nanotube device with side gates that aim to tune independently the transparency of the contacts.

In the experiment we performed, probing the dynamics of the junction was done by measuring the AC Josephson emission, which requires a voltage bias. This voltage drives the system out of equilibrium. Another experiment that could be done is to probe the dynamics of the junction by probing its AC response to a phase modulation, which can be induced by a nearby resonator. This way the system can stay closer to equilibrium and should help us to disentangle the effects of high frequency phase modulation and voltage bias which are inherent to AC Josephson effects experiments.

The detection of the AC Josephson effect has been done using a quantum detector which is coupled on-chip to the QD via a resonant coupling circuit. During this Ph.D., we have designed and measured a new type of resonators. We have fabricated and evaluated the performance of hybrid microwave resonators made by combining sputtered Nb thin films with Tungsten nanowires grown with a He-beam induced deposition technique. Both lumped and coplanar waveguide resonators were fabricated and measured at low temperature. Microwave characterization of the two resonators reveals that they exhibit resonance frequency in the GHz range, high internal quality factor, and a large kinetic inductance. We also verified that the resonators are immune to an in-plane magnetic field up to 130 mT. Thus, such a type of resonator is a good candidate for engineering a compact non-linear high impedance superconducting element for quantum electronics. A nice experiment could be by using such a resonator to couple a carbon nanotube Josephson Junction to an SIS detector, as this will improve and enhance the measured signal. It could be also very useful to probe the dynamics of junction based on topological systems.

Since all these measurements require very low temperature and very low noise measurement we have tested homemade filtering in a dry fridge and low noise voltage biasing. We have used a Coulomb blockade thermometer (a single electron transistor) to measure the electronic temperature of a dry fridge. We found $T_{electronic}$=23±2 mK, which is slightly higher than the base temperature. Additional thermalization and cooling techniques will lead to lower electronic temperature.

Publications

This Ph.D. will lead to the publications of two papers :

- "High kinetic inductance microwave resonators made by He-Beam assisted deposition of tungsten nanowires". J. Basset, **D. Watfa**, G. Aiello, M. Féchant, A. Morvan, J. Estève, J. Gabelli, M. Aprili, R. Weil, A. Kasumov, H. Bouchiat, and R. Deblock. . Appl. Phys. Lett. 114, 102601 (2019).
- "Collapse of the Josephson emission in a carbon nanotube junction in the Kondo regime". **D. Watfa**, R. Delagrange, A. Kadlecová, M. Ferrier, A. Kasumov, H. Bouchiat, and R. Deblock. (Watfa et al. arXiv:2009.09740)

Bibliography

[1] S. Iijima. "Helical microtubules of graphitic carbon". Nature, 354:56 (1991).

[2] S. Kruss, A. J. Hilmer, J. Zhang, N. F. Reuel, B. Mu, and M. S. Strano. "Carbon nanotubes as optical biomedical sensors". Advanced Drug Delivery Reviews Volume 65, Issue 15, December 2013, Pages 1933-1950.

[3] N. M. Iverson, P. W. Barone, M. Shandell, L. J. Trudel, S. Sen, F. Sen, V. Ivanov, E. Atolia, E. Farias, T. P. McNicholas. "In vivo biosensing via tissue-localizable near-infrared-fluorescent single-walled carbon nanotubes". Nat. Nanotechnol., vol. 8, no. 11, p. 873 (2013).

[4] Y. Yang, L. Ding, H. Chen, J. Han, Z. Zhang, and L.-M. Peng. "Carbon nanotube network film-based ring oscillators with sub 10-ns propagation time and their applications in radio-frequency signal transmission". Nano Research volume 11, pages300–310(2018).

[5] S. Park, M. Vosguerichian, and Z. Bao. A review of fabrication and applications of carbon nanotube film-based flexible electronics. Nanoscale, 2013,5, 1727-1752 (2013).

[6] A. Jeantet, Y. Chassagneux, C. Raynaud, P. Roussignol, J.-S. Lauret, B. Besga, J. Estève, J. Reichel, and C. Voisin. "Widely tunable singlephoton source from a carbon nanotube in the Purcell regime". Phys. Rev. Lett., vol. 116, no. 24, p. 247402, 2016.

[7] S. Khasminskaya, F. Pyatkov, K. Słowik, S. Ferrari, O. Kahl, V. Kovalyuk, P. Rath, A. Vetter, F. Hennrich, M. M. Kappes et al. "Fully integrated quantum photonic circuit with an electrically driven light source". Nat. Photonics, vol. 10, no. 11, p. 727, 2016.

[8] A. D. Franklin. "Electronics: The road to carbon nanotube transistors". Nature, vol. 498, no. 7455, p. 443, 2013.

[9] N.Saifuddin, A.Z.Raziah, A.R.Junizah. "Carbon Nanotubes: A Review on Structure and Their Interaction with Proteins". Journal of Chemistry, 2013, 1–18. doi:10.1155/2013/676815.

[10] A. H. Castro Neto, F. Guinea, N. M. R. Peres, K. S. Novoselov, and A. K. Geim. "The electronic properties of graphene". Rev. Mod. Phys. 81, 109 (2009).

[11] Liu CH1, Liu YY, Zhang YH, Wei RR, Zhang HL. "Tandem extraction strategy for separation of metallic and semiconducting SWCNTs using condensed benzenoid molecules: effects of molecular morphology and solvent". Phys. Chem. Chem. Phys., 2009,11, 7257-7267

[12] A. Y. Kasumov, K. Tsukagoshi, M. Kawamura, T. Kobayashi, Y. Aoyagi, K. Senba, T. Kodama, H. Nishikawa, I. Ikemoto, K. Kikuchi, V. T. Volkov, Y. A. Kasumov, R. Deblock, S. Guéron, and H. Bouchiat. "Proximity effect in a superconductor-metallofullerene-superconductor molecular junction". Phys. Rev. B 72, 033414 (2005)

[13] D. C. Ralph, C. T. Black, and M. Tinkham. "Gate-Voltage Studies of Discrete Electronic States in Aluminum Nanoparticles". Phys. Rev. Lett., vol. 78, no. 21, pp.4087–4090, May 1997.

[14] L P Kouwenhoven, D G Austing, and S Tarucha. "Few-electron quantum dots". Reports on Progress in Physics, 64(6):701 (2001).

[15] S. De Franceschi, J. A. Van Dam, E. P. a. M. Bakkers, L. F. Feiner, L. Gurevich, and L.P. Kouwenhoven. "Single electron tunneling in InP nanowires". Applied physics letters,vol. 83, no. 2, pp. 344–346.

[16] S. J. Tans, M. H. Devoret, H. Dai, A. Thess, R. E. Smalley, L. J. Geerligs, and C.Dekker. "Individual single-wall carbon nanotubes as quantum wires". Nature volume 386, pages474–477(1997).

[17] J. Svensson and E. E. B. Campbell. “Schottky barriers in carbon nanotube-metal contacts”. J. Appl. Phys. 110, 111101 (2011).

[18] K. Grove-Rasmussen, H. I. Jørgensen, P. E. Lindelof. "Fabry-Perot interference, Kondo effect and Coulomb blockade in carbon nanotubes". Physica E Volume 40, Issue 1, October 2007, Pages 92-98.

[19] Y. Oreg, K. Byczuk, and B. I. Halperin. "Spin Configurations of a Carbon Nanotube in a Nonuniform External Potential". Phys. Rev. Lett. 85, 365 (2000).

[20] Wenjie Liang, Marc Bockrath, Dolores Bozovic, Jason H. Hafner, M. Tinkham and Hongkun Park . "Fabry-Perot interference in a nanotube electron waveguide". Nature volume 411, pages665–669(2001).

[21] D.S.Bethune, C.H.Kiang, M.S.de Vries, G.Gorman, R.Savoy, J.Vazquez, R.Beyers. "Cobalt-catalysed growth of carbon nanotubes with single-atomic-layer walls". Nature, Volume 363, Issue 6430, pp. 605-607 (1993).

[22] A.Thess, R.Lee, P.Nikolaev, H.Dai, P.Petit, L.Robert, R.E.Smalley. "Crystalline Ropes of Metallic Carbon Nanotubes". Science, Vol. 273, Issue 5274, pp. 483-487 (1996)

[23] B.Zheng, C.Lu, G.Gu, A.Makarovski, G.Finkelstein, J.Liu. "Efficient CVD Growth of Single-Walled Carbon Nanotubes on Surfaces Using Carbon Monoxide Precursor". Nano Letters 2002, 2, 8, 895–898.

[24] R.Xiang, E.Einarsson, J.Okawa, Y.Miyauchi, S.Maruyama. "Acetylene-Accelerated Alcohol Catalytic Chemical Vapor Deposition Growth of Vertically Aligned Single-Walled Carbon Nanotubes". J. Phys. Chem. C 2009, 113, 18, 7511–7515.

[25] J.Kong, A.MCassell, H.Dai. "Chemical vapor deposition of methane for single-walled carbon nanotubes". Chemical Physics Letters, Volume 292, Issues 4–6, 14 August 1998, Pages 567-574.

[26] C.Du, N.Pan. "CVD growth of carbon nanotubes directly on nickel substrate". Materials Letters, 59(13), 1678–1682.

[27] Y.A. Kasumov, A. Shailos, I.I. Khodos, V.T. Volkov, V.I. Levashov, V.N. Matveev, S. Guéron, M. Kobylko, M. Kociak, H. Bouchiat, V. Agache, A.S. Rollier, L. Buchaillot, A.M. Bonnot, A.Y. Kasumov. "CVD growth of carbon nanotubes at very low pressure of acetylene". Applied Physics A volume 88, pages687–691(2007).

[28] H. I. Jorgensen, K. Grove-Rasmussen, T. Novotný, K. Flensberg, and P. E. Lindelof. "Electron Transport in Single-Wall Carbon Nanotube Weak Links in the Fabry-Perot Regime". Phys. Rev. Lett. 96, 207003 (2006).

[29] W. J. de Haas, J. de Boer, and G. J. van dën Berg. "The electrical resistance of gold, copper and lead at low temperatures". Physica, vol. 1, no. 7–12, pp. 1115–1124, May 1934.

[30] Jun Kondo. "Resistance minimum in dilute magnetic alloys". Progress of Theoretical Physics, Volume 32, Issue 1, July 1964, Pages 37–49.

[31] L. Kouwenhoven and L. Glazman. "Revival of the Kondo effect". Physics World, vol.14, no. 1, pp. 33–38, 2001.

[32] P. W. Anderson. "A poor man's derivation of scaling laws for the Kondo problem". J.Phys. C Solid State Phys. 3, 12(1970), pp. 2436–2441.

[33] K. G. Wilson. "The renormalization group: critical phenomena and the Kondo Problem". Rev. Mod. Phys. 47 (1975), pp. 773–839.

[34] G. Gruner, A. Zawadowski. "Magnetic Impurities in Non-Magnetic Metals". Rep. Prog. Phys., 1974, 37, 1497-1583.

[35] P. Noziéres, A. Blandin. "Kondo Effect in Real Metals. Journal De Physique, 1980, 41, 193-211.

[36] N. Andrei, k. Furuya, J.H. Lowenstein. "Solution of the Kondo Problem". Rev. Mod. Phys., 1983, 55, 331-402.

[37] P. W. Anderson. "Localized Magnetic States in Metals". Phys. Rev., 1961, 124, 41-53.

[38] J.R. Schrieffer, P.A Wolff. "Relation Between the Anderson and Kondo Hamiltonians". Phys. Rev., 1966, 149,491-492.

[39] L. I. Glazman and M. É. Raikh."Resonant Kondo transparency of a barrier with quasilocal impurity states". Soviet Journal of Experimental and Theoretical Physics Letters, vol. 47, p. 452, Apr. 1988.

[40] Ned S. Wingreen and Yigal Meir. "Anderson model out of equilibrium: Noncrossingapproximation approach to transport through a quantum dot". Phys. Rev. B, 49(16):11040–11052, Apr 1994.

[41] D. Goldhaber-Gordon, H. Shtrikman, D. Mahalu, D. Abusch-Magder, U. Meirav, and M. A. Kastner. "Kondo effect in a single-electron transistor". Nature, vol. 391, no.6663, pp. 156–159, Jan. 1998.

[42] J Nygård, D. H. Cobden, and P. E. Lindelof. "Kondo physics in carbon nanotubes". Nature 408, 6810 (2000), pp.342–346.

[43] J. Park, A. N. Pasupathy, J. I. Goldsmith, C. Chang, Y. Yaish, J. R. Petta, M. Rinkoski, J. P. Sethna, H. D. Abruna, P. L. McEuen, and D. C. Ralph. "Coulomb blockade and the Kondo effect in single-atom transistors". Nature, vol. 417, no. 6890, pp. 722–725, Jun.2002.

[44] T. S. Jespersen, M. Aagesen, C. Sørensen, P. E. Lindelof, and J. Nygård. "Kondo physics in tunable semiconductor nanowire quantum dots". Phys. Rev. B, vol. 74, no.23, p. 233304, Dec. 2006.

[45] S. De Franceschi and W. G. van der Wiel. "Kondo Effect in Quantum Dots". Handbook of Nanophysics: Nanoparticles and Quantum Dots 2012. Chap. 37, pp. 20–37.

[46] A. Cox, D. L.Zawadowski. "Exotic kondo effects in metals: magnetic ions in a crystalline electric field and tunnelling center"s. Adv. Phys., 47:599–942, 1998.

[47] O. Yu. Kolesnychenko, R. de Kort, M. I. Katsnelson, A. I. Lichtenstein, and H. van Kempen. "Real-space imaging of an orbital kondo resonance on the cr(001) surface". Nature, 415:507–509, 2002.

[48] P. Jarillo-Herrero, J. Kong, H. S. J. van der Zant, C. Dekker, L. P. Kouwenhoven, and S. D. Franceschi. "Orbital Kondo effect in carbon nanotubes". Nature, vol. 434, no.7032, pp. 484–488, Mar. 2005.

[49] M.S. Choi, R. López, and R. Aguado. "SU(4) Kondo Effect in Carbon Nanotubes". Phys. Rev. Lett., vol. 95, no. 6, p. 067204, 2005.

[50] A. Makarovski, A. Zhukov, J. Liu, and G. Finkelstein. "SU(2) and SU(4) Kondo effects in carbon nanotube quantum dots". Phys. Rev. B, vol. 75, no. 24, p. 241407, Jun. 2007.

[51] J.-P. Cleuziou, N. V. N'Guyen, S. Florens, and W. Wernsdorfer. "Interplay of the Kondo Effect and Strong Spin-Orbit Coupling in Multihole Ultraclean Carbon Nanotubes". Phys. Rev. Lett. 111, 136803 (2013).

[52] M. R. Galpin, F. W. Jayatilaka, D. E. Logan, and F. B. Anders. "Interplay between Kondo physics and spin-orbit coupling in carbon nanotube quantum dots". Phys. Rev.B, vol. 81, no. 7, Feb. 2010.

[53] F. Kuemmeth, S. Ilani, D. C. Ralph, and P. L. McEuen. "Coupling of spin and orbital motion of electrons in carbon nanotubes". Nature, vol. 452, no. 7186, pp. 448–452, Mar. 2008.

[54] T. Ando. "Spin–orbit interaction in carbon nanotubes". J. Phys. Soc. Jpn. 69,1757–1763 (2000).

[55] T. S. Jespersen, K. Grove-Rasmussen, J. Paaske, K. Muraki, T. Fujisawa, J. Nygård, and K. Flensberg. "Gate-dependent spin-orbit coupling in multielectron carbon nanotubes". Nature Physics, vol. 7, no. 4, pp. 348–353, Jan. 2011.

[56] M. Marganska, P. Chudzinski, and M. Grifoni. "The two classes of low-energy spectra in finite carbon nanotubes". Phys. Rev. B 92, 075433 (2015).

[57] A.M. Tsvelick and P.B. Wiegmann. "Exact results in the theory of magnetic alloys". Adv. Phys., 453 (1983).

[58] N. E. Bickers. "Review of techniques in the large-N expansion for dilute magnetic alloys". Rev. Mod. Phys. 59, 845 (1987).

[59] J. Basset. "High frequency quantum noise of mesoscopic systems and current-phase relation of hybrid junctions". PhD thesis. Universite Paris-Sud, 2011.

[60] Raphaelle Delagrange. "Josephson effect and high frequency emission in a carbon nanotube in the Kondo regime". Thése, Orsay (2016).

[61] B. Babić, T. Kontos, and C. Schönenberger. "Kondo effect in carbon nanotubes at half filling". Phys. Rev. B 70, 235419 (2004).

[62] R. Maurand, T. Meng, E. Bonet, S. Florens, L. Marty, and W. Wernsdorfer. "First-Order 0-π Quantum Phase Transition in the Kondo Regime of a Superconducting Carbon-Nanotube Quantum Dot". Phys. Rev. X 2, 011009 (2012).

[63] A. V. Kretinin, H. Shtrikman, D. Goldhaber-Gordon, M. Hanl, A. Weichselbaum, J. von Delft, T. Costi, and D. Mahalu. "Spin-1/2 Kondo effect in an InAs nanowire quantum dot: Unitary limit, conductance scaling, and Zeeman splitting". Phys. Rev. B 84, 245316 (2011).

[64] T. A. Costi, A. C. Hewson, and V. Zlatic. "Transport coefficients of the Anderson model via the numerical renormalization group". J. Phys.: Condens. Matter 6, 2519 (1994).

[65] D. H. Cobden, M. Bockrath, P. L. McEuen, A. G. Rinzler, and R.E. Smalley. "Spin Splitting and Even-Odd Effects in Carbon Nanotubes". Phys. Rev. Lett. 81, 681 (1998).

[66] J. S. Lim, M.-S. Choi, M. Y. Choi, R. López, and R. Aguado. "Kondo effects in carbon nanotubes: From SU(4) to SU(2) symmetry". Phys. Rev. B 74, 205119 (2006).

[67] Meydi Ferrier, Tomonori Arakawa,Tokuro Hata,Ryo Fujiwara,Raphaëlle Delagrange, Richard Deblock, Yoshimichi Teratani, Rui Sakano, Akira Oguri and Kensuke Kobayashi. "Quantum Fluctuations along Symmetry Crossover in a Kondo-Correlated Quantum Dot". Phys. Rev. Lett. 118, 196803 (2017)

[68] G. R. Stewart. "Unconventional superconductivity". Advances in Physics 66:2, 75-196.

[69] O. Stockert, J. Arndt, E. Faulhaber, K. Schmalzl, W. Schmidt, A. Schneidewind, H. S. Jeevan, C. Geibel, M. Loewenhaupt and F. Steglich. "Paramagnon-mediated superconductivity in CeCu2Si2?". Scientific report 2006 – 2008, p. 104–107 (2009).

[70] J. Bardeen, L. N. Cooper, and J. R. Schrieffer. "Theory of Superconductivity". Physical Review, 108(5):1175–1204 (1957).

[71] P. G. de Gennes. "Superconductivity of metals and alloys" (Addison-Wesley, New York, 1989). (Cited on pages 15, 20, and 184.)

[72] M. Tinkham. Introduction to superconductivity.

[73] B. Josephson. "Possible new effects in superconductive tunneling". Phys. Lett. 1, 7 (1962), pp. 251–253.

[74] K. K. Likharev. "Superconducting weak links". Rev. Mod. Phys. 51, 101.

[75] I. Giaever. "Detection of the ac Josehson effect". Phys. Rev. Lett. 14, 22 (1965),pp. 904–906.

[76] I. Yanson, V. Svistunov, and I. Dmitrenko. "Experimental Observation of the Tunnel Effect for Cooper Pairs with the Emission of Photons". Sov. Phys. JETP 21, 1933 (1965), p. 650.

[77] M. C. Cassidy, A. Bruno, S. Rubbert, M. Irfan, J. Kammhuber, R. N. Schouten, A. R. Akhmerov, and L. P. Kouwenhoven. "Demonstration of an ac junction laser". Science Vol. 355, Issue 6328, pp. 939-942.

[78] S. P. Benz and C. A. Hamilton. "Application of the Josephson effect to voltage metrology. Proceedings of the IEEE **92**, 1617 (2004).

[79] J. Basset, M. Kuzmanovic, P. Virtanen, T. T. Heikkilä, J. Estève, J. Gabelli, C. Strunk, and M. Aprili. "Nonadiabatic dynamics in strongly driven diffusive Josephson junctions". Phys. Rev. Research **1**, 032009 (2019).

[80] P.-M. Billangeon, F. Pierre, H. Bouchiat, R. Deblock. "Ac Josephson Effect and Resonant Cooper Pair Tunneling Emission of a Single Cooper Pair Transistor Phys". Rev. Lett. **98**, 216802 (2007).

[81] J. Wiedenmann, E. Bocquillon, R. S. Deacon, S. Hartinger, O. Herrmann, T. M. Klapwijk, L. Maier, C. Ames, C. Brüne, C. Gould, A. Oiwa, K. Ishibashi, S. Tarucha, H. Buhmann and L. W. Molenkamp. "4π-periodic Josephson supercurrent in HgTe-based topological Josephson junctions". Nature Communications **7**, 10303 (2016).

[82] R. S. Deacon, J. Wiedenmann, E. Bocquillon, F. Domínguez, T. M. Klapwijk, P. Leubner, C. Brüne, E. M. Hankiewicz, S. Tarucha, K. Ishibashi, H. Buhmann, and L. W. Molenkamp. "Josephson Radiation from Gapless Andreev Bound States in HgTe-Based Topological Junctions". Phys. Rev. X **7**, 021011 (2017).

[83] Dominique Laroche, Daniël Bouman, David J. van Woerkom, Alex Proutski, Chaitanya Murthy, Dmitry I. Pikulin, Chetan Nayak, Ruben J. J. van Gulik, Jesper Nygård, Peter Krogstrup, Leo P. Kouwenhoven and Attila Geresdi. "Observation of the 4π-periodic Josephson effect in indium arsenide nanowires". Nature Communications **10**, 245 (2019).

[84] Y.-J. Doh, J. A. van Dam, A. L. Roest, E. P. A. M. Bakkers, L. P. Kouwenhoven, and S. De Franceschi. "Tunable Supercurrent Through Semiconductor Nanowires". Science 309, 5732 (2005), pp. 272–275.

[85] C. C. Grimes and S.Shapiro. "Millimeter-Wave Mixing with Josephson Junctions". Physical Review 169, 397 (1968).

[86] A. A. Golubov, M. Y. Kupriyanov, and E. Il'ichev. "The current-phase relation in Josephson junctions". Rev. Mod. Phys. 76, 411 (2004).

[87] C.W.J. Beenakker. "Three universal mesoscopic josephson effects". Transport Phenomena in Mesoscopic Systems, edited by H. Fukuyama and T. Ando (Springer, Berlin, 1992).

[88] J-D. Pillet, C. H. L. Quay, P. Morn, C. Bena, a. Levy Yeyati, and P. Joyez. "Andreev bound states in supercurrent-carrying carbon nanotubes revealed". Nature Physics volume 6, pages965–969(2010).

[89] V. Ambegaokar and A. Baratoff. "Tunneling Between Superconductors". Phys. Rev. Lett. **10**, 486 (1963).

[90] Chuan Li, Jorrit C. de Boer, Bob de Ronde, Shyama V. Ramankutty, Erik van Heumen, Yingkai Huang, Anne de Visser, Alexander A. Golubov, Mark S. Golden and Alexander Brinkman. "4π-periodic Andreev bound states in a Dirac semimetal". Nature Materials **17**, 875-880(2018).

[91] Silvano De Franceschi, Leo Kouwenhoven, Christian Schönenberger, and Wolfgang Wernsdorfer. "Hybrid superconductor-quantum dot devices". Nature Nanotechnology, 5:703–711, 2010.

[92] J.-P. Cleuziou, W. Wernsdorfer, V. Bouchiat, T. Ondarçuhu and M. Monthioux. "Carbon nanotube superconducting quantum interference device". Nature Nanotechnology volume 1, pages53–59(2006).

[93] Jorden A. van Dam, Yuli V. Nazarov, Erik P. A. M. Bakkers, Silvano De Franceschi, Leo P. Kouwenhoven. "Supercurrent reversal in quantum dots". Nature 442, 667-670 (2006).

[94] L.Hofstetter, S.Csonka, J.Nygard, C.Schönenberger. "Cooper pair splitter realized in a two-quantum-dot Y-junction". Nature 461 (7266), 960-963.

[95] Travis Dirks, Taylor L. Hughes, Siddhartha Lal, Bruno Uchoa, Yung-Fu Chen, Cesar Chialvo, Paul M. Goldbart and Nadya Mason. "Transport through Andreev bound states in a graphene quantum dot". Nature Physics volume 7, pages386–390(2011)

[96] I. O. Kulik. "The Josephson tunnel effect in superconductors with paramagnetic impurities". Sov Phys JETP 23, 3 (1966).

[97] T Novotný, A. Rossini, and K. Flensberg. "Josephson current through a molecular transistor in a dissipative environment". Phys. Rev. B 72, 224502 (2005).

[98] B. I. Spivak and S. A. Kivelson. "Negative local superfluid densities: The difference between dirty superconductors and dirty Bose liquids". Phys. Rev. B 43, 4 (1991),pp. 3740–3743.

[99] L. Glazman and A Matveev. "Resonant Josephson current through Kondo impurities in a tunnel Barrier". JETP 49 (1989), p. 659.

[100] E. Vecino, A. Martín-Rodero, and A. Levy Yeyati. "Josephson current through a correlated quantum level: Andreev states and π junction behavior". Phys. Rev. B, 68(3):035105, Jul 2003.

[101] A.V. Rozhkov, D.P. Arovas. "Josephson Coupling through a Magnetic Impurity". Phys. Rev. Lett. 82 (1999) 2788.

[102] F. Siano, R. Egger. "A Reply to the Comment by Mahn-Soo Choi et al". Phys. Rev. Lett. 94 (2005) 229702.

[103] C. Karrasch, A. Oguri, V. Meden. "Josephson current through a single Anderson impurity coupled to BCS leads". Phys. Rev. B 77 (2008) 024517.

[104] M. R. Buitelaar, T. Nussbaumer, and C. Schönenberger. "Quantum Dot in the Kondo Regime Coupled to Superconductors". Phys. Rev. Lett. 89, 256801.

[105] A. Eichler, R. Deblock, M. Weiss, C. Karrasch, V. Meden, C. Schönenberger, and H. Bouchiat. "Tuning the josephson current in carbon nanotubes with the kondo effect". Phys. Rev. B, 79(16):161407, Apr 2009.

[106] R. Delagrange, R. Weil, A. Kasumov, M. Ferrier, H. Bouchiat and R. Deblock. "$0-\pi$ quantum transition in a carbon nanotube Josephson junction: Universal phase dependence and orbital degeneracy". Phys. Rev. B 93, 195437 (2016).

[107] A. Yu. Kasumov, R. Deblock, M. Kociak, B. Reulet, H. Bouchiat, I. I. Khodos, Yu. B. Gorbatov, V. T. Volkov, C. Journet, O. Stephan and M. Burghard, C. R. Acad. "Proximity-induced superconductivity in carbon nanotubes". Sci. Paris, t. 327, Série II b, p. 933-943, 1999.

[108] A. Kasumov, M. Kociak, M. Ferrier, R. Deblock, S. Guéron, B. Reulet, I. Khodos, O. Stéphan, and H. Bouchiat. "Quantum transport through carbon nanotubes: Proximity-induced and intrinsic superconductivity". Phys. Rev. B 68, 214521 (2003).

[109] E. Onac, F. Balestro, L. H. Willems van Beveren, U. Hartmann, Y. V. Nazarov, and L. P. Kouwenhoven. "Using a quantum dot as a high-frequency shot noise detector". Phys. Rev. Lett., 96(17):176601, May 2006.

[110] P.-M. Billangeon, F. Pierre, H. Bouchiat, and R. Deblock. "Emission and absorption asymmetry in the quantum noise of a josephson junction". Phys. Rev. Lett., 96(13):136804, Apr 2006.

[111] Richard Deblock, Eugen Onac, Leonid Gurevich, and Leo P. Kouwenhoven. "Detection of quantum noise from an electrically driven two-level system". Science,301(5630):203–206, 2003.

[112] G.-L. Ingold and Y. V. Nazarov. "Charge Tunneling Rates in Ultrasmall Junctions". Single Charg. tunneling 294 (2005), pp. 21–107.

[113] Ramón Aguado and Leo P. Kouwenhoven. "Double quantum dots as detectors of highfrequency quantum noise in mesoscopic conductors". Phys. Rev. Lett., 84(9):1986–1989, Feb 2000.

[114] J. Basset, H. Bouchiat, R. Deblock. "Emission and Absorption Quantum Noise Measurement with an On-Chip Resonant Circuit". Phys. Rev. Lett. **105**, 166801 (2010).

[115] M Göppl, A Fragner, M Baur, R Bianchetti, S Filipp, J. M. Fink, and P. J. Leek. "Coplanar waveguide resonators for circuit quantum electrodynamics". J. Appl. Phys.104, 113904 (2008).

[116] J. Basset, A. Yu. Kasumov, C. P. Moca, G. Zaránd, P. Simon, H. Bouchiat, and R. Deblock. "Measurement of Quantum Noise in a Carbon Nanotube Quantum Dot in the Kondo Regime". Phys. Rev. Lett. 108, 046802 (2012).

[117] P. Jarillo-Herrero, J. A. van Dam, and L. P. Kouwenhoven. "Quantum supercurrent transistors in carbon nanotubes". Nature, 953 (2006).

[118] H. I. Jorgensen, T. Novotný, K. Grove-Rasmussen, K. Flensberg, and P. E. Lindelof. "Critical Current $0-\pi$ Transition in Designed Josephson Quantum Dot Junctions". Nano Lett. 7, 2441 (2007).

[119] S. Y. Müller, M. Pletyukhov, D. Schuricht, and S. Andergassen. "Magnetic field effects on the finite-frequency noise and ac conductance of a Kondo quantum dot out of equilibrium". Phys. Rev. B **87**, 245115 (2013).

[120] A. Kaminski, Y. V. Nazarov, and L. I. Glazman. "Suppression of the Kondo effect in a quantum dot by external irradiation". Phys. Rev. Lett. 83, 384 (1999).

[121] A. Kaminski, Y. V. Nazarov, and L. I. Glazman. "Universality of the Kondo effect in a quantum dot out of equilibrium". Phys. Rev. B 62, 8154 (2000).

[122] J. Paaske, A. Rosch, J. Kroha, and P. Wölfle. "Nonequilibrium transport through a Kondo dot: Decoherence effects". Phys. Rev. B 70, 155301 (2004).

[123] R. Delagrange, J. Basset, H. Bouchiat, R. Deblock. "Emission noise and high frequency cut-off of the Kondo effect in a quantum dot". Phys. Rev. B 97, 041412(R) (2018).

[124] R. Zitko, NRG Ljubljana - open source numerical renormalization group code (2014), http://nrgljubljana.ijs.si

[125] R. Zitko and T. Pruschke. "Energy resolution and discretization artifacts in the numerical renormalization group". Phys. Rev. B 79, 085106 (2009).

[126] T. Kontos, M. Aprili, J. Lesueur, X. Grison, and L. Dumoulin Phys. Rev. Lett. **93**, 137001 (2004).

[127] D. M. Badiane, L. I. Glazman, M. Houzet, and J. S. Meyer. " Ac Josephson effect in topological Josephson junctions". Comptes Rendus Physique 14, 840 (2013).

[128] D. Averin and A. Bardas. "ac Josephson Effect in a Single Quantum Channel". Phys. Rev. Lett. 75, 1831 (1995).

[129] C. W. J. Beenakker and H. van Houten. "Josephson current through a superconducting quantum point contact shorter than the coherence length". Phys. Rev. Lett. 66, 3056 (1991).

[130] K. Mullen, Y. Gefen, and E. Ben-Jacob. "The dynamics of mesoscopic normal tunnel junctions". Physica B: Condensed Matter 152, 172 (1988).

[131] J. C. Cuevas, A. Martín-Rodero, and A. Levy Yeyati. "Hamiltonian approach to the transport properties of superconducting quantum point contacts". Phys. Rev. B 54, 7366 (1996).

[132] J. M. Martinis, M. Ansmann and J. Aumentado. "Energy decay in superconducting Josephson-junction qubits from nonequilibrium quasiparticle excitations". Phys. Rev. Lett. 103, 097002 (2009).

[133] G. Catelani, J. Koch, L. Frunzio, R. J. Schoelkopf, M. H. Devoret, L. I. Glazman. "Quasiparticle relaxation of superconducting qubits in the presence of flux". Phys. Rev. Lett. 106, 077002 (2011).

[134] P. Joyez, P. Lafarge, A. Filipe, D. Esteve and M. H. Devoret." Observation of parity-induced suppression of Josephson tunneling in the superconducting single-electron transistor". Phys. Rev. Lett. 72, 2458–2461 (1994).

[135] A. J. Ferguson, N. A. Court, F. E. Hudson and R. G. Clark. "Microsecond resolution of quasiparticle tunneling in the single-Cooper-pair transistor". Phys.Rev. Lett. 97, 106603 (2006).

[136] J. Aumentado, M. W. Keller, J. M. Martinis and M. H. Devoret. "Nonequilibrium quasiparticles and 2e periodicity in single-Cooper-pair transistors". Phys. Rev. Lett. 92, 066802 (2004).

[137] M. D. Shaw, R. M. Lutchyn, P. Delsing and P. M. Echternach. "Kinetics of nonequilibrium quasiparticle tunneling in superconducting charge qubits". Phys. Rev. B 78, 024503 (2008).

[138] M. Lenander, H. Wang, R. C. Bialczak, E. Lucero, M. Mariantoni, M. Neeley, A. D. O'Connell, D. Sank, M. Weides, J. Wenner, T. Yamamoto, Y. Yin, J. Zhao, A. N. Cleland and J. M. Martinis. "Measurement of energy decay in superconducting qubits from nonequilibrium quasiparticles". Phys. Rev. B 84,024501 (2011).

[139] N. M. Chtchelkatchev and Y. V. Nazarov. "Andreev quantum dots for spin manipulation". Phys. Rev. Lett. 90, 226806 (2003).

[140] M. Zgirski, L. Bretheau, Q. Le Masne, H. Pothier, D. Esteve and C. Urbina. "Evidence for long-lived quasiparticles trapped in superconducting point contacts". Phys. Rev. Lett. 106, 257003 (2011).

[141] A. Levy Yeyati, A. Martín-Rodero, and E. Vecino. "Nonequilibrium Dynamics of Andreev States in the Kondo Regime". Phys. Rev. Lett. 91, 266802 (2003).

[142] E. Vecino et al., Sol. Solid State Comun. 131,9-10, p. 625-630 (2004).

[143] D. G. Olivares, A. L. Yeyati, L. Bretheau, Ç. Ö. Girit, H. Pothier, and C. Urbina. "Dynamics of quasiparticle trapping in Andreev levels". Phys. Rev. B 89, 104504 (2014).

[144] Y.N.Demkov, V.I.Osherov. "Stationary and nonstationary problems in quantum mechanics that can be solved by means of contour integration". Sov.Phys.JETP 26, 916(1968).

[145] V. E. Manucharyan, J. Koch, L. I. Glazman, and M. H. Devoret, Science 326, 113 (2009).

[146] I. M. Pop, K. Geerlings, G. Catelani, R. J. Schoelkopf, L. I. Glazman, and M. H. Devoret, Nature 508, 369 (2014).

[147] Y.-H. Lin, L. B. Nguyen, N. Grabon, J. San Miguel, N. Pankratova, and V. E. Manucharyan, Phys. Rev. Lett. 120, 150503 (2018).

[148] N. Earnest, S. Chakram, Y. Lu, N. Irons, R. K. NaikN. Leung, J. Lawrence, J. Koch, and D. I. Schuster, Phys. Rev. Lett. 120, 150504 (2018).

[149] A. Stockklauser, P. Scarlino, J. V. Koski, S. Gasparinetti, C. K. Andersen, C. Reichl, W. Wegscheider, T. Ihn, K. Ensslin, and A. Wallraff, Phys. Rev. X 7, 011030 (2017).

[150] A. J. Landig, J. V. Koski, P. Scarlino, U. C. Mendes,A. Blais, C. Reichl, W. Wegscheider, A. Wallraff, K. Ensslin, and T. Ihn, Nature 560, 179 (2018).

[151] O. V. Astafiev, L. B. Ioffe, S. Kafanov, Y. A. Pashkin, K. Y. Arutyunov, D. Shahar, O. Cohen, and J. S. Tsai, Nature 484, 355 (2012).

[152] C. Altimiras, O. Parlavecchio, P. Joyez, D. Vion, P. Roche, D. Esteve, and F. Portier, Appl. Phys. Lett. 103, 212601 (2013).

[153] C. Rolland, A. Peugeot, S. Dambach, M. Westig, B. Kubala, C. Altimiras, H. le Sueur, P. Joyez, D. Vion, P. Roche, D. Esteve, J. Ankerhold, and F. Portier, arXiv:1810.06217 (2018).

[154] S. Sengupta, C. Li, C. Baumier, A. Kasumov, S. Guéron, H. Bouchiat, and F. Fortuna. "Superconducting nanowires by electron-beam-induced deposition". Appl. Phys. Lett. 106, 042601 (2015).

[155] E.S. Sadki, S. Ooi, K. Hirata. "Focused-ion-beam-induced deposition of superconducting nanowires". Appl. Phys. Lett. 85, 6206 (2004).

[156] E. S. Sadki, S. Ooi, and K. Hirata. "Focused ion beam induced deposition of superconducting thin films". Physica C: Superconductivity and Its Applications 426–431, Part 2, 1547 (2005).

[157] A. Shailos, W. Nativel, A. Kasumov, C. Collet, M. Ferrier, S. Guéron, R. Deblock, and H. Bouchiat. "Proximity effect and multiple Andreev reflections in few-layer graphene". EPL 79, 57008 (2007).

[158] F. Chiodi, M. Ferrier, S. Guéron, J. C. Cuevas, G. Montambaux, F. Fortuna, A. Kasumov, and H. Bouchiat. "Geometry-related magnetic interference patterns in long Josephson junctions". Phys. Rev. B 86, 064510 (2012).

[159] C. Li, A. Kasumov, A. Murani, S. Sengupta, F. Fortuna, K. Napolskii, D. Koshkodaev, G. Tsirlina, Y. Kasumov, I. Khodos, R. Deblock, M. Ferrier, S. Guéron, and H. Bouchiat. "Magnetic field resistant quantum interferences in bismuth nanowires based Josephson junctions". Phys. Rev. B 90, 245427 (2014).

[160] A. Murani, A. Kasumov, S. Sengupta, Y. A. Kasumov, V. T. Volkov, I. I. Khodos, F. Brisset, R. Delagrange, A. Chepelianskii, R. Deblock, H. Bouchiat, and S. Guéron. "Ballistic edge states in Bismuth nanowires revealed by SQUID interferometry". Nature Communications 8, ncomms15941 (2017).

[161] I. Guillamón, H. Suderow, A. Fernández-Pacheco, J. Sesé, R. Córdoba, J. M. De Teresa, M. R. Ibarra, and S. Vieira. "Direct observation of melting in a two-dimensional superconducting vortex lattice". Nat Phys 5, 651 (2009)

[162] W. Li, J. C. Fenton, C. Gu, and P. A. Warburton. "Superconductivity of ultra-fine tungsten nanowires grown by focused-ion-beam direct-writing". Microelectronic Engineering 88, 2636 (2011).

[163] B.W. Ward, J.A. Notte and N.P. Economou. "Helium ion microscope: A new tool for nanoscale microscopy and metrology". J. Vac. Sci. Technol. B 24,2871 (2006).

[164] J. Basset, D. Watfa, G. Aiello, M. Féchant, A. Morvan, J. Estève, J. Gabelli, M. Aprili, R. Weil, A. Kasumov, H. Bouchiat, and R. Deblock. "High kinetic inductance microwave resonators made by He-Beam assisted deposition of tungsten nanowires". Appl. Phys. Lett. 114, 102601 (2019).

[165] K. Makise, H. Terai, Y. Tominari, S. Tanaka, and B. Shinozaki. "Duality picture of Superconductor-insulator transitions on Superconducting nanowire". Scientific Reports 6, 27001 (2016).

[166] F. Qin, T. Ideue, W. Shi, X.-X. Zhang, M. Yoshida, A. Zak, R. Tenne, T. Kikitsu, D. Inoue, D. Hashizume, and Y. Iwasa. "Diameter-Dependent Superconductivity in Individual WS2 Nanotubes". Nano Lett. 2018, 18, 11, 6789–6794

[167] R. Córdoba, A. Ibarra, D. Mailly, and J. M. De Teresa. "Vertical Growth of Superconducting Crystalline Hollow Nanowires by He+ Focused Ion Beam Induced Deposition". Nano Lett. 18, 1379 (2018).

[168] P. H. Kes and C. C. Tsuei. "Two-dimensional collective flux pinning, defects, and structural relaxation in amorphous superconducting films". Phys. Rev. B 28, 5126 (1983).

[169] M. S. Khalil, M. J. A. Stoutimore, F. C. Wellstood, and K. D. Osborn. "An analysis method for asymmetric resonator transmission applied to superconducting devices". Journal of Applied Physics 111, 054510 (2012).

[170] D.E. Oates, A.C. Anderson, C.C. Chin, J.S. Derov, G. Dresselhaus, M.S. Dresselhaus. "Surface-impedance measurements of superconducting NbN films". Phys. Rev. B 43, 7655 (1991).

[171] M. Zemlicka, P. Neilinger, M. Trgala, M. Rehak, D. Manca, M. Grajcar, P. Szabo, P. Samuely, S. Gazi, U. Hubner, V.M. Vinokur, E. Il(ichev). "Finite quasiparticle lifetime in disordered superconductors". Phys. Rev. B **92**, 224506 (2015).

[172] N. Maleeva, L. Grünhaupt, T. Klein, F. Levy-Bertrand, O. Dupre, M. Calvo, F. Valenti, P. Winkel, F. Friedrich, W. Wernsdorfer, A. V. Ustinov, H. Rotzinger, A. Monfardini, M. V. Fistul, and I. M. Pop. "Circuit quantum electrodynamics of granular aluminum resonators". Nature Communications 9, 3889 (2018).

[173] N. Samkharadze, A. Bruno, P. Scarlino, G. Zheng, D. P. DiVincenzo, L. DiCarlo, and L. M. K. Vandersypen. " High-Kinetic-Inductance Superconducting Nanowire Resonators for Circuit QED in a Magnetic Field". Phys. Rev. Applied 5, 044004 (2016).

[174] H. LeSueur, A. Svilans, N. Bourlet, A. Murani, L. Bergé, L. Dumoulin and P. Joyez. "Microscopic charged fluctuators as a limit to the coherence of disordered superconductor devices". ArXiv:1810.12801 (2018).

[175] A. J. Annunziata, D. F. Santavicca, L. Frunzio, G. Catelani, M. J. Rooks, Aviad Frydman, and D. E. Prober. "Tunable superconducting nanoinductors". Nanotechnology 21, 445202 (2010).

[176] J. R. Souquet and A. A. Clerk. "Fock-state stabilization and emission in superconducting circuits using dc-biased Josephson junctions". Phys. Rev. A **93**, 060301 (2016).

[177] J. Estève, M. Aprili and J. Gabelli. "Quantum dynamics of a microwave resonator strongly coupled to a tunnel junction". ArXiv:1807.02364 (2018).

[178] L.J. Swenson, P.K. Day, B.H. Eom, H.G. Leduc, N. Llombart, C.M. McKenney, O. Noroozian, and J. Zmuidzinas. "Operation of a titanium nitride superconducting microresonator detector in the nonlinear regime". Journal of Applied Physics 113, 104501 (2013).

[179] Averin, D. V.; Likharev, K. K. (1986-02-01). "Coulomb blockade of single-electron tunneling, and coherent oscillations in small tunnel junctions". Journal of Low Temperature Physics. 62 (3–4): 345–373.

[180] T. A. Fulton and G. J. Dolan. "Observation of single-electron charging effects in small tunnel junctions". Phys. Rev. Lett. 59, 109.

[181] Beenakker, C. W. J. "Theory of coulomb-blockade oscillations in the conductance of a quantum dot". Phys. Rev. B 44, 1646–1656 (1991).

[182] D. I. Bradley, R. E. George, D. Gunnarsson, R. P. Haley, H. Heikkinen, Yu. A. Pashkin, J. Penttilä, J. R. Prance, M. Prunnila, L. Roschier, M. Sarsby. "Nanoelectronic primary thermometer below 4 mK". Nat.Commun. 7, 10455 (2016).

[183] Z. Iftikhar, A. Anthore, S. Jezouin, F. D. Parmentier, Y. Jin, A. Cavanna, A. Ouerghi, U. Gennser, F. Pierre. "Primary thermometry triad at 6mK in mesoscopic circuits". Nat. Commun. 7: 12908 doi: 10.1038/ncomms12908 (2016).

université PARIS-SACLAY
ÉCOLE DOCTORALE
Physique et ingénierie : électrons, photons, sciences du vivant (EOBE)

Titre: Supercourant et dynamique d'une jonction Josephson constituée d'un nanotube de carbone dans le régime Kondo.

Mots clés: Effet Josephson, effet Kondo, nanotube de carbone, boite quantique, transition 0-π

Résumé: Au cours de cette thèse nous avons étudié la compétition entre deux types d'états fortement corrélés : l'effet Kondo, qui correspond à l'écrantage d'un moment magnétique isolé par les électrons de conduction d'un métal, et l'effet de proximité supraconducteur. Cette compétition a déjà été sondée à l'équilibre, en mesurant la relation courant-phase dans des jonctions Josephson à base de nanotube de carbone. Ces expériences ont révélé que l'état fondamental du système pouvait être soit un état doublet magnétique ou bien un état singulet non-magnétique et qu'une transition entre ces deux états pouvait être contrôlée par une tension grille ou bien par la phase supaconductrice. Dans ce travail de thèse nous avons montré qu'une telle transition pouvait être induite dynamiquement en mesurant l'effet Josephson AC de la jonction. L'émission Josephson est mesurée en couplant sur le même échantillon le nanotube de carbone à un détecteur quantique grâce à un circuit résonant supraconducteur. L'expérience montre que cette émission est fortement réduite dans les zones de tension grille où le courant critique était augmenté du fait de l'action conjuguée de l'effet Kondo et de l'effet de proximité. En comparant nos données à des calculs utilisant les techniques numériques du groupe de renormalisation, nous attribuons la forte diminution de l'effet Josephson AC à la dynamique des quasiparticules dans la boite quantique constituée par le nanotube de carbone qui conduit à une transition entre l'état fondamental singulet et l'état excité doublet.

Pour améliorer la méthode de détection à basse température, nous avons réalisé deux autres expériences. Dans la première, nous avons testé des lignes de polarisation continue réalisée au laboratoire qui permettent d'atteindre de faible température électronique, température mesurée grâce à un transistor à un électron. Nous avons par ailleurs fabriqué et mesuré un nouveau type de micro-résonateur supraconducteur, basé sur un matériau à forte inductance cinétique, des nanofils de tungstène déposé sous faisceau d'ions hélium focalisé. Ce type de résonateurs pourrait s'avérer très utile en tant que circuit de couplage résonant pour la détection haute fréquence "on-chip" et plus généralement pour réaliser des éléments supraconducteurs non-linéaires compacts pour l'électronique quantique.

Title: Supercurrent and dynamics in carbon nanotube Josephson Junction in the Kondo regime

Keywords: Josephson effect, Kondo effect, carbon nanotube, quantum dot, 0-π transition.

Abstract: During this thesis, we have studied the competition between two many-body effects: the Kondo effect, which is the screening of a localized magnetic moment by the conduction electrons of a conductor, and proximity induced superconductivity. The competition between these two effects has been already investigated at equilibrium, by monitoring the current phase relation of carbon nanotube-based Josephson junctions. These experiments have revealed phase and gate dependent quantum transitions between the magnetic doublet state and the Kondo screened singlet non-magnetic state of the nanotube. In the present work we show that this transition can be dynamically induced by exploring the AC Josephson emission. The AC Josephson emission can be measured by coupling the carbon nanotube to an on-chip quantum detector via a resonant coupling circuit. Experimental results show that this emission is strikingly reduced in the gate region where the critical current is enhanced due to the interplay of the Kondo effect and superconducting proximity effect. By comparing our data to numerical renormalization group calculations, we showed that the collapse of AC Josephson emission is due to the dynamics of quasiparticle in the quantum dot which induce a transition between a singlet ground state and a doublet excited state.

To improve our detection methods at low temperatures, we performed two other experiments. In the first experiment, we have tested new homemade filtering of DC lines in a cryo-free dilution refrigerator, by measuring the electronic temperature of a single electron transistor. In the second experiment, we have designed and measured a new type of superconducting micro-resonator, based on a high kinetic inductance material, namely tungsten nanowires deposited using a helium focus ion beam. This kind of resonator can be very useful to improve the resonant coupling for on-chip detection and more generally to engineer a compact non-linear high impedance superconducting element for quantum electronics.

Université Paris-Saclay
Espace Technologique / Immeuble Discovery
Route de l'Orme aux Merisiers RD 128 / 91190 Saint-Aubin, France